

INL REPORT

INL/EXT-18-44453
Unlimited Release
Printed February 2018

Pronghorn Theory Manual

April J. Novak
Ling Zou
John W. Peterson
David Andrs
Joe Kelly
Rachel N. Slaybaugh
Richard C. Martineau
Hans D. Gougar

Prepared by
Idaho National Laboratory
Idaho Falls, Idaho 83415

The Idaho National Laboratory is a multiprogram laboratory operated by Battelle Energy Alliance for the United States Department of Energy under DOE Idaho Operations Office. Contract DE-AC07-05ID14517.

Approved for public release; further dissemination unlimited.



Issued by the Idaho National Laboratory, operated for the United States Department of Energy by Battelle Energy Alliance.

NOTICE: This report was prepared as an account of work sponsored by an agency of the United States Government. Neither the United States Government, nor any agency thereof, nor any of their employees, nor any of their contractors, subcontractors, or their employees, make any warranty, express or implied, or assume any legal liability or responsibility for the accuracy, completeness, or usefulness of any information, apparatus, product, or process disclosed, or represent that its use would not infringe privately owned rights. Reference herein to any specific commercial product, process, or service by trade name, trademark, manufacturer, or otherwise, does not necessarily constitute or imply its endorsement, recommendation, or favoring by the United States Government, any agency thereof, or any of their contractors or subcontractors. The views and opinions expressed herein do not necessarily state or reflect those of the United States Government, any agency thereof, or any of their contractors.

Printed in the United States of America. This report has been reproduced directly from the best available copy.



INL/EXT-18-44453
Unlimited Release
Printed February 2018

Pronghorn Theory Manual

A.J. Novak*, L. Zou[†], J.W. Peterson[†], D. Andrs[†],
J. Kelly[×], R.N. Slaybaugh*, R.C. Martineau[†], and H.D. Gougar[†]

* University of California, Berkeley
3115 Etcheverry Hall
Berkeley, CA 94708

* Idaho National Laboratory
Idaho Falls, ID 83402

[×] Nuclear Regulatory Commission
Rockville, MD 20852

Contents

1	Introduction	10
2	Physical Models	11
2.1	Preliminary Considerations	15
2.2	The “Math” Behind the Porous Media Equations	16
2.2.1	Properties of Averages	18
2.2.2	A Generic Transport Equation	22
2.3	The Continuity Equation	23
2.4	The Momentum Equation	25
2.4.1	Porous Media Momentum Losses	39
2.4.2	The Trans-Forchheimer Regime	43
2.4.3	Anisotropic Porous Media	46
2.5	The Fluid Energy Equation	47
2.6	The Solid Energy Equation	58
2.7	The Legacy Pronghorn Equations	61
2.8	A Unified Approach to Solving the Navier-Stokes Equations	61
2.9	Boundary Conditions	66
2.9.1	The Continuity Equation	67
2.9.2	The Momentum Equation	67
2.9.3	The Energy Equation	68
2.10	Nondimensionalization of the Governing Equations	68
2.10.1	The Momentum Equation	69
2.10.2	The Energy Equations	69
2.10.3	Compressible Versus Incompressible Flows	71
2.10.4	Definitions of Dimensionless Numbers	74
2.10.5	Expected Values for Dimensionless Numbers	76
2.11	Summary of Physical Models	77
3	Kernels	80
4	AuxKernels	82
5	Interface Kernels	83
6	Boundary Conditions	84
6.1	The Conservative Equation Set	85
6.2	The Primitive Equation Set	86
7	Equations of State	87
7.1	Barotropic Equation of State	87
7.2	Stiffened Gas Equation of State	87
7.3	Isentropic Stiffened Gas Equation of State	88
7.4	Linear Equation of State	88
7.5	Ideal Gas Equation of State	88
7.5.1	Isentropic Relations	89
8	Porosity, Coordination Number, and Tortuosity	91
8.1	Porosity	96
8.1.1	OscillatoryPorosityFunction	96
8.1.2	ExponentialPorosityFunction	96
8.1.3	AnnularExponentialPorosityFunction	96
8.2	Coordination Number	97

8.3	Tortuosity	97
9	Friction Coefficients	98
9.1	Pebble Bed Correlations	98
9.1.1	Friction Coefficients Independent of the Wall	99
9.1.1.1	ErgunDragCoefficients	99
9.1.1.2	PiecewiseLinearDragCoefficients	100
9.1.1.3	KTADragCoefficients	101
9.1.2	Friction Coefficients Dependent on the Wall	101
9.1.2.1	EisfeldDragCoefficients	102
9.2	Pipe Flow Correlations	102
9.2.1	ChurchillDragCoefficients	103
10	Heat Transfer Coefficients.....	104
10.1	Pebble Bed Correlations	104
10.1.1	Correlations Independent of Porosity Variation	105
10.1.1.1	WakaoPebbleBedHTC	106
10.1.2	Correlations Dependent on Porosity Variation	106
10.1.2.1	GnielinskiPebbleBedHTC	106
10.1.2.2	KTAPebbleBedHTC	107
10.2	Wall-to-Fluid Correlations	107
10.2.1	AchenbachPebbleBedWallHTC	108
10.2.2	WakaoPebbleBedWallHTC	108
11	Effective Solid Thermal Conductivity κ_s	109
11.1	Models for κ_s	110
11.1.1	Parallel and Series Heat Transfer	110
11.1.2	Zehner, Bauer, and Schlunder	111
11.2	Models for $\kappa_{\text{radiation}}$	112
11.2.1	ZBS.....	113
11.2.2	BreitbachBarthels	113
11.3	Models for κ_{fluid} conduction	113
11.3.1	ZBS.....	113
11.4	Models for κ_{solid} conduction	114
11.4.1	ChanTien	114
11.4.2	ZBS.....	115
11.5	Variation of κ_s with System Parameters	116
12	Effective Fluid Thermal Conductivity κ_f.....	118
12.1	Axial Effective Thermal Conductivity	120
12.2	Radial Effective Thermal Conductivity	121
13	Fluid Properties	122
13.1	Gases	122
13.1.1	Helium	122
13.2	Liquid Salts	123
13.2.1	LiF-BeF ₂	123
13.2.2	NaF-ZrF	124
13.2.3	LiF-NaF-KF	124
13.2.4	KF-ZrF ₄	124
14	Solid Properties.....	125
14.1	ElectricGraphite.....	125
14.2	StainlessSteel.....	125

15 Stabilization Methods	126
15.1 An Example: The 1-D Convection-Diffusion Equation.....	126
15.2 Upwinding.....	129
15.2.1 Petrov-Galerkin Stabilization.....	130
15.2.2 Isotropic Diffusion Stabilization.....	132
15.2.3 Modified Quadrature Rules and Weight Functions.....	132
15.3 Streamline-Upwind Petrov-Galerkin Stabilization.....	133
15.3.1 Solution, Inviscid Flux, Diffusive Flux, and Source Vectors.....	134
15.3.2 Variable Derivatives.....	134
15.3.3 Inviscid Flux Jacobian Matrices.....	136
15.3.4 Diffusive Flux Jacobian Matrices.....	136
15.3.5 The Stabilizing Effect.....	136
15.3.6 Shock-Capturing.....	138
15.3.7 Calculation of the Stabilization Parameter τ_{SUPG}	138
15.4 SUPG Stabilization with the Primitive Equation Set.....	143
15.5 SUPG Stabilization with a Single Equation.....	143
16 The Finite Element Method	144
16.1 Weighted Residual Methods and the Galerkin Method.....	144
16.2 The Finite Element Method.....	145
16.2.1 The Weak Form.....	146
16.2.2 Shape Functions.....	146
16.2.3 Implementation Considerations.....	147
16.3 The Accuracy of the Finite Element Method.....	150
16.4 The Choice of Mesh Size.....	152
17 Solution of Nonlinear Equations	153
17.1 Newton's Method.....	154
17.2 Solution of Linear Equations.....	155
17.2.1 Direct Methods.....	156
17.2.2 Iterative Methods.....	156
17.2.2.1 Matrix Splitting Methods.....	158
17.2.2.2 The Steepest Descent Method.....	158
17.2.2.3 The Conjugate Directions Method.....	161
17.2.2.4 The Conjugate Gradient Method.....	163
17.2.2.5 The Arnoldi Process and the GMRES Algorithm.....	163
17.3 The Jacobian-Free Newton-Krylov Method.....	165
17.4 Time Stepping.....	166
18 Mathematical Definitions and Concepts	168
18.1 The Material Derivative.....	168
18.2 Norms.....	168
18.3 Suffix Notation.....	168
18.4 Vectors and Tensors.....	169
18.5 Essential Linear Algebra.....	170
19 Appendix	172
19.1 Ideal Gas SUPG.....	172
19.1.1 1-D.....	172
19.1.2 2-D.....	172
19.1.3 3-D.....	173
20 Notation	174
20.1 Greek Symbols.....	174
20.2 English Symbols.....	176

20.3 Math Symbols	179
20.4 Subscripts	179
20.5 Superscripts and Overbars	180
References	181

Acronyms

BC	Boundary Condition
BCC	Body Centered Cubic
BE	Backward Euler
CD	Conjugate Directions
CE	Compressible Euler
CFD	Computational Fluid Dynamics
CG	Conjugate Gradient
CNS	Compressible Navier-Stokes
CPU	Central Processing Unit
DEM	Discrete Element Method
DG	Discontinuous Galerkin
EOS	Equation of State
FCC	Face Centered Cubic
FD	Finite Difference
FE	Finite Element
FEM	Finite Element Method
FV	Finite Volume
GLS	Galerkin Least Squares
GMRES	Generalized Minimum Residual Method
HCP	Hexagonal Close Packing
HTGR	High Temperature Gas Reactor
HTR	High Temperature Reactor
HTR-PM	High Temperature Reactor Power Module
IC	Initial Condition
INL	Idaho National Laboratory
JFNK	Jacobian-Free Newton Krylov
LHS	left-hand-side
LOCA	Loss of Coolant Accident
LWR	Light Water Reactor

MOL	Method of Lines
MOOSE	the Multiphysics Object-Oriented Simulation Environment
ODE	Ordinary Differential Equation
PB-FHR	Pebble Bed High-Temperature Fluoride-Salt Cooled Reactor
PBMR-400	Pebble Bed Modular Reactor-400
PBWR	Pebble Bed Water Reactor
PDF	Probability Density Function
PEBFD	PEBble Fluid Dynamics
QU	Quadrature Upwinding
RANS	Reynolds Averaged Navier Stokes
RHS	right-hand-side
RMS	Root Mean Square
SC	Simple Cubic
SD	Steepest Descent
SND	Symmetric Negative Definite
SOR	Successive Over-Relaxation
SPD	Symmetric Positive Definite
SUPG	Streamline-Upwind Petrov-Galerkin
T/H	Thermal-Hydraulic
THTR	Thorium High Temperature Reactor
TMSR	Thorium Molten Salt Reactor
TRISO	TRistructural ISotropic

1 Introduction

This manual is intended to provide a thorough description of the governing equations, the relations used for material, heat transfer, and fluid flow parameters, and the numerical method utilized in Pronghorn. Detailed derivations of the governing equations are given, beginning from first principles in order to be as explicit as possible about assumptions made along the way [1]. Additional explanatory or tangential information that is not required for detailed understanding of the governing equations used in Pronghorn is shown in gray boxes in the text. The convention used in this document is to represent all class names (or file names) in `typewriter` font. An extensive verification process is completed for each class; details of this verification process can be found in `doc/verification`. Pronghorn is under a continual validation process to expand the range of code applicability; details of this validation process can be found in the `doc/papers` directories. The most up-to-date theory manual can be found in `doc/manual`. Any errors in this manual should be reported to the Pronghorn development team by email (any of `novak@berkeley.edu`, `ling.zou@inl.gov`, or `jw.peterson@inl.gov` if outside the Idaho National Laboratory (INL) organization).

Knowledge of the assumptions made in the governing equations is crucial to the correct use of any code. The table below collects the most important of these assumptions to serve as a concise reference for categories of simulations for which Pronghorn may give erroneous results. Other assumptions that are standard in the computational fluids community are detailed in the text, but are not included in the table below because they constitute assumptions made in virtually all choices of fluids simulation tools.

Table 1: Summary of major assumptions made in the governing equations in Pronghorn. The section where each assumption is discussed is also given for reference.

Assumptions made	Do not use Pronghorn if modeling:	Section
Continuum approximation is valid	$Kn \ll 1$	2.1
No isolated voids	Non-connected voids of fluid	2.2.1
Single-phase flow	Multi-phase flow	2.2.2
All fluxes are differentiable	Shock waves or discontinuities	2.3
The only body force is gravity	Electromagnetic fluids	2.4
Fluid is Newtonian	Certain oils or fluids with internal structure	2.4
Zero viscous dissipation	Strong shock waves	2.4
Fluid is pure	Chemically-reacting flows	2.5
Local thermodynamic equilibrium	Strong shock waves	2.5
Negligible viscous stress in fluid	Highly viscous fluid, $Re \ll 1$	2.4, 2.10
Negligible viscous heating of fluid	Large deformations in the fluid, $Br/Pe \gg 1$	2.5, 2.10
Solid velocity is zero	Moving solid phase	2.5, 2.10
Porosity independent of time	Moving solid phase	2.11
Beds of spherical particles	Beds of non-spherical particles or broken pebbles	2, 8
No internal bed structure	Beds with inserted control rods	8
Bed to pebble diameter ratio greater than 10	Narrow beds or large particles	8, 9

This document is organized as follows. In Section 2, the governing equations used in Pronghorn are derived and discussed. These equations rely on closure relationships that are discussed in Sections 7-14. Methods used to stabilize the governing equations are discussed in Section 15. The numerical method used is discussed in Sections 16 and 17. Finally, important mathematical definitions and notation are given in Sections 18 and 20.

2 Physical Models

A porous media consists of a solid matrix with interconnected voids filled with gas and/or liquid. On a spatial scale on the order of the pore size, the flow characteristics are highly irregular. On the engineering scale, flow properties are regular and predictable. Porous media models use averaging processes to relate pore features to engineering-scale phenomena such as pressure drop and average temperature rise. This averaging can be performed in either a spatial manner, in which case quantities are averaged over a physical volume to give a representative value, or in a statistical manner such as the ensemble-averaging process commonly used to describe turbulent flows. The spatial averaging technique is used in Pronghorn because it removes the need to average repeated simulation results and is simpler to implement. The development of porous media models is primarily motivated by three considerations:

1. The computational cost of modeling the complex solid-fluid structure is prohibitive even for regularly-spaced voids due to the high number of mesh elements required. For a non-porous simulation, not only is the solid-fluid structure complex, but resolution of boundary layers is needed. Fig. 1 shows an example of such a finely-refined mesh required for a Computational Fluid Dynamics (CFD) simulation of a subsection of a Body Centered Cubic (BCC) lattice. For a steady-state CFD simulation of eight fuel pebbles, roughly 2×10^6 elements and about 40 Central Processing Unit (CPU) minutes of runtime are required. To model the same volume with a porous media model requires only 20% of the mesh elements and only about 0.5 CPU minutes due to simpler models [2]. Extrapolating these numbers to a full core containing 470,000 fuel pebbles [3], a full-core CFD simulation would take 39,000 CPU hours, while a full-core porous media simulation would only require 490 CPU hours. Porous media simulations require only about 1% or less of the runtime of a comparable CFD simulation. Even compared to subchannel codes, porous media codes are still less expensive [4].
2. Mesh generation for touching solid bodies is difficult, since the meshes at pebble contact points must be made to share nodes, which often results in highly distorted meshes that can impact convergence [5]. The "near miss" method, where the pebble diameter is set to 99.5% of its actual value to avoid the difficulty of mesh contact, is often used to avoid this issue [5–10]; this method is shown in Fig. 1. For a porous media simulation, the mesh can be a simple structured mesh, such as the `GeneratedMesh` feature in the Multiphysics Object-Oriented Simulation Environment (MOOSE).
3. Even if computational cost were not an issue, the precise knowledge of the physical geometry of the structure likely cannot be known, and some type of averaging process has to be performed anyways, or else effort spent on making a guess for the solid geometry and running repeated calculations to determine sensitivity of results to assumed pebble distribution.

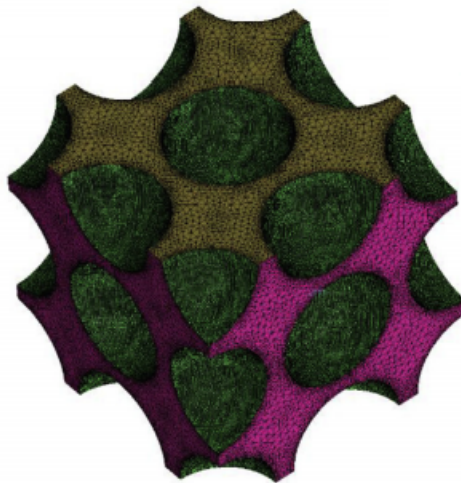


Figure 1: Computational mesh for fluid flow analysis of a subsection of a BCC lattice [7].

With porous media models, all quantities, such as velocities, densities, and temperatures, are volume-averaged, which eliminates the need to explicitly mesh the solid (and, technically, the fluid). Without a porous media model, roughly 10^{11} elements would be needed for the core. In addition, High Temperature Gas Reactor (HTGR) cores are often surrounded by large graphite reflectors that are not fully solid, but contain channels for core bypass flows that further extend the size of the mesh. Porous media models have a huge advantage in terms of mesh simplicity, which directly translates to a runtime reduction. An example of the difference between a porous and a non-porous mesh is shown in Fig. 2.

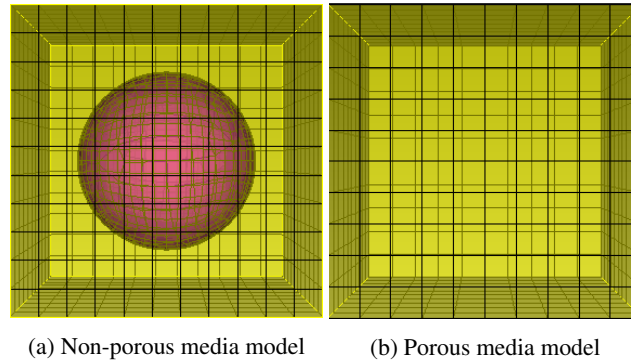


Figure 2: Difference between a mesh needed for (a) generic CFD calculations (no boundary layer mesh is shown) and (b) a porous media model.

Despite these substantial advantages of porous media models, porous media codes are not without their disadvantages. Porous media models cannot:

- Provide the exact fuel temperature profiles in the pebbles, since only a volume-averaged solid surface temperature is known. 1-D conduction solutions can be performed in the pebbles, but this only simulates “representative” pebbles. Peak fuel temperatures are roughly 100 °C higher than the surrounding gas temperatures [2] or molten salt temperatures [11]. This makes analysis of reactivity effects that are strongly dependent on fuel temperature distribution, such as the Doppler effect, challenging. Surface fuel temperature profiles shown in [7] are very complex, and reveal that temperatures are highest at stagnation points and in the recirculation flows that form behind the pebbles [8], and lowest at contact points aligned with the flow direction. The surface temperature on a single pebble varies by about 100-200°C for an ordered packing in flibe at nominal conditions, with the majority of the surface varying between 50-100°C [10].
- Reveal the locations of stagnation points. Stagnation points usually occur at or near the pebble contact points that are not aligned with the flow direction due to vortex formation and back flow [7, 12, 13]. Pressure is at a maximum at these stagnation points [7]. Fig. 3 shows the velocity vectors and fluid temperature for a BCC lattice. As can be seen, velocities are very low at the tops and bottoms of pebbles. Because convective cooling is directly dependent on fluid velocity, the lowest cooling occurs at the stagnation points, which may prove important for assessing fuel integrity and fluid phase change. The highest-temperature regions directly correlate to the lowest Nusselt numbers. Nusselt numbers typically range between 10 and 150 over the surface of a single sphere [14] and fuel temperatures vary by about 20 °C [2]. Porous media models cannot fully capture any spatial variation over pebble surfaces or interiors.

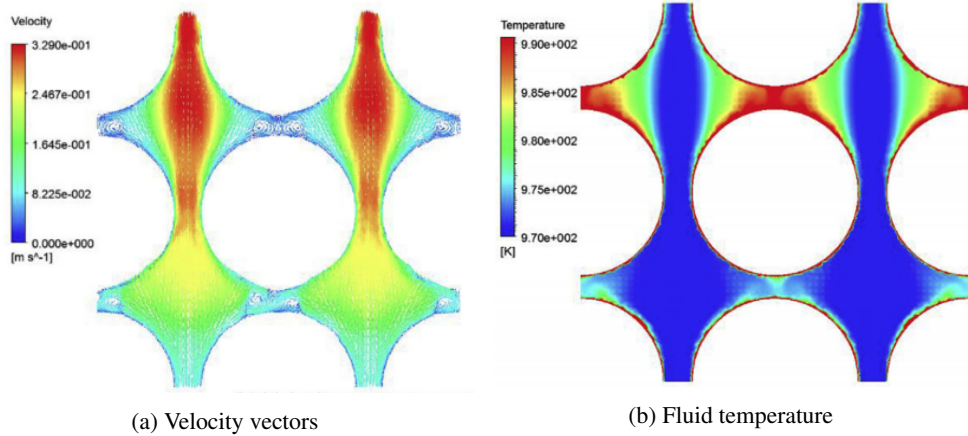


Figure 3: (a) Velocity vectors and (b) fluid temperature for a BCC lattice [7].

- Show velocity variation within the pores. The velocity in the center of the pores is about an order of magnitude larger than that on the edges as seen in Fig. 3(a), which like stagnation points, also has important consequences for heat transfer and drag [13].

Despite these disadvantages, it is generally agreed that porous media codes can reasonably capture global thermal-hydraulic characteristics like average velocities, temperatures, and pressure drops [2]. High-fidelity multiphysics simulations of pebble bed reactors usually allocate most of the computational cost to the neutronics solution, while porous media thermal-hydraulics is an acceptable simplification for the fluid flow and heat transfer provided the neutron migration length is larger than the porous media averaging length [15, 16]. Fig. 4 shows fluid velocities obtained with (a) non-porous and (b) porous media CFD. Porous media simulations represent homogenization of the flow results - multiplying the non-porous velocities by the porosity of about 0.38 according to Eq. (2.31) gives roughly the velocity magnitudes shown in the porous media solution. However, porous media models will not perfectly correspond to averaged CFD results - porous media models generally overpredict pressure drop relative to CFD models [2, 7]. Provided appropriate error bounds are assumed for the porous media results, porous media codes provide approximate spatially-averaged solutions.

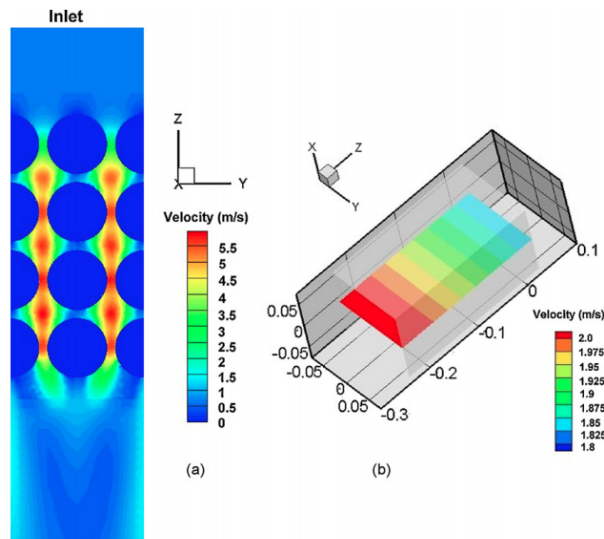


Figure 4: Velocity simulation results for a regular lattice for (a) non-porous and (b) porous CFD [2]. The porous media results are constant over the cross-section because constant porosity was used in the model.

Some of the limitations of porous media models could be partially overcome by coupling Pronghorn with a CFD code, which would use bulk simulation results from Pronghorn to evaluate more accurate Nusselt numbers and drag coefficients accounting for the velocity, temperature, and pressure distributions discussed above. However, care must be taken here, because the pebble packing arrangement in a bed is random, and CFD simulations performed for BCC and Face Centered Cubic (FCC) lattices actually show substantial variation from one another [8, 17]. Due to the tighter packing, enhanced turbulent mixing, and lack of larger pore spaces to support heat-transport-degrading vortices, FCC lattices have higher velocities (about 35% higher peak velocities) and better convective cooling (about 50% higher Nusselt number) than BCC lattices, which may be nonconservative in predicting fuel temperatures [10, 14]. More tortuous fluid paths in FCC lattices do result in higher pressure drops, which is conservative [10]. However, both BCC and FCC lattices differ considerably from randomly-generated beds. Pressure drops for a randomly-generated gas-cooled bed were 5.5 times larger than that in a BCC lattice of nearly equal porosity, while velocities were two times larger [17]. So, even CFD simulations cannot escape the need to generate many random meshes and evaluate by ensemble averaging the sensitivity of flow results to the geometry.

The majority of porous media research is found in the chemical, geological, and mechanical engineering fields. Example application areas include analysis of groundwater flow, heat transfer in tube-in-shell heat exchangers, and chemical reactions in complicated composite materials. In these fields, there are several common assumptions that are *not* valid when applied to nuclear reactors:

- The solid and fluid are in thermal equilibrium (at the same temperature). This is the default assumption in many codes such as FLUENT, and has been used incorrectly for the analysis of nuclear reactors in the past [7]. This assumption does not capture convective heat transfer between the solid and fluid.
- The flow is creeping, such that inertial and time dependent effects are neglected. This is an acceptable approximation for some experiments such as the SANA experiments [18], but is in general not valid.
- The porosity is constant in space. For geological applications, the domain is often so large and without a bounding, impermeable wall, that porosity can be treated as constant. Porosity variation near walls, discussed in Section 8, is essential to capturing flow channeling near reflector surfaces.
- The bed consists of fairly small particles on the order of 1 mm (except for the Pebble Bed Water Reactor (PBWR) design, which uses pebbles on the order of 2-10 mm housed in assemblies [9]). This can have a substantial impact on the fluid thermal dispersion (Section 12) and convective heat transfer (Section 10) for larger pebbles such as the 6 cm diameter fuel pebbles proposed for HTGR designs [19]. For example, the number and size of vortices in the pores generally increases with pore size [13].

These differences are important to keep in mind when borrowing models from these fields. These four assumptions cannot be made in Pronghorn, and for this reason the governing equations used are more complex than those found in many chemical and geological engineering papers. However, advantages in Pronghorn relative to the chemical, geological, and mechanical engineering fields include:

- All particles in the porous media are spherical. This eliminates difficulties associated with finding a representative particle diameter for correlations originally developed for beds of packed spheres. Throughout this document, it is assumed that the particles are spheres, and geometric shape factors appearing in correlations are neglected for simplicity.
- The particles are not themselves porous; no fluid flow occurs *through* the solid. Like the assumption of perfectly spherical particles, this also simplifies correlations.

Pronghorn solves the porous media equivalents of the Euler equations (conservation of mass, momentum, and energy in the fluid) and the solid conservation of energy equation. The discussion up to this point has focused exclusively on pebble bed systems. However, the porous media equations are valid for any mixture of solid and fluid provided the appropriate closure relationships describing interactions between the phases are used. Pronghorn is currently only applicable to pebble bed reactors. But, with the inclusion of anisotropic drag and effective thermal conductivity tensors,

Pronghorn may be used for plate and prismatic fuel systems. Porous medial models have been used for non-pebble bed type reactors in many cases [4]. Future work will involve this extension.

The development of Pronghorn was motivated by the fact that High Temperature Reactor (HTR)s are subject to different modeling limitations than Light Water Reactor (LWR)s, such as:

- While coolant in LWRs may experience a temperature increase of about 20-50°C across the core, HTRs operate with a several hundred °C increase, making incompressibility and Boussinesq assumptions invalid [20]. Pronghorn does not assume incompressibility.
- Many HTRs contain significant quantities of graphite, a high heat capacity material that greatly extends the time duration of equivalent transients in LWRs. The time to reach peak temperature in an HTR accident can be on the order of several days [21]. In addition, the renewed interest in salts, with higher heat capacities than helium, further increases the effective heat capacity of the core. The longer the transient, the more desirable a fully implicit solve that eliminates or reduces stability-related time step constraints. MOOSE contains both explicit and implicit solution methods.
- Pebble bed HTRs are often designed with sloping entrance and exit sections that may require unstructured meshes. LWR geometries, which always consist of parallel tubes in a cylindrical core, generally can use structured meshes. Pronghorn uses the Finite Element Method (FEM), which permits use of 3-D unstructured grids.
- HTRs are designed with a larger variety of coolants, such as helium, and fluoride salts. This requires a generic Equation of State (EOS) capability. Because Pronghorn uses the EOS from RELAP-7 or any custom user-provided EOS, Pronghorn can easily be used to model any type of fluid.

However, Pronghorn is also applicable to water-cooled pebble bed reactors such as the PBWR [9] provided the appropriate fluid properties are used and the constitutive laws hold for the range of dimensionless numbers expected. In this section, the governing equations will be presented by first deriving the non-porous media form of the governing equations. In order to derive the porous media versions of these equations, Section 2.2 introduces the spatial averaging theorems used. A summary of the equation set is given in Section 2.11.

2.1 Preliminary Considerations

The derivation of the conservation equations relies on the continuum approximation. As long as the flow length scale is much larger than the length scale on which atoms/molecules in the fluid exchange momentum, the fluid can be treated as a continuum. A fluid particle is defined as having a size intermediate to the flow and momentum exchange length scales, and consists of a group of atoms/molecules.

The validity of the continuum approximation can be quantified with the Knudsen number:

$$Kn = \frac{\lambda_{mfp}}{L} \quad (2.1)$$

where λ_{mfp} is the mean free path on which particles exchange momentum and L is the flow length scale. Using a highway as an example, small Kn signifies that heavy traffic results in one car influencing the behavior or another, while large Kn signifies a nearly empty highway where cars behave almost independently. For large Kn , statistical mechanics should be used to analyze fluid flow. Large Knudsen numbers are most likely to occur in gases; for gases at atmospheric pressure, $\lambda_{mfp} \approx 10^{-8}$ m. For reactor conditions, the mean free path will be even smaller due to operation at higher pressure.

This separation of scale is necessary in order to classify the types of forces experienced by a fluid particle and how those forces scale with the volume and surface area of the particle. There are two general types of forces experienced by a fluid particle:

1. External forces, or body forces, act on all molecules in the body. It is assumed that these forces, such as gravity, vary slowly over a fluid particle such that the force is proportional to the particle volume.
2. Internal forces, or surface forces, are exerted on a fluid particle by the surrounding fluid. It is assumed that these forces, such as shear stresses, are proportional to the surface area of the particle because the fluid particle is large relative to the length scale on which the atoms/molecules of the flow exchange momentum. This limits the momentum exchange to a thin surface layer.

The derivation of the governing equations for conservation of mass, momentum, and energy from first principles leads to the inclusion of terms that are often dropped in reactor applications because certain physics are insignificant. The ability to neglect terms in the governing equations depends on the magnitudes of certain parameters that can be obtained by non-dimensionalizing the governing equations. Because Pronghorn is intended to be a general code applicable to any reactor, it is imperative to ensure that dropping terms from the equations is valid for all classes of reactors (with single-phase coolant). It will be noted in this manual when terms are being neglected, and then in Section 2.10.5, representative values will be given for a variety of reactors to justify these simplifications.

Pronghorn can solve the governing equations derived in this section with one, two, or three dimensions. Reduced-dimension equations are theoretically obtained by averaging the general 3-D equation over one or more dimensions. This averaging process gives rise to additional terms that reflect averaged flow effects of the collapsed dimension(s) that must be provided by closure relationships [22] (chapter 1). While solving turbulence models in lower dimensions may justify including these terms, additional closure terms are neglected in all Pronghorn equations.

2.2 The “Math” Behind the Porous Media Equations

This section presents mathematical properties of averages that are required for the porous media equation derivation. The porous media equations are obtained by averaging the governing equations over a representative volume that contains both solid and liquid so that instead of solving for actual fluid and solid fields, we solve for the *averaged* fields. While solving for an averaged quantity initially seems easier than solving for the true physical quantity, the more you average the equations, the more supplementary information is required from experiments to regain lost information. This averaging approach is nearly equivalent to the temporal averaging of turbulent fluctuations that yield the Reynolds Averaged Navier Stokes (RANS) equations, except that here the averaging is done in space. This section presents theorems for relating a field Φ to its spatial average $\langle \Phi \rangle$. A k subscript is used to denote that a field Φ pertains to the k phase.

When a differential equation is averaged, the equation becomes an equation for the average of the original equation variable. For this average value to be a meaningful solution variable, it should not be dependent on the size of the volume that was used to compute it. For very small volumes, $\langle \Phi_k \rangle$ may be zero if there happens to be no phase k in that volume. As we increase the averaging volume size, $\langle \Phi_k \rangle$ will display statistical variation as the fraction of the phases in the volume varies. For a sufficiently large averaging volume, these variations will tend towards zero and the average becomes independent of the size of the averaging volume (provided the medium is fairly homogeneous). This requirement is no different than the requirement we flip a coin enough times to obtain a meaningful estimate of the fraction of the tosses that yield a heads-up coin. This independence of the average variable on the size of the averaging volume requires that the averaging volume be much larger than the volume on which the microscopic solution varies appreciably. This requirement can also be phrased in terms of length scales - if L is the length scale characterizing the averaging volume and l the length scale characterizing the scale on which the microscopic solution changes appreciably (often taken to be proportional to the pore diameter), then we require:

$$l \ll L \tag{2.2}$$

The requirement that an average be independent of the volume over which it is averaged is equivalent to the

requirement that the average of the average simply equals the average:

$$\langle\langle\Phi\rangle\rangle \equiv \langle\Phi\rangle \quad (2.3)$$

Eq. (2.3) also implies that $\langle\langle\Phi_k\rangle\rangle^k = \langle\Phi_k\rangle^k$.

Taking the average of the Taylor series expansion of $\langle\Phi\rangle$ about the centroid of the averaging volume can be used to estimate the order of accuracy of the assumption made in Eq. (2.3). Denoting the centroid with a subscript “c”, this Taylor series expansion is:

$$\langle\Phi\rangle = \langle\Phi\rangle_c + x_i \left(\frac{\partial\langle\Phi\rangle}{\partial x_i} \right)_c + \frac{x_i x_j}{2} \left(\frac{\partial^2\langle\Phi\rangle}{\partial x_i \partial x_j} \right)_c + \mathcal{O}(x_i x_j x_k) \quad (2.4)$$

Taking the average gives:

$$\langle\langle\Phi\rangle\rangle = \langle\Phi\rangle_c + \underbrace{\left(\frac{\partial\langle\Phi\rangle}{\partial x_i} \right)_c}_{\mathcal{O}(1/L^2)} \underbrace{\frac{1}{V} \int_V dV x_i}_{\mathcal{O}(l^2)} + \frac{1}{2} \underbrace{\left(\frac{\partial^2\langle\Phi\rangle}{\partial x_i \partial x_j} \right)_c}_{\mathcal{O}(1/L^2)} \underbrace{\frac{1}{V} \int_V dV x_i x_j}_{\mathcal{O}(l^2)} + \mathcal{O}(x_i x_j x_k) \quad (2.5)$$

where all terms that have been subscripted with “c” are independent of the averaging volume, and hence can be brought outside the integrals. The second term on the right-hand-side (RHS) is zero because the coordinate x_i is measured from the centroid of the averaging volume, so the integration represents an integral of an odd function. So, Eq. (2.3) is valid provided $l^2/L^2 \ll 1$, which is the same requirement in Eq. (2.2).

There is no inherent reason why volume integration, as opposed to area integration, would be preferred for the porous media derivation. Volume and area averages will be equivalent with second-order accuracy provided $l \ll L$. This result is most commonly used to equate porosity computed as a volume average and as an area average.

Express an area average as $\bar{\Phi}$:

$$\bar{\Phi} \equiv \frac{1}{S} \int_S \Phi dS \quad (2.6)$$

where S is a surface. Then, a volume average can be defined in terms of the area average by integrating all of the area averages taken perpendicular to the integration direction over the length l of the averaging volume:

$$\langle\Phi\rangle = \frac{1}{l} \int_{-l/2}^{+l/2} \bar{\Phi} dx \quad (2.7)$$

Expand the area average in a Taylor series about the centroid; because the integration is one-dimensional in space, suffix notation is not needed:

$$\bar{\Phi} = \bar{\Phi}_c + x \left(\frac{\partial\bar{\Phi}}{\partial x} \right)_c + \frac{x^2}{2} \left(\frac{\partial^2\bar{\Phi}}{\partial x^2} \right)_c + \frac{x^3}{6} \left(\frac{\partial^3\bar{\Phi}}{\partial x^3} \right)_c + \mathcal{O}(x^4) \quad (2.8)$$

Substituting this Taylor series into Eq. (2.7), the odd-order terms cancel because they represent integrations of

an odd function:

$$\begin{aligned}
\langle \Phi \rangle &= \frac{1}{l} \int_{-l/2}^{+l/2} dx \left(\bar{\Phi}_c + x \left(\frac{\partial \bar{\Phi}}{\partial x} \right)_c + \frac{x^2}{2} \left(\frac{\partial^2 \bar{\Phi}}{\partial x^2} \right)_c + \frac{x^3}{6} \left(\frac{\partial^3 \bar{\Phi}}{\partial x^3} \right)_c + \mathcal{O}(x^4) \right) \\
&= \bar{\Phi}_c + \underbrace{\frac{l^2}{24} \left(\frac{\partial^2 \bar{\Phi}}{\partial x^2} \right)_c}_{\mathcal{O}(1/L^2)} + \mathcal{O}(l^4)
\end{aligned} \tag{2.9}$$

So, area and volume averaging are equivalent provided Eq. (2.2) is valid.

2.2.1 Properties of Averages

In order to characterize the distribution of solid and fluid, a phase function f_k is defined to be unity in phase k and zero elsewhere:

$$f_k = \begin{cases} 1 & \text{in phase } k \\ 0 & \text{not in phase } k \end{cases} \tag{2.10}$$

$\langle \Phi_k \rangle$ is defined to be the average of Φ in the k -phase over the entire volume:

$$\langle \Phi_k \rangle \equiv \frac{1}{V} \int_V \Phi(\vec{x}, t) f_k(\vec{x}, t) dV \tag{2.11}$$

$\langle \Phi_k \rangle$ is often referred to as the phase, or extrinsic, average. Likewise, averages can be taken over the volume of just phase k :

$$\langle \Phi_k \rangle^k \equiv \frac{1}{V_k} \int_{V_k} dV \Phi(\vec{x}, t) f_k(\vec{x}, t) \tag{2.12}$$

$\langle \Phi_k \rangle^k$ is often referred to as the intrinsic phase average. Consider a domain consisting of solid and fluid. The density of the entire domain is the sum of the fluid density multiplied by the fluid volume and the solid density multiplied by the solid volume. In this case, $\langle \Phi_s \rangle$ represents the solid density averaged over the entire volume (the density of the volume if the fluid were void), while $\langle \Phi_s \rangle^s$ represents the average solid density (since the solid density is not necessarily constant in the solid volume). Both $\langle \Phi_k \rangle$ and $\langle \Phi_k \rangle^k$ are defined over all space, and are not restricted to existing in one or the other phase. Combining Eq. (2.12) and (2.11):

$$\langle \Phi_k \rangle = \varepsilon_k \langle \Phi_k \rangle^k \tag{2.13}$$

where a porosity for phase k is defined as the fraction of the total volume that is made up by phase k :

$$\begin{aligned}
\varepsilon_k &\equiv \frac{V_k}{V} \\
&= \frac{1}{V} \int_V f_k(\vec{x}, t) dV
\end{aligned} \tag{2.14}$$

In Pronghorn, the convention is that $\varepsilon_f \rightarrow \varepsilon$ represents the porosity of the fluid, while $\varepsilon_s \rightarrow 1 - \varepsilon$ is the porosity of the solid. In general, porosity is a function of space; models for porosity are discussed in Section 8. Isolated voids are not considered, so porosity is here strictly defined to refer to the ratio of *connected* void volume to total volume.

$$\varepsilon \equiv \frac{\text{(connected) void volume}}{\text{total volume}} \quad (2.15)$$

Taking averages of these averages just introduced gives two important identities for later use:

$$\langle \langle \Phi_k \rangle^k \rangle = \langle \Phi_k \rangle^k \quad (2.16)$$

$$\langle \langle \Phi_k \rangle \rangle^k = \langle \Phi_k \rangle \quad (2.17)$$

Eq. (2.16) is derived by swapping the order of integration:

$$\begin{aligned} \langle \langle \Phi_k \rangle^k \rangle &= \frac{1}{\mathcal{V}} \int_{\mathcal{V}} \langle \Phi_k \rangle^k d\mathcal{V} \\ &= \frac{1}{\mathcal{V}} \int_{\mathcal{V}} \left(\frac{1}{\mathcal{V}_k} \int_{\mathcal{V}_k} d\mathcal{V} \Phi(\vec{x}, t) f_k(\vec{x}, t) \right) d\mathcal{V} \\ &= \frac{1}{\mathcal{V}_k} \int_{\mathcal{V}_k} \left(\frac{1}{\mathcal{V}} \int_{\mathcal{V}} d\mathcal{V} \Phi(\vec{x}, t) f_k(\vec{x}, t) \right) d\mathcal{V} \\ &= \frac{1}{\mathcal{V}_k} \int_{\mathcal{V}_k} \langle \Phi_k \rangle d\mathcal{V} \\ &= \langle \Phi_k \rangle^k \end{aligned} \quad (2.18)$$

Likewise, the same procedure of swapping the order of integration can be used to give Eq. (2.17).

The porous media equations are derived by taking the spatial average of the governing equations. The goal of the derivation is to convert the solution variable from the microscopic variable to an averaged version of the same variable. The governing equation contains gradients, and hence identities to relate the averages of gradients with the gradients of averages is required. This derivation requires applying the general transport theorem in Eq. (2.44) to a material volume [23]:

$$\int_{\mathcal{V}} \nabla \Phi_k d\mathcal{V} = \nabla \int_{\mathcal{V}} \Phi_k d\mathcal{V} + \int_{S_i} \Phi_k \vec{n}_k dS \quad (2.19)$$

where S_i is the phase interface portion of the surface enclosing \mathcal{V} . Then, dividing each term by \mathcal{V} , Eq. (2.19) gives Eq. (2.20), where equality between the average of a gradient and the gradient of an average is offset by the integral of the solution over the phase interfacial area [24]. Eq. (2.20) shows two equivalent forms. Φ_k can be a scalar, vector, or a second-order tensor, and extension to cases where Φ_k is a vector simply change the gradients to divergences.

$$\langle \nabla \Phi_k \rangle = \nabla \langle \Phi_k \rangle + \frac{1}{\mathcal{V}} \int_{S_i} \Phi_k \vec{n}_k dS \quad (2.20a)$$

$$= \varepsilon_k \nabla \langle \Phi_k \rangle^k + \frac{1}{\mathcal{V}} \int_{S_i} \hat{\Phi}_k \vec{n}_k dS \quad (2.20b)$$

To derive Eq. (2.19), consider a point in the porous media located on a curve with an arc length s . At each point on this curve, we can define an averaging volume $\mathcal{V}(s)$ and the surface bounding that volume $S(s)$. By assuming that there is a continuous and invertible mapping between time t and arc length, t in Eq. (2.44) can be replaced by s :

$$\frac{d}{ds} \int_{\mathcal{V}(s)} \Phi d\mathcal{V} = \int_{\mathcal{V}(s)} \frac{\partial \Phi}{\partial s} d\mathcal{V} + \int_{S(s)} \Phi \frac{d\vec{x}}{ds} \cdot \vec{n} dS \quad (2.21)$$

where the velocity of the surface $\vec{V} = \partial \vec{x} / \partial t$ also substituted arc length for time. Φ only depends on arc length *implicitly* through its dependence on the spatial coordinate, so the first term on the RHS is zero. Due to the no-penetration condition, which requires that the normal component of velocity at a boundary must be zero, the nonzero component of $\partial \vec{x} / \partial s$ is perpendicular to the unit normal vector at the solid-fluid interfaces (giving a zero dot product). Hence, the area $S(s)$ that appears above can be simplified to the total area minus any solid-fluid interface area $S_i(s)$. For simplicity, this non-interface area is denoted as $S_e(s) \equiv S(s) - S_i(s)$:

$$\frac{d}{ds} \int_{\mathcal{V}(s)} \Phi d\mathcal{V} = \int_{S_e(s)} \Phi \frac{d\vec{x}}{ds} \cdot \vec{n} dS \quad (2.22)$$

Finally, each point along the curve is described by a position vector $\vec{x}_0(s)$ relative to some arbitrary origin. Let the vector $\vec{p}(s)$ represent the location of the points on the enclosing surface relative to a point on the curve. The vector representing points on the surface is then the sum of the vector to a point on the curve plus the vector to the point on the surface:

$$\vec{x}(s) = \vec{x}_0(s) + \vec{p}(s) \quad (2.23)$$

By the chain rule, the directional derivative with respect to the arc length is given as:

$$\begin{aligned} \frac{d}{ds} &= \frac{d}{dx_i} \frac{dx_i}{ds} \\ &= \nabla \cdot \frac{d\vec{x}}{ds} \end{aligned} \quad (2.24)$$

Using Eq. (2.23) and (2.24) in the transport theorem gives:

$$\frac{d\vec{x}_0}{ds} \cdot \left(\nabla \int_{\mathcal{V}(s)} \Phi d\mathcal{V} - \int_{S_e(s)} \Phi \vec{n} dS \right) = \int_{S_e(s)} \Phi \frac{d\vec{p}}{ds} \cdot \vec{n} dS \quad (2.25)$$

where $d\vec{x}_0/ds$ was removed from the integration because it is independent of the area integration variable for a fixed value of s . As long as $\mathcal{V}(s)$ is translated along the curve without rotation, then any differential change in \vec{p} is parallel to the surface, and hence the RHS term above is zero. Then, because the vector \vec{x}_0 was arbitrary, the expression must hold for any vector \vec{x}_0 , which means that the remaining multiplied term must be zero:

$$\nabla \int_{\mathcal{V}(s)} \Phi d\mathcal{V} - \int_{S_e(s)} \Phi \vec{n} dS = 0 \quad (2.26)$$

By the divergence theorem, a volume integral can be related to surface integrals:

$$\int_{\mathcal{V}(s)} \nabla \Phi d\mathcal{V} = \int_{S_e(s)} \Phi \vec{n} dS + \int_{S_i(s)} \Phi \vec{n} dS \quad (2.27)$$

Substituting Eq. (2.27) into Eq. (2.26) for the surface integral over the non-phase interface $S_e(s)$ gives Eq. (2.20)a.

Define a phase variable to be the sum of its average and a fluctuating component $\hat{\Phi}_k$; this is the same technique used in the derivation of the RANS equations, except that the porous media equations are averaged in space, while the RANS equations are averaged in time. By definition, the spatial average of the fluctuating component is zero.

$$\Phi_k f_k = \langle \Phi_k \rangle + \hat{\Phi}_k f_k \quad (2.28a)$$

$$= \langle \Phi_k \rangle^k + \hat{\Phi}_k f_k \quad (2.28b)$$

The presence of the phase function f_k indicates that Φ_k and $\hat{\Phi}_k$ both are zero in the non- k phases, which is why Eq. (2.28)b is also valid. Taking the average of the advective operator will require taking the average of a product, giving a term of the form $\langle \vec{V}_k \Phi_k \rangle$. By Eq. (2.14), an average over the entire volume can be related to an average over the phase volume, giving Eq. (2.29)a. Substituting Eq. (2.28) into Eq. (2.29)a for both \vec{V}_k and Φ_k gives Eq. (2.29)b and (2.29)c, where Eq. (2.29)c reuses Eq. (2.14).

$$\langle \vec{V}_k \Phi_k \rangle = \varepsilon_k \langle \vec{V}_k \Phi_k \rangle^k \quad (2.29a)$$

$$= \varepsilon_k \left(\langle \vec{V}_k \rangle^k \langle \Phi_k \rangle^k + \langle \vec{V}_k \hat{\Phi}_k \rangle^k \right) \quad (2.29b)$$

$$= \varepsilon_k \langle \vec{V}_k \rangle^k \langle \Phi_k \rangle^k + \langle \vec{V}_k \hat{\Phi}_k \rangle \quad (2.29c)$$

For some advective terms, an average of three terms will need to be performed. In this case, Eq. (2.29) becomes:

$$\begin{aligned} \langle a_k b_k c_k \rangle &= \varepsilon_k \langle a_k b_k c_k \rangle^f \\ &= \langle \hat{a}_k \hat{b}_k \hat{c}_k \rangle + \langle \hat{a}_k \hat{b}_k \rangle \langle c_k \rangle^k + \langle \hat{a}_k \hat{c}_k \rangle \langle b_k \rangle^k + \langle \hat{c}_k \hat{b}_k \rangle \langle a_k \rangle^k + \varepsilon_k \langle a_k \rangle^k \langle b_k \rangle^k \langle c_k \rangle^k \end{aligned} \quad (2.30)$$

According to Eq. (2.29)a, two different velocities can be defined for a porous media. \vec{v} represents the fluid velocity averaged over the entire medium (over solid and fluid). This velocity is often referred to as the Darcy velocity, the extrinsic phase velocity, or the superficial velocity. \vec{V} represents the fluid velocity averaged over only the fluid, and is referred to as the intrinsic phase velocity. Note that neither of these velocities are the actual *local* velocity of the fluid. These two representations of velocity are related to each other by the Dupuit-Forchheimer relationship, which derives from Eq. (2.29)a:

$$\vec{v} = \varepsilon \vec{V} \quad (2.31)$$

where the $\varepsilon_f \rightarrow \varepsilon$ notation has been used. Eq. (2.31) is used extensively in this manual, and is often referred to in the literature as the Dupuit-Forchheimer relationship.

Enough tools now exist to derive Eq. (2.20)b. Beginning from Eq. (2.14), use Eq. (2.28)a applied to gradients. Then, use Eq. (2.16) to rewrite $\langle \langle \nabla \Phi_k \rangle \rangle^k$ and Eq. (2.17) to rewrite $\langle \langle \nabla \hat{\Phi}_k \rangle \rangle^k$. Eq. (2.14) is then used to transform the last term.

$$\begin{aligned} \langle \nabla \Phi_k \rangle &= \varepsilon_k \langle \nabla \Phi_k \rangle^k \\ &= \varepsilon_k \left\langle \langle \nabla \Phi_k \rangle + \langle \nabla \hat{\Phi}_k \rangle \right\rangle^k \\ &= \varepsilon_k \left(\langle \nabla \langle \Phi_k \rangle^k \rangle + \langle \nabla \hat{\Phi}_k \rangle^k \right) \\ &= \varepsilon_k \langle \nabla \langle \Phi_k \rangle^k \rangle + \langle \nabla \hat{\Phi}_k \rangle \end{aligned} \quad (2.32)$$

Finally, apply Eq. (2.20)a to both terms on the RHS. Because there are no jump discontinuities in $\langle \Phi_k \rangle^k$ across the phase interface, the integral that arises due to $\langle \Phi_k \rangle^k$ is zero. Then, because the mean of any quantity related

to the fluctuation is zero, Eq. (2.20)b results.

$$\langle \nabla \Phi_k \rangle = \varepsilon_k \left[\nabla \langle \Phi_k \rangle^k + \frac{1}{V} \int_{S_i} \langle \Phi_k \rangle^k \vec{n} dS \right] + \nabla \langle \hat{\Phi}_k \rangle + \frac{1}{V} \int_{S_i} \hat{\Phi}_k \vec{n} dS \quad (2.33)$$

Adding Eqs. (2.20)a and (2.20)b and using Eq. (2.28) gives:

$$\frac{1}{V} \int_{S_i} \langle \Phi_k \rangle^k \vec{n} dS = -\langle \Phi_k \rangle^k \nabla \varepsilon_k \quad (2.34)$$

The integrals that appear in the two forms in Eq. (2.20) are specified by various constitutive relationships derived experimentally or semi-empirically for porous media. There is not general agreement on which form of Eq. (2.20) should be applied for each gradient and divergence that appears in the governing equations. So, great care must be taken when using correlations from the literature, since the author must specify whether Eq. (2.20)a or (2.20)b defines the constitutive relationship definition. Provided the author specifies whether the original or modified gradient averaging theorem is used, Eq. (2.34) can then be used to relate the author's correlation form to the other averaging theorem form. Gray shows this relationship for the mass transfer tortuosity, which is defined according to Eq. (2.20)b in Gray's work but according to Eq. (2.20)a in Slattery and Whitaker's works [25].

Finally, in order to express averages of time derivatives in terms of time derivatives of averages, divide each term in the general transport theorem in Eq. (2.44) by V and use the definitions of averages presented earlier [23]:

$$\frac{d}{dt} \frac{1}{V} \int_V \Phi_k dV = \frac{1}{V} \int_V \frac{\partial \Phi_k}{\partial t} dV + \frac{1}{V} \int_{S_i} \Phi_k \vec{w}_k \cdot \vec{n} dS \quad (2.35a)$$

$$\frac{d \langle \Phi_k \rangle}{dt} = \left\langle \frac{\partial \Phi_k}{\partial t} \right\rangle + \frac{1}{V} \int_{S_i} \Phi_k \vec{w}_k \cdot \vec{n} dS \quad (2.35b)$$

where \vec{w}_k is the velocity of the phase interface. Now that all of the mathematical tools for deriving the porous media version of an equation have been derived, Section 2.2.2 derives the porous media version of a generic transport equation.

2.2.2 A Generic Transport Equation

Consider a generic transport equation for phase k :

$$\frac{\partial \Phi}{\partial t} + \nabla \cdot (\Phi \vec{V}) = \nabla \cdot \tau - \nabla \mathcal{P} + S \quad (2.36)$$

where Φ is the conserved variable, \vec{V} the velocity, τ a generic deviatoric tensor, \mathcal{P} a general normal tensor, and S a source. The porous media version Eq. (2.36) is derived by first taking the phase average of each term by multiplying by f_k and integrating over the entire averaging volume:

$$\left\langle \frac{\partial \Phi_k}{\partial t} \right\rangle + \langle \nabla \cdot (\Phi_k \vec{V}_k) \rangle = \langle \nabla \cdot \tau_k \rangle - \langle \nabla \mathcal{P}_k \rangle + \langle S_k \rangle \quad (2.37)$$

Transform the time derivative using Eq. (2.35)b:

$$\left\langle \frac{\partial \Phi_k}{\partial t} \right\rangle \rightarrow \frac{\partial \langle \Phi_k \rangle}{\partial t} - \frac{1}{V} \int_{S_i} \Phi_k \vec{w}_k \cdot \vec{n} dS \quad (2.38)$$

Then, use Eq. (2.20) to transform the advective term, normal stress, and deviatoric stress terms. Two equivalent forms are given for each, and later discussion will select the most appropriate form for each.

$$\langle \nabla \cdot (\Phi_k \vec{V}_k) \rangle = \nabla \cdot \langle \Phi_k \vec{V}_k \rangle + \frac{1}{\mathcal{V}} \int_{S_i} \Phi_k \vec{V}_k \vec{n}_k dS \quad (2.39a)$$

$$= \epsilon_k \nabla \cdot \langle \Phi_k \vec{V}_k \rangle^k + \frac{1}{\mathcal{V}} \int_{S_i} \hat{\Phi}_k \hat{\vec{V}}_k \vec{n}_k dS \quad (2.39b)$$

$$\langle \nabla \cdot \mathcal{P}_k \rangle = \nabla \cdot \langle \mathcal{P}_k \rangle + \frac{1}{\mathcal{V}} \int_{S_i} \mathcal{P}_k \vec{n}_k dS \quad (2.40a)$$

$$= \epsilon_k \nabla \cdot \langle \mathcal{P}_k \rangle^k + \frac{1}{\mathcal{V}} \int_{S_i} \hat{\mathcal{P}}_k \vec{n}_k dS \quad (2.40b)$$

$$\langle \nabla \cdot \tau_k \rangle = \nabla \cdot \langle \tau_k \rangle + \frac{1}{\mathcal{V}} \int_{S_i} \tau_k \vec{n}_k dS \quad (2.41a)$$

$$= \epsilon_k \nabla \cdot \langle \tau_k \rangle^k + \frac{1}{\mathcal{V}} \int_{S_i} \hat{\tau}_k \vec{n}_k dS \quad (2.41b)$$

Finally, the source term is transformed using Eq. (2.29)a:

$$\langle S_f \rangle \rightarrow \epsilon_f \langle S_f \rangle^f \quad (2.42)$$

Combining Eqs. (2.37)-(2.42) provides the generic porous media transport equation. The appropriate version in Eqs. (2.39)-(2.41) must be selected. It is assumed that the fluid is single phase such that no phase change occurs. Pronghorn is therefore incapable of explicitly modeling phase change in liquid-cooled systems and several important transients, such as the pressure increase following water ingress [26]. In the case of no phase change, the velocity of the phase interface, \vec{w} , will simply equal the velocity at the interface, \vec{V} . So, for the advective term, the first form in Eq. (2.39) is selected because $\vec{V}_k = \vec{w}_k$ and the integral in Eq. (2.39) cancels the integral in Eq. (2.38). The next sections in this manual derive the conservation of mass, momentum, and energy equations for the fluid and solid phases for a porous media, beginning from the equations for a non-porous medium.

2.3 The Continuity Equation

Because mass is conserved, the rate of change of the mass within an arbitrary volume $\mathcal{V}(t)$ consisting of a system must be zero, because a system is defined such that its boundaries are closed to mass flow.

$$\frac{d}{dt} \int_{\mathcal{V}(t)} \rho d\mathcal{V} = 0 \quad (2.43)$$

where $d(\cdot)/dt$ represents the material derivative of (\cdot) , defined in Eq. (18.1). Taking the time derivative of an integral whose bounds depend on time requires the use of the general transport theorem:

$$\frac{d}{dt} \int_{\mathcal{V}(t)} \rho d\mathcal{V} = \int_{\mathcal{V}(t)} \frac{\partial \rho}{\partial t} d\mathcal{V} + \int_{S(t)} \rho \vec{w} \cdot \vec{n} dS \quad (2.44)$$

where \vec{w} is the velocity of the surface S , which in general does not need to equal the fluid velocity. If the general transport theorem is applied to a material volume that is enclosed by a material surface, then the velocity of that surface is simply equal to the fluid velocity. For application to material volumes, the general transport theorem is often referred to as the Reynolds Transport Theorem. By Eq. (2.44) applied to a material volume, the system perspective is converted to a control volume perspective:

$$\int_{\mathcal{V}(t)} \frac{\partial \rho}{\partial t} d\mathcal{V} + \oint_{S(t)} \rho \vec{V} \cdot \vec{n} dS = 0 \quad (2.45)$$

Throughout this manual, the divergence theorem will frequently be used to transform a surface integral into a volume integral. Inherent in this action is the assumption that the integrand of the surface integral is differentiable, which is not always true. For shock waves or discontinuities near surfaces, the fluxes that appear in surface integrals are *not* differentiable, and the divergence theorem cannot be used. In addition, if convective fluxes are not kept as surface terms, numerical errors in their volumetric representation will pollute the solution and cause violations of basic conservation of mass, momentum, and energy [22] (chapter 1). Despite this possibility, it is assumed in Pronghorn that all fluxes are continuous such that the divergence theorem can be used to convert a surface integral into a volume integral:

$$\int_{\mathcal{V}(t)} \frac{\partial \rho}{\partial t} d\mathcal{V} + \int_{\mathcal{V}(t)} \nabla \cdot (\rho \vec{V}) d\mathcal{V} = 0 \quad (2.46)$$

Then, because the selection of $\mathcal{V}(t)$ is arbitrary, the integrand must be zero, giving the conservation of mass equation, often referred to as the “continuity” equation:

$$\frac{\partial \rho}{\partial t} + \nabla \cdot (\rho \vec{V}) = 0 \quad (2.47)$$

Like all of the conservation equations to be derived in this manual, there are several *mathematically* equivalent forms. For instance, Eq. (2.47) can also be written as:

$$\frac{\partial \rho}{\partial t} + \vec{V} \cdot \nabla \rho + \rho \nabla \cdot \vec{V} = 0 \quad (2.48a)$$

$$\frac{d\rho}{dt} + \rho \nabla \cdot \vec{V} = 0 \quad (2.48b)$$

All of these forms are not necessarily equivalent once discretized with a numerical scheme [22] (chapter 1). When possible, all equations in Pronghorn will be solved in conservative form because it is then possible to exactly conserve mass, momentum, and energy. The conservative form of the continuity equation is given in Eq. (2.47), while the two above forms are in non-conservative, or “quasi-linear” form.

The porous media version of the continuity equation is derived beginning from Eq. (2.37) by replacing $\langle \Phi_k \rangle^k$ by $\langle \rho_f \rangle^f$. The time derivative is transformed with Eq. (2.38) and the advective term is transformed with Eq. (2.39)b. The deviatoric and normal stress terms are zero for the continuity equation. Because single phase fluid is assumed, there are no mass sources. The porous media continuity equation becomes:

$$\frac{\partial \langle \rho_f \rangle}{\partial t} + \nabla \cdot \langle \rho_f \vec{V}_f \rangle = 0 \quad (2.49a)$$

$$\frac{\partial (\epsilon \rho_f)}{\partial t} + \nabla \cdot (\epsilon \rho_f \vec{V}) = 0 \quad (2.49b)$$

In Pronghorn's notation, ρ_f represents the intrinsic phase average of the fluid density, and \vec{V} the intrinsic phase average of the fluid velocity.

2.4 The Momentum Equation

The momentum equation is derived in a similar manner as the continuity equation. Throughout the derivation of the momentum equation, suffix notation is used, which is described in Section 18.3 for those unfamiliar with the notation. The conservation of momentum equation is derived beginning from a general treatment of a balance of linear momentum for an arbitrary continuum. Consider a general balance of momentum:

$$\text{mass} \cdot \text{acceleration} = \text{body force} + \text{surface force} \quad (2.50)$$

Based on the continuum approximation, the mass-acceleration and body force terms scale as L^3 , while the surface force scales as L^2 . Dividing Eq. (2.50) through by L^2 , and then taking the limit as $L \rightarrow 0$ shows that at a point, surface forces are in equilibrium:

$$\lim_{L \rightarrow 0} \frac{1}{L^2} \oint_{S(t)} \vec{f}(\vec{n}) dS = 0 \quad (2.51)$$

where \vec{f} is the stress vector. It is the change in the stress, not the absolute value, that produces forces. Applying the principle of local stress equilibrium in Eq. (2.51) to a generic shape in a coordinate frame with mutually orthogonal axes \vec{e}_i will show that the surface force acting on the fluid particle is a linear, homogeneous function of the component of the unit normal \vec{n} . The coefficient of proportionality, which is independent of the surface normal, is defined to be the stress tensor σ :

$$\begin{aligned} f_i(\vec{n}) &= f_i(\vec{e}_j) n_j \\ &= \sigma_{ij} n_j \end{aligned} \quad (2.52)$$

To illustrate Eq. (2.52), consider the tetrahedron in Fig. 5 with surface dS on the slanted face and unit normal \vec{n} on the slanted face.

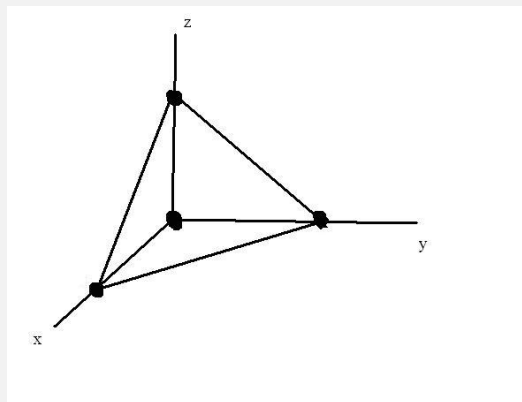


Figure 5: Tetrahedron defined in Cartesian space.

A stress vector \vec{f} produces a net force on this tetrahedron. The force acting on the slanted face must balance the forces acting on the other three faces. The area of one of the non-slanted faces is given by projecting the

slanted area onto the unit normal vector in that direction (i.e. the face perpendicular to the x -direction has area $n_x dS$).

$$\vec{f}(\vec{n}) \cdot dS + \vec{f}(-\vec{e}_1) \cdot n_x dS + \vec{f}(-\vec{e}_2) \cdot n_y dS + \vec{f}(-\vec{e}_3) \cdot n_z dS = 0 \quad (2.53)$$

By Newton's third law, $\vec{f}(\vec{n}) = -\vec{f}(-\vec{n})$. Inserting this above and canceling dS gives:

$$\vec{f}(\vec{n}) = \vec{f}(\hat{x})e_1 + \vec{f}(\hat{y})e_2 + \vec{f}(\hat{z})e_3 \quad (2.54)$$

In other words, $f_i(\vec{n}) = f_i(\vec{e}_j)n_j$. $f_i(\vec{e}_j)$ is defined to be the i -component of the stress vector acting on a surface of constant e_j , though this definition is sometimes reversed in the literature.

A general balance of linear momentum for a system follows the form in Eq. (2.50):

$$\underbrace{\frac{d}{dt} \int_{\mathcal{V}(t)} \rho V_i d\mathcal{V}}_{\text{rate of change of momentum}} = \underbrace{\int_{\mathcal{V}(t)} \rho b_i d\mathcal{V}}_{\text{body force}} + \underbrace{\oint_{S(t)} \sigma_{ij} n_j dS}_{\text{surface force}} \quad (2.55)$$

where \vec{b} is the body force vector, which for systems in which gravity is the only body force is \vec{g} , the gravity vector. The surface integral is converted to a volume integral using the divergence theorem:

$$\frac{d}{dt} \int_{\mathcal{V}(t)} \rho V_i d\mathcal{V} = \int_{\mathcal{V}(t)} \rho b_i d\mathcal{V} + \int_{\mathcal{V}(t)} \frac{\partial \sigma_{ij}}{\partial x_j} d\mathcal{V} \quad (2.56)$$

In order to differentiate under the integral sign, the integral on the left-hand-side (LHS) of Eq. (2.56) is split up into a finite series of N elements:

$$\frac{d}{dt} \int_{\mathcal{V}(t)} \rho V_i d\mathcal{V} \rightarrow \frac{d}{dt} \sum_{k=1}^N V_i(\rho d\mathcal{V}) \quad (2.57)$$

Because the mass of each element is constant by the assumption of conservation of mass in a system whose boundaries are closed to mass flow, the time differentiation can be moved inside the summation to act only on the velocity. Extending this argument to the continuous form in Eq. (2.56), and since Eq. (2.56) must apply for any arbitrary volume:

$$\rho \frac{dV_i}{dt} = \rho b_i + \frac{\partial \sigma_{ij}}{\partial x_j} \quad (2.58)$$

Eq. (2.58), often called the Cauchy equation, represents a balance of linear momentum for an arbitrary continuum, where the only assumption is that mass is conserved in that continuum. In its most general form the stress tensor contains nine unknowns ($i = 1, 2, 3$ and $j = 1, 2, 3$). The stress tensor is symmetric if the only moments on the fluid particle are due to the resultant body and surface forces. It is rare that a fluid experience moments in excess of the body and surface force moments, and symmetry of the stress tensor is assumed in virtually all fluids codes, reducing nine unknowns to six.

The conditions under which the stress tensor is symmetric can be shown by applying conservation of angular

momentum to a fluid particle:

$$\frac{d}{dt} \int_{\mathcal{V}(t)} (\vec{x} \times \rho \vec{V})_i d\mathcal{V} = \int_{\mathcal{V}(t)} (\vec{x} \times \rho \vec{b})_i d\mathcal{V} + \oint_{S(t)} (\vec{x} \times \sigma_{kl} n_l)_i dS \quad (2.59)$$

The divergence theorem is used to convert the surface integral to a volume integral, and the cross product on the LHS is expanded after assuming conservation of mass as in Eq. (2.57) such that the time integration only acts of $\vec{x} \times \vec{V}$:

$$\int_{\mathcal{V}(t)} \left(\frac{d\vec{x}}{dt} \times \vec{V} + \vec{x} \times \frac{d\vec{V}}{dt} \right)_i \rho d\mathcal{V} = \int_{\mathcal{V}(t)} (\vec{x} \times \rho \vec{b})_i d\mathcal{V} + \int_{\mathcal{V}(t)} \frac{\partial}{\partial x_l} (\vec{x} \times \sigma_{kl})_i d\mathcal{V} \quad (2.60)$$

The material derivative of \vec{x} is expanded as follows, where $\partial \vec{x} / \partial t$ is zero due to the assumption of a fixed reference frame:

$$\begin{aligned} \frac{d\vec{x}}{dt} &= \frac{\partial \vec{x}}{\partial t} + V_i \frac{\partial x_j}{\partial x_i} \\ &= V_i \delta_{ij} \\ &= V_i \end{aligned} \quad (2.61)$$

After inserting suffix notation for cross products according to Eq. (18.4), where ϵ_{ijk} is the permutation symbol defined in Eq. (18.5), and recognizing that the selection of the volume is arbitrary:

$$\rho \epsilon_{ijk} x_j \frac{dV_k}{dt} = \rho \epsilon_{ijk} x_j b_k + \frac{\partial}{\partial x_l} (\epsilon_{ijk} x_j \sigma_{kl}) \quad (2.62)$$

The stress tensor is symmetric if the only moments in the material are due to the body and surface forces. Because Eq. (2.58) represents a balance of linear momentum due to only body and surface forces, inserting Eq. (2.58) into the LHS of Eq. (2.62) for $\rho dV_k/dt$ satisfies this assumption:

$$\epsilon_{ijk} x_j \left(\rho g_k + \frac{\partial \sigma_{kl}}{\partial x_l} \right) = \epsilon_{ijk} x_j \rho b_k + \epsilon_{ijk} \left(x_j \frac{\partial \sigma_{kl}}{\partial x_l} + \frac{\partial x_j}{\partial x_l} \sigma_{kl} \right) \quad (2.63)$$

Canceling terms, and recognizing that $\frac{\partial x_j}{\partial x_l} = \delta_{jl}$, Eq. (2.63) reduces to:

$$\epsilon_{ijk} \sigma_{jk} = 0 \quad (2.64)$$

A useable form of the momentum equation is obtained by inserting a constitutive relation for σ_{ij} into Eq. (2.58). To understand this constitutive relation, the kinematics of deformation must be understood. The motion of a material element can be decomposed into three contributions - 1) translation, 2) rigid rotation, and 3) stretching. To understand the form of each of these components, consider two points in a fluid that are sufficiently close such that their separation $\vec{\delta r}$ can be approximated by a one-term Taylor series:

$$\begin{aligned} V_i(\vec{r} + \vec{\delta r}, t) - V_i(\vec{r}, t) &= \frac{d}{dt} (\delta r_i) \\ &\approx \delta r_j \frac{\partial V_i}{\partial x_j} \end{aligned} \quad (2.65)$$

The \approx symbol is replaced by $=$ for the remainder of this discussion. Translation of a fluid particle is simply related to the magnitude of the velocity. The other two components require more explanation. Any tensor can be written as

the sum of symmetric and antisymmetric parts:

$$\frac{\partial V_i}{\partial x_j} = \underbrace{\frac{1}{2} \left(\frac{\partial V_i}{\partial x_j} + \frac{\partial V_j}{\partial x_i} \right)}_{\text{symmetric}} + \underbrace{\frac{1}{2} \left(\frac{\partial V_i}{\partial x_j} - \frac{\partial V_j}{\partial x_i} \right)}_{\text{antisymmetric}} \quad (2.66)$$

where the symmetric and antisymmetric components are denoted as:

$$e_{ij} = \frac{1}{2} \left(\frac{\partial V_i}{\partial x_j} + \frac{\partial V_j}{\partial x_i} \right) \quad (2.67)$$

$$\xi_{ij} = \frac{1}{2} \left(\frac{\partial V_i}{\partial x_j} - \frac{\partial V_j}{\partial x_i} \right) \quad (2.68)$$

Within the applicability of a one-term Taylor series, ξ_{ij} represents a rigid rotation of the fluid particle.

To understand ξ_{ij} , assume for the time being that $e_{ij} = 0$. Combining Eqs. (2.65) and (2.68):

$$\frac{d}{dt}(\delta r_i) = \delta r_j \xi_{ij} \quad (2.69)$$

Taking the scalar product with δr_i gives:

$$\delta r_i \frac{d}{dt}(\delta r_i) = \delta r_i \delta r_j \xi_{ij} \quad (2.70)$$

$\delta r_i \delta r_j$ is symmetric, while ξ_{ij} is antisymmetric. The product of any symmetric tensor with an asymmetric tensor must be zero by Eq. (18.10), so the above becomes:

$$\frac{1}{2} \frac{d}{dt}(\delta r_i)^2 = 0 \quad (2.71)$$

Hence, if only the antisymmetric component ξ_{ij} is present, because δr_i^2 is constant in time, δr_i is also constant in time, and ξ_{ij} cannot represent stretching, since stretching would change δr_i . Because translation is accounted for simply by the magnitude of the velocity V_i , ξ_{ij} therefore represents a rigid rotation.

To determine the angular velocity characterizing this rigid rotation, Eq. (2.68) can be rewritten as:

$$\xi_{ij} = -\frac{1}{2} \epsilon_{ijk} \omega_k \quad (2.72)$$

where ω is the vorticity:

$$\omega = \nabla \times \vec{V} \quad (2.73)$$

Hence, the angular velocity of the rigid rotation is $\omega/2$. Because the symmetric component must be associated with stretching, the vorticity can also be interpreted as twice the instantaneous angular velocity of a material line element that is originally aligned along one of the eigenvectors of e_{ij} (in which case e_{ij} does not contribute anything to the angular velocity).

Within the limits of the one-term Taylor series, e_{ij} , which is often referred to as the “deformation tensor,” represents stretching of the fluid particle along the principal axes (eigenvectors) of e_{ij} . The rate of stretching along an eigenvector is given by the eigenvalue corresponding to that eigenvector. When both e_{ij} and ξ_{ij} are nonzero (a material line not parallel to one of the principal axes of e_{ij}), the fluid particle is both stretched and rotated.

To understand e_{ij} , consider for the time being that $\xi_{ij} = 0$. Then, Eq. (2.65) reduces to:

$$\begin{aligned}\frac{d}{dt}(\delta r_i) &= \delta r_j e_{ij} \\ &= \delta r_j \frac{\partial V_i}{\partial x_j}\end{aligned}\quad (2.74)$$

Apply the chain rule to the velocity gradient term, and in the last step switch the dummy index i with k :

$$\begin{aligned}\frac{d}{dt}(\delta r_i) &= \delta r_j \frac{\partial V_i}{\partial x_k} \frac{\partial x_k}{\partial x_j} \\ &= \delta r_j \frac{\partial V_i}{\partial x_i} \delta_{ij}\end{aligned}\quad (2.75)$$

where λ_e are the eigenvalues and δr_j are the eigenvectors. Because e_{ij} is a 3×3 symmetric, real, matrix, there will be three unique, real, and mutually orthogonal eigenvectors. These eigenvectors are referred to as the “principal axes,” and the eigenvalues as the “principal strain rates” of e_{ij} . Because the relative velocity is along δr_j , e_{ij} represents stretching with rate λ_e in three mutually orthogonal directions (along the eigenvectors of e_{ij}).

The diagonal components of e_{ij} represent stretching, while the off-diagonal components represent rotation of eigenvectors relative to another eigenvector (as opposed to ξ_{ij} representing instantaneous rotation).

In order to interpret the shear components of e_{ij} , consider two material line elements \vec{l} and \vec{m} which at $t = 0$ are orthogonal. Applying Eq. (2.65) to these two line elements gives:

$$\frac{d}{dt}(l_i) = l_j \frac{\partial V_i}{\partial x_j} \quad (2.76)$$

$$\frac{d}{dt}(m_i) = m_j \frac{\partial V_i}{\partial x_j} \quad (2.77)$$

Taking the scalar product of each equation with m_i and l_i , respectively, and then adding these two equations and reversing the chain rule:

$$\begin{aligned}\frac{d}{dt}(l_i m_i) &= m_i l_j \frac{\partial V_i}{\partial x_j} + l_i m_j \frac{\partial V_i}{\partial x_j} \\ &= m_i l_j \frac{\partial V_i}{\partial x_j} + l_j m_i \frac{\partial V_j}{\partial x_i} \\ &= 2m_i l_j e_{ij}\end{aligned}\quad (2.78)$$

where the indices have been exchanged on the second term because the summation is symmetric with respect to i and j and Eq. (2.67) has been used to insert e_{ij} . Using Eq. (18.3), and defining $\vec{l} = l\hat{l}$ and $\vec{m} = m\hat{m}$, the LHS expands to:

$$\frac{d}{dt}(\vec{l} \cdot \vec{m}) = lm \frac{d}{dt}(\hat{l} \cdot \hat{m}) + (\hat{l} \cdot \hat{m}) \frac{d}{dt}(lm) \quad (2.79)$$

where the fact that \vec{l} and \vec{m} are orthogonal at $t = 0$ cancels the second term. Combining Eqs. (2.79) and (2.78), and using the properties of a dot product $\vec{l} \cdot \vec{m} = lm \cos(\theta)$:

$$\frac{d}{dt} \cos(\theta) = 2\hat{m}_i \hat{l}_j e_{ij} \rightarrow \frac{d\theta}{dt} = -2\hat{m}_i \hat{l}_j e_{ij} \quad (2.80)$$

where again, $\theta(t = 0) = \pi/2$ has been used. Because \vec{l} and \vec{m} are assumed orthogonal, the only nonzero terms occur for $i \neq j$. From this result, $2e_{12}$ is the magnitude of the angular velocity of \vec{l} relative to \vec{m} . Hence, the off-diagonal components of e_{ij} represent a rotation of eigenvector i relative to eigenvector j .

From Eq. (2.67), the trace of the deformation tensor is equal to the divergence of velocity:

$$\text{Tr}(e_{ij}) = \nabla \cdot \vec{V} \quad (2.81)$$

For a small volume, the time rate of change of the volume is approximately equal to the velocity of the surface dotted with the unit normal, which can be rewritten using the divergence theorem:

$$\begin{aligned} \frac{d\mathcal{V}}{dt} &\approx \oint_{S(t)} \vec{V} \cdot \vec{n} dS \\ &= \int_{\mathcal{V}(t)} \nabla \cdot \vec{V} d\mathcal{V} \end{aligned} \quad (2.82)$$

If the volume is sufficiently small such that the divergence of the velocity can be taken as constant over the volume, the divergence of the velocity can be interpreted as the fractional rate of increase of an infinitesimal volume:

$$\frac{1}{\mathcal{V}} \frac{d\mathcal{V}}{dt} \approx \nabla \cdot \vec{V} \quad (2.83)$$

Knowing that $\nabla \cdot \vec{V}$ represents a volume expansion, the motion at a point described by Eq. (2.65) can be separated into 1) an isotropic radial expansion (characterized by $\nabla \cdot \vec{V}$), 2) a volume-preserving motion obtained by subtracting off the volume change from e_{ij} , and 3) a rigid rotation:

$$\begin{aligned} V_i(\vec{r} + \delta\vec{r}, t) - V_i(\vec{r}, t) &= \delta r_j \frac{\partial V_i}{\partial x_j} \\ &= \delta r_j e_{ij} - \frac{1}{2} \delta r_j \varepsilon_{ijk} \omega_k \\ &= \underbrace{\frac{1}{3} \delta r_i \nabla \cdot \vec{V}}_{\text{radial expansion}} + \underbrace{\delta r_j \left(e_{ij} - \frac{1}{3} \nabla \cdot \vec{V} \delta_{ij} \right)}_{\text{constant-volume motion}} - \underbrace{\frac{1}{2} \delta r_j \varepsilon_{ijk} \omega_k}_{\text{rigid rotation}} \end{aligned} \quad (2.84)$$

A factor of $1/3$ appears to cancel the 3 that results from summation over i and j in δ_{ij} . To formulate the Navier-Stokes equations requires a constitutive relation for the stress tensor σ_{ij} . The Navier-Stokes equations assume a Newtonian fluid constitutive relationship. A fluid is defined to be Newtonian if σ_{ij} is a linear, isotropic, function of the deformation tensor e_{ij} . Because ξ_{ij} causes a rigid rotation, but no deformation, there is no contribution in the stress tensor due to ξ_{ij} . For simple fluids, the Newtonian approximation is an excellent assumption over a wide range of strain rates, but for molecules consisting of long chains of atoms, or with suspended solid particles, shearing the fluid breaks down an internal structure that can align the molecules such that the shear stress is not a linear function of the velocity gradient. For example, paint on a brush has high enough viscosity to not drip off the paint brush, but once sheared on a wall, viscous forces decrease such that it can be easily applied. Conversely, quicksand becomes more

viscous the more it is sheared. Neither paint nor quicksand are well-described as Newtonian fluids. The constitutive relationship for a Newtonian fluid is, in its most general form:

$$\sigma_{ij} = -P\delta_{ij} + c_{ijkl}e_{kl} \quad (2.85)$$

where P is the thermodynamic pressure determined from an equation of state and c_{ijkl} is a fourth-order tensor. The first term on the RHS represents isotropic shear stresses due to pressure forces, a requirement to match hydrostatic observations.

A decomposition of the stress vector into normal and shear components is:

$$\vec{f} = \underbrace{\vec{f} \cdot \vec{n} \vec{n}}_{\text{normal}} + \underbrace{(\vec{f} - \vec{f} \cdot \vec{n} \vec{n})}_{\text{shear}} \quad (2.86)$$

In the absence of deformation, the shear stress is zero, so \vec{f} must be parallel to \vec{n} , and hence the hydrostatic term in Eq. (2.85) is multiplied by δ_{ij} to reflect the fact that pressure only acts normal to a fluid particle surface when there is no motion.

In order to reduce the 81 components of c_{ijkl} to a fewer number of unique parameters, isotropy of the stress is assumed. If the axes of a rectangular prism of fluid are aligned with the eigenvectors of e_{ij} , then the fluid element will not rotate, but will experience a stretching along the eigenvectors of e_{ij} . For an isotropic fluid, the stresses on the faces of that prism should be purely normal - if this were not the case, then the fluid would have a preferred direction of deformation, a characteristic that is anisotropic. In order to show that selecting axes along the principal axes of e_{ij} for an isotropic fluid produces a diagonal e_{ij} (since a diagonal e_{ij} means that there are only normal stresses inducing stretching, and no shear stresses inducing rotation), it must be required that when the principal axes of σ_{ij} coincide with the principal axes of e_{ij} , σ_{ij} is diagonal (no shear stresses).

In order to demonstrate that the principal axes of e_{ij} coincide with those of σ_{ij} for an isotropic fluid, and that both are therefore diagonal, consider a change of axes that gives the following transformation rule:

$$a_{ij} = \vec{e}_i' \cdot \vec{e}_j = \begin{bmatrix} +1 & 0 & 0 \\ 0 & -1 & 0 \\ 0 & 0 & -1 \end{bmatrix} \quad (2.87)$$

where a_{ij} is a transformation matrix given by Eq. (18.8). By the transformation rule for tensors given in Eq. (18.9),

$$\sigma_{i'j'} = a_{ik}a_{jl}\sigma_{kl} \quad (2.88)$$

For the test problem in Eq. (2.87), due to Eq. (2.88), $\sigma_{12} = -\sigma_{12}$. By applying the vector transformation rule in Eq. (18.8) to e_{ij} , the components of e_{ij} are unchanged by the coordinate transformation. Hence, from Eq. (2.85):

$$\sigma_{12} = c_{12kl}e_{kl} \quad (2.89a)$$

$$-\sigma_{12} = c_{12kl}e_{kl} \quad (2.89b)$$

The only way these can simultaneously be satisfied is if $\sigma_{12} = 0$. Similar arguments can be made for each component of σ_{ij} .

This requirement gives $c_{12kl} = 0$ for all k and l . Physically, this means that the same stress rate in different coordinate frames does not give rise to different shear stresses. This reduces the 81 components of c_{ijkl} to nine.

Isotropy also requires that $c_{1122} = c_{1133}$, since rotation of axes by 90° should not change the fluid response. With these requirements, the constitutive relationship for a Newtonian fluid is:

$$\sigma_{ij} = -P\delta_{ij} + 2\mu e_{ij} + \lambda \nabla \cdot \vec{V} \delta_{ij} \quad (2.90)$$

where μ is the dynamic viscosity and λ is a second parameter that is in general very difficult to measure. By investigating the form of σ_{11} , $2\mu = c_{1111} - c_{1122}$ and $\lambda = c_{1122}$; hence, μ and λ just represent combinations of the entries of the c_{ijkl} tensor. For Newtonian fluids, the dynamic viscosity is only a function of pressure and temperature, while for non-Newtonian fluids, there is a nonlinear relationship between μ and pressure, temperature, and the rate of shearing strain (assuming that the Newtonian constitutive law is still used).

The viscosity of gases is commonly described by Sutherland's model, where $\mu \propto T^{3/2}/(T + 110)$. That is, for gases, viscosity increases with temperature. For liquids, viscosity decreases with temperature. While Newtonian fluids in general allow viscosity to also be a function of pressure, the dependence is generally very weak [22] (chapter 1).

Interpreting the significance of each of the terms in Eq. (2.90) is difficult unless the equation is rearranged similar to Eq. (2.84) by subtracting out the component associated with a volume change:

$$\sigma_{ij} = -P\delta_{ij} + \underbrace{2\mu \left(e_{ij} - \frac{1}{3} \nabla \cdot \vec{V} \delta_{ij} \right)}_{\text{deviatoric stress tensor}} + \underbrace{\left(\lambda + \frac{2\mu}{3} \right) \nabla \cdot \vec{V} \delta_{ij}}_{\text{volume dissipative term}} \quad (2.91)$$

The deviatoric stress tensor τ , also known as the viscous shear stress tensor, represents volume-preserving deformation (no volume change), which can be represented in both suffix and vector notation as:

$$\begin{aligned} \tau &\equiv 2\mu \left(e_{ij} - \frac{1}{3} \nabla \cdot \vec{V} \delta_{ij} \right) \\ &\equiv \mu \left(\nabla V_i + (\nabla V_i)^T \right) - \frac{2\mu}{3} \nabla \cdot \vec{V} \mathbf{I} \end{aligned} \quad (2.92)$$

Due to competing effects of volume change and isochoric deformation, measuring λ is virtually impossible. The Navier-Stokes equations are therefore usually posed in terms of μ and ζ , the bulk viscosity:

$$\zeta = \lambda + \frac{2\mu}{3} \quad (2.93)$$

The second law of thermodynamics requires μ and ζ to be positive, while nothing can be said of the sign of λ . The bulk viscosity, also referred to as the second coefficient of viscosity, is only important for highly compressible fluids (very high temperatures and pressures) [22] (chapter 1). In compression or expansion, internal processes act to restore thermodynamic equilibrium. These restoration processes usually act very quickly such that they almost exactly coincide with the change in volume of the fluid particle. However, if there is a significant discrepancy between the attainment of thermal equilibrium and the change in volume, then ζ may be much larger than μ , and cannot be neglected. The term proportional to ζ is often referred to as the viscous dissipation term. This term is only present if $\nabla \cdot \vec{V} \neq 0$, and hence is zero for incompressible fluids. In situations with significantly nonzero $\nabla \cdot \vec{V}$, the physics are often so different that an entirely different constitutive equation should be used.

Substituting Eq. (2.91) into Eq. (2.58) gives the Navier-Stokes equations, where Eq. (2.67) is used to insert the

definition of e_{ij} and Eq. (2.93) for the definition of ζ :

$$\begin{aligned}\rho \frac{dV_i}{dt} &= \rho b_i + \frac{\partial}{\partial x_j} \left\{ -P\delta_{ij} + 2\mu \left[\frac{1}{2} \left(\frac{\partial V_i}{\partial x_j} + \frac{\partial V_j}{\partial x_i} \right) - \frac{1}{3} \nabla \cdot \vec{V} \delta_{ij} \right] + \zeta \nabla \cdot \vec{V} \delta_{ij} \right\} \\ &= \rho b_i - \nabla P + \nabla \cdot \left[\mu \left(\nabla V_i + (\nabla V_i)^T \right) - \frac{2\mu}{3} \nabla \cdot \vec{V} \mathbf{I} \right] + \nabla \cdot (\zeta \nabla \cdot \vec{V})\end{aligned}\quad (2.94)$$

The volume dissipative term is commonly neglected by setting $\lambda = -2\mu/3$, i.e. setting $\zeta = 0$ [27]. This gives the conservation of momentum equation most commonly used:

$$\frac{\partial(\rho \vec{V})}{\partial t} + \nabla \cdot (\rho \vec{V} \vec{V}) = \rho \vec{b} - \nabla P + \nabla \cdot \tau \quad (2.95)$$

where $\vec{V} \vec{V}$ is short-hand notation for $\vec{V} \otimes \vec{V} = V_i V_j$, which represents an outer product of \vec{V} with itself.

Eq. (2.95) has been expressed in conservative form by using the chain rule such that the time rate of change term acts on momentum, instead of velocity.

$$\frac{\partial}{\partial t} (\rho \vec{V}) + \nabla \cdot (\rho \vec{V} \vec{V}) = \rho \frac{\partial \vec{V}}{\partial t} + \underbrace{\vec{V} \cdot \left[\frac{\partial \rho}{\partial t} + \nabla \cdot (\rho \vec{V}) \right]}_{\text{continuity}} + \rho \vec{V} \cdot \nabla \vec{V} \quad (2.96)$$

Conservation of mass is assumed in the Cauchy momentum equation, and hence can be canceled. This same process can be performed for any material derivative of the form $\rho d\Phi/dt$, where $\rho\Phi$ is a conserved variable and mass is conserved, and will be used frequently throughout this manual.

Many equivalent forms of Eq. (2.95) can be derived through manipulations of mechanical and thermodynamic relations. The Crocco-Vazsonyi and Bernoulli forms are derived here for later use in specifying stagnation Boundary Condition (BC)s. By expressing $\partial V_i/\partial x_j$ in terms of e_{ij} defined in Eq. (2.67) and ξ_{ij} defined in Eqs. (2.68) and (2.72), and taking the inner product with V_j , gives:

$$V_j \frac{\partial V_i}{\partial x_j} = \nabla \cdot \left(\frac{1}{2} V^2 \right) + \vec{\omega} \times \vec{V} \quad (2.97)$$

Inserting the above result and the enthalpy differential defined in Eq. (2.167) into Eq. (2.95) gives the Crocco-Vazsonyi form of the Navier-Stokes equations:

$$\frac{\partial \vec{V}}{\partial t} + \nabla \cdot \left(\frac{1}{2} V^2 + h + gz \right) - T \nabla s - \vec{V} \times \vec{\omega} - \frac{1}{\rho} \nabla \cdot \tau = 0 \quad (2.98)$$

where it was assumed that $\vec{b} = \vec{g}$ and gravity was moved inside the gradient by assuming that $\vec{g} = -g \vec{e}_z$ such that $\nabla(gz) = g \vec{e}_z$. Eq. (2.98) reveals that steady flow will be rotational in a stationary reference frame unless the flow is isentropic, frictionless, isoenergetic (term in parentheses is constant), and the inlet BC is irrotational. The Bernoulli equation can be derived from Eq. (2.98) using two different approximations. If the flow is isentropic, steady, irrotational, and frictionless:

$$\nabla \cdot \left(\frac{1}{2} V^2 + h + gz \right) = 0 \quad (2.99)$$

Eq. (2.99) applies *anywhere* in the flow field. The second approach for deriving the Bernoulli equation takes the scalar product of Eq. (2.98) with velocity to obtain a form of the equation that only applies along a streamline in isentropic, steady, and frictionless flow:

$$\vec{V} \cdot \nabla \left(\frac{1}{2} V^2 + h + gz \right) = 0 \quad (2.100)$$

Eq. (2.100) does not require the irrotational assumption made in Eq. (2.99). It is also frequently assumed in the Bernoulli equation that the flow is incompressible, in which case $e = e(\rho, s)$ is constant, and h in Eqs. (2.99) and (2.100) could be replaced by P/ρ . These equations will be revisited in Section 7 for defining stagnation BCs for the ideal gas EOS.

The incompressible form of Eq. (2.94) is derived by expanding all terms and setting $\nabla \cdot \vec{V} = 0$. This gives, in vector notation, the Navier-Stokes equation for an incompressible fluid:

$$\rho \frac{d\vec{V}}{dt} = \rho \vec{b} - \nabla P + \nabla \cdot (\mu \nabla \vec{V}) \quad (2.101)$$

For constant viscosity, the Laplace operator $\nabla \cdot \nabla(\cdot)$ can be seen to represent isotropic diffusion. Assuming $\vec{b} = \vec{g}$, Eq. (2.101) is sometimes written without the gravitational term by bundling gravity into the pressure term by assuming incompressible flow. Assume that gravity is equal $\vec{g} = g \vec{e}_3$ and introduce a reduced pressure P' :

$$P' = P + \rho g z \quad (2.102)$$

Then, as long as ρ is uniform (incompressible flow), the gravitational term appearing in Eq. (2.101) can be represented as:

$$\rho \vec{g} \rightarrow \rho g \vec{e}_z \rightarrow \nabla(\rho g z) \quad (2.103)$$

Then, gravity can be bundled in with the pressure term in Eq. (2.101):

$$\rho \frac{d\vec{V}}{dt} = -\nabla P' + \nabla \cdot \tau \quad (2.104)$$

If there are no free surfaces in the domain, then pressure will not appear as a BC, and within the constraints of incompressible flow, gravity does not impact the solution. The thermodynamic pressure P must be used in force calculations, but you can compute forces using the reduced pressure provided a buoyancy term is added to compensate.

By nondimensionalization arguments, the Navier-Stokes equations will only provide a good representation of a fluid if both the normalized velocity and surface force (drag) are dependent only on the scaled spatial and time scales and Re . This is often referred to as “Reynolds number similarity.”

Nondimensionalize Eq. (2.104) with the following nondimensional variables:

$$V^+ = \frac{V}{V_o}, \quad x^+ = \frac{x}{L}, \quad t^+ = \frac{t}{L/V_o}, \quad P'^+ = \frac{P' - P_\infty}{\rho V_o^2} \quad (2.105)$$

where the pressure is scaled such that it balances $\rho d\vec{V}/dt$. After dividing by the coefficient on the advective term:

$$\frac{dV^+}{dt^+} = -\nabla P'^+ + \frac{1}{Re} \nabla^2 V^+ \quad (2.106)$$

An alternative nondimensionalization of $P'^+ = (P' - P_\infty)/(\mu V_o/L)$ could have been selected had the problem been expected to be dominated by viscous forces. With this selection, Re would appear on the advective term instead of on the viscous term. By inspection, the nondimensional solution depends only on the nondimensional spatial and time scales and Re :

$$V^+ = f(x^+, t^+, Re) \quad (2.107)$$

For a fluid to satisfy the Navier-Stokes equations, Reynolds number similarity requires that the above observation must hold. The *solution* \vec{V}/V_o should be the same for geometrically similar bodies on a nondimensional time scale with the same Reynolds number. However, pressure need not be the same between two physical scenarios that match the terms on the RHS of Eq. (2.107). Reynolds number similarity can be extended to show how the surface force on a body should scale with nondimensional quantities. The surface force on a body is:

$$F_i = \oint_{S(t)} \sigma_{ij} n_j dS \quad (2.108)$$

Introducing the following nondimensional quantities:

$$dS^+ = \frac{dS}{L^2}, \quad \sigma_{ij}^+ = \frac{\sigma_{ij}}{\rho V_o^2} \quad (2.109)$$

Then, the force on a body is nondimensionalized such that it is only a function of nondimensional time and Re :

$$\frac{F_i}{\rho V_o^2 L^2} = \oint_{S(t)} \sigma_{ij}^+ n_j dS^+ = f(x^+, t^+, Re) \quad (2.110)$$

For geometrically similar objects, the resultant surface force is only a function of the nondimensional time and length scales and Re . Some fluids that have different viscosities when being stretched or sheared may appear to be Newtonian at low shear stresses, but fail to satisfy Reynolds number similarity. This provides an additional method of verifying that a fluid is Newtonian.

To derive the porous media version of Eq. (2.95), replace Φ_k by $\rho_k \vec{V}_k$ in Eq. (2.37). The time derivative term is rewritten using Eqs. (2.38) and (2.29):

$$\left\langle \frac{\partial(\rho \vec{V})}{\partial t} \right\rangle \rightarrow \frac{\partial(\varepsilon \langle \rho_f \rangle^f \langle \vec{V}_f \rangle^f)}{\partial t} + \frac{\partial \langle \hat{\rho}_f \hat{\vec{V}}_f \rangle}{\partial t} - \frac{1}{V} \int_{S_i} \rho_f \vec{V}_f \vec{w}_f \cdot \vec{n}_f dS \quad (2.111)$$

The advective term is rewritten using Eq. (2.39)a and Eq. (2.29):

$$\begin{aligned} \langle \nabla \cdot (\rho_f \vec{V}_f \vec{V}_f) \rangle &\rightarrow \nabla \cdot \left[\varepsilon \langle \rho_f \rangle^f \langle \vec{V}_f \rangle^f \langle \vec{V}_f \rangle^f + \langle \hat{\rho}_f \hat{\vec{V}}_f \rangle \langle \vec{V}_f \rangle^f \right] + \\ &\nabla \cdot \left[\langle \hat{\rho}_f \hat{\vec{V}}_f \rangle \langle \hat{\vec{V}}_f \rangle^f + \langle \rho_f \rangle^f \langle \hat{\vec{V}}_f \hat{\vec{V}}_f \rangle + \langle \hat{\rho}_f \hat{\vec{V}}_f \hat{\vec{V}}_f \rangle \right] + \frac{1}{V} \int_{S_i} \rho_f \vec{V}_f \vec{V}_f \cdot \vec{n}_f dS \end{aligned} \quad (2.112)$$

The normal stress term is $\mathcal{P} = P$, and is transformed using Eq. (2.40)b:

$$\langle \nabla P_f \rangle \rightarrow \varepsilon_f \nabla \langle P_f \rangle^f + \frac{1}{V} \int_{S_i} \hat{P}_f \vec{n}_f dS \quad (2.113)$$

This averaging theorem, rather than Eq. (2.40)a, is the form used by many authors because the correct zero-velocity physics are obtained using the porous media closure relations readily available in the literature [28]. If Eq. (2.40)a

were used instead, then for a zero-velocity, non-constant porosity system, the gradient in porosity would induce a nonphysical flow. The deviatoric stress term is transformed using Eq. (2.41)a:

$$\langle \nabla \cdot \boldsymbol{\tau}_f \rangle \rightarrow \nabla \cdot \langle \boldsymbol{\tau}_f \rangle + \frac{1}{\mathcal{V}} \int_{S_i} \boldsymbol{\tau}_f \vec{n}_f dS \quad (2.114)$$

Finally, the source term is $S_f = -\rho_f \nabla \phi_{g,f}$, where it has been assumed that $\vec{b} = \vec{g}$ and $\phi_{g,f}$ is the gravitational potential function:

$$\nabla \phi_{g,f} \equiv -g \vec{e}_z \quad (2.115)$$

Using Eq. (2.29), then Eq. (2.20)b, gives:

$$\langle S_f \rangle \rightarrow -\langle \rho_f \nabla \phi_{g,f} \rangle \quad (2.116a)$$

$$\rightarrow -\langle \rho_f \rangle^f \langle \nabla \phi_{g,f} \rangle - \langle \hat{\rho}_f \nabla \hat{\phi}_{g,f} \rangle \quad (2.116b)$$

$$\rightarrow -\varepsilon_f \langle \rho_f \rangle^f \nabla \langle \phi_{g,f} \rangle^f - \frac{\langle \rho_f \rangle^f}{\mathcal{V}} \int_{S_i} \hat{\phi}_{g,f} \vec{n}_f dS \quad (2.116c)$$

where the fluctuating product is zero because the gravitational acceleration is assumed constant. Combining all of these terms gives:

$$\begin{aligned} & \frac{\partial(\varepsilon \langle \rho_f \rangle^f \langle \vec{V}_f \rangle^f)}{\partial t} + \frac{\partial \langle \hat{\rho}_f \hat{V}_f \rangle}{\partial t} + \nabla \cdot \left[\varepsilon \langle \rho_f \rangle^f \langle \vec{V}_f \rangle^f \langle \vec{V}_f \rangle^f + \langle \hat{\rho}_f \hat{V}_f \rangle \langle \vec{V}_f \rangle^f \right] \\ & \frac{1}{\mathcal{V}} \int_{S_i} \rho_f \vec{V}_f (\vec{V}_f - \vec{w}_f) \cdot \vec{n}_f dS + \nabla \cdot \left[\langle \hat{\rho}_f \hat{V}_f \rangle \langle \hat{V}_f \rangle^f + \langle \rho_f \rangle^f \langle \hat{V}_f \hat{V}_f \rangle + \langle \hat{\rho}_f \hat{V}_f \hat{V}_f \rangle \right] = \\ & \nabla \cdot \langle \boldsymbol{\tau}_f \rangle + \frac{1}{\mathcal{V}} \int_{S_i} \boldsymbol{\tau}_f \vec{n}_f dS - \varepsilon_f \nabla \langle P_f \rangle^f - \frac{1}{\mathcal{V}} \int_{S_i} (\hat{P}_f - \langle \rho_f \rangle^f \hat{\phi}_{g,f}) \vec{n}_f dS - \varepsilon_f \langle \rho_f \rangle^f \nabla \langle \phi_{g,f} \rangle^f \end{aligned} \quad (2.117)$$

where $\langle \rho_f \rangle^f$ has been moved inside the surface integral of the gravitational force for later illustration. Assuming no phase change between the fluid and solid, $\vec{V}_f - \vec{w}_f = 0$. For flows in which thermal and pressure gradients are not very large, density gradients will be much smaller than velocity gradients at the microscopic level. Therefore, terms containing $\hat{\rho}_f$ can be neglected [23]. This simplifies Eq. (2.117) to:

$$\begin{aligned} & \frac{\partial(\varepsilon \langle \rho_f \rangle^f \langle \vec{V}_f \rangle^f)}{\partial t} + \nabla \cdot \left[\varepsilon \langle \rho_f \rangle^f \langle \vec{V}_f \rangle^f \langle \vec{V}_f \rangle^f + \langle \rho_f \rangle^f \langle \hat{V}_f \hat{V}_f \rangle \right] = \\ & \nabla \cdot \langle \boldsymbol{\tau}_f \rangle + \frac{1}{\mathcal{V}} \int_{S_i} \boldsymbol{\tau}_f \vec{n}_f dS - \varepsilon_f \nabla \langle P_f \rangle^f - \frac{1}{\mathcal{V}} \int_{S_i} (\hat{P}_f - \langle \rho_f \rangle^f \hat{\phi}_{g,f}) \vec{n}_f dS - \varepsilon_f \langle \rho_f \rangle^f \nabla \langle \phi_{g,f} \rangle^f \end{aligned} \quad (2.118)$$

Assuming a Newtonian fluid such that $\boldsymbol{\tau}$ is given by Eq. (2.92), $\nabla \cdot \langle \boldsymbol{\tau}_f \rangle$ becomes:

$$\begin{aligned} \nabla \cdot \langle \boldsymbol{\tau}_f \rangle & \rightarrow \nabla \cdot (\mu_f \nabla \langle \vec{V}_f \rangle) + \nabla \cdot (\mu \nabla \langle \vec{V}_f \rangle)^T - \frac{2}{3} \nabla (\mu \nabla \cdot \langle \vec{V}_f \rangle) + \\ & \nabla \cdot \frac{\mu}{\mathcal{V}} \int_{S_i} \vec{V}_f \vec{n}_f dS + \nabla \cdot \frac{\mu}{\mathcal{V}} \int_{S_i} (\vec{V}_f)^T \vec{n}_f dS + \frac{2}{3} \nabla \frac{\mu}{\mathcal{V}} \int_{S_i} \vec{V}_f \cdot \vec{n}_f dS \end{aligned} \quad (2.119)$$

where it has been assumed that the dynamic viscosity does not change appreciably over the averaging volume such that Eq. (2.29) is not needed for products of viscosity with velocity gradients and divergences. Because the no-slip

condition is satisfied at the phase interfaces, provided the medium does not deform very rapidly, all three integral terms in Eq. (2.119) are zero.

The $\tau_f \vec{n}_f$ integral in Eq. (2.118) represents the average viscous drag of the solid on the fluid. This average viscous stress can be expressed in terms of the difference in intrinsic velocities between the phases, since the viscous stress should be zero if neither phase is moving. Express the dependence as a second-order Taylor series expansion as a function of the phase velocity difference:

$$\frac{1}{V} \int_{S_i} \tau_f \cdot \vec{n}_f dS \rightarrow \mu \epsilon_f \mathcal{A} \left(\langle \vec{V}_s \rangle^s - \langle \vec{V}_f \rangle^f \right) + \mu \epsilon_f \mathcal{B} : \left(\langle \vec{V}_s \rangle^s - \langle \vec{V}_f \rangle^f \right) \cdot \left(\langle \vec{V}_s \rangle^s - \langle \vec{V}_f \rangle^f \right) \quad (2.120)$$

where \mathcal{A} is a second-order tensor and \mathcal{B} a third-order tensor [23]. The $\langle \hat{\vec{V}}_f \hat{\vec{V}}_f \rangle$ term will only be zero if the fluid moves at the same velocity as the fluid-solid interface. This requirement can also be expressed as a two-term Taylor series, where Eq. (2.14) is first used to obtain an intrinsic phase average:

$$\begin{aligned} \langle \hat{\vec{V}}_f \hat{\vec{V}}_f \rangle &\rightarrow \epsilon_f \langle \hat{\vec{V}}_f \hat{\vec{V}}_f \rangle^f \\ &\rightarrow \epsilon_f \mathcal{C} \cdot \left(\langle \vec{V}_s \rangle^s - \langle \vec{V}_f \rangle^f \right) + \epsilon_f \mathcal{L} : \left(\langle \vec{V}_s \rangle^s - \langle \vec{V}_f \rangle^f \right) \left(\langle \vec{V}_s \rangle^s - \langle \vec{V}_f \rangle^f \right) \end{aligned} \quad (2.121)$$

where \mathcal{C} is a third-order tensor and \mathcal{L} is a fourth-order tensor. Because $\langle \hat{\vec{V}}_f \hat{\vec{V}}_f \rangle^f$ is symmetric, both of these tensors must be symmetric in their first two indices, and \mathcal{L} also in the last two indices. Only one more constitutive relationship is required to fully express the momentum equation. This can be reasoned by showing that the fluctuating pressure and gravitational field are nonzero perturbations that can still satisfy $\nabla \langle P_f \rangle^f + \langle \rho_f \rangle^f \nabla \langle \phi_{g,f} \rangle^f = 0$, such as in cases where the fluid is hydrostatic. Therefore, using a second-order Taylor series in terms of the known quantities,

$$\begin{aligned} \frac{1}{V} \int_{S_i} \left(\hat{P}_f + \langle \rho_f \rangle^f \hat{\phi}_{g,f} \right) \vec{n}_f dS &\rightarrow \epsilon_f \mathcal{E} \cdot \left(\nabla \langle P_f \rangle^f + \langle \rho_f \rangle^f \nabla \langle \phi_{g,f} \rangle^f \right) + \\ &\epsilon_f \mathcal{M} : \left(\nabla \langle P_f \rangle^f + \langle \rho_f \rangle^f \nabla \langle \phi_{g,f} \rangle^f \right) \left(\nabla \langle P_f \rangle^f + \langle \rho_f \rangle^f \nabla \langle \phi_{g,f} \rangle^f \right) \end{aligned} \quad (2.122)$$

where \mathcal{E} is a second-order tensor and \mathcal{M} is a third-order tensor that is symmetric in its second and third indices. A factor of ϵ_f arbitrarily appears for later convenience. Combining Eqs. (2.119)-(2.122) into Eq. (2.118) gives the porous media momentum equation for a Newtonian fluid:

$$\begin{aligned} \frac{\partial (\epsilon \langle \rho_f \rangle^f \langle \vec{V}_f \rangle^f)}{\partial t} + \nabla \cdot \left[\epsilon \langle \rho_f \rangle^f \langle \vec{V}_f \rangle^f \langle \vec{V}_f \rangle^f \right] + \nabla \cdot \left[\epsilon_f \langle \rho_f \rangle^f \mathcal{C} \cdot \left(\langle \vec{V}_s \rangle^s - \langle \vec{V}_f \rangle^f \right) \right] + \\ \nabla \cdot \left[\epsilon_f \langle \rho_f \rangle^f \mathcal{L} : \left(\langle \vec{V}_s \rangle^s - \langle \vec{V}_f \rangle^f \right) \left(\langle \vec{V}_s \rangle^s - \langle \vec{V}_f \rangle^f \right) \right] = \\ \nabla \cdot (\mu_f \nabla \langle \vec{V}_f \rangle) + \nabla \cdot (\mu \nabla \langle \vec{V}_f \rangle)^T - \frac{2}{3} \nabla (\mu \nabla \cdot \langle \vec{V} \rangle) + \\ \mu \epsilon_f \mathcal{A} \left(\langle \vec{V}_s \rangle^s - \langle \vec{V}_f \rangle^f \right) + \mu \epsilon_f \mathcal{B} : \left(\langle \vec{V}_s \rangle^s - \langle \vec{V}_f \rangle^f \right) \cdot \left(\langle \vec{V}_s \rangle^s - \langle \vec{V}_f \rangle^f \right) \\ - \epsilon_f (\mathbf{I} + \mathcal{E}) \cdot \left(\nabla \langle P_f \rangle^f + \langle \rho_f \rangle^f \nabla \langle \phi_{g,f} \rangle^f \right) \\ - \mathcal{M} : \left(\nabla \langle P_f \rangle^f + \langle \rho_f \rangle^f \nabla \langle \phi_{g,f} \rangle^f \right) \left(\nabla \langle P_f \rangle^f + \langle \rho_f \rangle^f \nabla \langle \phi_{g,f} \rangle^f \right) \end{aligned} \quad (2.123)$$

At this point, experimentally-determined values for all of the tensors that appear in Eq. (2.123) do not exist. But, simplifications can be made for isotropic flows or slow flows such that advection and the time rate of change of momentum can be neglected.

\mathcal{M} , \mathcal{C} , and \mathcal{B} are third-order tensors that are symmetric in two of their indices. There are no isotropic symmetric third-order tensors, so all of these tensors must be zero for isotropic media [23]. The only symmetric second-order tensor is a multiple of the identity matrix, such that $\mathcal{A} = A\mathbf{I}$, where A is a constant. Likewise, $\varepsilon_f(\mathbf{I} + \mathcal{E}) = E\mathbf{I}$. Therefore, Eq. (2.123) becomes for isotropic flows:

$$\begin{aligned} & \frac{\partial(\varepsilon\langle\rho_f\rangle^f\langle\vec{V}_f\rangle^f)}{\partial t} + \nabla \cdot \left[\varepsilon\langle\rho_f\rangle^f\langle\vec{V}_f\rangle^f\langle\vec{V}_f\rangle^f \right] + \\ & \nabla \cdot \left[\varepsilon_f\langle\rho_f\rangle^f\mathcal{L} : \left(\langle\vec{V}_s\rangle^s - \langle\vec{V}_f\rangle^f \right) \left(\langle\vec{V}_s\rangle^s - \langle\vec{V}_f\rangle^f \right) \right] = \\ & \nabla \cdot (\mu_f\nabla\langle\vec{V}_f\rangle) + \nabla \cdot (\mu\nabla\langle\vec{V}_f\rangle)^T - \frac{2}{3}\nabla(\mu\nabla \cdot \langle\vec{V}\rangle) + \\ & \mu\varepsilon_f A \left(\langle\vec{V}_s\rangle^s - \langle\vec{V}_f\rangle^f \right) - E \cdot \left(\nabla\langle P_f\rangle^f + \langle\rho_f\rangle^f\nabla\langle\phi_{g,f}\rangle^f \right) \end{aligned} \quad (2.124)$$

Eq. (2.124) can be further simplified. A generic fourth-order isotropic tensor can be written in component form as:

$$\mathcal{L}_{ijkl} = L\delta_{ij}\delta_{kl} + \frac{l}{2}(\delta_{ik}\delta_{jl} + \delta_{il}\delta_{jk}) + q(\delta_{ik}\delta_{jl} - \delta_{il}\delta_{jk}) \quad (2.125)$$

where L , l , and q are constants. Because \mathcal{L} is symmetric in its first two indices, as well as in its last two indices, the last term above is zero. This only requires the definition of the constants L , l , and A . So, the momentum equation for an isotropic porous media is [23]:

$$\begin{aligned} & \frac{\partial(\varepsilon\langle\rho_f\rangle^f\langle\vec{V}_f\rangle^f)}{\partial t} + \nabla \cdot \left[\varepsilon\langle\rho_f\rangle^f\langle\vec{V}_f\rangle^f\langle\vec{V}_f\rangle^f \right] + \\ & \nabla \cdot \left[\varepsilon_f\langle\rho_f\rangle^f L \left(\langle\vec{V}_s\rangle^s - \langle\vec{V}_f\rangle^f \right) \cdot \left(\langle\vec{V}_s\rangle^s - \langle\vec{V}_f\rangle^f \right) \right] + \\ & \nabla \cdot \left[\varepsilon_f\langle\rho_f\rangle^f l \left(\langle\vec{V}_s\rangle^s - \langle\vec{V}_f\rangle^f \right) \left(\langle\vec{V}_s\rangle^s - \langle\vec{V}_f\rangle^f \right) \right] = \\ & \nabla \cdot (\mu_f\nabla\langle\vec{V}_f\rangle) + \nabla \cdot (\mu\nabla\langle\vec{V}_f\rangle)^T - \frac{2}{3}\nabla(\mu\nabla \cdot \langle\vec{V}\rangle) + \\ & \mu\varepsilon_f A \left(\langle\vec{V}_s\rangle^s - \langle\vec{V}_f\rangle^f \right) - E \cdot \left(\nabla\langle P_f\rangle^f + \langle\rho_f\rangle^f\nabla\langle\phi_{g,f}\rangle^f \right) \end{aligned} \quad (2.126)$$

For slow flows where the advection and time rate of change of momentum is negligible, Eq. (2.123) instead simplifies to:

$$\begin{aligned} & \nabla \cdot (\mu_f\nabla\langle\vec{V}_f\rangle) + \nabla \cdot (\mu\nabla\langle\vec{V}_f\rangle)^T - \frac{2}{3}\nabla(\mu\nabla \cdot \langle\vec{V}\rangle) + \mu\varepsilon_f A \left(\langle\vec{V}_s\rangle^s - \langle\vec{V}_f\rangle^f \right) + \\ & \mu\varepsilon_f \mathcal{B} : \left(\langle\vec{V}_s\rangle^s - \langle\vec{V}_f\rangle^f \right) \cdot \left(\langle\vec{V}_s\rangle^s - \langle\vec{V}_f\rangle^f \right) - \varepsilon_f(\mathbf{I} + \mathcal{E}) \cdot \left(\nabla\langle P_f\rangle^f + \langle\rho_f\rangle^f\nabla\langle\phi_{g,f}\rangle^f \right) \\ & - \mathcal{M} : \left(\nabla\langle P_f\rangle^f + \langle\rho_f\rangle^f\nabla\langle\phi_{g,f}\rangle^f \right) \left(\nabla\langle P_f\rangle^f + \langle\rho_f\rangle^f\nabla\langle\phi_{g,f}\rangle^f \right) = 0 \end{aligned} \quad (2.127)$$

The second-order Taylor series terms and the viscous stress terms are also negligible for slow flows [23]. Eq. (2.127) then reduces to Darcy's law:

$$\mathcal{K} \left(\nabla\langle P_f\rangle^f + \langle\rho_f\rangle^f\nabla\langle\phi_{g,f}\rangle^f \right) = \mu\varepsilon_f \left(\langle\vec{V}_s\rangle^s - \langle\vec{V}_f\rangle^f \right) \quad (2.128)$$

where the second-order permeability tensor \mathcal{K} is defined as:

$$\mathcal{K} \equiv \varepsilon_f(\mathbf{I} + \mathcal{E})A^{-1} \quad (2.129)$$

The permeability depends only on the geometry of the medium (i.e. not on any fluid properties)

In Pronghorn, mechanical effects of the solid on the fluid are neglected such that $\mathcal{C} = \mathbf{0}$ and $\mathcal{L} = \mathbf{0}$. Second-order effects of the pressure and gravitational forces are also neglected such that $\mathcal{M} = 0$. Both of these approximations are valid for relatively slow flows [23]. Viscous effects are neglected such that all terms in Eq. (2.119) are assumed zero. This approximation is valid for porous media because the length over which the deviatoric stress acts is on the order of several pore diameters, and hence can be neglected [28]. The solid is assumed stationary. Finally, $\epsilon_f \mu_f \mathcal{A}(\mathbf{I} + \mathcal{E})^{-1}$ and $\epsilon_f \mu_f \mathcal{B}(\mathbf{I} + \mathcal{E})^{-1}$ are approximated as vectors, instead of tensors. The sum of these two terms (with \mathcal{A} divided by $\langle \rho_f \rangle^f$ to obtain the proper units) is denoted as W . W represents a combined Darcy and Forchheimer friction coefficient. This gives the porous media momentum equation used in Pronghorn:

$$\frac{\partial(\epsilon_f \langle \rho_f \rangle^f \langle \vec{V}_f \rangle^f)}{\partial t} + \nabla \cdot (\epsilon_f \langle \rho_f \rangle^f \langle \vec{V}_f \rangle^f \langle \vec{V}_f \rangle^f) = -W \langle \rho_f \rangle^f \langle \vec{V}_f \rangle^f + \epsilon_f \nabla \langle P_f \rangle^f + \epsilon_f \langle \rho_f \rangle^f \nabla \langle \phi_{g,f} \rangle^f \quad (2.130a)$$

$$\frac{\partial(\epsilon \rho_f \vec{V})}{\partial t} + \nabla \cdot (\epsilon \rho_f \vec{V} \vec{V}) = -W \rho_f \vec{V} + \epsilon \nabla P + \epsilon \rho_f \vec{g} \quad (2.130b)$$

In Pronghorn's notation, ρ_f represents the intrinsic phase average of the fluid density, \vec{V} the intrinsic phase average of the fluid velocity, and P the intrinsic phase average of the pressure. It has been argued that in porous media, because the flow of the fluid is continually disrupted by the presence of solid particles, the transfer of momentum is severely impeded such that the advective term can be neglected. This is not done here, however, because Pronghorn is intended to model nuclear reactors that have much higher velocities than the groundwater flows for which porous media models were initially developed. Eq. (2.130) could also have been derived by assuming directly in the Cauchy momentum equation balance in Eq. (2.58) that:

$$\vec{b} \equiv \vec{g} + W \vec{V} \quad (2.131)$$

In other words, the body force on a fluid particle is the sum of the gravitational force and the distributed friction force.

2.4.1 Porous Media Momentum Losses

Eq. (2.130) contains W , a friction coefficient that accounts for additional drag on the fluid caused by solid flow obstructions. The Navier-Stokes equations by themselves do not contain any friction factor terms, because in principle the Navier-Stokes equations are exact (within the limitations of a Newtonian fluid constitutive law). But, to accurately capture the momentum losses experienced by a fluid flowing in the presence of a solid, whether this solid be pipe walls or a porous solid matrix, the solid material must be modeled in complete detail. All of the surface roughness and pocks and grooves in the solid surface must be modeled *exactly* if the Navier-Stokes equations are to correctly account for momentum losses due to friction and form drag at the solid surfaces. Because this level of modeling is not possible, especially when considering a porous media, the most common approach to account for this microscopic effects is through the use of a friction factor. In other words, the effect of shear stresses on the fluid is assumed to be distributed - this type of model is often referred to as a distributed loss model [22] (chapter 2). When included in the Euler equations, the equations are no longer isentropic because energy is always dissipated along the fluid path.

The previous section showed how this friction factor arises from the spatial averaging technique; this section describes the physical meaning of the components of W . While the title of this section refers to porous media, the discussion here is actually of a more general nature - the use of friction factors in non-porous media is also very common to capture the engineering-scale effects of shear stresses on fluid flow. With the use of an anisotropic friction factor for pipe flow and a porosity of 1, Pronghorn can also be used to model channel flows, such as present in holes in reflector blocks or pipes. These anisotropic friction factors are provided at the end of Section 9.

Friction factors are provided in the literature by dimensionless semi-empirical correlations in terms of the solid surface roughness, the Reynolds number, and the packing of the solid for porous media. Friction factors represent a

normalized pressure drop. At low flowrates, the pressure drop is linearly proportional to velocity (a viscous effect):

$$\nabla P \propto \frac{\mu V}{D^2}, \quad (2.132)$$

while at high flowrates, the pressure drop is proportional to the square of velocity (a kinetic effect):

$$\nabla P \propto \frac{\rho V^2}{D} \quad (2.133)$$

For steady, laminar, fully-developed, and incompressible flow with negligible gravitational forces, the momentum equation reduces to:

$$\rho \vec{V} \cdot \nabla \vec{V} = -\nabla P + \nabla \cdot \mu \nabla \vec{V} \quad (2.134)$$

Assuming unidirectional flow ($V_\theta = V_r = 0$) along an axis z aligned with the length of the circular pipe, and fully-developed flow such ($V_z \neq f(z)$), all advective terms cancel, giving:

$$\frac{\partial P}{\partial z} = \frac{\mu}{r} \frac{\partial}{\partial r} \left(r \frac{\partial V_z(r)}{\partial r} \right) \quad (2.135)$$

The above equation could also have been obtained for a generic 1-D system if the advective effects were neglected (in which case the following results are interpreted as *viscous* effects). Integrating twice and assuming that the pressure drop per unit length is constant for fully-developed flow, a parabolic velocity profile is obtained. By symmetry, the velocity profile satisfies $V_z(R) = 0$ and $\partial V_z(0)/\partial r = 0$:

$$V_z(r) = \frac{1}{4\mu} \frac{\partial P}{\partial z} (r^2 - R^2) \quad (2.136)$$

In order to relate the friction drag to the velocity in the pipe, an average velocity \bar{V}_z must be defined by integrating the velocity over the cross-sectional area of the pipe.

$$\begin{aligned} \bar{V}_z &\equiv \frac{\int_0^{2\pi} d\theta \int_0^R \rho V_z(r) r dr}{\rho \pi R^2} \\ &= -\frac{1}{32\mu} \frac{\partial P}{\partial z} D^2 \end{aligned} \quad (2.137)$$

At high Reynolds numbers, viscous effects can be neglected, in which case the momentum equation instead simplifies to:

$$\rho \vec{V} \cdot \nabla \vec{V} = -\nabla P \quad (2.138)$$

While analytic solution to this nonlinear equation is more difficult than for the linear equation encountered for viscous flows, the proportionality of pressure drop to the square of velocity for 1-D flows is clear. Expressing the gradient $\nabla \vec{V}$ as \vec{V}/D , where D is a characteristic length of the system, gives Eq. (2.133). These results also hold in the presence of gravitational effects, in which case the reduced pressure defined in Eq. (2.102) is used.

The total momentum loss can be approximated well as the sum of the viscous and kinetic losses [29]:

$$\nabla P = A \frac{\mu V}{D^2} + B \frac{\rho V^2}{D} \quad (2.139)$$

where A and B are constants of proportionality. Two different normalizations are possible for defining the friction

factor, by normalizing the pressure drop per unit normalized length by either the dynamic pressure $\rho V^2/2$ or the viscous shear stress $\mu V/D$:

$$\nabla P \frac{2D}{\rho V^2} = A \frac{1}{Re} + B \quad (2.140a)$$

$$\nabla P \frac{D^2}{\mu V} = A + B Re \quad (2.140b)$$

where the coefficients A and B in Eqs. (2.140)a and (2.140)b are not the same. The normalization shown in Eq. (2.140)a is used almost exclusively in the literature, for both porous and non-porous flows, though Eq. (2.140)b is sometimes plotted in order to make evaluation of A and B simpler.

For a cylindrical body of fluid in steady, fully-developed, unidirectional flow, a balance of pressure and viscous shear stresses on the surface of the body reveals that:

$$-\nabla P = \frac{4\tau_{wall}}{D} \quad (2.141)$$

where τ_{wall} is the viscous shear stress at the wall. Inserting Eq. (2.141) into Eq. (2.140)a shows that a friction factor defined as the normalized pressure drop normalized by the dynamic pressure is equivalent to the wall shear stress normalized by the dynamic pressure:

$$\nabla P \frac{2D}{\rho V^2} = \frac{8\tau_{wall}}{\rho V^2} \quad (2.142)$$

The proportionality of the viscous and inertial pressure drops with porosity is different, though many earlier researchers did not recognize this, which severely limited the ranges of applicability of their friction factor correlations [30]. The most common method for expressing these friction effects uses the hydraulic radius model, in which case appropriate scalings of velocity and characteristic length D for spherical porous media are introduced. For Eq. (2.132), V can be transformed to v using Eq. (2.31), and D can be interpreted as the hydraulic diameter in Eq. (2.289), neglecting the factor of 4/6:

$$\nabla P_{viscous} \propto \frac{(1-\epsilon)^2}{\epsilon^3} \frac{\mu}{d_p^2} v \quad (2.143)$$

Likewise, the kinetic term proportionality on porosity is:

$$\nabla P_{kinetic} \propto \frac{(1-\epsilon)}{\epsilon^3} \frac{\rho_f}{d_p} v^2 \quad (2.144)$$

These scalings are valid for beds of spherical pebbles, and must be respected in all friction factor correlations for porous media, or else the correlation would not be independent of porosity under appropriate transformations to a non-porous media system [30]. For plate or prismatic solid geometries, Eq. (2.143) and (2.144) have different forms due to the different interpretation of the hydraulic diameter. Using these proportionalities in Eq. (2.139) gives:

$$\nabla P \frac{\epsilon^3}{1-\epsilon} \frac{2d_p}{\rho v^2} = A \frac{1-\epsilon}{Re} + B \quad (2.145a)$$

$$\nabla P \frac{\epsilon^3}{(1-\epsilon)^2} \frac{d_p^2}{\mu v} = A + B \frac{Re}{1-\epsilon} \quad (2.145b)$$

With the scaling in Eq. (2.145)a, at $Re > 6 \times 10^4$ (or lower values on the order of 4×10^3 [6]), the friction factor becomes relatively independent of Re [31]. At intermediate to low Re , the friction factor scales as $(1 - \epsilon)/Re$ [30].

There are a large number of porous media friction factor correlations available in the literature. There is a strong relationship between these friction factor correlations and the early models for flow in porous media. For example, Darcy's law is a simplification of the Navier-Stokes momentum equation for stationary, creeping, and incompressible flow. The original form derived by Darcy assumes constant porosity, but this can be rearranged to the non-constant porosity form by multiplying both sides by porosity [32]:

$$\begin{aligned}\epsilon \nabla P &= -\mu \mathcal{K}^{-1} \epsilon \vec{v} \\ &= -\mu \mathcal{K}^{-1} \epsilon^2 \vec{V} \\ &= -\mathcal{D} \vec{V}\end{aligned}\tag{2.146}$$

By comparing Eq. (2.146) with Eq. (2.132), it can be seen that correlations for the permeability are proportional to correlations for the viscous friction factor. So, Darcy's law is none other than a viscous drag proportionality between pressure gradient and velocity, because the kinetic friction losses were assumed negligible. The permeability must be proportional to:

$$\mathcal{K}^{-1} \propto \frac{(1 - \epsilon)^2}{\epsilon^3} \frac{1}{d_p^2}\tag{2.147}$$

For simplicity, the coefficient on \vec{V} can be bundled into \mathcal{D} , which will be referred to as the ‘‘Darcy prefactor’’ in this manual. For isotropic media, \mathcal{D} simplifies to a scalar. Because Darcy's law assumes negligible kinetic friction losses, it is only valid as a model for low Reynolds number flows. As Re increases, the drag transitions from linear to nonlinear behavior as boundary layers begin to separate, and neglecting the kinetic friction losses is no longer valid. Darcy could not obtain very high flowrate data because his water source was a hospital - perhaps if he had a reliable experimental setup, he would have included a kinetic friction loss term [33].

Other early researchers built upon Darcy's law by recognizing that the kinetic friction component should also be included. Forchheimer's law is one such extension, which simply adds the kinetic friction component to Darcy's flow model. So, Forchheimer's law is none other than a balance between pressure gradient and the sum of viscous and kinetic friction effects. The original form derived by Forchheimer assumes constant porosity, but this can be rearranged to give the non-constant porosity form by multiplying both sides by porosity [32]:

$$\begin{aligned}\epsilon \nabla P &= -\mu \mathcal{K}^{-1} \epsilon \vec{v} - \epsilon C_f \mathcal{K}^{-1/2} \rho_f |\vec{v}| \vec{v} \\ &= -\mu \mathcal{K}^{-1} \epsilon^2 \vec{V} - \epsilon C_f \mathcal{K}^{-1/2} \epsilon^2 \rho_f |\vec{V}| \vec{V} \\ &= -\mathcal{D} \vec{V} - \mathcal{F} \rho_f |\vec{V}| \vec{V}\end{aligned}\tag{2.148}$$

where C_f is a form drag coefficient. By comparing Eq. (2.148) with Eq. (2.144), it can be seen that correlations for $C_f \mathcal{K}^{-1/2}$ are equivalent to correlations for the kinetic friction factor! This term must be proportional to:

$$C_f \mathcal{K}^{-1/2} \propto \frac{(1 - \epsilon)}{\epsilon^3} \frac{1}{d_p}\tag{2.149}$$

In a porous media, Forchheimer's law accounts for nonlinear flow effects that are not necessarily present *because* of turbulence. Forchheimer's law accounts for streamline bending around particles and expansion/contraction between the large and small pore spaces [34]. The analytical proportionalities for sudden expansions/contractions from fundamental fluid mechanics also scale as ρv^2 .

To simplify later description of these kinetic friction factor correlations, the coefficient on $\rho_f |\vec{V}| \vec{V}$ will be bundled into \mathcal{F} , which will be referred to as the “Forchheimer prefactor” in this manual. For isotropic media, \mathcal{F} simplifies to a scalar. Correlations for \mathcal{D} and \mathcal{F} are provided in Section 9. With the hydraulic radius model, \mathcal{D} and \mathcal{F} scale as:

$$\mathcal{D} \propto \frac{(1 - \varepsilon)^2}{d_p^2 \varepsilon} \mu \quad (2.150)$$

$$\mathcal{F} \propto \frac{(1 - \varepsilon)}{d_p} \quad (2.151)$$

From these definitions it can be seen that the friction drag scales as the inverse of the pebble area, while the form drag scales as the inverse of the length of the wake region (on the order of d_p since the next pebble in the flow field disturbs the wake). Based on the definition of W , it is clear that:

$$W \equiv \frac{\mathcal{D}}{\rho_f} + \mathcal{F} |\vec{V}| \quad (2.152)$$

In addition to Darcy and Forchheimer models, other researchers have suggested alternative $\varepsilon \nabla P$ scalings. For example, Brinkman extended Darcy’s law to include a viscous term similar to the traditional Laplacian found in the incompressible Navier-Stokes equations in order to enforce the no-slip condition at solid walls [32]:

$$\varepsilon \nabla P = -\mu \mathcal{K}^{-1} \varepsilon \vec{v} + \varepsilon \tilde{\mu} \nabla^2 \vec{v} \quad (2.153)$$

where $\tilde{\mu}$ is an effective viscosity. There is substantial disagreement on the correct selection of $\tilde{\mu}$, though several researchers have obtained experimental fits as a function of Re [35]. Generally, $\tilde{\mu}$ increases with Re due to enhanced mixing, though some particle shapes show no dependence on Re . The selection of $\tilde{\mu}$ only impacts the flow field in the vicinity of the wall (within about a half pebble diameter), since Brinkman’s model is only used to capture the near-wall maxima of velocity [35, 36]. Most porous media codes do not include a Brinkman term, but Auwerda et. al select $\tilde{m}u$ somewhat arbitrarily as 100μ for helium-cooled HTGRs due to a lack of experimental correlations; variation by two orders of magnitude results in fairly similar temperature profiles [36]. Brinkman’s model is essentially an attempt to capture additional wall shear stress [37].

Brinkman’s equation does not have the same experimental validation basis as either Darcy’s or Forchheimer’s laws, and is generally thought to only be applicable for $\varepsilon > 0.8$. At low porosities, the solid matrix impedes direct transfer of momentum due to viscous forces and the majority of stresses are communicated via pressure [32]. The Brinkman model is not used in Pronghorn, but is shown here for perspective on how a no-slip condition could be obtained in an inviscid flow model. Some authors staunchly defend Brinkman’s hypothesis, however [38].

2.4.2 The Trans-Forchheimer Regime

The quadratic drag effect modeled by the Forchheimer relationship is only applicable for laminar flow. That is, Forchheimer’s law only applies to inertia-dominated *laminar* flows, and represents fundamentally different physics than the quadratic velocity dependence that is also observed for turbulent flows [39]. Researchers have observed six general flow regimes in porous media, which are shown pictorially in Fig. 6 [28, 39, 40].

1. *Pre-Darcy* regime - non-Newtonian fluid behavior causes small countercurrents to form at the pore walls. In this regime, the pressure drop actually increases as the flow is reduced, and a finite pressure drop exists for zero Re . Fand estimates this pre-Darcy regime to occur in an exceptionally narrow Reynolds number range, but Kececioglu estimates the pre-Darcy regime width to be the same as the Darcy regime [28, 40].

2. *Darcy* regime - the flow is dominated by viscous forces.
3. *Transitional* regime - transition from Darcy to Forchheimer flow; this flow regime is often referred to as the “weak inertia” regime.
4. *Forchheimer* regime - steady, nonlinear laminar flow, characterized by the onset of boundary layer separation. The Forchheimer regime is often referred to as the “inertial” regime.
5. *Transitional* regime - oscillations and vortices begin to develop.
6. *Turbulent* regime - highly unsteady and chaotic flow that is dominated by eddies.

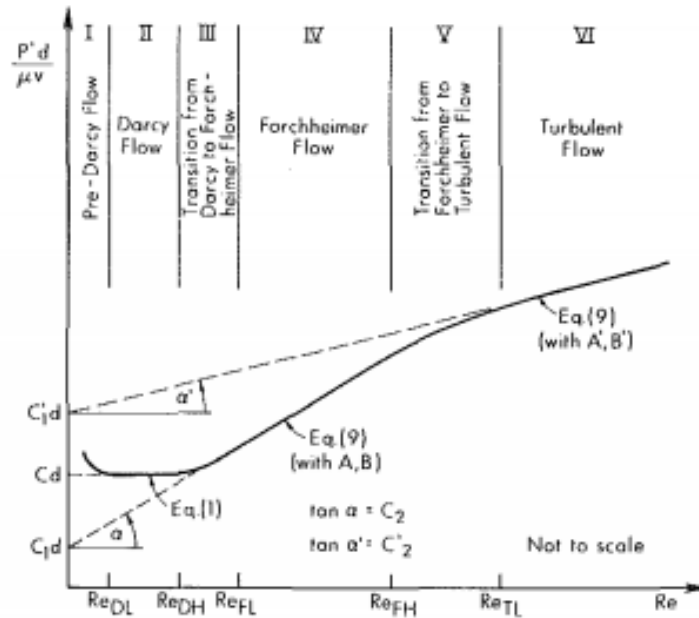


Figure 6: Flow regimes in porous media [40]. Solid lines represents friction coefficients normalized by the viscous friction component according to Eq. (??). If a single Darcy-Forchheimer relationship with a single set of A and B coefficients were viable over the entire range of Reynolds numbers, then a single straight line would be observed.

The Reynolds numbers defining the bounds of these flow regimes as determined by several researchers is shown in Table 2. A complication associated with characterizing flows with a Reynolds number is that the length and velocity scales used in the Reynolds number can vary widely. The Reynolds number used to characterize the onset of various flow regimes must take into account the sphere diameter, because the largest spheres trigger turbulence as the fluid must travel a longer path length without boundary layer separation if the flow is to remain viscous-dominated. Re_k , the Reynolds number based on the square root of the permeability as a length scale, shows the smallest variation between researchers. Sources that reported bounds in terms of other Reynolds numbers are approximately converted to Re_k assuming a porosity of 0.4.

Table 2: Differences in flow regime boundaries as computed by various researchers. The transitional regimes are not shown, and are inferred to complete the range gaps between the regimes in the table.

Source	Darcy	Forchheimer	Turbulent
[28, 40]	$Re_k < 0.26$	$0.57 < Re_k < 9.00$	$Re_k > 13.5$
[28]	$0.06 < Re_k < 0.12$	$0.34 < Re_k < 2.30$	$Re_k > 3.40$

The Darcy-Forchheimer flow model in Eq. (2.148) is technically only applicable up to and including the Forchheimer regime. There is not general agreement on how to model the Trans-Forchheimer regime characterized by $Re_k > 10$. Some researchers propose that Eq. (2.148) be used throughout all ranges in Reynolds number using a single set of proportionality constants, while others believe that a different model is required. Researchers have even taken data thought to demonstrate a continuous Darcy-Forchheimer regime, and shown that a different interpretation of the data clearly illustrates a Trans-Forchheimer regime [41]. Among the researchers who believe a new model is required, there is not consistent agreement on what that model should look like, let alone what physical behavior is to be expected in the Trans-Forchheimer regime.

Of the researchers that believe a new model is required for the Trans-Forchheimer regime, there is disagreement on how the viscous and kinetic friction components differ between the Darcy-Forchheimer and Trans-Forchheimer regimes. Many authors report a drag-reduction effect in the fully turbulent regime, whereby the Darcy prefactor tends to increase, but the Forchheimer prefactor decreases [28,33,40,42]. At the high velocities characteristic of turbulence, the Forchheimer term dominates, and the overall effect is to observe a reduction in drag. Drag reduction effects might be explained by:

- At higher flowrates, the fluid follows streamlines more efficiently, reducing inertial losses in circulating motions in the bed [33].
- At low flowrates, only the largest flow channels contribute to the overall flow. At higher flowrates, the resistance of the smaller flow channels becomes less important, and more flow channels contribute to the overall flow so that the flow becomes more evenly distributed [33].
- The separated boundary layer region in a porous medium cannot grow unbounded, so at very high velocities the drag effect is limited by the solid obstacles [43].

A drag reduction effect for turbulent flows is not in agreement with trends observed for internal pipe flows, however. From the Moody diagram, extrapolation of the friction factor for laminar flows to higher Re would be *lower*, not higher, than that actually observed in the turbulent regime [44]. Lage states that the Forchheimer prefactor can either increase *or* decrease relative to its laminar value upon reaching the turbulent regime, which would explain the disagreement amongst researchers on this effect. Whether the coefficient increases or decreases generally depends on whether the transition to turbulence is triggered by viscous or kinetic effects. If the transition is dominated by kinetic effects, then the Forchheimer prefactor should decrease, but if the transition is dominated by viscous effects typical of transitions in internal pipe flows, the Forchheimer prefactor should increase [44]. Because porous media consist of many closely-packed bodies, rather than a single body for which the transition is well-known to be kinetic-dominated, it is unclear immediately if the Forchheimer prefactor change upon the onset of turbulence can be well-characterized. Most researchers report a decreased Forchheimer prefactor, so it can be inferred that a porous media transitions to turbulence due to kinetic transitions, though this is not always supported by experimental evidence. For example, Lage reported a Forchheimer prefactor increase, which was attributed to the use of a non-conventional porous media where the flow transition is controlled by viscous drag effects [44].

Considering all of the different interpretations of how the drag coefficients should change upon turbulence, there are four common approaches for modeling the Trans-Forchheimer regime:

1. Use a single Darcy-Forchheimer correlation for the entire range in Re [29, 30, 45]. When the Darcy and Forchheimer prefactors are only generated according to low Re data, an order or magnitude higher deviation is obtained than when the coefficients are fit with a wider range of Reynolds number data, illustrating the error in extrapolating too far between regimes [44].
2. Modify the Darcy and Forchheimer coefficients once reaching the turbulent regime to a different set of *constants*. This approach is performed in [28, 40].
3. Add a term proportional to v^3 to Eq. (2.148). Forchheimer's was the first to suggest such a cubic dependence [33]. From Reynolds number similarity requirements, the drag must scale as ρv^2 at high Re , so this approach

is theoretically only valid in the transitional flow regime between Forchheimer and fully turbulent flows. This transitional regime is very narrow for 3-D flows, and can effectively be neglected [39]. Nevertheless, Lage added a cubic velocity proportionality to his correlation, and found that when low-Reynolds number data is used to obtain the Darcy and Forchheimer prefactors, that this method provided the best experimental fit [44].

4. Use non-constant Darcy and Forchheimer prefactors. Researchers using this method have reported drag reduction effects [33,42].

Turbulence is expected in nuclear reactor systems, so the correlations for W discussed in Section 9 will provide one or more of the four options listed above.

2.4.3 Anisotropic Porous Media

The drag models discussed up to now are almost always reduced to isotropic forms due to a lack of modeling information for how to properly treat anisotropies. However, anisotropy may prove critical for accurate modeling of porous media [34]. Anisotropy arises from the geometry and the flow field itself. Anisotropic geometries will cause the flow to have preferred directions of motion that do not perfectly align with the pressure gradient. Anisotropies in the flow field, such as different heating rates in different sections, will cause natural anisotropies in the flow.

The error in approximating the Darcy and Forchheimer drag coefficients as constants depends on the degree of anisotropy in the system. In spherical particle porous media, the largest anisotropies exist at the walls, where the wall significantly retards flow perpendicular to the wall, but the high-porosity region aligned with the walls encourages flow parallel to the walls. The porosity appears greater looking at the wall, but is much lower looking parallel to the wall. The establishment of natural circulation can be sensitive to anisotropy, since boundary layer thickness at the walls can severely retard circulation flows [46]. Depending on the core design, the presence of thermalizing graphite reflectors at the bed edges may further contribute to the importance of anisotropic effects. A proper anisotropic treatment should also consider the anisotropy of the heat transfer coefficient and effective thermal conductivities.

Anisotropic porous media have most frequently been studied for banks of cylindrical tubes due to modeling simplicity [46,47]. These researchers have concluded that correctly accounting for anisotropy can yield as large as a 100% change in the heat transfer and fluid flow. There are generally two approaches pursued to model anisotropic porous media -

1. Use a tensorial \mathcal{D} and \mathcal{F} , heat transfer coefficient, and effective thermal conductivities.
2. Approximate anisotropy by replacing $|\vec{V}|$ in Eq. (2.148) by the vector velocity. Likewise, any time a Reynolds number appears in a drag/heat transfer coefficient/effective thermal conductivity correlation, the velocity in the Reynolds number should be the component velocity. In other words, use correlations developed for isotropic porous media, but apply them in a vectorized form.

This second approach is the easiest to implement, but is inaccurate in that isotropic correlations are used to approximate anisotropy. However, to a first order approximation, the use of component-wise velocities should be used to account for the fact that the smallest velocity components do not experience the same drag as the large components [46,47]. Using a vectorized drag coefficient would likely have a large impact in Pronghorn, because the majority of flow is oriented upwards. A vectorized drag coefficient is *not* the standard, however, and the majority of researchers use velocity magnitudes, rather than components, in Reynolds numbers and in the Forchheimer prefactor [48].

Wang et. al shows that \mathcal{F} responds very strongly to anisotropy, increasing by a factor of 17 for some systems as anisotropy is increased. \mathcal{D} is less sensitive to anisotropy (though it also increases with anisotropy). By varying anisotropy in only one direction, all components of the \mathcal{D} and \mathcal{F} tensors are affected because fluid becomes forced through other regions. However, the magnitude of the anisotropy is greatest in the directions with greatest anisotropy. Anisotropic models for friction and heat transfer are not yet implemented in Pronghorn, so all friction coefficients discussed in Section 9 use an isotropic treatment.

2.5 The Fluid Energy Equation

This section presents two derivations of the conservation of energy equation. One of these equations will be an equation for total energy (a conserved quantity), while the other equation will be an equation for temperature (not a conserved quantity). Therefore, these two versions of an “energy” equation will be referred to as “conservative” or “non-conservative,” referring specifically to the fact that energy, but not temperature, is physically conserved.

The first law of thermodynamics relates the rate of change of energy in a volume to the rate of energy and heat addition. The total energy is the sum of internal energy and kinetic energy. The internal energy per unit mass, e , represents the potential energy due to bond stretching plus the mean kinetic energy of molecules when moving in a frame of reference moving with the center of mass velocity (i.e. vibratory motion). The total energy per unit mass, E , is the sum of this internal energy and kinetic energy of the body per unit mass.

$$E = e + \frac{1}{2} V_i V_i \quad (2.154)$$

Conservation of total energy requires a balance between the power supplied by the contact and body forces and the heat addition. This balance is obtained by multiplying all the forces in the momentum balance in Eq. (2.56) by velocity, since power equals force times velocity.

$$\underbrace{\frac{d}{dt} \int_{\mathcal{V}(t)} \rho E d\mathcal{V}}_{\text{rate of change of total energy}} = \underbrace{\int_{\mathcal{V}(t)} \rho b_i V_i d\mathcal{V}}_{\text{power from body forces}} + \underbrace{\oint_{S(t)} V_i \sigma_{ij} n_j dS}_{\text{power from viscous forces}} - \underbrace{\oint_{S(t)} q_i n_i dS + \int_{\mathcal{V}(t)} \dot{q} d\mathcal{V}}_{\text{heat addition}} \quad (2.155)$$

where \vec{q} is the heat flux vector representing heat flow out of the fluid particle and \dot{q} is a volumetric heat source in the fluid particle that has been included in addition to the forces present in the general momentum balance. The divergence theorem is applied to convert surface integrals to volume integrals:

$$\frac{d}{dt} \int_{\mathcal{V}(t)} \rho E d\mathcal{V} = \int_{\mathcal{V}(t)} \rho b_i V_i d\mathcal{V} + \int_{\mathcal{V}(t)} \frac{\partial}{\partial x_j} (V_i \sigma_{ij}) d\mathcal{V} - \int_{\mathcal{V}(t)} \frac{\partial q_j}{\partial x_j} d\mathcal{V} + \int_{\mathcal{V}(t)} \dot{q} d\mathcal{V} \quad (2.156)$$

By the same argument that was used to bring the time differentiation under the integral in Eq. (2.57) and by recognizing that the choice of the volume is arbitrary, Eq. (2.156) simplifies to:

$$\begin{aligned} \rho \frac{dE}{dt} &= \rho \vec{b} \cdot \vec{V} + \frac{\partial}{\partial x_j} (V_i \sigma_{ij}) - \nabla \cdot \vec{q} + \dot{q} \\ &= \rho \vec{b} \cdot \vec{V} + \underbrace{V_i \frac{\partial \sigma_{ij}}{\partial x_j}}_{\text{contact power}} + \underbrace{\sigma_{ij} \frac{\partial V_i}{\partial x_j}}_{\text{deformation power}} - \nabla \cdot \vec{q} + \dot{q} \end{aligned} \quad (2.157)$$

By inserting the constitutive relation for σ_{ij} from Eq. (2.91) into Eq. (2.157), a form useful for implementation is obtained in Eq. (2.158)a. Eq. (2.158)b uses the continuity equation to rewrite the material derivative in terms of the conserved total energy.

$$\rho \frac{dE}{dt} = \rho \vec{b} \cdot \vec{V} - \nabla \cdot (P \vec{V}) + \nabla \cdot (\tau \vec{V}) - \nabla \cdot \vec{q} + \dot{q} \quad (2.158a)$$

$$\frac{\partial(\rho E)}{\partial t} + \nabla \cdot ((\rho E + P) \vec{V}) = \rho \vec{b} \cdot \vec{V} + \nabla \cdot (\tau \vec{V}) - \nabla \cdot \vec{q} + \dot{q} \quad (2.158b)$$

The enthalpy per unit mass h and total enthalpy per unit mass H are defined as:

$$\rho h = \rho e + P \quad (2.159)$$

$$\rho H = \rho E + P \quad (2.160)$$

where a differential in h is provided, where v is the specific volume. Inserting Eq. (2.160) into Eq. (2.158)b, neglecting the $\nabla \cdot (\tau \vec{V})$ viscous heating effects, and assuming that $\vec{q} = -k\nabla T$ represents the conduction heating, the conservative energy equation becomes:

$$\frac{\partial(\rho E)}{\partial t} + \nabla \cdot (\rho H \vec{V}) - \rho \vec{b} \cdot \vec{V} - \nabla \cdot (k\nabla T) - \dot{q} = 0 \quad (2.161)$$

where k is the thermal conductivity. The body force \vec{b} in the above equation can have two different forms, depending on the interpretation of the derivation of the porous media equations. Eq. (2.131) was derived by averaging the momentum equation in space. Whether \vec{b} in Eq. (2.161) should be interpreted as \vec{g} or as $\vec{g} + W\vec{V}$ depends on whether the porous media version of the energy equation should be derived by using a) the non-porous or b) porous Cauchy equation in the derivation of the energy equation. In other words, should the process used to obtain the $W\rho_f\vec{V}$ term for the momentum equation be carried through to the energy equation? Another simple example of this issue is obvious for incompressible flows. The microscopic continuity equation is $\nabla \cdot \vec{V} = 0$ - should the porous media version of this equation be $\nabla \cdot (\epsilon\vec{V}) = 0$ or $\partial\epsilon/\partial t + \nabla \cdot (\epsilon\vec{V}) = 0$? PEBble Fluid Dynamics (PEBFD) assumes the latter form [49].

Nield suggests that Eq. (2.131) be used for \vec{b} ; he refers to the $\rho\vec{b} \cdot \vec{V}$ term as the “viscous dissipation” [43]. While the Forchheimer drag term is independent of μ , $\rho\mathcal{F}|\vec{V}|\vec{V} \cdot \vec{V}$ still represents a *viscous* loss because form drag arises due to the interaction of inertial, viscous, and pressure forces. Without viscosity, there is no boundary layer, and hence no boundary layer separation to result in form drag.

This issue in selecting \vec{b} only arises in the use of the conservative energy equation. However, it appears that most porous media codes using the conservative energy equation neglect the $W\vec{V}$ component in \vec{b} [50]. Whether the $W\vec{V}$ portion can be neglected for different reactor designs will be addressed in Section 2.10.5.

The thermal conductivity of gases generally increases with temperature, while it is nearly constant for liquids. Both gases and liquids show very weak dependence of thermal conductivity with pressure [22] (chapter 1).

The derivation of the non-conservative energy equation is more lengthy. Equilibrium thermodynamics is used to relate total energy to entropy, and then entropy to temperature to transform Eq. (2.157) to an equation entirely for temperature. In order to obtain the entropy equation, the mechanical energy component of Eq. (2.157) is subtracted out by first forming the mechanical energy equation by taking the scalar product of the Cauchy momentum equation in Eq. (2.58) with velocity (since power equals force multiplied by velocity).

$$\begin{aligned} \rho b_i V_i + V_i \frac{\partial \sigma_{ij}}{\partial x_j} &= V_i \rho \frac{dV_i}{dt} \\ &= \rho \frac{d}{dt} \left(\frac{1}{2} V_i^2 \right) \end{aligned} \quad (2.162)$$

Recognizing that $V_i \partial \sigma_{ij} / \partial x_j$ appears in the total energy equation in Eq. (2.157), a balance of internal energy equation is obtained by subtracting Eq. (2.162) from Eq. (2.157):

$$\rho \frac{de}{dt} = \sigma_{ij} \frac{\partial V_i}{\partial x_j} - \nabla \cdot \vec{q} \quad (2.163)$$

Consider a simple shear flow with $\vec{V} = kx_2 \vec{e}_1$ with $\vec{b} = \vec{g} = -g \vec{e}_2$. Eq. (2.162) simplifies to $V_i \partial \sigma_{ij} / \partial x_j = 0$. Recognizing that $V_i \partial \sigma_{ij} / \partial x_j$ appears in Eq. (2.157), the total energy balance becomes:

$$\rho \frac{dE}{dt} = \sigma_{ij} \frac{\partial V_i}{\partial x_j} - \nabla \cdot \vec{q} \quad (2.164)$$

Hence, $\sigma_{ij} \partial V_i / \partial x_j$ represents deformation work, and is often referred to as the “viscous dissipation rate.” It is this phenomenon that causes heating of boundary layers, and represents the conversion of mechanical energy to thermal energy. Because this deformation work is present in the internal energy equation in Eq. (2.163), this term contributes to an increase in internal energy, but not kinetic energy, producing heat.

In order to obtain equations for temperature and entropy, relations from equilibrium thermodynamics are needed. But, the dissipative terms on the RHS of Eq. (2.157) do not represent equilibrium conditions at all. Hence, *local* thermodynamic equilibrium must be assumed. While in a global sense the system is not in thermodynamic equilibrium, each fluid particle is assumed to be in equilibrium, a valid approximation provided a fluid particle reaches equilibrium with its surroundings quickly. The time scale on which a fluid particle reaches equilibrium with its surroundings can usually be cast as some multiple of the collision frequency. Provided this time scale is much smaller than the time scale characterizing the problem, local thermodynamic equilibrium can be assumed. In other words, local equilibrium is attained when local changes in pressure and temperature are relatively small with respect to the far-field values of pressure and temperature.

The classification of a system depends on the number of available energy transfer modes. Any system always has at least two modes of energy transfer - work and heat. Simple systems only experience pressure-volume work, and are not subject to work by electromagnetic fields or other means. Hence, there are two ways by which to change the energy of a simple system - by pressure-volume work and by heat transfer. One thermodynamic property is needed to fix the state of a system for each mode of energy transfer, so the state of a simple, pure system can be fixed with two properties. From the first law of thermodynamics, for a simple, pure system:

$$de = \delta q + \delta w \quad (2.165)$$

where q represents heat addition and w represents work done on the body. δ indicates a change that is not dependent solely on the beginning and end states. For an internally reversible process, $\delta q = T ds$, where s is the entropy of the fluid. For a pure fluid, the only mode of energy transfer besides heat addition is pressure-volume work, so $\delta w = -P dv$, where v is the specific volume. While no fluid is truly pure, a fluid can be approximated as pure as long as 1) the components are well-mixed, 2) there is no significant reaction between the components, and 3) the components do not break apart in the flow. Inserting these definitions into Eq. (2.165), the Gibbs identity is obtained:

$$de = T ds - P dv \quad (2.166)$$

Because local thermodynamic equilibrium is assumed, the Gibbs identity also applies for irreversible processes. The Gibbs identity is an exact differential, meaning that any form of a differential in e , s , and v produce the form above. Substituting Eq. (2.159) into Eq. (2.166) gives a differential for enthalpy:

$$\begin{aligned} dh &= de + P dv + v dP \\ &= T ds + v dP \end{aligned} \quad (2.167)$$

Using Eq. (2.166), the internal energy equation in Eq. (2.163) can be formulated into an equation for entropy conservation.

$$\rho \left(T \frac{ds}{dt} - P \frac{dv}{dt} \right) = \sigma_{ij} \frac{\partial V_i}{\partial x_j} - \nabla \cdot \vec{q} \quad (2.168)$$

The second term on the LHS can be related to the velocity using the continuity equation, Eq. (2.47):

$$\begin{aligned}\frac{d}{dt}(\rho^{-1}) &= \frac{-1}{\rho^2} \frac{d\rho}{dt} \\ &= \frac{\nabla \cdot \vec{V}}{\rho}\end{aligned}\quad (2.169)$$

Inserting this into Eq. (2.168), and using the constitutive relation for a Newtonian fluid from Eq. (2.90):

$$\begin{aligned}\rho T \frac{ds}{dt} - P \nabla \cdot \vec{V} &= \left(-P \delta_{ij} + 2\mu e_{ij} + \lambda \nabla \cdot \vec{V} \delta_{ij} \right) \frac{\partial V_i}{\partial x_j} - \nabla \cdot \vec{q} \\ \rho T \frac{ds}{dt} &= 2\mu e_{ij} \frac{\partial V_i}{\partial x_j} + \lambda (\nabla \cdot \vec{V})^2 - \nabla \cdot \vec{q}\end{aligned}\quad (2.170)$$

Using the definition of $\partial V_i / \partial x_j$ in Eq. (2.67), Eq. (2.170) can be rephrased using the property of the multiplication of the symmetric tensor e_{ij} with the antisymmetric tensor ξ_{ij} given in Eq. (18.10).

$$\begin{aligned}\rho T \frac{ds}{dt} &= 2\mu e_{ij} (e_{ij} + \xi_{ij}) + \lambda (\nabla \cdot \vec{V})^2 - \nabla \cdot \vec{q} \\ &= 2\mu e_{ij}^2 + \lambda (\nabla \cdot \vec{V})^2 - \nabla \cdot \vec{q} \\ &= 2\mu \left[\left(\frac{\tau}{2\mu} \right)^2 + \frac{2}{3} \nabla \cdot \vec{V} \left(\frac{\tau}{2\mu} \right) \delta_{ij} + \left(\frac{1}{3} \nabla \cdot \vec{V} \delta_{ij} \right)^2 \right] + \lambda (\nabla \cdot \vec{V})^2 - \nabla \cdot \vec{q} \\ &= \frac{\tau^2}{2\mu} + \zeta (\nabla \cdot \vec{V})^2 - \nabla \cdot \vec{q}\end{aligned}\quad (2.171)$$

and $\tau \delta_{ij} = \text{Tr}(\tau) = 0$ because the volume change has been subtracted out in the definition of the deviatoric stress tensor. In addition, $\delta_{ij} \delta_{ij} = 3$. Eqs. (2.171) and (2.170) show that the flow is nearly isentropic (along streamlines) for 1) low-viscous-dissipation, 2) minimally compressive (no shock waves), and 3) adiabatic (no heat conduction) flows.

The classical Euler equations are a simplification of the Navier-Stokes equations for inviscid flow with no external heat sources or conductive heating. Based on the equations derived previously, several analytical tools can be used to assess numerical errors made in solving the Euler equations. For the steady Euler equations with no external body forces, Eq. (2.161) shows that H should be constant along streamlines. If the inflow BCs specify a constant H , then the entire flow field is characterized by a constant H . Eq. (2.171) shows that for initially continuous flow variations (such that $\zeta \approx 0$ can be assumed without significant loss of accuracy), s should also be constant along streamlines. If the inflow BCs specify a constant s , then the entire flow field is characterized by a constant s . Therefore, for totally uniform inflow BCs, the classical Euler equations are equivalent to the potential flow equations, and the entire flow field has constant entropy and total enthalpy.

Divide Eq. (2.171) by T and then integrate over a volume:

$$\int_{\mathcal{V}(t)} \rho \frac{ds}{dt} d\mathcal{V} = \int_{\mathcal{V}(t)} \frac{\tau^2}{2\mu} + \zeta (\nabla \cdot \vec{V})^2 d\mathcal{V} - \int_{\mathcal{V}(t)} \frac{\nabla \cdot \vec{q}}{T} d\mathcal{V} + \int_{\mathcal{V}(t)} \frac{\dot{q}}{T} d\mathcal{V} \quad (2.172)$$

where a generic \dot{q} is added for completeness. Apply the chain rule to $\nabla \cdot (\vec{q}/T)$ term to introduce an equivalent

expression for the $(\nabla \cdot \vec{q})/T$ term, and then apply the divergence theorem:

$$\underbrace{\int_{\mathcal{V}(t)} \rho \frac{ds}{dt} d\mathcal{V}}_{\text{entropy generation}} + \underbrace{\oint_{S(t)} \frac{\vec{q} \cdot \vec{n}}{T} dS}_{\text{entropy with heat flow}} - \underbrace{\int_{\mathcal{V}(t)} \frac{\dot{q}}{T} d\mathcal{V}}_{\text{heat production}} = \int_{\mathcal{V}(t)} \frac{\frac{\tau^2}{2\mu} + \zeta(\nabla \cdot \vec{V})^2}{T} d\mathcal{V} - \int_{\mathcal{V}(t)} \frac{\vec{q} \cdot \nabla T}{T^2} d\mathcal{V} \quad (2.173)$$

The second law of thermodynamics can be phrased in many equivalent manners. The Clausius-Duhem inequality is one manifestation of the second law of thermodynamics, and requires that the entropy generation be greater than or equal to sum of the entropy with heat flow and heat production. This is equivalent to requiring that the RHS in Eq. (2.173) be greater than or equal to zero. For the Clausius-Duhem inequality to hold:

$$\frac{1}{2\mu} \tau^2 + \zeta(\nabla \cdot \vec{V})^2 \geq 0 \quad (2.174a)$$

$$\vec{q} \cdot \nabla T \leq 0 \quad (2.174b)$$

For the case of incompressible flow, $\nabla \cdot \vec{V} = 0$, so $\mu \geq 0$. For a spherically-symmetric radial expansion, $e_{ij} = 0$, so $\zeta \geq 0$. The second requirement shows that $k \geq 0$. The second law of thermodynamics therefore places restrictions on allowable constitutive laws. Performing a change of variables according to the procedure described in Section 2.8 to entropy variables discretely satisfies the second law of thermodynamics without the need to include additional dissipative mechanisms such as the stabilization schemes discussed in Section 15 [51].

Equilibrium thermodynamics is now used to provide a relationship between entropy, temperature, and one other state variable. Pressure is selected as this state variable because it is directly related to the BCs and forces. A choice such as ρ would complicate the equation, since it itself is a function of the other state variable, temperature. With this choice, the derivative of entropy is given by the chain rule as:

$$\frac{ds}{dt} = \left(\frac{\partial s}{\partial T} \right)_P \frac{dT}{dt} + \left(\frac{\partial s}{\partial P} \right)_T \frac{dP}{dt} \quad (2.175)$$

Specific heats are defined according to the amount of heat required to increase temperature, where several equivalent forms are obtained using Eqs. (2.166) and (2.167):

$$C_p \equiv \left(\frac{\delta q}{\delta T} \right)_P \quad (2.176a)$$

$$= \left(\frac{\partial h}{\partial T} \right)_P \quad (2.176b)$$

$$= T \left(\frac{\partial s}{\partial T} \right)_P \quad (2.176c)$$

$$C_v \equiv \left(\frac{\delta q}{\delta T} \right)_v \quad (2.177a)$$

$$= \left(\frac{\partial e}{\partial T} \right)_v \quad (2.177b)$$

$$= T \left(\frac{\partial s}{\partial T} \right)_v \quad (2.177c)$$

Hence, the coefficient on the first term on the RHS of Eq. (2.175) is C_p/T . The second coefficient in Eq. (2.175) can be determined by manipulating the Gibbs identity in Eq. (2.166). This manipulation gives a thermodynamic relationship known as the Maxwell identity:

$$-\left(\frac{\partial s}{\partial P} \right)_T = \left(\frac{\partial v}{\partial T} \right)_P \quad (2.178)$$

The Gibbs function G is defined as:

$$G \equiv e - Ts + Pv \quad (2.179)$$

The derivative of G is, by the chain rule:

$$\begin{aligned} dG &= de - Tds - sdT + Pdv + vdP \\ &= -sdT + vdP \end{aligned} \quad (2.180)$$

where Eq. (2.166) has been used. Because the Gibbs identity is an exact differential, Eq. (2.180) can be manipulated to provide the following relationships:

$$-s = \left(\frac{\partial G}{\partial T} \right)_P \quad (2.181)$$

$$v = \left(\frac{\partial G}{\partial P} \right)_T \quad (2.182)$$

Combining Eqs. (2.181) and (2.182) gives Eq. (2.178).

The expansivity, or volumetric coefficient of thermal expansion, is defined as:

$$\begin{aligned} \beta &\equiv \frac{1}{v} \left(\frac{\partial v}{\partial T} \right)_P \\ &= -\frac{1}{\rho} \left(\frac{\partial \rho}{\partial T} \right)_P \end{aligned} \quad (2.183)$$

where $\partial v/\partial T = \partial(1/\rho)/\partial T$ was expanded to give the second form. Combining Eqs. (2.183), (2.178), (2.176), and (2.175) gives:

$$\frac{ds}{dt} = \frac{C_p}{T} \frac{dT}{dt} - \beta v \frac{dP}{dt} \quad (2.184)$$

Substituting Eq. (2.184) into Eq. (2.171), assuming $\vec{q} = -k\nabla T$, and including a volumetric heat source q in the

same manner as was done in Eq. (2.155) gives the nonconservative energy equation:

$$\underbrace{\rho C_p \frac{dT}{dt}}_{\text{stored energy}} - \underbrace{T \beta \frac{dP}{dt}}_{\text{compression work}} = \underbrace{\frac{\tau^2}{2\mu}}_{\text{viscous heat}} + \underbrace{\zeta(\nabla \cdot \vec{V})^2}_{\text{volume viscous heat}} + \underbrace{\nabla \cdot (k \nabla T) + q}_{\text{heat source}} \quad (2.185)$$

An alternative form of the temperature equation is sometimes seen in the literature. Instead of taking entropy as a function of pressure and temperature as in Eq. (2.175), the entropy could alternatively have been taken as a function of specific volume and temperature.

$$\frac{ds}{dt} = \left(\frac{\partial s}{\partial T} \right)_v \frac{dT}{dt} + \left(\frac{\partial s}{\partial v} \right)_T \frac{dv}{dt} \quad (2.186)$$

From Eq. (2.177), the first coefficient on the RHS is C_v/T . The second coefficient can be expanded:

$$\left(\frac{\partial s}{\partial v} \right)_T = \left(\frac{\partial s}{\partial P} \right)_T \left(\frac{\partial P}{\partial v} \right)_T \quad (2.187)$$

An isothermal bulk modulus is defined as:

$$K_T = -v \left(\frac{\partial P}{\partial v} \right)_T \quad (2.188)$$

From Eq. (2.178), Eq. (2.183), and Eq. (2.186):

$$\begin{aligned} \frac{ds}{dt} &= \frac{C_v}{T} \frac{dT}{dt} + \beta K_T \frac{dv}{dt} \\ &= \frac{C_v}{T} \frac{dT}{dt} - \beta K_T \frac{1}{\rho^2} \frac{d\rho}{dt} \end{aligned} \quad (2.189)$$

Then, the entropy equation in Eq. (2.171) becomes:

$$\rho C_v \frac{dT}{dt} - \frac{T \beta K_T}{\rho} \frac{d\rho}{dt} = \frac{\tau^2}{2\mu} + \zeta(\nabla \cdot \vec{V})^2 - \nabla \cdot \vec{q} + q \quad (2.190)$$

This is an equivalent expression of nonconservative equation, except that some authors erroneously conclude that for negligible viscous heating and for incompressible flow, the equation reduces to $\rho C_v dT/dt = -\nabla \cdot \vec{q}$. This is incorrect, however, since the condition for incompressible flow given in Eq. (2.267) is not the same as $(1/\rho)d\rho/dt = 0$.

By neglecting compression work, viscous heating, and volumetric viscous heating, the non-conservative form of the energy equation is:

$$\rho C_p \frac{\partial T}{\partial t} + \rho C_p \vec{V} \cdot \nabla T - \nabla \cdot (k \nabla T) - q = 0 \quad (2.191)$$

The porous media versions of Eqs. (2.161) and (2.191) can be derived using properties defined in Section 2.2. Both versions of the energy equation will be derived simultaneously because there is some overlap.

Eq. (2.191) has neglected compression work. Some accuracy could be regained by using a low Mach number model [20, 52]. Low Mach number models are based on splitting the pressure into a spatially uniform

thermodynamic pressure P and a nonuniform hydrodynamic pressure $P_d \ll P$:

$$P^*(\vec{r}, t) = P(t) + P_d(\vec{r}, t) \quad (2.192)$$

where P^* is the total pressure. A pressure term appears in both the momentum equation in Eq. (2.94) and the energy equation in Eq. (2.185). Low Mach models split the pressure such that the thermodynamic pressure is used in the energy equation, while the hydrodynamic pressure is used in the momentum equation. This decouples variations in density from acoustic waves, and essentially filters them out. The pressure EOS is assumed to refer to the thermodynamic pressure. Substituting the EOS into the continuity equation provides the additional equation needed to close the system. Two common additional simplifications are the 1) variable density model, in which P is assumed constant, and 2) the Boussinesq model, where in addition to a constant P , ρ is constant except in the buoyancy term in the momentum equation. Application of the Boussinesq model and the more general low Mach model to an HTR suggests that a compressible model needs to be used for gas reactor applications [20].

The time derivative in Eq. (2.161) is rewritten using Eqs. (2.38) and (2.29), giving Eq. (2.193)a. If fluctuations in density are neglected, and no phase change occurs and the solid is stationary such that $\vec{w}_f = 0$, Eq. (2.193)a simplifies to Eq. (2.193)b.

$$\left\langle \frac{\partial(\rho E)}{\partial t} \right\rangle \rightarrow \frac{\partial(\epsilon_f \langle \rho_f \rangle^f \langle E_f \rangle^f)}{\partial t} + \frac{\partial \langle \hat{\rho}_f \hat{E}_f \rangle}{\partial t} - \frac{1}{V} \int_{S_i} \rho_f E_f \vec{w}_f \cdot \vec{n}_f dS \quad (2.193a)$$

$$\rightarrow \frac{\partial(\epsilon_f \langle \rho_f \rangle^f \langle E_f \rangle^f)}{\partial t} \quad (2.193b)$$

The time derivative term in Eq. (2.191) is first expanded using Eq. (2.30) to give Eq. (2.194).

$$\begin{aligned} \rho C_p \left\langle \frac{\partial T}{\partial t} \right\rangle &\rightarrow \left\langle \hat{\rho}_f \hat{C}_{pf} \frac{\partial \hat{T}_f}{\partial t} \right\rangle + \left\langle \hat{\rho}_f \frac{\partial \hat{T}_f}{\partial t} \right\rangle \langle C_{pf} \rangle^f + \left\langle \hat{C}_{pf} \frac{\partial \hat{T}_f}{\partial t} \right\rangle \langle \rho_f \rangle^f + \\ &\left[\epsilon_f \langle \rho_f \rangle^f \langle C_{pf} \rangle^f + \langle \hat{\rho}_f \hat{C}_{pf} \rangle \right] \left\langle \frac{\partial T_f}{\partial t} \right\rangle^f \end{aligned} \quad (2.194)$$

Then, neglecting fluctuations in density and specific heat relative to fluctuations in temperature gives Eq. (2.195)a. Next, Eq. (2.38) is used to rewrite the time derivative, as shown in Eq. (2.195)b. Then, all variables are expressed in terms of intrinsic averages and no phase change and a stationary solid are assumed such that $\vec{w}_f = 0$, giving Eq. (2.195)c.

$$\rho C_p \left\langle \frac{\partial T}{\partial t} \right\rangle \rightarrow \langle \rho_f \rangle^f \langle C_{pf} \rangle^f \left\langle \frac{\partial T_f}{\partial t} \right\rangle \quad (2.195a)$$

$$\rightarrow \langle \rho_f \rangle^f \langle C_{pf} \rangle^f \left(\frac{\partial \langle T_f \rangle}{\partial t} - \frac{1}{V} \int_{S_i} T_f \vec{w}_f \cdot \vec{n}_f dS \right) \quad (2.195b)$$

$$\rightarrow \langle \rho_f \rangle^f \langle C_{pf} \rangle^f \frac{\partial(\epsilon_f \langle T_f \rangle^f)}{\partial t} \quad (2.195c)$$

The advective term in Eq. (2.161) is first rewritten using Eq. (2.20)a, giving Eq. (2.196).

$$\langle \nabla \cdot (\rho_f H_f \vec{V}_f) \rangle \rightarrow \nabla \cdot \langle \rho_f H_f \vec{V}_f \rangle + \frac{1}{V} \int_{S_i} \rho_f H_f \vec{V}_f \cdot \vec{n}_f dS \quad (2.196a)$$

$$\rightarrow \nabla \cdot \varepsilon_f \langle \rho_f H_f \vec{V}_f \rangle^f + \frac{1}{V} \int_{S_i} \rho_f H_f \vec{V}_f \cdot \vec{n}_f dS \quad (2.196b)$$

Then, Eq. (2.30) is used to expand the gradient argument. Then, neglect fluctuations in density to give Eq. (2.197b).

$$\varepsilon_f \langle \rho_f H_f \vec{V}_f \rangle^f \rightarrow (\varepsilon_f \langle \rho_f \rangle^f \langle H_f \rangle^f + \langle \hat{\rho}_f \hat{H}_f \rangle) \langle \vec{V}_f \rangle^f + \langle \hat{\rho}_f \hat{V}_f \rangle \langle \hat{H}_f \rangle^f + \langle \rho_f \rangle^f \langle \hat{H}_f \hat{V}_f \rangle + \langle \hat{\rho}_f \hat{H}_f \hat{V}_f \rangle \quad (2.197a)$$

$$\rightarrow \varepsilon_f \langle \rho_f \rangle^f \langle H_f \rangle^f \langle \vec{V}_f \rangle^f + \langle \rho_f \rangle^f \langle \hat{H}_f \hat{V}_f \rangle \quad (2.197b)$$

Inserting Eq. (2.197) into Eq. (2.196b), with the assumption of no phase change or moving solid such that $\vec{V}_f = 0$, gives the final form of the advective term for the conservative energy equation:

$$\langle \nabla \cdot (\rho_f H_f \vec{V}_f) \rangle \rightarrow \nabla \cdot \left(\varepsilon_f \langle \rho_f \rangle^f \langle H_f \rangle^f \langle \vec{V}_f \rangle^f + \langle \rho_f \rangle^f \langle \hat{H}_f \hat{V}_f \rangle \right) \quad (2.198)$$

The advective term in Eq. (2.191) is first rewritten using Eq. (2.30):

$$\begin{aligned} \langle \rho_f C_{pf} \vec{V}_f \cdot \nabla T_f \rangle &\rightarrow \langle \hat{\rho}_f \hat{C}_{pf} \hat{V}_f \cdot \nabla T_f \rangle + \langle \hat{\rho}_f \hat{C}_{pf} \nabla T_f \rangle \cdot \langle \vec{V}_f \rangle^f + \langle \hat{\rho}_f \hat{V}_f \cdot \nabla T_f \rangle \langle C_{pf} \rangle^f + \\ &\langle \hat{C}_{pf} \hat{V}_f \cdot \nabla T_f \rangle \langle \rho_f \rangle^f + \langle \rho_f \rangle^f \langle C_{pf} \rangle^f \langle \hat{V}_f \cdot \nabla T_f \rangle + \langle \vec{V}_f \rangle^f \langle C_{pf} \rangle^f \langle \hat{\rho}_f \cdot \nabla T_f \rangle + \\ &\langle \rho_f \rangle^f \langle \vec{V}_f \rangle^f \cdot \langle \hat{C}_{pf} \nabla T_f \rangle + \left(\langle \hat{\rho}_f \hat{C}_{pf} \rangle \langle \vec{V}_f \rangle^f + \langle \hat{\rho}_f \hat{V}_f \rangle \langle C_{pf} \rangle^f \right) \cdot \langle \nabla T_f \rangle^f + \\ &\left(\langle \hat{V}_f \hat{C}_{pf} \rangle \langle \rho_f \rangle^f + \varepsilon_f \langle \rho_f \rangle^f \langle C_{pf} \rangle^f \langle \vec{V}_f \rangle^f + \langle \hat{\rho}_f \hat{C}_{pf} \hat{V}_f \rangle \right) \cdot \langle \nabla T_f \rangle^f \end{aligned} \quad (2.199)$$

Then, neglecting fluctuations in density and specific heat simplify Eq. (2.199) to Eq. (2.200a). Then, apply Eq. (2.20)b to express the gradient term, giving Eq. (2.200)c.

$$\langle \rho_f C_{pf} \vec{V}_f \cdot \nabla T_f \rangle \rightarrow \langle \rho_f \rangle^f \langle C_{pf} \rangle^f \langle \hat{V}_f \cdot \nabla T_f \rangle + \varepsilon_f \langle \rho_f \rangle^f \langle C_{pf} \rangle^f \langle \vec{V}_f \rangle^f \cdot \langle \nabla T_f \rangle^f \quad (2.200a)$$

$$\rightarrow \langle \rho_f \rangle^f \langle C_{pf} \rangle^f \langle \hat{V}_f \cdot \nabla T_f \rangle + \langle \rho_f \rangle^f \langle C_{pf} \rangle^f \langle \vec{V}_f \rangle^f \cdot \langle \nabla T_f \rangle \quad (2.200b)$$

$$\rightarrow \langle \rho_f \rangle^f \langle C_{pf} \rangle^f \langle \hat{V}_f \cdot \nabla T_f \rangle + \langle \rho_f \rangle^f \langle C_{pf} \rangle^f \langle \vec{V}_f \rangle^f \cdot \left(\varepsilon_f \nabla \langle T_f \rangle^f + \frac{1}{V} \int_{S_i} T_f \vec{n}_f dS \right) \quad (2.200c)$$

The integral in Eq. (2.200)c represents the tortuosity advective flux, or the increase in advection caused by mechanical effects of the solid on the fluid. It is neglected in Pronghorn. Averaging the heat conduction term first using Eq. (2.20)b gives Eq. (2.201)a. Then, apply Eq. (2.29) to give Eq. (2.201)b, followed by Eq. (2.20)b to give Eq. (2.201)c. By neglecting the fluctuation in thermal conductivity, Eq. (2.201)d results.

$$\langle \nabla \cdot k_f \nabla T_f \rangle \rightarrow \nabla \cdot \langle k_f \nabla T_f \rangle + \frac{1}{V} \int_{S_i} k_f \nabla T_f \vec{n}_f dS \quad (2.201a)$$

$$\rightarrow \nabla \cdot \epsilon_f \langle k_f \rangle^f \langle \nabla T_f \rangle^f + \nabla \cdot \langle \hat{k}_f \nabla \hat{T}_f \rangle + \frac{1}{V} \int_{S_i} k_f \nabla T_f \vec{n}_f dS \quad (2.201b)$$

$$\rightarrow \nabla \cdot \langle k_f \rangle^f \left(\epsilon_f \nabla \langle T_f \rangle^f + \frac{1}{V} \int_{S_i} \hat{T}_f \vec{n}_f dS \right) + \nabla \cdot \langle \hat{k}_f \nabla \hat{T}_f \rangle + \frac{1}{V} \int_{S_i} k_f \nabla T_f \vec{n}_f dS \quad (2.201c)$$

$$\rightarrow \nabla \cdot \langle k_f \rangle^f \left(\epsilon_f \nabla \langle T_f \rangle^f + \frac{1}{V} \int_{S_i} \hat{T}_f \vec{n}_f dS \right) + \frac{1}{V} \int_{S_i} k_f \nabla T_f \vec{n}_f dS \quad (2.201d)$$

The first integral in Eq. (2.201d) is often represented as the tortuosity heat flux (though some authors define the tortuosity heat flux based on the use of Eq. (2.20)a, rather than Eq. (2.20)b) [53]. This tortuosity heat flux is often very small because convection dominates conduction, and hence it can be neglected [53]. The second integral in Eq. (2.201d) represents the average heat flux from the fluid to the solid at the fluid-solid boundary. This can be expressed using Newton's law of cooling as:

$$\frac{1}{V} \int_{S_i} k_f \nabla T_f \vec{n}_f dS = \alpha \left(\langle T_s \rangle^s - \langle T_f \rangle^f \right) \quad (2.202)$$

where α is the convective heat transfer coefficient between the two intrinsic phase averaged temperatures. To obtain the correct units for the convective cooling term, α represents the heat transfer coefficient h_c (which appears in Nusselt number correlations) multiplied by a_w :

$$\alpha \equiv a_w h_c \quad (2.203)$$

where a_w represents the ratio of the wetted area through which heat transfer can occur in a length of δx per unit volume of length δx , in the limit of δx going to zero. In other words, a_w represents the heat transfer area per unit volume.

$$a_w = \lim_{\delta x \rightarrow 0} \frac{\text{wetted heat transfer area of length } \delta x}{\text{volume of length } \delta x} \quad (2.204)$$

For spherical particles, a_w is defined in terms of the solid area and volume, and then multiplied by $(1 - \epsilon)$ to reflect the portion of the volume that is solid.

$$\begin{aligned} a_w &= 4 \frac{\pi (d_p/2)^2}{(4/3)\pi (d_p/2)^3} (1 - \epsilon) \\ &= \frac{6(1 - \epsilon)}{d_p} \end{aligned} \quad (2.205)$$

Dixon and Cresswell suggest that a_w has an additional component in pebble bed systems that accounts for the presence and shape of the solid particles [32]:

$$a_w \rightarrow a_w \frac{k_s}{10k_s + Nu k_f} \quad (2.206)$$

Correlations for Nu are discussed in Section 10. Finally, the source term is $S_f = -\rho_f \vec{V}_f \cdot \vec{g} - q$ for the conservative equation. For the nonconservative equation, the gravitational acceleration term was subtracted out earlier in the

formation of the internal energy equation, and is not needed. Eq. (2.29) is used to rewrite the product term, giving Eq. (2.207)b.

$$\langle S_f \rangle \rightarrow -\langle \rho_f \vec{V}_f \cdot \vec{b} \rangle - \langle q_f \rangle \quad (2.207a)$$

$$\rightarrow -\varepsilon_f \langle \rho_f \rangle^f \langle \vec{V}_f \rangle^f \cdot \langle \vec{b} \rangle^f - \varepsilon_f \langle \hat{\rho}_f \hat{V}_f \rangle \cdot \langle \vec{b} \rangle^f - \langle q_f \rangle \quad (2.207b)$$

For flows in which thermal and pressure gradients are not very large, density gradients will be much smaller than velocity gradients at the microscopic level. Combining these derivations together gives the porous media versions of Eqs. (2.161) and (2.191):

$$\begin{aligned} \frac{\partial(\varepsilon_f \langle \rho_f \rangle^f \langle E_f \rangle^f)}{\partial t} + \nabla \cdot [\varepsilon_f \langle \rho_f \rangle^f \langle H_f \rangle^f \langle \vec{V}_f \rangle^f] + \nabla \cdot [\langle \rho_f \rangle^f \langle \hat{H}_f \hat{V}_f \rangle] \\ - \nabla \cdot (\varepsilon_f \langle k_f \rangle^f \nabla \langle T_f \rangle^f) + \alpha (\langle T_f \rangle^f - \langle T_s \rangle^s) - \varepsilon_f \langle \rho_f \rangle^f \langle \vec{V}_f \rangle^f \cdot \vec{b} - \langle q_f \rangle = 0 \end{aligned} \quad (2.208)$$

$$\begin{aligned} \langle \rho_f \rangle^f \langle C_{pf} \rangle^f \frac{\partial(\varepsilon_f \langle T_f \rangle^f)}{\partial t} + \langle \rho_f \rangle^f \langle C_{pf} \rangle^f \langle \hat{V}_f \nabla \hat{T}_f \rangle + \varepsilon_f \langle \rho_f \rangle^f \langle C_{pf} \rangle^f \langle \vec{V}_f \rangle^f \nabla \langle T_f \rangle^f + \\ - \nabla \cdot (\varepsilon_f \langle k_f \rangle^f \nabla \langle T_f \rangle^f) + \alpha (\langle T_f \rangle^f - \langle T_s \rangle^s) - \langle q_f \rangle = 0 \end{aligned} \quad (2.209)$$

This equation still leaves one term that needs to be described with a constitutive model. Thermal energy dispersion arises due to additional mixing caused by the porous media due to 1) changes in flow direction initiated by the solid particles, 2) recirculation flows within the pores, and 3) eddy diffusion in turbulence. Following a procedure very similar to the derivation of the Reynolds stress transport equation, it can be shown that this thermal dispersion term can be approximated with a gradient diffusion hypothesis as [53]:

$$\langle \rho_f \rangle^f \langle C_{pf} \rangle^f \langle \hat{V}_f \nabla \hat{T}_f \rangle \approx -\nabla \cdot (k_d \nabla \langle T_f \rangle^f) \quad (2.210)$$

where k_d is a thermal dispersion conductivity. The thermal dispersion conductivity captures enhanced diffusion due to velocity and temperature perturbations in the porous media, and only appears in the fluid energy equation. The thermal dispersion conductivity is in general a second-order tensor. Correlations representing $k_f + k_d$ are frequently given in the literature as the “effective fluid thermal conductivity” κ_f . Correlations for κ_f are discussed in Section 12. Eqs. (2.208) and (2.209) written in Pronghorn’s notation become:

$$\frac{\partial(\varepsilon \rho_f E)}{\partial t} + \nabla \cdot (\varepsilon H_f \rho_f \vec{V}) - \nabla \cdot (\kappa_f \nabla T_f) - \varepsilon \rho_f \vec{b} \cdot \vec{V} + \alpha(T_f - T_s) - q_f = 0 \quad (2.211)$$

$$\rho_f C_{pf} \frac{\partial(\varepsilon T_f)}{\partial t} + \varepsilon \rho_f C_{pf} \vec{V} \cdot \nabla T_f + \nabla \cdot (\kappa_f \nabla T_f) + \alpha(T_f - T_s) - q_f = 0 \quad (2.212)$$

Hence, E_f , H_f , T_f , C_{pf} , and k_f represent the fluid intrinsic average total energy, total enthalpy, temperature, specific heat, and thermal conductivity, respectively. α represents the extrinsic average convective heat transfer coefficient (which is the same for both the fluid and solid, and hence can also be interpreted as the intrinsic average convective heat transfer coefficient). q_f represents the fluid extrinsic average heat source.

Eq. (2.212) is sometimes shown in a conservative (but more restrictive) form in terms of $\rho C_p T$. The conserva-

tive time and advection of $\rho C_p T$ can be expanded as:

$$\begin{aligned} \frac{\partial(\rho C_p T)}{\partial t} + \nabla \cdot (\rho C_p T \vec{V}) &\equiv C_p T \left(\frac{\partial \rho}{\partial t} + \rho \nabla \cdot \vec{V} + \vec{V} \cdot \nabla \rho \right) + \\ &+ \rho C_p \frac{\partial T}{\partial t} + \rho T \frac{\partial C_p}{\partial t} + \rho C_p \vec{V} \cdot \nabla T + \rho T \vec{V} \cdot \nabla C_p \end{aligned} \quad (2.213)$$

where the continuity equation cancels. Provided the specific heat is constant in both space $\nabla C_p = 0$ and time $\partial C_p / \partial t = 0$, the following equality exists, and the nonconservative energy equation can be written in conservative form:

$$\frac{\partial(\epsilon \rho C_p T)}{\partial t} + \nabla \cdot (\epsilon \rho C_p T \vec{V}) \equiv \rho C_p \frac{\partial(\epsilon T)}{\partial t} + \epsilon \rho C_p \vec{V} \cdot \nabla T \quad (2.214)$$

where porosity has been inserted as appropriate.

As a final remark, the governing equations in Pronghorn allow for compressibility of the fluid, so long as the compression is not so large that compression work or volume dissipative effects become important.

2.6 The Solid Energy Equation

To obtain the solid energy equation, simply set $\vec{V} = 0$ in Eq. (2.211) or (2.212) with ϵ replaced by $1 - \epsilon$ to reflect the fraction of the volume that is solid. The assumptions made in the derivation of the solid energy equation are therefore the same as those made in the derivation of the fluid energy equation, except that the solid is also assumed stationary. Because EOS are often only available for solids in terms of pressure and temperature, the nonconservative energy equation in Eq. (2.212) is used exclusively for the solid:

$$(1 - \epsilon) \rho_s C_{ps} \frac{\partial T_s}{\partial t} - \nabla \cdot (\kappa_s \nabla T_s) + \alpha(T_s - T_f) - q_s = 0 \quad (2.215)$$

where κ_s is the effective solid thermal conductivity that represents the effective thermal dispersion in the solid phase, ρ_s represents the solid intrinsic average density, and C_{ps} represents the solid intrinsic average specific heat. Correlations for κ_s are generally more complex than those for κ_f , because κ_s captures the combined effects of solid-to-solid radiation, solid-fluid-solid conduction, and solid-to-solid conduction. Models for these components of κ_s are given in Section 11.

$$\kappa_s = \kappa_{\text{radiation}} + \kappa_{\text{fluid conduction}} + \kappa_{\text{solid conduction}} \quad (2.216)$$

Even if there are no heat sources in either phase, the temperatures of the phases will not match at the edges of the bed if any heat transfer occurs from the bed to the ambient. The velocity channeling effect at the bed edges causes higher convective heat transfer between the walls and the fluid [54]. Because the fluid has some nonzero heat capacity, there is a time delay for heat transfer to the solid, by which time the fluid has continued through the bed, resulting in a temperature difference between the solid and fluid phases. Fig. 7 shows solid and fluid temperatures for flow towards the right of a 300 K inlet temperature with walls held at 400 K [5]. This effect has also been observed in the SANA validation tests [55].

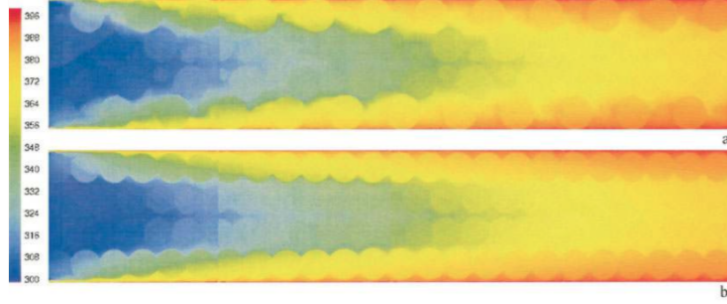


Figure 7: Solid and fluid temperatures for two vertical planes cut through a cylindrical bed [5]. Flow is to the right, entering with a temperature of 300 K with walls held at 400 K. The slight discontinuity in the temperatures is caused by neglecting axial conduction.

Similarly, if there is a large k_s/k_f , differences in conductive heat transport will also produce temperature differences. So, even if the phases are in approximate thermal equilibrium, using two energy equations will still provide more accurate results. Fig. 7 also illustrates why radiation heat transfer from the pebbles to the wall can be significant - despite touching the wall, the solid is not necessarily at the same temperature as the wall.

While the volume averaging approach was used to obtain Eq. (2.215), most porous media codes interpret T_s as a volume-averaged solid *surface* temperature, rather than as a volume average over all regions of the solid [10, 36, 49, 50, 56]. This assumption permits a relatively straightforward solution of the solid temperature profile. This approach is most commonly performed by using an element-wise average or maximum T_s as a Dirichlet BC imposed on the solid surface. For pebble fuels, because each solid is relatively small, without significant loss of accuracy a single Dirichlet temperature BC is imposed over the entire surface, reducing the solution of the fuel temperature profile to a 1-D heat conduction problem in many independent pebbles:

$$(\rho C_p)_p \frac{\partial T_p}{\partial t} - \nabla \cdot (k_p \nabla T_p) - (1 - \epsilon) \dot{q}_s = 0 \quad (2.217)$$

where p subscript refers to “pebble,” but strictly speaking the above formulation is also valid for non-spherical solid shapes. \dot{q}_s is the heat source in the solid phase, and to properly conserve energy in the fuel temperature solution, this quantity must be scaled by $1 - \epsilon$. No pebbles are explicitly modeled *in* the flow field, but are rather superimposed on the problem, i.e. a “representative” pebble is modeled at spatial locations that may or may not actually correspond to a physical pebble location.

For steady-state 1-D radial conduction with constant thermal properties and uniform \dot{q}_s , the analytical solution for a single-region pebble is linear in \dot{q}_s and $T_p(R_p)$ and quadratic in R_p :

$$T_p(r) = -\frac{(1 - \epsilon) \dot{q}_s}{6k_p} (r^2 - R_p^2) + T_p(R_p) \quad (2.218)$$

Unfortunately, for the TRistructural ISOtropic (TRISO) that is used in pebble fuels, a significant level of heterogeneity exists in a single pebble. Fuel kernels on the order of a mm in size are packed in a graphite matrix that is most often surrounded by a graphite shell, with a pebble diameter on the order of cm. This poses significant problems for even performing a 1-D conduction solution in a pebble due to the randomness and complicated mesh required. While Eq. (2.217) can be used in the homogeneous graphite shell, a common simplification of the fuel-graphite matrix region involves homogenization with spatially-uniform thermal properties. A homogenized fuel temperature T_{pf} and graphite matrix temperature T_{pm} are then solved in this region, with each equation having the form in Eq. (2.217), with the inclusion of an extra phase coupling term to simulate heat transfer between the TRISO particles and their

immediately-surrounding graphite matrix [57]:

$$(\rho C_p)_{p_f} \frac{\partial T_{p_f}}{\partial t} - \nabla \cdot (k_{p_f} \nabla T_{p_f}) + \eta (T_{p_f} - T_{p_m}) - (1 - \epsilon) \dot{q}_s = 0 \quad (2.219)$$

$$(\rho C_p)_{p_m} \frac{\partial T_{p_m}}{\partial t} - \nabla \cdot (k_{p_m} \nabla T_{p_m}) - \eta (T_{p_f} - T_{p_m}) = 0 \quad (2.220)$$

where p_f subscript denotes the homogenized fuel temperature, p_m the homogenized graphite matrix temperature, and η is a coupling coefficient between the phases. Average values for $(\rho C_p)_p$ and k_p need to be determined. The simplest averaging techniques involve parallel and series heat transfer arguments such as sometimes used in evaluating κ_s in Eqs. (11.2) and (11.3). Strictly parallel or series heat transfer provide bounds on the actual thermal properties, but differences in pebble centerline temperatures have been shown to differ by 60°C between these two methods for gas reactor systems [57]. Even simpler, some have just used graphite thermal properties for the fuel region, since the graphite matrix constitutes the majority of the region [58]. More advanced Monte Carlo methods have been developed to solve the conduction problem to provide reference solutions for least-squares fitting of $(\rho C_p)_p$ and k_p , but are relatively expensive [57,59].

These Monte Carlo methods are based on similarity in the Poisson equation and the neutron diffusion equation with no fission or absorption. If custom cross sections are defined for the simulation to obtain equivalence between the thermal conductivity and the neutron diffusion coefficient, then the Monte Carlo results are stochastic solutions to the heat conduction equation, and tallies can be used to evaluate effective thermal properties [59]. Special treatments are required at boundaries, since the Dirichlet or Neumann-type BCs used in the heat equation do not have immediate analogues in the neutron diffusion equation and the diffusion equation is invalid near boundaries. Scaling the problem to obtain a smaller mean free path and/or imposing transport-corrected BCs on the Monte Carlo output results have both been shown to be effective [59].

It may simply be sufficient to evaluate $(\rho C_p)_p$ and k_p as the average of the series and parallel heat transfer bounds to a first order approximation [59]. Reference solutions or other analytical approximations are required for estimating η , however. Assuming a method exists for computing a homogenized solid temperature profile, for TRISO fuel, this homogenized temperature does not correspond to the fuel kernel temperature, which is most often the parameter of interest for reactivity feedback calculations. To obtain the temperature distribution within a single TRISO particle, another similar level of multiscale extrapolation is performed. A 1-D heat conduction solution can be performed within a “representative” TRISO particle by applying a Dirichlet temperature BC obtained from either the fuel region average or peak temperature, depending on the metric of interest. This multi-level superposition of pebble in a bed and fuel particle within a pebble has been frequently used [11,57], and is very straightforward to implement within the MOOSE MultiApp system. Each MOOSE “animal” is a MultiApp that has many capabilities in place to exchange information with other MOOSE MultiApps. The tree-level coupling hierarchy between MOOSE applications permits straightforward multiscale analysis of pebble bed reactors.

A MasterApp controls the execution of a coupled simulation of any number of applications. A multiscale core Thermal-Hydraulic (T/H) simulation can be performed by setting Pronghorn as the MasterApp that controls many parallel instances of a fuels performance MultiApp such as BISON [60]. This fuels performance MultiApp receives fuel surface temperatures from Pronghorn and solves many fuel pebbles independently. Each of these fuels performance MultiApps would then each control a TRISO performance MultiApp that solves for a representative TRISO particle in each fuel pebble. This multiscale coupling capability is available in Pronghorn and all other MOOSE applications, and will be described in more detail in the user manual.

2.7 The Legacy Pronghorn Equations

In order to compare physical results with the legacy version of Pronghorn circa 2008, additional kernels and BCs are included that represent additional assumptions that are more restrictive than the governing equations discussed in Sections 2.3, 2.4, 2.5, and 2.6 [61]. Pronghorn includes capabilities for using the same equations as the legacy Pronghorn, except that density may come from any EOS (i.e. the ideal gas law is no longer hard-wired into the source code). The remainder of this section presents the mass, momentum, fluid energy, and solid energy equations for backwards compatibility.

The legacy version of Pronghorn neglected the advection and time terms in the momentum equation and set $\vec{b} \equiv \vec{g}$, giving the following momentum equation [61]:

$$\epsilon \nabla P - \epsilon \rho_f \vec{g} + W \rho_f \vec{V} = 0 \quad (2.221)$$

Eq. (2.221) is solved for momentum. Substituting $\rho_f \vec{V}$ in Eq. (2.221) into the continuity equation in Eq. (2.49) gives a Poisson equation that can be solved for density or pressure:

$$\epsilon \frac{\partial \rho_f}{\partial t} + \nabla \cdot \left[\frac{\epsilon}{W} (\epsilon \rho_f \vec{g} - \epsilon \nabla P) \right] = 0 \quad (2.222)$$

The legacy fluid energy equation was Eq. (2.212), written in conservative form according to Eq. (2.214), which is only valid if the specific heat is constant. Because the legacy Pronghorn always assumed the ideal gas law, the specific heat was always constant (this is an inherent assumption in this EOS), which is why the conservative form was valid. However, the modern Pronghorn removes this restriction, and in general the conservative form is not valid. Eq. (2.215) was used for the solid energy.

2.8 A Unified Approach to Solving the Navier-Stokes Equations

The previous sections have described the derivation of the conservation of mass, momentum, and energy equations for the fluid and solid phases for a general compressible fluid and a stationary solid. Because the coupling of the fluid and solid energy equations only occurs through the convective heat transfer term, the solid energy equation is not tightly coupled to the fluid equations, and is excluded from the discussion in this section.

The Navier-Stokes equations, on the other hand, must be solved in terms of the three components of velocity (or momentum) and two thermodynamic state variables, such as P and T or ρE and ρ . One choice of solution variables will not necessarily be ideal for *all* flows. For example, flibe is a nearly incompressible fluid, since its variation with pressure is very small. If the Navier-Stokes equations were solved for velocity, density, and temperature, determining pressure from the EOS as a function of density and temperature would require a very large number of significant digits (and would introduce stiffness and contamination of the solution), since density varies so little with pressure. For molten salts, $(\partial \rho / \partial P)_T \approx 1.73 \times 10^{-7}$, giving a compressibility $\alpha_T = 8.66 \times 10^{-11}$, a very small number [62]! Numerical error in the density will result in very inaccurate pressure calculations, requiring an incompressible model [15, 49]. Solving the governing equations for some other variable besides density would be a wise choice. Gases are often treated as compressible, in which case density varies strongly with both pressure and temperature, and the best choice of solution variables are often the conserved quantities of mass, momentum, and energy [63]. There is no clean dividing line between compressible and incompressible flows, so some approach for unifying these flows under a single set of solution variables would be desirable.

Section 2.5 showed the derivation of the fluid energy equation in terms of a conservative variable (ρE) and a primitive variable (T_f). Similar derivations could be performed to transform the mass, momentum, and energy equations for the conserved variables to equations for *any* choice of solution variables. However, Hauke and Hughes have developed a unified approach to solving the Navier-Stokes equations for any choice of solution variables that does not rely on

direct manipulation of each equation. This unified approach is obtained by multiplying the conservative form of the compressible Navier-Stokes equations by matrices representing the derivatives of the conserved quantities with respect to a new set of variables. This permits the solution of both incompressible and compressible flows, for any solution variables, with only minor modifications to the source code and no lengthy by-hand derivations that use thermodynamic relationships to transform equations of one variable to equations of a different variable [64]. See the derivation of Eq. (2.212) from Eq. (2.211) in Section 2.5 for the alternative (but not conducive to easy implementation) approach to what is described in this section.

The unified solution method is best described by writing the system of fluid equations to be solved in Pronghorn in condensed form as:

$$\frac{\partial(\varepsilon\vec{U})}{\partial t} + \frac{\partial(\varepsilon\vec{F}_i)}{\partial x_i} - \frac{\partial\vec{G}_i}{\partial x_i} + \vec{S} = \vec{0} \quad (2.223)$$

where \vec{U} is the vector of unknowns, \vec{F}_i is the inviscid flux vector, \vec{G}_i is the diffusive flux vector, and \vec{S} is the source vector:

$$\vec{U} = \begin{bmatrix} \rho_f \\ \rho_f V_1 \\ \rho_f V_2 \\ \rho_f V_3 \\ \rho_f E \end{bmatrix}, \quad \vec{F}_i = \begin{bmatrix} \rho_f V_i \\ \rho_f V_1 V_i + P\delta_{1i} \\ \rho_f V_2 V_i + P\delta_{2i} \\ \rho_f V_3 V_i + P\delta_{3i} \\ H_f \rho_f V_i \end{bmatrix}, \quad \vec{G}_i = \begin{bmatrix} 0 \\ 0 \\ 0 \\ 0 \\ \kappa_f \frac{\partial T_f}{\partial x_i} \end{bmatrix}, \quad \vec{S} = \begin{bmatrix} 0 \\ -\varepsilon\rho_f g_1 + W\rho_f V_1 - P\frac{\partial\varepsilon}{\partial x_1} \\ -\varepsilon\rho_f g_2 + W\rho_f V_2 - P\frac{\partial\varepsilon}{\partial x_2} \\ -\varepsilon\rho_f g_3 + W\rho_f V_3 - P\frac{\partial\varepsilon}{\partial x_3} \\ -\varepsilon\rho_f b_i V_i + \alpha(T_f - T_s) - \dot{q}_f \end{bmatrix} \quad (2.224)$$

where for simplicity ε is kept within the time differentiation term, though it should be noted that it is assumed time-independent in Pronghorn. $\varepsilon\nabla P$ has been expanded as $\nabla(\varepsilon P) - P\nabla\varepsilon$ such that εP could be moved inside the flux term. This equation can be written in quasi-linear form using the chain rule:

$$\frac{\partial(\varepsilon\vec{U})}{\partial t} + \varepsilon\mathbf{A}_i \frac{\partial\vec{U}}{\partial x_i} + \vec{F}_i \frac{\partial\varepsilon}{\partial x_i} - \frac{\partial}{\partial x_i} \left(\mathbf{K}_{ij} \frac{\partial\vec{U}}{\partial x_j} \right) + \vec{S} = \vec{0} \quad (2.225)$$

$$\equiv \vec{R}(\vec{U})$$

where \mathbf{A}_i are the inviscid flux Jacobian matrices:

$$\mathbf{A}_i \equiv \frac{\partial\vec{F}_i}{\partial\vec{U}} \quad (2.226)$$

and \mathbf{K}_{ij} are the diffusive flux Jacobian matrices:

$$\mathbf{K}_{ij} \frac{\partial\vec{U}}{\partial x_j} \equiv \vec{G}_i \quad (2.227)$$

and $\vec{R}(\vec{U})$ is the strong residual vector. \vec{F}_i is homogeneous of degree 1 in the conservative variables \vec{U} if $\vec{F}_i(\alpha\vec{U}) = \alpha\vec{F}_i(\vec{U})$, which occurs if $P(\alpha\rho, e) = \alpha P(\rho, e)$, where α is a positive constant. If this homogeneity property holds, then:

$$\vec{F}_i = \mathbf{A}_i \vec{U} \quad (2.228)$$

While Eq. (2.228) does not hold for a generic EOS, it holds for the ideal gas EOS.

Eq. (2.228) for the ideal gas law can be shown for \vec{F}_1 by simply performing the multiplication:

$$\mathbf{A}_1 \begin{bmatrix} \rho \\ \rho V_1 \\ \rho V_2 \\ \rho V_3 \\ \rho E \end{bmatrix} = \begin{bmatrix} \rho V_1 \\ \rho V_1 V_1 + (\gamma - 1) \left[\rho E - \frac{1}{2} \rho (V_1 V_1 + V_2 V_2 + V_3 V_3) \right] \\ \rho V_1 V_2 \\ \rho V_1 V_3 \\ V_1 \rho E + V_1 (\gamma - 1) \left[\rho E - \frac{1}{2} \rho (V_1 V_1 + V_2 V_2 + V_3 V_3) \right] \end{bmatrix} \quad (2.229)$$

Recognizing the ideal gas EOS for pressure from Eq. (7.10)b and the definition of total energy from Eq. (2.154) and total enthalpy from Eq. (2.160) the above becomes:

$$\mathbf{A}_1 \begin{bmatrix} \rho \\ \rho V_1 \\ \rho V_2 \\ \rho V_3 \\ \rho E \end{bmatrix} = \begin{bmatrix} \rho V_1 \\ \rho V_1 V_1 + P \\ \rho V_1 V_2 \\ \rho V_1 V_3 \\ V_1 h \end{bmatrix} \quad (2.230)$$

which matches \vec{F}_1 defined in Eq. (15.26). A similar procedure can be performed for $\mathbf{A}_2 \vec{U}$ and $\mathbf{A}_3 \vec{U}$.

Eq. (2.223) is an equation for the set of variables in \vec{U} given in Eq. (2.224), and has the following weak form:

$$\int_{\Omega} \left(\vec{w} \cdot \frac{\partial(\varepsilon \vec{U})}{\partial t} - \varepsilon \frac{\partial \vec{w}}{\partial x_i} \cdot \vec{F}_i + \frac{\partial \vec{w}}{\partial x_i} \cdot \mathbf{K}_{ij} \frac{\partial \vec{U}}{\partial x_j} + \vec{w} \cdot \vec{S} \right) d\Omega = \int_{\partial\Omega} \left(-\varepsilon \vec{w} \cdot \vec{F}_i + \vec{w} \cdot \mathbf{K}_{ij} \frac{\partial \vec{U}}{\partial x_j} \right) n_i d\Gamma \quad (2.231)$$

Instead, the governing equations can be solved for an arbitrary set of variables \vec{U} by replacing $\partial \vec{U} / \partial \xi_i$ by $\mathbf{M} \partial \vec{U} / \partial \xi_i$, where ξ is either the spatial or time derivatives. Then, in order to retain the same type of weak form structure, multiply all terms in the weak form by \mathbf{M}^{-1} from the left, giving:

$$\int_{\Omega} \left(\vec{w} \cdot \frac{\partial(\varepsilon \vec{U})}{\partial t} - \varepsilon \frac{\partial \vec{w}}{\partial x_i} \cdot \vec{F}_i + \frac{\partial \vec{w}}{\partial x_i} \cdot \tilde{\mathbf{K}}_{ij} \frac{\partial \vec{U}}{\partial x_j} + \vec{w} \cdot \vec{S} \right) d\Omega = \int_{\partial\Omega} \left(-\varepsilon \vec{w} \cdot \vec{F}_i + \vec{w} \cdot \tilde{\mathbf{K}}_{ij} \frac{\partial \vec{U}}{\partial x_j} \right) n_i d\Gamma \quad (2.232)$$

\vec{F}_i and \vec{S} are then evaluated at the new solution variables \vec{U} . \mathbf{M} is a matrix representing the partial derivative of the conservative set of variables to the new set of variables:

$$\mathbf{M} \equiv \frac{\partial \vec{U}}{\partial \vec{U}} \quad (2.233)$$

and $\tilde{\mathbf{K}}_{ij}$ is defined as:

$$\tilde{\mathbf{K}}_{ij} \equiv \mathbf{M}^{-1} \mathbf{K}_{ij} \mathbf{M} \quad (2.234)$$

In order to evaluate the strong residual in Eq. (2.225), reverse-integrate Eq. (2.232) by parts:

$$\frac{\partial(\epsilon\vec{U})}{\partial t} + \epsilon\tilde{\mathbf{A}}_i \frac{\partial\vec{U}}{\partial x_i} + \vec{F}_i \frac{\partial\epsilon}{\partial x_i} - \frac{\partial}{\partial x_i} \left(\mathbf{K}_{ij}\mathbf{M} \frac{\partial\vec{U}}{\partial x_j} \right) + \vec{S} = 0 \quad (2.235)$$

where $\tilde{\mathbf{A}}_i$ is defined as:

$$\tilde{\mathbf{A}}_i \equiv \mathbf{M}^{-1}\mathbf{A}_i\mathbf{M} \quad (2.236)$$

To solve the Navier-Stokes equations for any set of variables simply requires determining Eq. (2.233) and forming the above matrices. \mathbf{M} will depend on the EOS. Not only is this method clean and easy to implement, but by beginning from the conservative Navier-Stokes equations, incompressible flows can be simulated while retaining two important features of compressible Finite Element (FE) formulations [63]:

1. A conservative method, which is important for obtaining correct shock structure;
2. Flexibility to use equal-order interpolation functions. FE simulations of incompressible flows are often subject to strict requirements to use different interpolation orders for the solution variables that are not present for compressible flows.

For incompressible fluids, density is constant, so $\alpha_T = \beta = 0$. If density is selected as a solution variable for a nearly incompressible system, entries in the inviscid flux Jacobian matrices defined in Eq. (2.226) for the new system of variables will tend to infinity as α_T and β tend to zero. This condition would certainly be met for molten salts, with α_T being on the order of 10^{-11} . In other words, the condition number of the \mathbf{A}_i gets increasingly large, and the system stiffer and stiffer, as the system becomes less and less compressible [63]. Using the conserved variables ρ , ρV , and ρE will also not behave well in the incompressible limit.

By using either entropy variables or P - V - T variables, both compressible and incompressible flows can be simulated, with the incompressible limit well-behaved [51, 63]. In addition, the use of entropy variables yields symmetric $\tilde{\mathbf{A}}_i$, $\tilde{\mathbf{K}}_{ij}$, and \mathbf{M} matrices, which generally improves the iterative solution [51]. The matrices involved may become rank deficient as α_T and β tend to zero, so the inverses should always be computed analytically. A challenge with this unified approach is defining a stabilization scheme that works well for both compressible and incompressible flows, since the stabilization parameter is often defined separately for these regimes. A simple interpolation scheme has been proposed [63]:

$$\tau_{SUPG} = \frac{\tau_{SUPG,inc} + \left(\frac{Ma}{M_o}\right)^{k_o} \tau_{SUPG,comp}}{1 + \left(\frac{Ma}{M_o}\right)^{k_o}} \quad (2.237)$$

where $\tau_{SUPG,inc}$ and $\tau_{SUPG,comp}$ are the Streamline-Upwind Petrov-Galerkin (SUPG) stabilization matrices derived for incompressible and compressible flows, respectively; Ma is the Mach number; and M_o and k_o are constants.

The following sections provide derivations of the M matrices for several choices of solution variables. Work is currently ongoing to implement this change-of-variables approach to solve for incompressible flows. All choices of variables give results of comparable accuracy as the mesh is refined, but differences are present for coarser meshes [63]. In taking the derivatives of variables with respect to one another, derivatives of velocity with respect to thermodynamic properties are zero because velocity is strictly a flow property that is only influenced through the governing equations, rather than through thermodynamic relationships. In addition, when taking derivatives of a variable with respect to one thermodynamic quantity (such as the derivative of density with respect to pressure), the other thermodynamic variable in \vec{U} must be held constant. Throughout the derivations that follow, the Gibbs identity in Eq. (2.166) and the Maxwell

identity in Eq. (2.178) are used, along with definitions of specific heats in Eqs. (2.176) and (2.177), the volumetric thermal expansion coefficient in Eq. (2.183), and the enthalpy and total enthalpy in Eqs. (2.159) and (2.160). The compressibility α_T will be used, and is defined as:

$$\begin{aligned}\alpha_T &\equiv \frac{1}{\rho} \left(\frac{\partial \rho}{\partial P} \right)_T \\ &= -\frac{1}{v} \left(\frac{\partial v}{\partial P} \right)_T\end{aligned}\quad (2.238)$$

Density Primitive Variables - ρ , V , and T

For a transformation from the solution variables in Eq. (15.25) to the following primitive variables,

$$\vec{U} = [\rho \quad V_1 \quad V_2 \quad V_3 \quad T]^T \quad (2.239)$$

\mathbf{M} and its inverse become [63]:

$$\mathbf{M} = \begin{bmatrix} 1 & 0 & 0 & 0 & 0 \\ V_1 & \rho & 0 & 0 & 0 \\ V_2 & 0 & \rho & 0 & 0 \\ V_3 & 0 & 0 & \rho & 0 \\ H - \beta T / (\alpha_T \rho) & \rho V_1 & \rho V_2 & \rho V_3 & \rho C_v \end{bmatrix} \quad (2.240)$$

$$\mathbf{M}^{-1} = \begin{bmatrix} 1 & 0 & 0 & 0 & 0 \\ -\frac{V_1}{\rho} & \frac{1}{\rho} & 0 & 0 & 0 \\ -\frac{V_2}{\rho} & 0 & \frac{1}{\rho} & 0 & 0 \\ -\frac{V_3}{\rho} & 0 & 0 & \frac{1}{\rho} & 0 \\ \frac{\|\vec{V}\|_2^2 - [H - \beta T / (\alpha_T \rho)]}{\rho C_v} & -\frac{V_1}{\rho C_v} & -\frac{V_2}{\rho C_v} & -\frac{V_3}{\rho C_v} & \frac{1}{\rho C_v} \end{bmatrix} \quad (2.241)$$

Pressure Primitive Variables - P , V , and T

For a transformation from the solution variables in Eq. (15.25) to the following primitive variables,

$$\vec{U} = [P \quad V_1 \quad V_2 \quad V_3 \quad T]^T \quad (2.242)$$

\mathbf{M} and its inverse become [63]:

$$\mathbf{M} = \begin{bmatrix} \rho \alpha_T & 0 & 0 & 0 & -\rho \beta \\ \rho \alpha_T V_1 & \rho & 0 & 0 & -\rho \beta V_1 \\ \rho \alpha_T V_2 & 0 & \rho & 0 & -\rho \beta V_2 \\ \rho \alpha_T V_3 & 0 & 0 & \rho & -\rho \beta V_3 \\ \rho \alpha_T H - \beta T & \rho V_1 & \rho V_2 & \rho V_3 & \rho C_p - \rho \beta H \end{bmatrix} \quad (2.243)$$

$$\mathbf{M}^{-1} = \frac{1}{\rho} \begin{bmatrix} \frac{\rho C_p - \rho \beta H + \rho \beta \|\vec{V}\|_2^2}{\rho \alpha_T C_v} & -\frac{\beta V_1}{\alpha_T C_v} & -\frac{\beta V_2}{\alpha_T C_v} & -\frac{\beta V_3}{\alpha_T C_v} & \frac{\beta}{\alpha_T C_v} \\ -V_1 & 1 & 0 & 0 & 0 \\ -V_2 & 0 & 1 & 0 & 0 \\ -V_3 & 0 & 0 & 1 & 0 \\ \frac{\rho \alpha_T \|\vec{V}\|_2^2 - (\rho \alpha_T H - \beta T)}{\rho \alpha_T C_v} & -\frac{V_1}{C_v} & -\frac{V_2}{C_v} & -\frac{V_3}{C_v} & \frac{1}{C_v} \end{bmatrix} \quad (2.244)$$

2.9 Boundary Conditions

This section specifies the BCs for the governing equations derived in the previous sections from a theoretical perspective. Section 6 defines the BCs that arise from the FEM. The BCs will be presented here for the general governing equations for a Newtonian fluid, and then simplifications will be made for the particular application range expected. All BCs are derived by considering a general interface between two regions. Statements can only be made about the normal components of quantities of interest such as velocity and momentum. This is also reflected in the BCs actually implemented within the finite element framework.

If an interface S is defined as a function $S(\vec{x}, t) = 0$, the material derivative of S must also equal zero:

$$\frac{\partial S}{\partial t} + \frac{\partial x_i}{\partial t} \frac{\partial S}{\partial x_i} = 0 \quad (2.245)$$

A unit surface normal to the surface S is defined as:

$$\vec{n} = \frac{\nabla S}{|\nabla S|} \quad (2.246)$$

Inserting this definition into Eq. (2.245) and dividing through by $|\nabla S|$:

$$\frac{\partial S / \partial t}{|\nabla S|} + \frac{\partial x_i}{\partial t} n_i = 0 \quad (2.247)$$

Only the normal component of velocity appears in Eq. (2.247), which demonstrates why only conclusive statements can be made of the normal component of quantities of interest.

It is commonplace to see BCs applied to tangential components of velocity, such as in the no-slip condition which requires $\vec{V} \cdot \vec{s} = 0$, where \vec{s} is a unit tangential vector to the surface. These BCs are to the discretion of the modeler, and only the normal conditions are strictly required from conservation of mass, momentum, and energy. These required BCs are derived by selecting a control volume straddling an interface, where the interface moves with velocity \mathcal{V} . The control volume selected moves with the interface, with relative velocity \vec{V}' defined by:

$$\vec{V}' = \vec{V} - \mathcal{V} \cdot \vec{n} \quad (2.248)$$

The BCs are developed for a relative velocity, where the control volume moves with the interface. This is required so that integrals over the control volume are finite, which in the limit of zero volume signifies that the integrals also go to zero. All jump terms are evaluated on either side of the interface. Gradients are typically large directly at the interface, but on either side are small, and this observation will justify neglecting some terms in the BCs.

2.9.1 The Continuity Equation

Balancing mass as in Eq. (2.47) over an interface moving, with the positive direction defined pointing from side “1” to side “2”:

$$\int_{\mathcal{V}} \frac{\partial \rho}{\partial t} d\mathcal{V} = -\rho \vec{V}' \cdot \vec{n} \Big|_1^2 + \text{mass flow} \parallel \text{ to interface} \quad (2.249)$$

In the limit of the thickness of the control volume (perpendicular to the interface) going to zero, the term on the LHS and the parallel flow term both go to zero. Then, the mass balance BC is given in Eq. (2.250)a.

$$\rho \vec{V}' \cdot \vec{n} \Big|_1^2 = 0 \quad (\text{general interface}) \quad (2.250a)$$

$$\vec{V} \cdot \vec{n} \Big|_1^2 = 0 \quad (\text{material interface}) \quad (2.250b)$$

A material interface is defined as an interface between two materials that do not exchange mass, such as the case for a fluid flowing along a solid boundary, assuming that none of the fluid converts to the solid and vice versa. To reduce Eq. (2.250)a to a relation for a material interface, the speed of the material interface is defined to be:

$$\mathcal{V} \equiv \vec{V} \cdot \vec{n} \quad (2.251)$$

Inserting Eq. (2.251) into Eq. (2.250)a, for $\vec{V} = \vec{V}_1$ or $\vec{V} = \vec{V}_2$ gives Eq. (2.250)b. For a material interface with no exchange of material, the normal component of the velocity must be continuous. Hence, for a solid wall that has zero velocity, fluid in contact with that wall must have a zero normal component of velocity. This is sometimes referred to as the “kinematic,” or “no penetration” BC.

2.9.2 The Momentum Equation

Balancing momentum as in Eq. (2.58) over the same control volume:

$$\int_{\mathcal{V}} \frac{\partial}{\partial t} (\rho V'_i) d\mathcal{V} = -\rho V'_i \vec{V}'_i \cdot \vec{n} \Big|_1^2 + \sigma_{ij} n_j \Big|_1^2 + f_{s,i} + \int_{\mathcal{V}} \rho g_i d\mathcal{V} + \text{momentum flow} \parallel \text{ to interface} \quad (2.252)$$

where f_s represents the resultant surface tension force. Note that the positive sign on the net contact force term $\sigma_{ij} n_j$ occurs due to the definition of σ_{ij} representing the force acting *on* the volume *by* its surroundings. In the limit of the thickness of the control volume going to zero, Eq. (2.253)a arises. Inserting Eq. (2.251) into Eq. (2.253), Eq. (2.253)a reduces to Eq. (2.253)b for a material interface.

$$\rho V'_i \vec{V}'_i \cdot \vec{n} \Big|_1^2 = \sigma_{ij} n_j \Big|_1^2 + f_{s,i} \quad (\text{general interface}) \quad (2.253a)$$

$$0 = \sigma_{ij} n_j \Big|_1^2 + f_{s,i} \quad (\text{material interface}) \quad (2.253b)$$

The free jet BC commonly encountered in introductory fluids courses results from Eq. (2.253)b by assuming the Newtonian constitutive relationship in Eq. (2.90) and neglecting viscous and surface tension forces. Then, the BC for a free jet is simply that the pressure everywhere in the jet equals the atmospheric pressure. Because viscous and surface tension effects are neglected in Pronghorn, Eq. (2.253) simplifies to:

$$\rho V_i' \vec{V}_i' \cdot \vec{n} \Big|_1^2 = P \Big|_1^2 \quad (\text{general interface}) \quad (2.254a)$$

$$0 = P \Big|_1^2 \quad (\text{material interface}) \quad (2.254b)$$

Because the reactor systems modeled are expected to be dominated by inertial forces, the ratio of surface tension to inertial forces should be small, so the above simplification is valid.

2.9.3 The Energy Equation

Balancing energy as in Eq. (2.157) over the same control volume:

$$\int_{\mathcal{V}} \frac{\partial(\rho E)}{\partial t} d\mathcal{V} = -\rho E \vec{V}' \cdot \vec{n} \Big|_1^2 - \vec{q} \cdot \vec{n} \Big|_1^2 + \sigma_{ij} n_j V_i' \Big|_1^2 + \int_{\mathcal{V}} \rho b_i V_i d\mathcal{V} \quad (2.255)$$

In the limit of the thickness of the control volume going to zero and assuming the Newtonian constitutive relationship in Eq. (2.90) and the definition of enthalpy in Eq. (2.160), Eq. (2.256)a results. Inserting Eq. (2.251) into Eq. (2.256)a gives Eq. (2.256)b.

$$\rho \left(\frac{1}{2} |V|^2 + h \right) \vec{V}' \cdot \vec{n} \Big|_1^2 = -\vec{q} \cdot \vec{n} \Big|_1^2 + (\tau + \zeta \nabla \cdot \vec{V} \delta_{ij}) n_j V_i' \Big|_1^2 \quad (\text{general interface}) \quad (2.256a)$$

$$0 = -\vec{q} \cdot \vec{n} \Big|_1^2 + (\tau + \zeta \nabla \cdot \vec{V} \delta_{ij}) n_j V_i' \Big|_1^2 \quad (\text{material interface}) \quad (2.256b)$$

For an interface at which a phase change is occurring, h_1^2 represents the enthalpy of vaporization. For virtually all situations, the enthalpy of vaporization is of much larger magnitude than the kinetic energy change, and hence the kinetic energy term can be neglected. Because viscous and volumetric viscosity effects are neglected in Pronghorn, Eq. (2.256) simplifies to:

$$\rho \left(\frac{1}{2} |V|^2 + h \right) \vec{V}' \cdot \vec{n} \Big|_1^2 = -\vec{q} \cdot \vec{n} \Big|_1^2 \quad (\text{general interface}) \quad (2.257a)$$

$$0 = -\vec{q} \cdot \vec{n} \Big|_1^2 \quad (\text{material interface}) \quad (2.257b)$$

2.10 Nondimensionalization of the Governing Equations

This section presents the non-dimensionalization of the governing equations for momentum and energy in order to justify why certain terms can be neglected in Pronghorn. No terms are neglected in the mass conservation equation,

so this equation does not need to be nondimensionalized. Operating conditions for representative reactor systems are reviewed to show that neglecting terms is valid for the range of applicability of Pronghorn. In addition to the classical nondimensionalization approach, a brief discussion on the validity of a compressible versus incompressible flow model is provided in order to guide the selection of solution variables (conservative versus primitive) based on dimensionless numbers.

2.10.1 The Momentum Equation

Eq. (2.95), with the material derivative expanded, is repeated here for convenience:

$$\rho \frac{\partial V_i}{\partial t} + \rho \vec{V} \cdot \nabla V_i = \rho g_i - \nabla P + \nabla \cdot \left[\mu \left(\nabla V_i + (\nabla V_i)^T \right) - \frac{2\mu}{3} \nabla \cdot \vec{V} \right]$$

The following non-dimensional quantities are defined:

$$t^+ = \frac{t}{t_o}, \quad V^+ = \frac{V_i}{V_o}, \quad P^+ = \frac{P}{P_o}, \quad x^+ = \frac{x}{L}, \quad g^+ = \frac{g_i}{g_o} \quad (2.258)$$

Two different choices can be made to scale pressure, where the selection is based on the flow regime. For flows dominated by inertial forces, P_o can be set to ρV_o^2 . For example, for flow past a cylinder, the highest pressure in the system is the stagnation pressure, which can be shown to equal ρV_o^2 from a simple application of the Bernoulli equation (which assumes inviscid flow). For flows dominated by viscous forces, a different selection can be made by selecting $P_o = \mu V_o / L$. $P_o = \rho V_o^2$ is selected here because the flows to be modeled by Pronghorn are expected to be dominated by inertial forces.

Inserting these nondimensional quantities into the 1-D form of the Navier-Stokes equations:

$$\frac{\rho V_o}{t_o} \frac{\partial V^+}{\partial t^+} + V^+ \frac{\rho V_o^2}{L} \frac{\partial V^+}{\partial x^+} = \rho g^+ g_o - \frac{\rho V_o^2}{L} \frac{\partial P^+}{\partial x^+} + \frac{\mu V_o}{L^2} \frac{\partial}{\partial x^+} (\diamond) \quad (2.259)$$

where the complicated form of the viscous term is denoted as \diamond for simplicity. Dividing through by the coefficient on the advective term:

$$\frac{L}{V_o t_o} \frac{\partial V^+}{\partial t^+} + V^+ \frac{\partial V^+}{\partial x^+} = \frac{L g_o}{V_o^2} g^+ - \frac{\partial P^+}{\partial x^+} + \frac{1}{Re} \frac{\partial}{\partial x^+} (\diamond) \quad (2.260)$$

All of the terms in the Navier-Stokes equations are retained in Pronghorn except the terms with $1/Re$ coefficients, i.e. the terms representing viscous forces. Therefore, $Re \gg 1$ is required. If surface tension forces are small, then Eq. (2.254) holds.

2.10.2 The Energy Equations

Because the temperature and energy forms of the energy equation are equivalent and it is difficult to define a nondimensional energy $E^+ = E/E_o$, the temperature form will be nondimensionalized to see which terms can be neglected. The temperature form of the energy equation is repeated here for reference, with the material derivatives expanded, Fourier's law inserted for the conductive heat flux, and with $\zeta = 0$:

$$\rho C_p \left(\frac{\partial T}{\partial t} + \vec{V} \cdot \nabla T \right) - T\beta \left(\frac{\partial P}{\partial t} + \vec{V} \cdot \nabla P \right) = \frac{\tau^2}{2\mu} + \nabla \cdot (k\nabla T)$$

Using the same nondimensionalization in Eq. (2.258), the above becomes in 1-D form:

$$\rho C_p \left(\frac{1}{t_o} \frac{\partial T}{\partial t} + V^+ \frac{V_o}{L} \frac{\partial T}{\partial x^+} \right) - T\beta \left(\frac{1}{t_o} \frac{\partial P}{\partial t} + V^+ \frac{V_o}{L} \frac{\partial P}{\partial x^+} \right) = \frac{\mu V_o^2}{L^2} (\diamond) - \frac{k}{L^2} \frac{\partial T^2}{\partial x^{+2}} \quad (2.261)$$

where for simplicity the nondimensionalized, complicated viscous power term is indicated as (\diamond) . Several additional nondimensionalizations are needed for the energy equation:

$$T^+ = \frac{T}{\Delta T}, \quad P^+ = \frac{P}{\rho V_o^2}, \quad t^+ = \frac{t}{L/V_o} \quad (2.262)$$

The temperature is scaled according to the maximum temperature increase in the domain. Because $Re \gg 1$ for the application space of interest to Pronghorn, pressure can be scaled as $P^+ = P/\rho V_o^2$. Also, because the terms of interest for scaling contain the dimensionless time t_o (while this term did not appear in the momentum equation because the only nondimensional number of interest was Re), time is scaled with $t_o = L/V_o$. Inserting these additional nondimensionalizations:

$$\frac{\Delta T \rho C_p V_o}{L} \frac{dT^+}{dt^+} - T^+ \beta \frac{\rho V_o^3}{L} \frac{dP^+}{dt^+} = \frac{\mu V_o^2}{L^2} (\diamond) - \frac{\Delta T k}{L^2} \frac{\partial T^{+2}}{\partial x^{+2}} \quad (2.263)$$

Dividing through by the coefficient on the temperature material derivative:

$$\frac{dT^+}{dt^+} - \beta Ec T^+ \frac{dP^+}{dt^+} = \frac{Br}{Pe} (\diamond) - \frac{1}{Pe} \frac{\partial T^{+2}}{\partial x^{+2}} \quad (2.264)$$

where Pe is the Peclet number defined in Eq. (2.295), Ec is the Eckert number defined in Eq. (2.297), and Br is the Brinkman number defined in Eq. (2.298). The viscous and pressure work terms are neglected in the solid by assuming that the solid has zero velocity and pressure changes in the solid are negligible. Both of these assumptions are obvious, and do not require proof. In addition, the viscous work term is neglected, which is valid provided $Br/Pe \ll 1$. To neglect thermal energy diffusion, $Pe \gg 1$ must be satisfied. However, as shown in Section 2.10.5, this would be invalid for certain reactor systems, so thermal energy diffusion must be retained. In the energy BCs, as long as $Br/Pe \ll 1$, the viscous power term can be neglected.

The $\rho \vec{b} \cdot \vec{V}$ term in Eq. (2.161) is often approximated as $\rho \vec{g} \cdot \vec{V}$. To assess the validity of this approximation, normalize the neglected term by the diffusive term, since the diffusive term is included based on the dimensionless number arguments in Table 3 [43]:

$$\begin{aligned} \frac{\rho W \vec{V} \cdot \vec{V}}{\nabla \cdot (k\nabla T)} &\approx \frac{150\mu(V^+)^2 + 1.75\rho(V^+)^3 d_p}{k\Delta T} \left(\frac{D}{d_p} \right)^2 \\ &= 150Br \left(\frac{D}{d_p} \right)^2 + 1.75ReEcPr \frac{D}{d_p} \end{aligned} \quad (2.265)$$

where Eq. (2.152) is used to expand W and the Ergun correlation in Eq. (9.1) is used to obtain realistic proportionality constants on the two drag terms since the coefficient on the friction drag term is not of order unity. In order to neglect the viscous dissipation due to the porous media friction forces, the above dimensionless number should be much smaller than unity.

2.10.3 Compressible Versus Incompressible Flows

This section discusses the dimensionless numbers that should be used to judge when a flow should be treated as compressible or incompressible. Many discussions of this concept are found alongside discussions of the Euler equations, where the influence of compressibility is only shown to be related to the Mach number [22] (chapter 11). However, the choice to use an incompressible model must also consider temperature gradients, the length scales involved, and hydrostatic pressure changes.

The conditions under which flow can be treated as incompressible can be determined by investigating the continuity equation in Eq. (2.47), rearranged here to give:

$$\nabla \cdot \vec{V} + \frac{1}{\rho} \frac{d\rho}{dt} = 0 \quad (2.266)$$

A flow is incompressible if $d\rho/dt = 0$, which results in a simplified continuity equation $\nabla \cdot \vec{V} = 0$. For this approximation to be valid, the second term on the LHS above has to be small with respect to the maximum of $|\partial V_x/\partial x|$, $|\partial V_y/\partial y|$, and $|\partial V_z/\partial z|$. In other words, for the flow to be incompressible:

$$\left| \frac{1}{\rho} \frac{d\rho}{dt} \right| \ll |\nabla \cdot \vec{V}| \quad (2.267)$$

For a pure fluid, ρ is related to two state variables. Pressure is selected as one of these variables because it appears directly in the Navier-Stokes equations and is related to the BCs. Entropy is chosen as the second variable because it has its own conservation equation that is related to molecular processes that can more easily be argued to be significant/insignificant in a nondimensionalization analysis. The derivative of ρ can then be expressed as:

$$\begin{aligned} \frac{d\rho}{dt} &= \left(\frac{\partial \rho}{\partial P} \right)_s \frac{dP}{dt} + \left(\frac{\partial \rho}{\partial s} \right)_P \frac{ds}{dt} \\ &= \frac{1}{c^2} \frac{dP}{dt} - \frac{\rho \beta T}{C_p} \frac{ds}{dt} \end{aligned} \quad (2.268)$$

where the speed of sound c is defined as:

$$c^2 \equiv \left(\frac{\partial P}{\partial \rho} \right)_s \quad (2.269)$$

To determine dP/dt , consider sound waves where viscous effects can be neglected. The inviscid form of the Navier-Stokes equation in Eq. (2.95) with $\vec{b} \equiv \vec{g}$ gives a relationship for the gradient of pressure:

$$\rho \frac{d\vec{V}}{dt} = -\nabla P + \rho \vec{g} \quad (2.270)$$

This can be used in the general chain rule form of dP/dt for ∇P :

$$\begin{aligned} \frac{dP}{dt} &= \frac{\partial P}{\partial t} + \vec{V} \cdot \nabla P \\ &= \frac{\partial P}{\partial t} + \vec{V} \cdot \left(\rho \vec{g} - \rho \frac{d\vec{V}}{dt} \right) \end{aligned} \quad (2.271)$$

Combining the above with Eq. (2.268) and Eq. (2.267) gives the condition for which the flow can be treated as incompressible:

$$\left| \frac{1}{\rho c^2} \frac{\partial P}{\partial t} + \frac{1}{\rho c^2} \vec{V} \cdot \left(\rho \vec{g} - \rho \frac{d\vec{V}}{dt} \right) - \frac{\beta T}{C_p} \frac{ds}{dt} \right| \ll |\nabla \cdot \vec{V}| \quad (2.272)$$

The following nondimensional quantities are introduced in order to quantitatively discuss Eq. (2.272).

$$V^+ = \frac{V}{V_o}, \quad x^+ = \frac{x}{L}, \quad g^+ = \frac{g}{g_o} \quad (2.273)$$

Introducing these into Eq. (2.272):

$$\left| \frac{1}{\rho c^2} \frac{\partial P}{\partial t} + \frac{g_o V_o}{c^2} V^+ g^+ - \frac{V_o^3}{c^2 L} V^+ \frac{dV^+}{dt} - \frac{\beta T}{C_p} \frac{ds}{dt} \right| \ll \left| \frac{V_o}{L} \right| \quad (2.274)$$

For sound waves, $\partial P/\partial t$ may be non-negligible, in which case, the unsteady pressure derivative $\partial P/\partial t$ requires a separate scaling. For the propagation of a sound wave, gravitational effects are negligible and advection of momentum can be neglected on the scale of the sound wave. Then, Eq. (2.270) further reduces to:

$$\rho \frac{\partial \vec{V}}{\partial t} = -\nabla P \quad (2.275)$$

For a sound wave propagating with frequency n , the above can be nondimensionalized as:

$$\rho n V_o = \frac{\delta P}{L} \quad \rightarrow \quad \frac{\partial P}{\partial t} = \rho n^2 V_o L \quad (2.276)$$

For a sound wave, the frequency of the sound wave is related to its wavelength and the speed of sound approximately by $c = \lambda n$. Introducing this into the above equation and in Eq. (2.274) adds to the incompressibility condition:

$$\left| \frac{V_o}{L} \left(\frac{L^2}{\lambda^2} \frac{\partial P}{\partial t} + \frac{g_o L}{c^2} V^+ g^+ - \frac{V_o^2}{c^2} V^+ \frac{dV^+}{dt} - \frac{\beta T}{C_p} \Delta s \right) \right| \ll \left| \frac{V_o}{L} \right| \quad (2.277)$$

where the entropy contribution is quantified by a time scaling chosen as $\Delta t = L/V_o$. So, for a generic fluid to be incompressible, the following conditions must be met:

$$\left(\frac{L}{\lambda} \right)^2 \ll 1, \quad \left(\frac{g_o L}{c^2} \right) \ll 1, \quad Ma^2 \ll 1, \quad \left(\frac{\beta T \Delta s}{C_p} \right) \ll 1 \quad (2.278)$$

where Ma is the Mach number defined in Eq. (2.296). For an ideal gas, $\beta T = 1$, and by $T \Delta s \approx C_p \Delta T$ suggested by Eq. (2.176), the last term reduces to $\Delta T/T$. In essence, the above statements require that:

1. the length scale of the body be much smaller than the length scale of a sound wave,
2. hydrostatic pressure changes be small,
3. the Mach number be small, and

4. $\Delta T/T \ll 1$.

The limits imposed by Ma and $\Delta T/T$ are likely to be important for certain classes of reactors and operating conditions, while the first two considerations are assumed negligible. Values for Ma and $\Delta T/T$ are provided in Table 3. Neglecting compressibility essentially leads to errors in the estimation of dynamic pressure. At $Ma = 0.2$, an error of approximately 1% is made on the dynamic pressure - $Ma \leq 0.2$ is often selected in this manner to signify the onset of important compressibility effects [22] (chapter 11).

The interpretation of the speed of sound is derived by applying a perturbation in density, pressure, and velocity to the governing equations. These perturbations are assumed small such that the multiplication of any two perturbations can be neglected. Spatial averages of the o subscripted quantities are zero. These perturbations are:

$$\rho = \rho_o + \hat{\rho}(\vec{x}, t) \quad (2.279a)$$

$$P = P_o + \hat{P}(\vec{x}, t) \quad (2.279b)$$

$$\vec{V} = \vec{0} + \hat{V}(\vec{x}, t) \quad (2.279c)$$

Inserting the perturbations into Eq. (2.47) and neglecting small and zero terms:

$$\frac{\partial \hat{\rho}(\vec{x}, t)}{\partial t} + \hat{V}(\vec{x}, t) \cdot \nabla \rho_o + \rho_o \nabla \cdot \hat{V}(\vec{x}, t) = 0 \quad (2.280)$$

Taking the time derivative of the above expression, and neglecting small or zero terms:

$$\frac{\partial^2 \hat{\rho}(\vec{x}, t)}{\partial t^2} + \frac{\partial (\nabla \cdot \hat{V}(\vec{x}, t))}{\partial t} \rho_o = 0 \quad (2.281)$$

For sound waves, gravitational and inertial forces are negligible. With these assumptions, the Navier-Stokes equations in Eq. (2.95) simplify to the following, where the second equation takes the gradient of both sides and expands the material derivative.

$$\rho \frac{d\vec{V}}{dt} = -\nabla P \quad (2.282a)$$

$$\rho \nabla \left(\frac{\partial \vec{V}}{\partial t} + \vec{V} \cdot \nabla \vec{V} \right) + \left(\frac{\partial \vec{V}}{\partial t} + \vec{V} \cdot \nabla \vec{V} \right) \nabla \rho = -\nabla^2 P \quad (2.282b)$$

Then, inserting the perturbed quantities defined in Eq. (2.279) and canceling the small or zero terms:

$$\rho_o \frac{\partial \nabla \cdot \hat{V}(\vec{x}, t)}{\partial t} = -\nabla^2 \hat{P}(\vec{x}, t) \quad (2.283)$$

where the gradient was moved inside the time derivative term because a gradient is only a function of space. Combining Eq. (2.281) with the above gives:

$$\frac{\partial^2 \hat{\rho}(\vec{x}, t)}{\partial t^2} = \nabla^2 \hat{P}(\vec{x}, t) \quad (2.284)$$

For sound waves, the flow is nearly isentropic because viscous dissipation is negligible and sound waves travel relatively slowly so that volumetric viscous effects can be neglected. Hence, while pressure normally is a function of density and entropy, it can be taken as only a function of density as $P = f(\rho)$. By the chain rule:

$$\nabla \hat{P}(\vec{x}, t) = f'(\rho) \nabla \hat{\rho}(\vec{x}, t) \quad (2.285)$$

Hence, Eq. (2.284) becomes:

$$\frac{\partial^2 \hat{p}(\vec{x}, t)}{\partial t^2} = f'(\rho) \nabla \hat{p}(\vec{x}, t) \nabla^2 \hat{p}(\vec{x}, t) \quad (2.286)$$

Eq. (2.286) can be recognized as the wave equation, where $f'(\rho) \nabla \hat{p}(\vec{x}, t)$ is recognized to be the speed of sound. Hence, the speed of sound is defined as in Eq. (2.269).

2.10.4 Definitions of Dimensionless Numbers

A challenge associated with porous media is that there are several natural length and velocity scales, and there is no consistency in their use in dimensionless numbers. This section defines the notation used in this manual to refer to important dimensionless numbers, where focus is generally places on beds of spherical particles through the reference to d_p . The Reynolds number can in general be defined in five (or more) different ways:

$$Re = \frac{\rho v d_p}{\mu} \quad (2.287a)$$

$$Re_h = \frac{\rho V D}{\mu} \quad (2.287b)$$

$$Re_i = \frac{\rho V d_p}{\mu} \quad (2.287c)$$

$$Re_b = \frac{\rho v D}{\mu} \quad (2.287d)$$

$$Re_k = \frac{\rho V \sqrt{\|\mathcal{K}\|/\varepsilon}}{\mu} \quad (2.287e)$$

Correlations for heat transfer and friction coefficients will often be in terms of one of these definitions. Eq. (2.287a) is most often used, since it is good at describing the overall characteristics of a porous medium. The other forms shown above are less-frequently used, but have been useful for correlating experimental data. The Reynolds number with a characteristic length based on the square root of the permeability, Re_k , has been used successfully to uniquely define flow regime transitions [28]. While Re_k does contain porosity in its definition, the dependence is weaker, thus reducing dependence on an experimental property. The hydraulic diameter is defined in the standard manner:

$$D = \frac{4V_f}{a_w} \quad (2.288)$$

where V_f is the fluid flow volume per unit total volume. From the definition of porosity, $V_f = \varepsilon$. Using the definitions from Eq. (2.288) and (2.205), the hydraulic diameter for a pebble bed is:

$$D = \frac{4\varepsilon}{6(1-\varepsilon)} d_p \quad (2.289)$$

Note that this hydraulic diameter is only valid in the center of the bed. Near the wall, porosity goes to 1, in which case the hydraulic diameter according to Eq. (2.289) tends to infinity. Clearly this is nonphysical, since the wall limits the hydraulic diameter to finite values. In actuality, the hydraulic diameter reaches a maximum near the wall, but decreases in the immediate vicinity of the wall [65].

Nu for a porous medium can be expressed either in terms of the pebble diameter or the hydraulic diameter:

$$Nu = \frac{h_c d_p}{k} \quad (2.290a)$$

$$Nu_h = \frac{h_c D}{k} \quad (2.290b)$$

Many of these dimensionless numbers are linearly related to one another. Substituting in Eq. (2.31) for \vec{V} and Eq. (2.289) for D into Eq. (2.287), Re_h can be expressed in terms of Re , where the factor of 4/6 has been neglected, which is common in practice [66, 67].

$$Re_h = Re \frac{1}{(1 - \epsilon)} \quad (2.291)$$

Likewise, by Eq. (2.31), Re_i is also directly related to Re :

$$Re_i = \frac{Re}{\epsilon} \quad (2.292)$$

Substituting Eq. (2.289) for D into Eq. (2.290)b, where the factor of 4/6 has been neglected:

$$Nu_h = \frac{\epsilon}{1 - \epsilon} Nu \quad (2.293)$$

For prismatic reactors, both Re and Nu are defined in terms of the hydraulic diameter D , since there is no corresponding d_p . The Prandtl number is another important dimensionless number that represents the ratio of the momentum diffusivity μ/ρ to the thermal diffusivity $k/\rho C_p$:

$$Pr \equiv \frac{\mu C_p}{k} \quad (2.294)$$

The Prandtl number therefore represents the relative thicknesses of the momentum and thermal boundary layers. High-Prandtl number fluids, such as molten salts, at Reynolds number typical of reactor operation display greater heat transfer caused by turbulence than diffusion [10]. The Peclet number indicates the ratio of a representative velocity and length scale to a diffusivity δ :

$$Pe \equiv \frac{VL}{\delta} \quad (2.295)$$

where the diffusivity depends on the particular equation. For the fluid energy equation, $\delta = k/\rho C_p$, but for the momentum equation, $\delta = \mu/\rho$ (in which case the Peclet number is equivalent in interpretation as the Reynolds number). In practice, the diffusivity in Eq. (2.295) is taken to be the diffusivity for the fluid energy equation, in which case $Pe = Re \cdot Pr$. The Mach number is defined as:

$$Ma \equiv \frac{\|\vec{V}\|}{c} \quad (2.296)$$

Additional dimensionless numbers used in this manual include the Eckert number:

$$Ec = \frac{V^2}{C_p \Delta T} \quad (2.297)$$

and the Brinkman number:

$$Br = \frac{\mu V^2}{k\Delta T} \quad (2.298)$$

2.10.5 Expected Values for Dimensionless Numbers

In order to justify the simplifications made based on dimensionless numbers characterizing the momentum and energy equations and BCs described in the previous sections, the following requirements must be met:

1. $Re \gg 1$ to neglect viscous forces, which eliminates the $\nabla \cdot \tau$ term in Eq. (2.95). This then naturally neglects the viscous component in Eq. (2.253).
2. $Br/Pe \ll 1$ to neglect viscous power, which eliminates the viscous component in Eq. (2.185) (and by a similar argument, the viscous component in Eq. (2.158)). This then naturally neglects the viscous component in Eq. (2.257).
3. Surface tension forces negligible, which eliminates the $f_{s,i}$ term in Eq. (2.253).
4. Pressure changes in the solid are negligible, which when combined with the above requirement, leads to no compression work in the solid, neglecting the dP/dt term in Eq. (2.185).

These requirements in general, cannot all be met. However, it is not the intention that Pronghorn be used to model flows as different as supersonic flows and highly viscous flows. Pronghorn is to be used for nuclear reactor applications, and hence to determine the range of applicability of the above claims, the coolants commonly used in the nuclear power industry are investigated. Example reactor designs using these coolants are then selected to determine the operating range in Re , Pe , and Br to justify neglecting the terms mentioned above. Table 3 provides very rough estimates for the dimensionless numbers that appear in the equations governing conservation of momentum and energy for five representative reactor designs. For all of these reactors, viscous heating effects can be neglected because Br/Pe is on the order of 10^{-9} . There is a larger variation in Re , but in general Re is relatively high. Salt reactors tend to have relatively small Re on the order of 10^3 , but this still satisfies the requirement that $Re \gg 1$. Note that thermal energy conduction could safely be neglected in all reactor choices except liquid-metal-cooled reactors, due to the high thermal conductivity of metals. For these reactors, Pe is rather small, on the order of 100, and could drop to the range of 25 - 35 for certain transients [68]. In these cases, it is not appropriate to neglect thermal energy conduction in the fluid.

Values for Eq. (2.265) vary widely among the reactor types presented, and in general the $W\vec{V}$ term in \vec{b} should not be neglected if the diffusive term is not neglected, since in many cases these two terms are roughly the same order of magnitude. However, $W\vec{V}$ is currently neglected - future work must investigate the impact on simulation results.

Table 3: Operating conditions for representative nuclear reactor designs using a variety of coolants. All material properties are evaluated at the median of the operating temperature range. The parameters shown in the third and fourth sections are very approximate, and only reflect expected values over normal operating conditions. d_p for the THTR and PB-FHR are obtained from Table 15. “—” denotes that Eq. (2.265) is not evaluated for non-pebble bed designs. Speed of sound is evaluated using Eq. (7.18) at the lower operating temperature.

	PFBR [69, 70]	THTR [71]	PB-FHR [3]	AP-1000 [72, 73]	Torness AGR
Coolant	sodium	helium	flibe	water	CO ₂
Power (MW _{th})	1250	750	236	3400	1623
Fuel	assembly	pebble	pebble	assembly	assembly
Type	pool	loop	loop	loop	loop
P (MPa)	0.1	4.0	0.1	15.5	4.1
Temperature (°C)	397/547	250/750	600/700	279/325	339/639
Flowrate (kg/s)	6385	298	976	13705	4067
Velocity (m/s)	4.8	12.0	0.4	4.8	1.6
D (mm)	5.0	26.0	13.0	11.7	38.0
ρ (kg/m ³)	840.9	2.5	1999.7	720.2	28.4
μ (10 ⁻⁵ Pa·s)	24.6	3.85	678.08	8.73	3.4
k (W/m·K)	139.0	0.30	1.09	0.56	0.05
C_p (J/kg·K)	1268.1	5195	2416	5534	1157
c (m/s)	582	1346	275	527	371
Pr	0.002	0.67	15.0	0.86	0.79
Br	2.7×10^{-7}	3.7×10^{-5}	9.9×10^{-6}	7.8×10^{-5}	5.8×10^{-6}
Re	8.2×10^4	2.0×10^4	1.5×10^3	4.6×10^5	5.0×10^4
Pe	1.8×10^2	1.3×10^4	2.3×10^4	4.0×10^5	4.0×10^4
Ec	1.2×10^{-4}	5.5×10^{-5}	6.6×10^{-7}	9.0×10^{-5}	7.4×10^{-6}
Br/Pe	1.5×10^{-9}	2.8×10^{-9}	4.3×10^{-10}	2.0×10^{-10}	1.5×10^{-10}
Ma	8.2×10^{-3}	8.9×10^{-3}	1.4×10^{-3}	9.1×10^{-3}	4.3×10^{-3}
$\Delta T/T$	2.2×10^{-1}	9.6×10^{-1}	1.1×10^{-1}	8.3×10^{-2}	4.9×10^{-1}
Eq. (2.265)	—	0.6×10^0	1.1×10^{-2}	—	—

2.11 Summary of Physical Models

This manual presents the theory and equations used in the modern Pronghorn circa 2017. The remaking of Pronghorn was motivated by a restructuring of the MOOSE framework and the desire to include a fully conservative equation set for more flexible modeling. The key differences between modern and legacy Pronghorn are:

- *Conservative vs. Primitive kernels* - Using conservative variables in the modern version is somewhat more convenient because messy chain rule time derivatives can be avoided, and both RELAP-7 and BIGHORN are written in conservative form, allowing a high degree of code re-use. For backwards compatibility, a primitive variable formulation is still available.
- *Less physics neglected* - The modern Pronghorn includes additional advection and time derivative terms that had previously been neglected.
- *Flexible fluid EOS* - The legacy version was restricted to the ideal gas EOS. The modern version can use any set of fluid properties that derives from the fluid properties MOOSE module.
- *Flexibly solid properties* - The legacy Pronghorn hard-coded solid properties for graphite. The modern Pronghorn can use any set of solid properties that derives from the new modular class structure.
- *Flexible constitutive relationships* - The modern Pronghorn has restructured the friction coefficients, heat transfer coefficients, and effective solid thermal conductivity into more modular class structures that permit easier extension. Additional options have also been provided.

- *Consistent stabilization* - The modern Pronghorn permits consistent SUPG stabilization for the fluid continuity, momentum, and energy equations for both the primitive and conservative variable formulations, when only very rudimentary stabilization had been applied in the legacy version.
- *No neutronics* - Due to the great advancements made in RATTLESNAKE, there is no need to duplicate neutron diffusion physics in Pronghorn, so all neutronics physics have been removed.

Table 4 shows the difference between the legacy and modern equation sets, where both the primitive and conservative modern formulations are shown.

Table 4: Equation differences between modern and legacy Pronghorn. The modern version has both a conservative and primitive variable formulation.

Equation	Version	Equations
continuity	legacy	$\frac{\varepsilon}{R} \frac{\partial}{\partial t} \left(\frac{P}{T_f} \right) + \nabla \cdot \left[\frac{\varepsilon}{\bar{W}} \left(\frac{\varepsilon P \vec{g}}{RT_f} - \varepsilon \nabla P \right) \right] = 0$
	modern (prim.)	$\varepsilon \frac{\partial \rho_f}{\partial t} + \nabla \cdot \left[\frac{\varepsilon}{\bar{W}} \left(\varepsilon \rho_f \vec{g} - \varepsilon \nabla P \right) \right] = 0$
	modern (cons.)	$\varepsilon \frac{\partial \rho_f}{\partial t} + \nabla \cdot \left(\varepsilon \rho_f \vec{V} \right) = 0$
momentum	legacy	$\varepsilon \nabla P - \varepsilon \rho_f \vec{g} + W \rho_f \vec{V} = 0$
	modern (prim.)	$\varepsilon \nabla P - \varepsilon \rho_f \vec{g} + W \rho_f \vec{V} = 0$
	modern (cons.)	$\varepsilon \frac{\partial (\rho_f \vec{V})}{\partial t} + \nabla \cdot \left(\varepsilon \rho_f \vec{V} \vec{V} \right) + \varepsilon \nabla P - \varepsilon \rho_f \vec{g} + W \rho_f \vec{V} = 0$
fluid energy	legacy	$\varepsilon \frac{\partial}{\partial t} \left(\rho_f C_p T_f \right) + \nabla \cdot \left(\varepsilon \rho_f C_p \vec{V} T_f \right) - \nabla \cdot \left(\varepsilon \kappa_f \nabla T_f \right) + \alpha (T_f - T_s) = 0$
	modern (prim.)	$\varepsilon \rho_f C_{p,f} \frac{\partial T_f}{\partial t} + \varepsilon \rho_f C_{p,f} \vec{V} \cdot \nabla T_f - \nabla \cdot \left(\kappa_f \nabla T_f \right) + \alpha (T_f - T_s) - q_f = 0$
	modern (cons.)	$\varepsilon \frac{\partial (\rho_f E)}{\partial t} + \nabla \cdot \left(\varepsilon H_f \rho_f \vec{V} \right) - \nabla \cdot \left(\kappa_f \nabla T \right) - \varepsilon \rho_f \vec{g} \cdot \vec{V} + \alpha (T_f - T_s) - q_f = 0$
solid energy	legacy	$(1 - \varepsilon) \frac{\partial}{\partial t} \left(\rho_s C_p T_s \right) - \nabla \cdot \left(\kappa_s \nabla T_s \right) + \alpha (T_s - T_f) - q_s = 0$
	modern (prim.)	$(1 - \varepsilon) \rho_s C_{p,s} \frac{\partial T_s}{\partial t} - \nabla \cdot \left(\kappa_s \nabla T_s \right) + \alpha (T_s - T_f) - q_s = 0$
	modern (cons.)	$(1 - \varepsilon) \rho_s C_{p,s} \frac{\partial T_s}{\partial t} - \nabla \cdot \left(\kappa_s \nabla T_s \right) + \alpha (T_s - T_f) - q_s = 0$

It is assumed that porosity is independent of time; this approximation is discussed further in Section 8. The modern, conservative equation set is:

$$\varepsilon \frac{\partial \rho_f}{\partial t} + \nabla \cdot \left(\varepsilon \rho_f \vec{V} \right) = 0 \quad (2.299a)$$

$$\varepsilon \frac{\partial (\rho_f \vec{V})}{\partial t} + \nabla \cdot \left(\varepsilon \rho_f \vec{V} \vec{V} \right) + \varepsilon \nabla P - \varepsilon \rho_f \vec{g} + W \rho_f \vec{V} = 0 \quad (2.299b)$$

$$\varepsilon \frac{\partial (\rho_f E)}{\partial t} + \nabla \cdot \left(\varepsilon H_f \rho_f \vec{V} \right) - \nabla \cdot \left(\kappa_f \nabla T \right) - \varepsilon \rho_f \vec{g} \cdot \vec{V} + \alpha (T_f - T_s) - q_f = 0 \quad (2.299c)$$

$$(1 - \varepsilon) \rho_s C_{p,s} \frac{\partial T_s}{\partial t} - \nabla \cdot \left(\kappa_s \nabla T_s \right) + \alpha (T_s - T_f) - q_s = 0 \quad (2.299d)$$

The weak forms are derived by multiplying each term by a weight function ψ , integrating over phase space, and applying the divergence theorem when possible. The following inner product notation is used for conciseness:

$$\int_{\Omega} f \psi d\Omega \equiv (f, \psi) \quad (2.300a)$$

$$\int_{\Gamma} f \psi \vec{n} d\Omega \equiv \langle f, \psi \rangle \quad (2.300b)$$

where Ω represents integration over the interior and Γ represents integration over a boundary. The weak forms of the equations listed in Eq. (2.299) are as follows:

$$\begin{aligned}
& \left(\varepsilon \frac{\partial \rho_f}{\partial t}, \psi \right) + \left(-\varepsilon \rho_f \vec{V}, \nabla \psi \right) + \left\langle \varepsilon \rho_f \vec{V}, \psi \right\rangle = 0 \\
& \left(\varepsilon \frac{\partial \rho_f V_i}{\partial t} - \varepsilon \rho_f g_i + W \rho_f V_i - P \nabla \varepsilon, \psi \right) + \left(-\varepsilon \rho_f V_i \vec{V} - \varepsilon P, \nabla \psi \right) + \left\langle \varepsilon \rho_f V_i \vec{V} + \varepsilon P, \psi \right\rangle = 0 \\
& \left(\varepsilon \frac{\partial (\rho_f E)}{\partial t} - \varepsilon \vec{g} \cdot \rho_f \vec{V} + \alpha (T_f - T_s) - q_f, \psi \right) + \left(-\varepsilon H_f \rho_f \vec{V} + \kappa_f \nabla T_f, \nabla \psi \right) + \left\langle \varepsilon H_f \rho_f \vec{V} - \kappa_f \nabla T_f, \psi \right\rangle = 0 \\
& \left((1 - \varepsilon) \rho_s C_{p,s} \frac{\partial T_s}{\partial t} + \alpha (T_s - T_f) - q_s, \psi \right) + \left(\kappa_s \nabla T_s, \nabla \psi \right) - \left\langle \kappa_s \nabla T_s, \psi \right\rangle = 0
\end{aligned} \tag{2.301}$$

The modern, primitive equation set is:

$$\varepsilon \frac{\partial \rho_f}{\partial t} + \nabla \cdot \left[\frac{\varepsilon}{W} (\varepsilon \rho_f \vec{g} - \varepsilon \nabla P) \right] = 0 \tag{2.302a}$$

$$\varepsilon \nabla P - \varepsilon \rho_f \vec{g} + W \rho_f \vec{V} = 0 \tag{2.302b}$$

$$\varepsilon \rho_f C_{p,f} \frac{\partial T_f}{\partial t} + \varepsilon \rho_f C_{p,f} \vec{V} \cdot \nabla T_f - \nabla \cdot (\kappa_f \nabla T_f) + \alpha (T_f - T_s) - q_f = 0 \tag{2.302c}$$

$$(1 - \varepsilon) \rho_s C_{p,s} \frac{\partial T_s}{\partial t} - \nabla \cdot (\kappa_s \nabla T_s) + \alpha (T_s - T_f) - q_s = 0 \tag{2.302d}$$

The weak forms for Eq. (2.302) is:

$$\left(\varepsilon \frac{\partial \rho_f}{\partial t}, \psi \right) + \left(\frac{\varepsilon}{W} [\varepsilon \nabla P - \varepsilon \rho_f \vec{g}], \nabla \psi \right) + \left\langle \frac{\varepsilon}{W} (\varepsilon \rho_f \vec{g} - \varepsilon \nabla P), \psi \right\rangle = 0 \tag{2.303a}$$

$$(\varepsilon \nabla P - \varepsilon \rho_f g_i + W \rho_f V_i, \psi) = 0 \tag{2.303b}$$

$$\left(\varepsilon \rho_f C_{p,f} \frac{\partial T_f}{\partial t} + \varepsilon \rho_f C_{p,f} \vec{V} \cdot \nabla T_f + \alpha (T_f - T_s) - q_f, \psi \right) + \left(\kappa_f \nabla T_f, \nabla \psi \right) + \left\langle -\kappa_f \nabla T_f, \psi \right\rangle = 0 \tag{2.303c}$$

$$\left((1 - \varepsilon) \rho_s C_{p,s} \frac{\partial T_s}{\partial t} + \alpha (T_s - T_f) - q_s, \psi \right) + \left(\kappa_s \nabla T_s, \nabla \psi \right) - \left\langle \kappa_s \nabla T_s, \psi \right\rangle = 0 \tag{2.303d}$$

Gradients are inferred to correspond to the i direction for the momentum equations in Eqs. (2.299) and (2.303).

3 Kernels

This section summarizes the class names that correspond to the kernels available in Pronghorn.

Table 5: Kernels for use in the Pronghorn mass equation(s).

Strong Form	Weak Form	Name	Options
$\epsilon \frac{\partial \rho_f}{\partial t}$	$\left(\epsilon \frac{\partial \rho_f}{\partial t}, \psi \right)$	ConservativeTime	
$\epsilon \frac{\partial P}{\partial t}$	$\left(\epsilon \frac{\partial P}{\partial t}, \psi \right)$	PressureTime	
$\nabla \cdot (\epsilon \rho_f \vec{V})$	$\left(-\epsilon \rho_f \vec{V}, \nabla \psi \right)$	ContinuityEqn	
$\nabla \cdot \left(\frac{\epsilon}{W} [-\epsilon \nabla P + \epsilon \rho_f \vec{g}] \right)$	$\left(\frac{\epsilon}{W} [\epsilon \nabla P - \epsilon \rho_f \vec{g}], \nabla \psi \right)$	PressurePoisson	

Table 6: Kernels for use in the i -th Pronghorn momentum equation(s).

Strong Form	Weak Form	Name	Options
$\epsilon \frac{\partial (\rho_f V_i)}{\partial t}$	$\left(\epsilon \frac{\partial \rho_f V_i}{\partial t}, \psi \right)$	ConservativeTime	
$\nabla \cdot (\epsilon \rho_f V_i \vec{V})$	$\left(-\epsilon \rho_f V_i \vec{V}, \nabla \psi \right)$	MomConvectiveFlux	
$\nabla(\epsilon P)$	$(-\epsilon P, \nabla \psi)$	MomPressureGradient*	
$\nabla(\epsilon P)$	$(\nabla(\epsilon P), \psi)$	MomPressureGradient [†]	divergence = false
$W \rho_f V_i$	$(W \rho_f V_i, \psi)$	MomFrictionForce	
$-P \nabla \epsilon$	$(-P \nabla \epsilon, \psi)$	MomPressureGradientPorosity	
$-\epsilon \rho_f g_i$	$(-\epsilon \rho_f g_i, \psi)$	MomGravityForce	

Table 7: Kernels for use in the Pronghorn fluid energy equation(s).

Strong Form	Weak Form	Name	Options
$\epsilon \frac{\partial \rho_f E}{\partial t}$	$\left(\epsilon \frac{\partial \rho_f E}{\partial t}, \psi \right)$	ConservativeTime	
$\epsilon \rho_f C_p \frac{\partial T_f}{\partial t}$	$\left(\epsilon \rho_f C_p \frac{\partial T_f}{\partial t}, \psi \right)$	FluidEnergyTime*	
$\epsilon C_p \frac{\partial \rho_f T_f}{\partial t}$	$\left(\epsilon C_p \frac{\partial (\rho_f T_f)}{\partial t}, \psi \right)$	FluidEnergyTime [†]	constant_cp = true
$\nabla \cdot (\epsilon H_f \rho_f \vec{V})$	$\left(-\epsilon H_f \rho_f \vec{V}, \nabla \psi \right)$	FluidEnergyConvectiveFlux	
$\epsilon \rho_f C_p \vec{V} \cdot \nabla T_f$	$\left(\epsilon \rho_f C_p \vec{V} \cdot \nabla T_f, \psi \right)$	FluidEnergyAdvection*	
$\nabla \cdot (\epsilon \rho_f C_p T_f \vec{V})$	$\left(-\epsilon \rho_f C_p T_f \vec{V}, \nabla \psi \right)$	FluidEnergyAdvection [†]	constant_cp = true
$-\nabla \cdot (\kappa_f \nabla T_f)$	$(\kappa_f \nabla T_f, \nabla \psi)$	FluidEnergyDiffusion	
$-\epsilon \rho_f \vec{g} \cdot \vec{V}$	$(-\epsilon \rho_f \vec{g} \cdot \vec{V}, \psi)$	FluidEnergyGravityForce	
$\alpha(T_f - T_s)$	$(\alpha(T_f - T_s), \psi)$	FluidSolidConvection	
$-q_f$	$(-q_f, \psi)$	HeatSrc	

Table 8: Kernels for use in the Pronghorn solid energy equation(s).

Strong Form	Weak Form	Name	Options
$(1 - \epsilon)\rho_s C_{ps} \frac{\partial T_s}{\partial t}$	$\left((1 - \epsilon)\rho_s C_{p,s} \frac{\partial T_s}{\partial t}, \Psi \right)$	SolidEnergyTime	
$-\nabla \cdot (\kappa_s \nabla T_s)$	$(\kappa_s \nabla T_s, \nabla \Psi)$	SolidEnergyDiffusion	
$\alpha(T_s - T_f)$	$(\alpha(T_s - T_f), \Psi)$	SolidFluidConvection	
$-q_s$	$(-q_s, \Psi)$	HeatSrc	

4 AuxKernels

This section summarizes the auxiliary kernels used in Pronghorn. Some of these auxiliary kernels are developed specifically for Pronghorn, while others are available in BIGHORN or the MOOSE Navier-Stokes module. A summary of these auxiliary kernels is given in Table 9. Note that `TotalFluidEnergyAux` is only intended for use in isothermal calculations because otherwise a circular logic exists with its dependencies.

Table 9: Auxiliary kernels used in Pronghorn.

AuxVariable Computed	AuxKernel	Dependency
Pe_{el}	CellPecletAux	\vec{V} , h_e , and thermal diffusivity
H_f	EnthalpyAux	ρ_f , $\rho_f E$, and P
ρ_f	FluidDensityAux	P and T_f
V_i	NSVelocityAux	ρ_f and $\rho_f V_i$
P	PressureAux	v_f , e
e	SpecificInternalEnergyAux	$\rho_f E$ and $\rho \vec{V}$
v_f	SpecificVolumeAux	ρ_f
T_f	TemperatureAux	v_f , e
E	TotalFluidEnergyAux	ρ_f , e , and \vec{V} (isothermal only)

5 Interface Kernels

Interface kernels are used to apply Neumann-type BCs (flux BCs) on interior mesh sidesets to link variables defined on two different regions of the mesh. For example, a fluid flowing next to a solid is linked to the solid by conjugate heat transfer. The heat flux between the two phases is governed by Newton’s law of cooling. The heat flux from the fluid to the solid is $q'' = h(T_f - T_s)$, while the heat flux from the solid to the fluid is the negative of this expression. Note that interface kernels can only be used to exchange flux between two regions that are *connected* by a mesh sideset. Interface kernels could not, for example, be used to model radiation heat transfer between two non-connecting surfaces, since those two surfaces would not share a sideset.

Interface kernels use a Discontinuous Galerkin (DG) formulation to specify a Neumann-type residual contribution from one surface to another. So, the equations used to specify the flux between regions simply require specification of the discontinuous numerical flux. When the flux is governed by a variable difference, such as is the case for convection and radiation fluxes, the variable difference appears the “same” from both sides of the discontinuous interface. So, numerical flux functions for convection and radiation transfer can be written without approximation. However, when the flux appears different depending on the side of the interface, such as for conduction flux, a numerical approximation to the true flux must be made.

This section presents the interface kernels available in Pronghorn. The flux between two regions, 1 and 2, is represented as $q''_{1 \rightarrow 2}$ and $q''_{2 \rightarrow 1}$, where $q''_{2 \rightarrow 1} = -q''_{1 \rightarrow 2}$ because the areas of the two surfaces are the same because they must share a sideset. Table 10 summarizes the interface kernels available in Pronghorn.

Table 10: Interface kernels available in Pronghorn.

Interface Kernel	$q''_{1 \rightarrow 2}$	Interpretation
HeatConvectionInterface	$h(T_1 - T_2)$	Convective heat flux
ThermalRadiationInterface	$\sigma(T_1^4 - T_2^4) / \left(\frac{1}{\epsilon_{r,1}} + \frac{1}{\epsilon_{r,2}} + 1 \right)$	Thermal radiation (gray bodies)
HeatDiffusionInterface	$q''_{1 \rightarrow 2} = \frac{1}{2} \left(-k_1 \frac{\partial T_1}{\partial x} \vec{n} - k_2 \frac{\partial T_2}{\partial x} \vec{n} \right)$	Thermal diffusion heat flux

The diffusive flux interface kernel uses the Bassi and Rebay numerical flux formulation to simply take the average of the two fluxes; a simpler formulation such as those for convection and radiation is not possible because the gradient of the solution on either side of the discontinuous interface is not the same.

6 Boundary Conditions

This section discusses the BCs used in Pronghorn. There are two general types of BCs available within Pronghorn - Dirichlet BCs, which strongly enforce a value for a variable, and Neumann BCs, which weakly enforce either a flux or a value for a variable. For Neumann BCs, only the *integral*, rather than the value, of the quantity is imposed. Often, the same mathematical BC can be applied in either manner, but numerical differences will exist.

Neumann-type BCs are additive, allowing some BCs to be split into more than one BC for modularity. For instance, in the conservative form of the fluid energy equation, boundary terms arise due to the convective transport of enthalpy and the diffusion of temperature. The correct BCs for this equation will include both terms, but because Neumann-type BCs are additive, this combined BC is split into two BCs that are summed.

Below is a table summarizing the BCs available in Pronghorn for both the conservative and primitive equation sets. i subscripts denote known quantities. Quantities without subscripts denote the implicit solution value. Neumann-type BCs are shown in the boundary integral notation defined in Eq. (2.300)b, while strongly-enforced Dirichlet conditions are shown in the form $F = F_i$. “Walls” are assumed stationary. Some BCs are implemented in a “vectorized” form to ensure consistent usage of BCs in the involved equations. For example, frequently only the combination of BCs specified will yield a well-posed problem. In the tables below, if a BC name appears in multiple tables below, it is a vectorized BC, and the equation to which it is applied is indicated by the `var_num` parameter, which is 0 for the mass equation, $1 \cdots n_s$ for the momentum equation(s), and $n_s + 1$ for the energy equation. Sections 6.1 and 6.2 explain these BCs for the conservative and primitive equation sets, respectively.

Table 11: Summary of BCs used in the mass equation in Pronghorn.

Weak Form	Name	Boundary Type
$\langle \epsilon \rho_f (P_{stag,i}, T_{stag,i}) \vec{V}, \psi \rangle$	ConsVecStagnationInlet	Inflow
$\langle \epsilon (\rho_f \vec{V})_i, \psi \rangle$	ConsVecSubsonicInlet	Inflow
$\langle \epsilon \rho_f \vec{V}, \psi \rangle$	ConsVecSubsonicOutlet	Outflow
$\langle \epsilon \rho_f \vec{V}, \psi \rangle$	ContinuityFreeBC	Outflow
$\langle \epsilon \rho_{f,i} \vec{V}, \psi \rangle$	ContinuityInflowBC	Inflow
$\rho_f = \rho_{f,i}$	DirichletBC	Inflow
$\langle 0, \psi \rangle$	NoSlipBC	Wall
$\langle \epsilon \rho_f \vec{V}, \psi \rangle$	PressurePoissonInflowBC	Inflow
$P = P_o$	PressurePoissonOutflowBC	Outflow
$\langle 0, \psi \rangle$	PressurePoissonWallBC	Wall

Table 12: Summary of BCs used in the momentum equation in Pronghorn. BCs are shown only for the x -direction momentum equation.

Weak Form	Name	Boundary Type
$\epsilon \rho_f (P_{stag,i}, T_{stag,i}) V_x \vec{V} + P_{stag,i}, \psi \rangle$	ConsVecStagnationInlet	Inflow
$\epsilon \rho_f \vec{V} V_x + \epsilon P_i, \psi \rangle$	ConsVecSubsonicOutlet	Outflow
$\rho_f V_x = (\rho_f V_x)_i$	DirichletBC	Inflow
$\langle \epsilon \rho_f V_x \vec{V}, \psi \rangle$	MomFreeBC	Outflow
$\langle \epsilon (\rho_f V_x)_i \vec{V}, \psi \rangle$	MomInflowBC	Inflow
$\langle \epsilon P, \psi \rangle$	MomImplicitPressureBC	Inflow/wall
$\langle \epsilon P_i, \psi \rangle$	MomWeakPressureBC	Inflow/outflow
$\langle 0, \psi \rangle$	NoSlipBC	Wall

Table 13: Summary of BCs used in the fluid energy equation in Pronghorn. \bar{q} represents a known heat flux.

Weak Form	Name	Boundary Type
$\langle \varepsilon \left(\rho_f (P_{stag,i}, T_{stag,i}) E_f(T_{stag,i}, \vec{V}) + P_{stag,i} \right) \vec{V}, \psi \rangle$	ConsVecStagnationInlet	Inflow
$\langle \varepsilon \left((\rho_f \vec{V})_i H_f - k_f \nabla T_f \right), \psi \rangle$	ConsVecSubsonicInlet	Inflow
$\langle \varepsilon \rho_f \vec{V} H_f(E, \rho_f, P_i) - \varepsilon k_f \nabla T_f, \psi \rangle$	ConsVecSubsonicOutlet	Outflow
$\langle h_c(T_f - T_\infty), \psi \rangle$	ConvectionBC	Convection to ambient/wall
$\langle \varepsilon \rho_f C_{pf} \vec{V} T_f, \psi \rangle$	FluidEnergyAdvectionFreeBC	Outflow
$\langle \varepsilon \rho_f C_{pf} \vec{V} T_{f,i}, \psi \rangle$	FluidEnergyAdvectionInflowBC	Inflow
$\langle \varepsilon H_f \rho_f \vec{V}, \psi \rangle$	FluidEnergyFreeBC	Outflow
$\langle \varepsilon H_{f,i} \rho_f \vec{V}, \psi \rangle$	FluidEnergyInflowBC	Inflow
$\langle \varepsilon \bar{q}, \psi \rangle$	HeatFluxBC	\bar{q} in fluid
$\langle \bar{q}, \psi \rangle$	NeumannBC	\bar{q} from fluid to boundary

Table 14: Summary of BCs used in the solid energy equation in Pronghorn. \bar{q} represents a known heat flux.

Weak Form	Name	Boundary Type
$\langle (1 - \varepsilon) \bar{q}, \psi \rangle$	HeatFluxBC	\bar{q} in solid
$\langle \bar{q}, \psi \rangle$	NeumannBC	\bar{q} from solid to boundary

The inflow BC for the pressure Poisson equation is the same as that used for the continuity equation, since the pressure Poisson equation was obtained by substituting the momentum equation into the continuity equation. Because the inflow BC associated with the continuity equation cannot be applied on outflow boundaries, there is no corresponding outflow BC for the pressure Poisson equation. However, the Laplacian of pressure in this equation does require some condition on pressure to be specified on outflow boundaries. This is commonly a Dirichlet condition, so this BC sets a Dirichlet condition for pressure on outflow boundaries for use with the `PressurePoisson` kernel.

Because the `HeatFluxBC` multiplies the heat flux by the phase porosity, this BC is used to set a known value for the heat flux in one phase. Note that this is different from setting a value for $\varepsilon_k \kappa_k \nabla T_k$. The `ConsVecStagnationInlet` BC currently only applies for the ideal gas EOS.

6.1 The Conservative Equation Set

For the conservative equation set in Eq. (2.301), the flux vector that is integrated over a boundary is:

$$\vec{B} \equiv \begin{bmatrix} \varepsilon \rho_f \vec{V} \cdot \vec{n} \\ \varepsilon \eta_1 \vec{V} \cdot \vec{n} + \varepsilon P n_1 \\ \varepsilon \eta_2 \vec{V} \cdot \vec{n} + \varepsilon P n_2 \\ \varepsilon \eta_3 \vec{V} \cdot \vec{n} + \varepsilon P n_3 \\ \varepsilon h \vec{\eta} \cdot \vec{n} - \kappa_f \nabla T_f \cdot \vec{n} \\ -\kappa_s \nabla T_s \cdot \vec{n} \end{bmatrix} \quad (6.1)$$

6.2 The Primitive Equation Set

For the primitive equation set in Eq. (2.303), the flux vector that is integrated over a boundary is:

$$\vec{B} \equiv \begin{bmatrix} \frac{\epsilon}{W} (\epsilon \rho_f \vec{g} - \epsilon \nabla P) \cdot \vec{n} \\ 0 \\ 0 \\ 0 \\ -\kappa_f \nabla T_f \cdot \vec{n} \\ -\kappa_s \nabla T_s \cdot \vec{n} \end{bmatrix} \quad (6.2)$$

7 Equations of State

For the conservative equation set shown in Eq. (2.299), an EOS is needed to calculate P and T_f :

$$P = P(\rho_f, e) \quad (7.1a)$$

$$T_f = T_f(\rho_f, e) \quad (7.1b)$$

For the primitive equation set, an EOS is required for density in terms of P and T_f . These primitive EOS are described in Section 13 because the term EOS is often reserved for equation sets that are based on thermodynamic theory and easily codified for a wide range of fluids (such as the ideal gas law), rather than experimental measurements (such as the density variation of flibe with pressure). Any EOS available in RELAP-7 can be used to calculate P and T_f as a function of specific volume and specific internal energy of the fluid.

Eq. (7.1)a and (7.1)b are incomplete EOSs because they consist of a pair of equations. A complete EOS would specify $e = e(v, s)$, where s is the entropy per unit mass. Differentiating this complete EOS with respect to s holding v constant, or with respect to v holding s constant, will produce the EOS pair. However, the existence of the incomplete pair EOS does not necessarily imply the reverse. The Euler equations do not require a complete EOS for smooth flows, and hence the use of an incomplete EOS is acceptable in Pronghorn. Note that Pronghorn is currently only capable of modeling single-phase flows.

7.1 Barotropic Equation of State

Flows in which density is only a function of pressure are barotropic flows. For pure systems, normally two state variables are required to specify the state of the system - density, and either entropy or temperature. Hence, the barotropic EOS can only be used for isothermal or isentropic flows, both of which are situations very unlikely to be in the application space of Pronghorn. This EOS implies a constant speed of sound, given the definition in Eq. (2.269). This EOS will not produce any shocks or discontinuities in the solution unless the initial conditions have discontinuities (in which case those discontinuities are simply advected without further steepening). This EOS should not be used for modeling applications, and is only described here because it is useful for testing. The pressure is specified as [74]:

$$P = P_0 + a^2(\rho_f - \rho_{f,o}) \quad (7.2)$$

where P_0 is a reference pressure, $\rho_{f,o}$ is the density at P_0 , and a is a constant that can be interpreted as the speed of sound.

7.2 Stiffened Gas Equation of State

This compressible EOS, which applies to both liquids and gases, is the simplest EOS that contains the essential phenomena in fluids. Pressure is provided according to [74]:

$$P = \underbrace{(\varpi - 1)\rho(e - q_B)}_{\text{repulsion}} - \underbrace{\varpi P_\infty}_{\text{attraction}} \quad (7.3)$$

where q_B is the binding energy of the fluid and ϖ and P_∞ are empirical fluid constants. The higher the P_∞ the “stiffer” the fluid. For gases, P_∞ is often zero or very close to zero, in which case Eq. (7.3) reduces to the ideal gas law

in Eq. (7.10)b. Solving the above for the internal energy gives:

$$e = \frac{P + \bar{\omega}P_\infty}{(\bar{\omega} - 1)\rho} + q_B \quad (7.4)$$

An EOS for the temperature requires an additional caloric law $T_f = T_f(P, \rho_f)$:

$$T_f = \frac{P - P_\infty}{(\bar{\omega} - 1)C_v \rho_f} \quad (7.5)$$

Combining Eqs. (7.4) and (7.5) to eliminate $\bar{\omega}$, the temperature EOS is derived:

$$T_f = \frac{1}{C_v} \left(e - q_B - \frac{P_\infty}{\rho_f} \right) \quad (7.6)$$

7.3 Isentropic Stiffened Gas Equation of State

The isentropic version of the Stiffened Gas EOS discussed in Section 7.2 gives pressure as [74]:

$$P = (P_o + P_\infty) \left(\frac{\rho_f}{\rho_{f,o}} \right)^{\bar{\omega}} - P_\infty \quad (7.7)$$

where P_∞ , $\rho_{f,o}$, and $\bar{\omega}$ are fluid-dependent constants. Representative values for water are $P_\infty = 3.3 \times 10^8$ Pa, $\bar{\omega} = 7.15$, and $\rho_{f,o} = 10^3$ kg/m³. Because this equation of state assumes the system is isentropic, it is not sufficient for capturing shock behavior. This EOS is usually used for modeling incompressible fluids, and is an improvement on the barotropic EOS because the speed of sound is no longer constant.

7.4 Linear Equation of State

Generic linear equations of state for pressure and internal energy are defined using the chain rule [74]:

$$P = P_o + \left(\frac{\partial P}{\partial \rho} \right)_T (\rho_f - \rho_{f,o}) + \left(\frac{\partial P}{\partial T_f} \right)_\rho (T_f - T_{f,o}) \quad (7.8)$$

$$e = e_o + \left(\frac{\partial e}{\partial \rho_f} \right)_{T_f} (\rho_f - \rho_{f,o}) + \left(\frac{\partial e}{\partial T_f} \right)_{\rho_f} (T_f - T_{f,o}) \quad (7.9)$$

where the partial derivatives are evaluated at $\rho_{f,o}$ and $T_{f,o}$. Rearranging Eq. (7.9) gives an EOS for temperature of the form in Eq. (7.1)b.

7.5 Ideal Gas Equation of State

The ideal gas law specifies pressure as:

$$P = \rho RT \quad (7.10a)$$

$$= (\gamma - 1)\rho e \quad (7.10b)$$

where R is the ideal gas constant and γ is the specific heat ratio:

$$\gamma = \frac{C_p}{C_v} \quad (7.11)$$

This EOS is most accurate at low pressures, high temperatures, and far from phase change. Under these conditions interactions between gas molecules is minimal. Eq. (2.159) gives enthalpy as:

$$h = e + RT \quad (7.12)$$

Eqs. (2.176) and (2.177) give:

$$C_p = C_v + R \quad (7.13)$$

The specific heats of an ideal gas are assumed constant because R is a constant. Because h and e depend only on the quantity RT , the partial derivatives in the definitions of C_p and C_v in Eqs. (2.176) and (2.177) are taken as whole derivatives. This gives:

$$T = \frac{e}{C_v} \quad (7.14)$$

$$h = C_p T \quad (7.15)$$

Inserting Eqs. (7.14) and (7.13) into Eq. (7.10) gives the form in Eq. (7.10)b.

7.5.1 Isentropic Relations

For isentropic flow, several important identities can be derived that will be used for defining ideal-gas-specific BCs in Section 6. Setting $T ds = 0$ and using differential forms of Eqs. (7.14) and (7.15) in Eqs. (2.166) and (2.167) gives:

$$\frac{T_2}{T_1} = \left(\frac{v_1}{v_2} \right)^{\gamma-1} \quad (7.16a)$$

$$= \left(\frac{P_2}{P_1} \right)^{\frac{\gamma-1}{\gamma}} \quad (7.16b)$$

where numeric subscripts indicate two arbitrary states. Eq. (7.16) can be rearranged to show that:

$$P\rho^{-\gamma} = \text{constant} \quad (7.17a)$$

$$\ln(P) - \gamma \ln(\rho) = \text{constant} \quad (7.17b)$$

where the second form has been obtained by taking the natural logarithm of both sides. Then, differentiating both sides and using the definition of the speed of sound in Eq. (2.269) gives the speed of sound in an isentropic ideal gas:

$$c = \sqrt{\gamma RT} \quad (7.18)$$

Inserting Eq. (7.15) into Eq. (2.100) defines the stagnation temperature for an ideal gas, assuming $gz \ll V^2/2 + h$:

$$\begin{aligned} T_{stag} &= \frac{1}{2} \frac{V^2}{C_p} + T \\ &= T \left(1 + \frac{\gamma-1}{2} Ma^2 \right) \end{aligned} \quad (7.19)$$

where Eq. (7.18) has been used to introduce the speed of sound in the Mach number. Combining Eqs. (7.15) and (7.19) gives:

$$H = C_p T_{stag} \quad (7.20)$$

Using Eq. (7.16)b and Eq. (7.19) gives the stagnation pressure:

$$P_{stag} = P \left(1 + \frac{\gamma-1}{2} Ma^2 \right)^{\frac{\gamma}{\gamma-1}} \quad (7.21)$$

For isentropic flow, P_{stag} is constant.

8 Porosity, Coordination Number, and Tortuosity

This section describes the functions used to calculate the porosity, coordination number, and tortuosity of the porous media. The emphasis is entirely placed on beds of spherical particles, so none of the correlations shown in this section should be used for plate or prismatic solid geometries. In addition, the following geometrical features are not considered in this section because they have very different porosity profiles, but can be added through custom functions:

- Particle shapes aside from spheres [35], or packings caused by dimpled walls;
- Aligned pebbles near in-bed control rods or broken pebbles caused by control rod impact [6, 75];
- Non-cylindrical walls, such as in the ASTRA [16] and Thorium Molten Salt Reactor (TMSR) experimental facilities [7]; and
- Asymmetric axial configurations, such as converging/diverging conical sections, where the average porosity sharply transitions to a value several percent higher than the cylindrical region of the bed and the oscillatory porosity profile near the walls has wider peaks [76].

Discrete Element Method (DEM) simulations can be performed to determine the porosity profile for any desired geometry. The porosity is generally a function of height and distance from a wall. This section will discuss these dependencies separately, and to employ both dependencies, the correlations would simply need to be multiplied together and scaled appropriately. However, correlations currently available only treat the radial dependence. Correlations for ϵ have been determined experimentally and numerically in many ways. It is common to use a DEM code to numerically generate a packed bed [76–78]. Experimentalists often simply fill a cylinder with spheres, pour in a wax or resin that is allowed to solidify, and then chop the cylinder into pieces for weighing. Some researchers have also used image analysis and radiography. However, there still exists variation amongst correlations given by researchers due to how the bed is initially filled with pebbles. A pebble bed can generally be filled in four different ways, which show progressive decreases in the infinite bed porosity ϵ_∞ [79]:

1. Drain fluid from a fluidized bed containing spheres: $\epsilon_\infty \approx 0.44$.
2. Drop spheres individually into the bed or allow them to roll into place: $\epsilon_\infty \approx 0.395 - 0.4$.
3. Pour spheres into the bed: $\epsilon_\infty \approx 0.375 - 0.391$.
4. Shake down the packed bed by vibration: $\epsilon_\infty \approx 0.359 - 0.375$.

In general, gentler filling methods lead to higher porosities because less pebble motion is induced while filling the bed. For natural media, ϵ usually varies from 0.2 – 0.6. For beds of equal-sized spheres, the limits on ϵ are 0.2595 for rhombohedral packing and 0.4764 for Simple Cubic (SC) packing. The rougher the pebbles, the more resistant the pebbles to slipping into a higher packing fraction. However, none of the correlations discussed here consider the roughness of the pebbles.

The radial porosity profile is a damped oscillatory function of the distance from the wall. A minimum (of about 0.2 for $\epsilon_\infty \approx 0.4$) is reached at about $d_p/2$ from the wall due to sphere alignment. Most experimental results show that a constant porosity is reached within four to five pebble diameters from the wall [78, 79]. The largest porosity (except that right at the wall) is obtained one pebble diameter from the wall. While the porosity tends to unity right at the wall, fluid stagnation points act to artificially decrease the porosity, such that a wall porosity of 1.0 is not necessarily “seen” by the fluid [35]. When using a spatially-varying porosity, it should be noted that the governing equations generally become stiff and difficult to converge in the near-wall regions where $\epsilon = 1$ [38] or in very low flow regions where $\epsilon = 0$ [80]. For this reason, it may help convergence to assume a constant porosity to avoid numerical stiffness issues associated with $\epsilon \rightarrow 1$ and $\epsilon \rightarrow 0$. It is also a common approximation to treat the porosity as a piecewise function, with

one value used in the center of the bed, and a different, higher, value (but not unity) used at the periphery of the bed; this may be supported by the apparent decrease in porosity at the walls caused by stagnation points [19].

The axial porosity profile is also a damped oscillatory function of the distance from the bounding walls. However, most beds will only have one axially-bounding wall, either on the top for beds filled from the bottom, or on the bottom for beds filled from the top. At the free end of the bed, the porosity smoothly approaches unity [49, 77]. Inner bed structures, such as guiding plates to enforce pebble zoning, also impact the porosity profile. During motion, pebbles diffuse less than one pebble diameter from the mean flow streamlines, so even though guiding plates typically only extend into the bed for a fraction of the total bed height, the porosity profile may be affected throughout the entire height of the bed [76]. In addition to wall structures, the weights of the pebbles also impact the porosity. For gas-cooled reactors, where the pebbles have very little buoyancy force, the average porosity will be slightly higher towards the bottom of the bed, though not all researchers have observed this effect numerically or experimentally [77]. Pebble weight will likely have an even smaller impact for liquid-cooled reactors, since the pebbles are closer to neutrally buoyant. In beds with a free axial surface such as the Pebble Bed High-Temperature Fluoride-Salt Cooled Reactor (PB-FHR), the flow profile results in either a convex or concave pebble structure [15].

Overall, the radial porosity profile has a stronger effect on the bed flow than the axial profile. The radial increase in porosity near the walls impacts the friction coefficients discussed in Section 9, the heat transfer coefficients discussed in Section 10, and the effective thermal conductivities discussed in Sections 11 and 12. The velocity is the field variable most impacted by a spatially-varying porosity [54] - the radial velocity profile is almost entirely determined by the porosity [49]. High porosity near the walls generally results in lower drag coefficients because the Darcy and Forchheimer prefactors scale as $(1 - \epsilon)^2/\epsilon$ and $1 - \epsilon$, respectively. The dependence of the drag coefficients on porosity produces a flow-channeling effect - the velocity shows a large peak that is contained within a half pebble diameter of the wall [38]. Fig. 8 shows an example of these velocity profiles near the wall in a pebble bed.

As long as a Brinkman-type model is not used (the no-slip condition is not enforced at the walls), the velocity field will almost exactly follow the porosity profile, so using an oscillatory profile yields an oscillatory velocity [36, 38]. With a constant porosity, the velocity profile is nearly constant along a cross-section [7, 36, 54, 81], with slightly higher values in regions where the heating is greatest (from mass conservation principles). With a non-constant porosity, the flow channeling effect at the walls results in bypass flow that causes less effective cooling of the fuel, and higher overall temperatures in the bed (on the order of tens of degrees) [36, 81] and a more nonuniform outlet temperature [82]. The porosity profile also impacts the overall pressure drop. If the high-porosity region is confined to a relatively small region of the bed, the overall pressure drop may differ by only about 2.5% from the pressure drop obtained using a uniform porosity [36]. The majority of packed beds are designed with fairly low d_p/d_{bed} ratios, so the wall effects tend to be fairly minimal. However, it should be noted that using a constant porosity is non-conservative in the sense that flow bypassing the fuel is not captured and some non-uniformity of the outlet flow is not captured. Table 15 provides example values for several packed bed reactors and experimental facilities. For annular beds, the bed diameter is taken as the difference in the outer and inner diameters.

Table 15: Core geometries and d_p/d_{bed} ratios for several packed bed reactors and experimental facilities. “—” denotes that an inner diameter cannot be defined for cylindrical beds. The PB-FHR inner and outer diameters are for the mid-plane of the bed, and the height was estimated based on the number of central reflector blocks of height 25 cm adjacent to the core (not including the defueling chutes).

System	Bed Type	Active Height (m)	Inner Diameter (m)	Outer Diameter (m)	d_p (m)	d_p/d_{bed}
HTR-10 [83]	cylindrical	1.97	—	1.8	0.06	0.033
HTR-PM [21]	cylindrical	11	—	3.0	0.06	0.020
PB-FHR [3]	annular	4.5	0.70	2.5	0.03	0.012
PBMR-400 [84]	annular	11.0	2.0	3.7	0.03	0.018
SANA [18]	annular	1.0	0.141	1.5	0.06	0.044
THTR [71]	cylindrical	6.0	—	5.6	0.06	0.011

So, many researchers assume constant porosity ϵ_o [7, 11]:

$$\epsilon = \epsilon_o \quad (8.1)$$

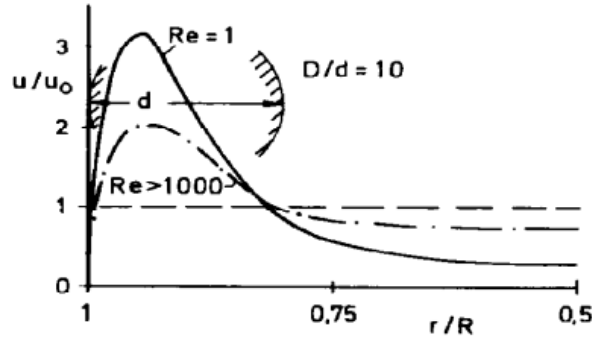


Figure 8: Velocity flow channeling effect at the wall of a pebble bed for two different Reynolds numbers [85]. The figure shows the velocity normalized by the bed-averaged superficial velocity.

Larger pebble diameters produce wider, but shallower, velocity peaks near walls [54]. The ratio of the peak superficial velocity to the bed-center superficial velocity is in the range of 2-10. Because high Re flow is characterized by better momentum transfer, the width of the velocity peak is larger for high Re flows since the channeling region extends farther into the bed. Therefore, the ratio of superficial velocities decreases with Re , and is in the range of 2-4 for $10 < Re < 1000$ [38]. Generally, the flow channeling region does not decrease to nil at very large Reynolds numbers, but eventually becomes stationary. By defining the percentage of flow that is bypass flow as the fraction of velocities above the average bed velocity, higher Re leads to a lower percentage of bypass flow [38]. At higher temperatures, because gas viscosity increases with temperature, viscous diffusion also causes the flow channeling peak to become wider. Faster velocities at the edges of the core lead to a lower overall bed pressure drop than had a constant porosity been used. However, this bypass flow results in less cooling of pebbles. The bypass flow does produce greater convective cooling of the bounding wall, which can help extend component lifetimes. For annular packed beds, there is essentially no difference in the porosity structure near the inner versus outer walls. As the fluid heats up in the core, by conservation of mass the velocity generally increases, resulting in more significant drag effects as the fluid moves through the core [2, 17, 49].

The correlations discussed in this section do not consider any stochastic behavior in the local porosity. By computing the average porosity over small clusters of about 45 pebbles, Auwerda determined approximate Probability Density Function (PDF)s for porosity in a cylindrical packed bed, shown in Fig. 9 [78]. The variation in porosity is lower in the inner bed region; but, near the walls, both very large and very small packing fractions are obtained. These wide variations show that hot spots can occur, especially near the walls if adjacent to reflectors, which would not be captured by any of the porosity correlations discussed in this section. Accounting for hot spots is more important for gas-cooled beds than for liquid-cooled beds since gas viscosity increases with temperature, increasing friction drag and reducing convective cooling velocity [3].

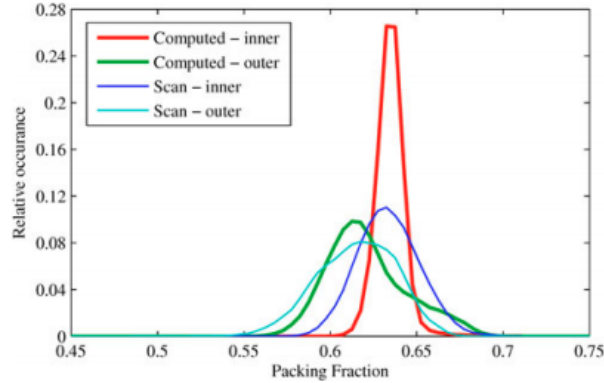


Figure 9: PDF of the coordination number for the inner (far from walls) and outer (within several pebble diameters of the walls) regions of a cylindrically-packed bed for experimental (denoted as “scan”) and numerical data [78].

The correlations discussed in this section also assume that the porosity is independent of the fluid flow. In reality, the fluid exerts drag forces on the pebbles, causing them to move slightly. To fully account for pebble motion, a coupled DEM-CFD simulation would need to be performed, and the drag on the pebbles use a nonzero solid velocity [49]. Using DEM and CFD, Li et. al assess the pebble motion due to drag forces exerted by the fluid in the annular Pebble Bed Modular Reactor-400 (PBMR-400) reactor, and find that at the entrance of the bed, the fluid causes the axial porosity to *increase* from roughly 0.4 to 0.5 [86]. The fluid flow generally causes the pebbles to move from the outer wall of the annular core to the inner wall, resulting in increase channeling effects at the outer wall. Neither of these effects are very significant in the bulk or at the bottom of the bed, where contact forces prevail. No impact on the coordination number was observed. For beds of floating pebbles, such as salt-cooled systems, the kinetic energy of the pebbles is essentially zero, even for the pebbles at the lower plenum that are free to move [87]. Due to the great complications associated with running DEM simulations to obtain porosity distributions that are a function of the fluid flow (thus introducing a coupling, since the fluid flow is dependent on the porosity), the assumption of a time-dependent porosity is used in Pronghorn.

A time-dependent porosity based on the online refueling pebble recirculation motion (about 0.5% of pebbles are removed each day [71]) is also not considered, because this rate tends to be very low for packed bed reactors and experimental facilities. For example, for the PB-FHR, pebbles pass through the core an average of eight times over 1.4 years, giving an average pebble velocity of only 10^{-7} m/s [3]. Therefore, most researchers assume a time-independent porosity [11].

In addition to the fluid flow and heat transfer, porosity has an important impact on the neutronics of a pebble bed system via its impact on neutron streaming. Though mostly outside the scope of this document, a brief discussion may be useful for those directly using the porosity correlations in Pronghorn for coupling to a neutronics code. Some neutronics models homogenize the entire bed using an average porosity. But, there are two more sophisticated modeling options -

1. Divide the reactor into zones of homogeneous porosity. When using a piecewise constant porosity in the neutronics solution, corrections to diffusion coefficients attempt to regain lost accuracy.
2. Explicitly model all pebbles.

The average porosity of a bed is lower than the median porosity due to structuring near walls, so using a piecewise constant porosity generally increases the multiplication factor by 50-100 pcm because less fuel is located near the periphery than suggested by a totally homogeneous bed [88]. However, using explicit pebble models best captures the overall leakage increase effect. For a helium-filled cylindrical bed of a 1:1 ratio of moderator to fuel pebbles, Auwerda et.al calculate a 606 pcm *decrease* in the multiplication factor when explicitly modeling the pebbles versus the piecewise constant approach. The standard deviation of 104 pcm indicates the strong impact the local porosity

has on the neutron streaming [88], though the lack of any treatment is significant [89]. The most important impact of the porous nature of the bed is the increase in streaming and leakage - the decrease in resonance self-shielding at the edge of the bed is not statistically significant [88]. If using a Pronghorn porosity correlation in a neutronics code that is not capable of explicitly modeling the individual pebbles, an oscillatory porosity correlation combined with diffusion coefficient correction factors may be the next-best approach. If only using the neutronics code to obtain global parameters, a constant porosity may be sufficient, but local reaction rates (which can show on the order of 40% difference from homogenized rates) require spatially-varying porosity [89].

Correlations for porosity either smooth out the physical oscillations, or retain them in some average sense. Both options are available in Pronghorn. In the correlations that follow, many give results in terms of a nondimensional distance from the wall that is defined here for reference:

$$\zeta = \frac{d_{\text{bed}}/2 - r}{d_p} \quad (8.2)$$

The coordination number N_c , or the number of pebbles contacting a pebble, is another important property of packed beds that varies with position in the bed. N_c is important for calculating the solid-to-solid contact conduction component of the effective solid thermal conductivity discussed in Section 11.

To be stable, a pebble needs at least three contacts. At the wall, one of these contacts can be provided by the wall, so the minimum N_c are 3 far from the walls and 2 at the walls. The maximum theoretical coordination number is 12, corresponding to Hexagonal Close Packing (HCP). By investigating the axial porosity, the radial distribution of pebble-to-pebble center distances, and angles between touching pebbles, Auwerda shows that near walls, the pebbles are ordered in a packing very similar to HCP packing [78]. This structuring has important consequences for the coordination number within the bed. Auwerda computed the PDF of the coordination number using both a numerically-generated bed and an experimental setup, with results shown in Fig. 10. As can be seen, there is a large variation in the coordination number within a bed, with significant variation in different regions of the bed. In the inner bed region, there is less spread in the predicted coordination numbers. Interestingly, at the edges of the bed, higher coordination numbers are possible due to the semi-ordered HCP packing. So, despite the lower porosity, coordination numbers can be higher at the edges of the bed. For SC packings, $N_c = 6$, for BCC packings, $N_c = 8$, and for FCC packings, $N_c = 12$. For randomly-packed pebble beds, the coordination number is some combination of these various packing structures, and a wide range of coordination numbers are reported in the literature [17, 86].

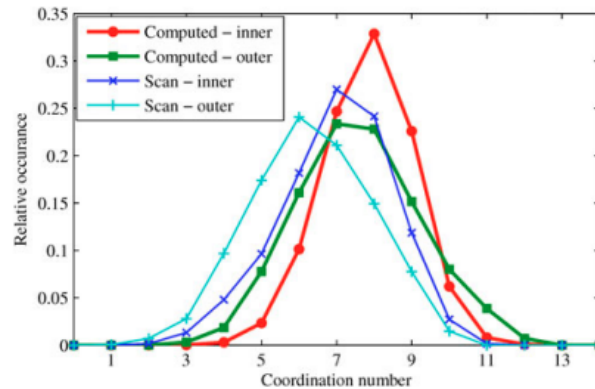


Figure 10: PDF of the coordination number for the inner (far from walls) and outer (within several pebble diameters of the walls) regions of a cylindrically-packed bed for experimental (denoted as “scan”) and numerical data [78].

In addition to porosity and coordination number, the tortuosity \mathcal{T} is another geometric characteristic of a porous media. The tortuosity is a measure of the average fluid particle path length to the straight-line distance between the same points. In other words, the tortuosity is a measure of the increase in the fluid particle path length due to flow obstructions caused by the solid porous matrix. The tortuosity is an important factor in the effective fluid thermal

conductivity discussed in Section 12. Tortuosity can be measured by performing mass transfer experiments to ensure no conductance through the solid phase, or by comparing diffusion coefficients in non-porous and porous media. The tortuosity will always be lower than $1/\varepsilon$, since $\mathcal{T} = 1/\varepsilon$ signifies that the only impedance occurs to a loss of flow area, and underestimates tortuosity due to bending around solid particles [90].

8.1 Porosity

This section describes the functions available in Pronghorn to calculate porosity. Porosity may also be specified as a constant value or with some other user-defined function.

8.1.1 OscillatoryPorosityFunction

Klerk correlated porosity as a function of radial position for cylindrical packed beds of spheres [79]. The period of the oscillation is taken to be constant because it has not been successfully correlated with the bed to pebble diameter ratio. The correlation is split into two zones because the first layer of pebbles in contact with the wall will be fully ordered, while all other layers will not. This correlation requires $d_{\text{bed}}/d_p > 2$.

$$\varepsilon(r) = \begin{cases} 2.14\mathcal{Z}^2 - 2.53\mathcal{Z} + 1 & \mathcal{Z} \leq 0.637 \\ \varepsilon_\infty + 0.29e^{-0.6\mathcal{Z}} \cos(2.3\pi(\mathcal{Z} - 0.16)) + 0.15e^{-0.9\mathcal{Z}} & \mathcal{Z} > 0.637 \end{cases} \quad (8.3)$$

8.1.2 ExponentialPorosityFunction

Hunt and Tien calculate the radial porosity for a cylindrical bed of spheres as [91]:

$$\varepsilon(r) = \varepsilon_\infty + (1 - \varepsilon_\infty)e^{-6\mathcal{Z}} \quad (8.4)$$

This function gives the infinite bed porosity towards the center of the bed, and an exponential increase to a porosity of 1 at the wall. Other authors use similar exponential formulations that do not rely on any numerical factors, such as $\varepsilon(r) = \varepsilon_\infty (1 + Ce^{1-\mathcal{Z}})$ [38]. Vortmeyer et. al provides a semi-analytical expression for the velocity profile in a porous media near a bounding wall assuming an exponential porosity formulation such as in Eq. (8.4) that can be used for comparing constant-porosity and non-constant porosity results for isothermal flows [38, 85].

8.1.3 AnnularExponentialPorosityFunction

For annular cylindrical beds with an outside radius r_o and an inside radius r_i , many authors have expressed porosity in the following form [77]:

$$\varepsilon(r) = \begin{cases} \varepsilon_0 \left[1 + C_1 \exp\left(-N_1 \frac{r-r_i}{d_p}\right) \right] & r_1 \leq r \leq \frac{r_o-r_i}{2} \\ \varepsilon_0 \left[1 + C_2 \exp\left(-N_2 \frac{r_o-r}{d_p}\right) \right] & \frac{r_o-r_i}{2} < r \leq r_o \end{cases} \quad (8.5)$$

where there is varied interpretation of the meaning of ε_0 and the values used for N_1 and N_2 . Unity porosity can be enforced at the walls by taking $C_1 = C_2 = 1/\varepsilon_0 - 1$. Du Toit recommends usage of Hunt and Tien's version of this correlation, where $N_1 = N_2 = 6$ and ε_0 is taken to be the bulk porosity of the bed [77]. For simplicity, here it is assumed that the bulk porosity is equal to ε_∞ . Note that this correlation is not strictly continuous at $r = (r_o - r_i)/2$, but

because N is selected as 6, the jump at this point is small unless a very narrow annular is modeled (in which case the porous media approximation is less accurate anyways).

8.2 Coordination Number

You et. al calculate N_c as a function of porosity as [92]:

$$N_c = (1.008E - 2)\varepsilon^{-4.785} + 5.6480 \quad (8.6)$$

which is valid for $0.26 \leq \varepsilon \leq 0.476$. By performing DEM simulations, You estimates 10% accuracy of Eq. (8.6), though the equation provides slightly higher N_c than actually observed. Propagating this uncertainty to the correlations used for $\kappa_{\text{solid conduction}}$ results in only a 1% difference in $\kappa_{\text{solid conduction}}$, and hence the error in Eq. (8.6) is acceptable. Note that Eq. (8.6) does not account for any local stochastic variations in N_c illustrated by Fig. 10. However, Eq. (8.6) gives reasonable packing fractions that agree with the mean values shown in Fig. 10. There are no function-type classes to compute N_c in Pronghorn, but Eq. (8.6) is used directly in Section 11.

8.3 Tortuosity

Of the constitutive relationships discussed in this document, the variation in tortuosity correlations seems to be very wide. Several researchers have predicted constant values of \mathcal{T} ($\sqrt{2}$ for beds of spheres [19]), but in principle \mathcal{T} should depend on porosity [93]. Boudreau collected a variety of tortuosity correlations available in the literature, and showed that the majority have one of the following dependencies, where a , b , and n represent tunable constants:

$$\mathcal{T}^{-1} = \sqrt{\varepsilon^n} \quad (8.7a)$$

$$\mathcal{T}^{-1} = \sqrt{1 + a(1 - \varepsilon)} \quad (8.7b)$$

$$\mathcal{T}^{-1} = \sqrt{1 - b \ln(\varepsilon^n)} \quad (8.7c)$$

None of these correlations provide a very good fit over wide experimental data sets, so the choice of tortuosity representation may not be very crucial for correct modeling. By fitting experimental data to the three forms shown above, the highest r^2 value obtained by Boudreau was only 0.65 - statistically significant, but not an impressive match to experimental data [93]. Boudreau recommended selecting:

$$\mathcal{T}^{-1} = \sqrt{1 - \ln(\varepsilon^2)} \quad (8.8)$$

Alternatively, by fitting mass transfer data, the tortuosity has been approximated as [85,90]:

$$\mathcal{T}^{-1} = 1 - \sqrt{1 - \varepsilon} \quad (8.9)$$

Eq. (8.9) often overpredicts the tortuosity [90]. The tortuosity is an important factor in the effective fluid thermal conductivity discussed in Section 12. While no function-type classes exist in Pronghorn to compute tortuosity, currently the simple approximation that $\mathcal{T} = 1/\varepsilon$ is used, though future developments may involve more sophisticated tortuosity models. Tortuosities measured in the radial and axial directions show only slight differences, and hence it is unlikely that a tensorial form of tortuosity be required [94].

9 Friction Coefficients

This section provides values for the friction coefficient W that appears in Eq. (2.152). Section 9.1 provides isotropic correlations for beds of spherical particles, while Section 9.2 provides anisotropic correlations for pipe flow that may be used to represent reflector coolant channels or other components. No correlations are currently implemented for plate or prismatic solid geometries. All friction coefficients available in Pronghorn are a function of Reynolds number, porosity for pebble bed correlations, and pipe roughness for pipe flow correlations.

9.1 Pebble Bed Correlations

This section presents correlations for friction factors to be used for pebble bed geometries. These friction coefficients depend on several design parameters -

1. Randomness of the pebble packing; all correlations discussed in this section are applicable to randomly-packed beds, and applying these correlations to ordered packings at the same Reynolds number generally overpredicts the pressure drop due to the more tortuous fluid paths in random beds [10, 17].
2. The bed to pebble diameter ratio d_{bed}/d_p ; friction exists due to both the solid pebbles and the containing wall, and the extent to which the wall friction contributes to the overall bed pressure drop depends on the d_{bed}/d_p ratio. When $d_{\text{bed}}/d_p < 10$, wall effects can constitute a significant portion of the flow, and whether the overall pressure drop is higher or lower than that of an infinite bed depends on two competing factors [31]: 1) The lower porosity at the wall *reduces* friction due to the lower number of flow obstructions, and 2) The presence of the wall *increases* friction, analogous to flow in a pipe. The factor that dominates depends on the Reynolds number. For low Reynolds number, the boundary layer on the wall is relatively thick such that the viscous drag is most significant. For high Reynolds number, the boundary layer is so thin that the high porosity effect dominates. This means that, for small d_{bed}/d_p , the viscous drag is greater for low Reynolds numbers, while the kinetic drag is lower for high Reynolds numbers. Section 9.1.1 provides correlations that neglect dependence on d_{bed}/d_p that can be used for the majority of beds as shown in Table 15, while Section 9.1.2 provides correlations that account for d_{bed}/d_p , and should be used for relatively narrow beds.
3. Pebble diameter; both \mathcal{D} and \mathcal{F} decrease with larger pebble diameters in the laminar regime due to wall effects, since the velocity peak extends further into the bed. However, in the turbulent regime, such drag reduction effects may not be observed because turbulence enhances mixing to the point that the wall effect is less significant [40].
4. Porosity; pressure drop tends to decrease linearly with porosity. For example, a 1% change in the porosity in the Ergun correlation will produce a 10% change in the pressure drop [95].
5. Pebble surface roughness; in practice, this dependence is negligible, and hence roughness is neglected in all pebble bed correlations shown in this section. However, surface roughness could be taken into account via the calculation of the pebble surface area in Eq. (2.204).
6. Prandtl number; few friction factor correlations are a function of Prandtl number, but because inertial forces dominate the total pressure drop for Reynolds numbers typical of reactor conditions, high Prandtl number fluids will be characterized by less vortices. Most of the correlations in this section were developed for fluids with Prandtl numbers on the order of 1, and the use of these correlations for higher Prandtl number fluids will generally overpredict the pressure drop [10].

The correlations presented in this section have primarily been developed for isothermal straight channel flow, and may not be valid for converging/diverging geometries or combined axial and cross flow in high-temperature-gradient conditions. In addition, all of the correlations discussed in this section have been obtained using bed-average values of velocity, porosity, and thermophysical properties. Despite these correlations representing global friction coefficients, it is assumed that these correlations are *locally* valid such that local values of system parameters, rather than medium-averaged values, are used [24, 35, 37, 38]. In this heuristic approximation, squares of velocity are transformed to

$|\vec{v}| \vec{v}$ [37]. Caution should be taken with the particular drag correlation used, since many are not valid up to $\varepsilon = 1$. The range of validity may require the use of a different porosity profile.

The strong dependence of the pressure drop on porosity causes a flow channeling effect near the walls of the core where the porosity is high. This strong bypass flow is not treated consistently among experimentalists, and is likely the main source of scatter among the correlations discussed in this section [67]. If the bypass flow isn't taken into account, then the superficial velocity will be larger than the actual local values, giving a smaller friction coefficient.

The pressure drop per unit length tends to be approximately constant over the core for reactor systems [7, 10, 48], with the total pressure drop being on the order of 0.06-0.3 MPa for gas-cooled systems [36, 48, 81] and 0.06 kPa for salt-cooled systems [11]. The magnitude of the pressure drop depends on the flow profile, as partial or full radial flow substantially reduces the pressure drop [11, 84].

9.1.1 Friction Coefficients Independent of the Wall

This section contains friction coefficient correlations that don't account for wall effects on the whole-bed solution. Fig. 11 shows a comparison of the many friction factor correlations available in the literature that fall into this category. As can be seen, there is considerable spread among these correlations, which is partially explained by the use of different d_{bed}/d_p ratios.

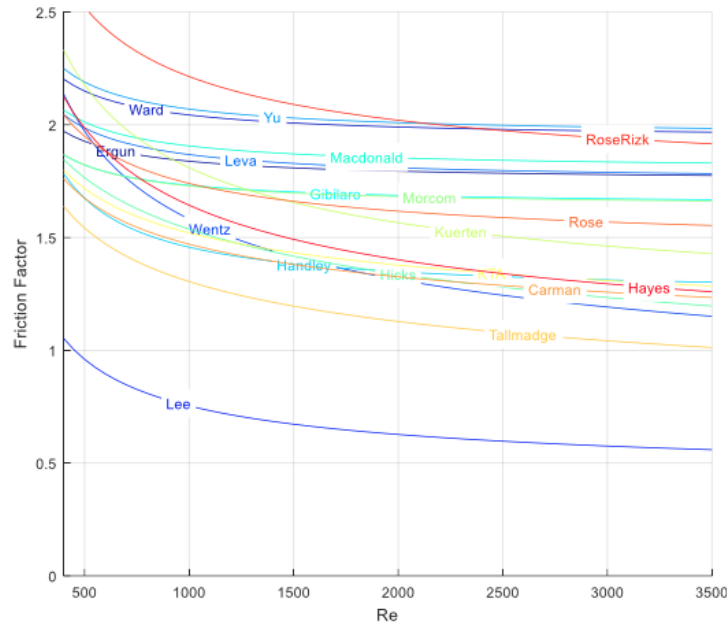


Figure 11: A comparison of the friction factor computed from the many available correlations for pebble beds that do not account for the presence of the bounding wall [95].

9.1.1.1 ErgunDragCoefficients

Based on the proportionalities shown in Eqs. (2.143) and (2.144), the simplest friction factor correlation can specify constant proportionalities A and B for each of the contributions to the total pressure drop:

$$\varepsilon \nabla P = -A \frac{(1-\varepsilon)^2}{d_p^2 \varepsilon} \mu \vec{V} - B \frac{1-\varepsilon}{d_p} \rho_f |\vec{V}| \vec{V} \quad (9.1)$$

Ergun analyzed a wide variety of experimental data and concluded that $A = 150$ and $B = 1.75$ most accurately represents the data. From theoretical grounds, however, there is no reason to expect that A and B are universal constants, and assigning any constant value simply represents a best fit to data. Ergun's correlation covers the range of Reynolds numbers up to fully turbulent flow, and is valid for $0.08 < Re_k < 196$ and a wide variety of porosities and particle shapes [28]. This correlation has been supported by a great deal of experimental validation; 92 out of 98 data sets correlated with an r -value greater than 0.9 when correlated with an Ergun-type equation [30–32]. Ergun's correlation is the most commonly-used friction factor correlation for pebble beds, and it is the correlation used in TRACE [95]. There is disagreement on whether this correlation predicts the pressure drop well for HTGRs - Seker et. al recommend Eq. (9.4), while Becker et. al find no difference in temperatures and velocities when using Eq. (9.1) versus Eq. (9.4) [81, 96].

Other researchers have proposed different proportionality constants A and B in Eq. (9.1). For example, Macdonald concluded that a better fit could be obtained with $A = 180$ and B in the range of 1.8 (smooth particle) to 4.0 (very rough particle) [29]. This dependence of B on particle roughness fits with the analogy of internal pipe flow, though others have contradicted any dependence of B on roughness [31]. So, while Ergun's correlation with constant coefficients provides only one curve, in reality there may be many curves at higher Re , dependent on the surface roughness. For at least one data set, it appeared that A and B are not actually constant, but have weak variation on porosity, where A was better fit proportional to $\varepsilon^{-5.5}$ rather than $(1 - \varepsilon)^2/\varepsilon^3$. However, MacDonald also suggests that the pressure drop is rather insensitive to the values of the coefficients - varying A and B by $\pm 25\%$ did not lead to substantial differences in the overall pressure drop. Based on this analysis, and because Macdonald's correlation shown in Fig. 11 is not very different from Ergun's correlation, Ergun's correlation is implemented in Pronghorn using $A = 150$ and $B = 1.75$.

9.1.1.2 PiecewiseLinearDragCoefficients

Several researchers have developed correlations for drag coefficients that are piecewise-linear in Reynolds number, where one correlation is to be used in the Forchheimer regime, and the other in the fully turbulent regime. In other words, the A and B that appear in Eq. (9.1) are different based on the flow regime. Fand et. al developed a piecewise correlation based on beds of both uniform- and mixed-diameter spheres [40]:

$$\mathcal{D}_{fand} = \begin{cases} 182 \frac{(1-\varepsilon)^2}{d_p^2 \varepsilon} \mu & 5 < Re < 80 \\ 225 \frac{(1-\varepsilon)^2}{d_p^2 \varepsilon} \mu & Re \geq 120 \end{cases} \quad (9.2)$$

$$\mathcal{F}_{fand} = \begin{cases} 1.92 \frac{1-\varepsilon}{d_p} & 5 < Re < 80 \\ 1.61 \frac{1-\varepsilon}{d_p} & Re \geq 120 \end{cases} \quad (9.3)$$

In order to implement the Fand correlation numerically, the entire range of Reynolds numbers must be covered. It is assumed that the Forchheimer regime is extended to cover the range from zero Reynolds number to the Reynolds number at which the flow enters the transitional regime. On the lower spectrum, it is assumed that the inertial forces are always present, such that the Darcy-Forchheimer relationship in Eq. (2.148) extends to zero Reynolds number as well. This is a very good approximation that is supported by least-squares analysis performed by MacDonald that shows that uncertainty in computed values of B in Eq. (9.1) has negligible impact on the computed drag in the viscous-dominated regime [29]. Linear interpolation is performed within this transitional regime since most authors do not provide a correlation describing the transitional regime.

9.1.1.3 KTADragCoefficients

KTA developed an empirical correlation for the pressure drop in pebble bed reactors that is widely used in nuclear applications [42]:

$$\epsilon \nabla P = \Psi \frac{1-\epsilon}{2d_p} \rho_f |\vec{V}| \vec{V} \quad (9.4)$$

where Ψ is defined as:

$$\Psi = 320 \left(\frac{Re}{1-\epsilon} \right)^{-1} + 6 \left(\frac{Re}{1-\epsilon} \right)^{-0.1} \quad (9.5)$$

This correlation is valid for $1 < Re_h < 10^5$, $0.36 < \epsilon < 0.42$, d_{bed}/d_p above a limiting curve provided in [42], and the height of the bed being at least five times greater than the pebble diameter. The lower the Reynolds number, the greater the diameter of the bed required to use Eq. (9.4); at low Reynolds number, the magnitude of the velocity peak at the walls is very large, and a strong bypass flow develops that for higher Reynolds number flows would be more smeared. From the curve in [42], for $Re_h = 1$ the bed must be roughly 35 pebbles wide.

The fluid viscosity should be determined at the average of the fuel surface temperature and the fluid temperature. Beyond about $Re_h = 10^5$, the pressure drop becomes independent of Re_h [67], which agrees in approximate order of magnitude with values reported by [31].

9.1.2 Friction Coefficients Dependent on the Wall

This section contains friction coefficient correlations that account for the bed to particle diameter ratio d_{bed}/d_p . These correlations are only required for relatively narrow beds, i.e. $d_{\text{bed}}/d_p < 10$. While the pebble discharge/fueling tubes are typically narrow, because the neutron flux is usually intentionally small to avoid damage to fueling components [11, 15], using correlations in Section 9.1.1 will likely not produce a significant modeling error. But, temperatures can be large if fueling tubes are fed by high-temperature coolant such as near the core outlet, in which case the use of correlations in this section may be more important. For a given infinite medium porosity, Fig. 12 shows the friction factor computed using the Einfeld correlation as a function of the bed to pebble diameter.

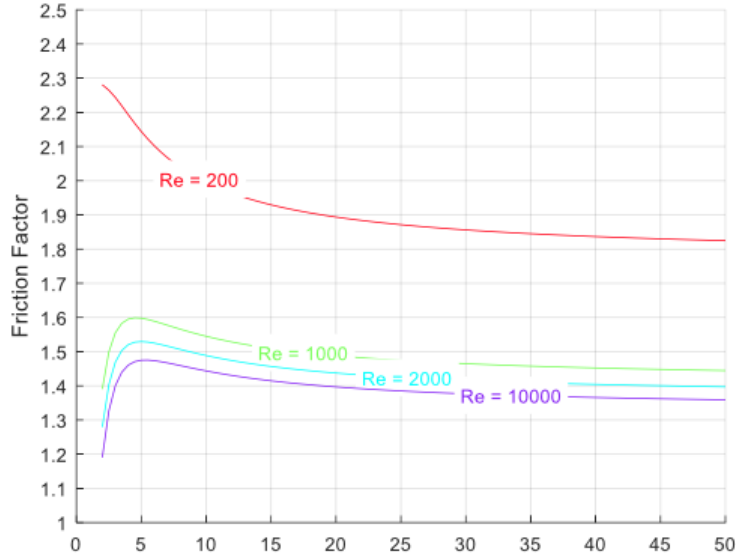


Figure 12: A comparison of the friction factor computed using the Einfeld correlation as a function of the bed to pebble diameter [95].

9.1.2.1 EinfeldDragCoefficients

Einfeld correlated experimental data using an Ergun-type correlation [31]:

$$\mathcal{D}_{einfeld} = 154A_w^2 \frac{(1-\epsilon)^2}{\epsilon d_p^2} \mu \quad (9.6)$$

$$\mathcal{F}_{einfeld} = \frac{A_w}{B_w} \frac{1-\epsilon}{d_p} \quad (9.7)$$

where A_w and B_w represent modified Ergun-type drag coefficients:

$$A_w = 1 + \frac{2}{3 \frac{d_{bed}}{d_p} (1-\epsilon)} \quad (9.8)$$

$$B_w = \left[1.15 \left(\frac{d_p}{d_{bed}} \right)^2 + 0.87 \right]^2 \quad (9.9)$$

This correlation is valid for $0.01 < Re < 17365$, $1.6 < d_{bed}/d_p < 250$, and $0.33 < \epsilon < 0.882$. This correlation gives a lower Root Mean Square (RMS) deviation than correlations that do not account for the bounding wall. The Einfeld correlation is used in TRACE when the bed to particle diameter ratio is sufficiently small [95].

9.2 Pipe Flow Correlations

This section presents correlations for friction factors to be used for pipe flow. Unlike the correlations presented in Section 9.1, the correlations in this section must be anisotropic to reflect the fact that there is a preferred flow direction.

Pipe flow friction correlations typically bundle the friction and kinetic drag components into a single term that is often very difficult or analytically impossible to detangle into separate \mathcal{D} and \mathcal{F} , so all correlations in this section simply present W , rather than its individual components.

9.2.1 ChurchillDragCoefficients

Churchill combined several correlations for laminar, transitional, and turbulent flow to obtain a correlation valid for all Re and relative pipe surface roughness ε_{pipe}/D [97]:

$$W = \frac{\varepsilon \|\vec{V}\|_2}{2D} \left[\left(\frac{8}{Re} \right)^{12} + \frac{1}{(A_c + B_c)^{3/2}} \right]^{1/12} \quad (9.10)$$

where the factor of $\varepsilon \|\vec{V}\|_2 / 2D$ appears in order to use this friction factor to represent $\varepsilon \nabla P$, and A_c and B_c are defined as:

$$A_c = \left\{ 2.457 \ln \left[\frac{1}{\left(\frac{7}{Re} \right)^{0.9} + 0.27 \frac{\varepsilon_{pipe}}{D}} \right] \right\}^{16} \quad (9.11)$$

$$B_c = \left(\frac{37530}{Re} \right)^{16} \quad (9.12)$$

10 Heat Transfer Coefficients

This section describes the correlations available for calculating heat transfer coefficients. The emphasis is placed entirely on beds of spherical particles, so none of the correlations shown in this section should be used for plate or prismatic solid geometries. These correlations were obtained specifically for beds of randomly-packed pebbles; application of these correlations to ordered packings generally results in overprediction of the Nusselt number for an ordered packing at the same porosity [10].

Heat transfer coefficient closure laws are required to describe the solid-to-fluid within-bed heat transfer and the bed-to-wall heat transfer that occurs at the edges of the core. The within-bed heat transfer is represented by α , while the bed-to-wall heat transfer coefficient is represented by α_w . α appears directly in the fluid and solid energy equations, while α_w appears in convection BCs on the bed fluid phase. Because α appears within the volumetric conservation equations, it must be multiplied by the specific surface area a_w in Eq. (2.205).

The convective heat transfer is about two times lower in the entrance region of a packed bed than for an average bed location because the turbulence and boundary layers are smaller [67]. This difference between observed and predicted heat transfer is more significant for larger Reynolds numbers. However, other researchers have shown substantial improvements in heat transfer in the entrance region. Ferng et. al show that α in the first pebble layer is nearly double that in the bulk of the bed; α decreases over the first six to seven pebble layers as the flow becomes thermally fully-developed [14]. Song et. al show that Nu is about 20% higher in the entrance region than the bulk bed value for BCC lattices; the lack of a significant entrance effect for an FCC configuration suggests this effect may be packing structure-dependent [10]. These apparent disagreements need to be further investigated, but most of the correlations discussed in this section do not take this account into effect.

10.1 Pebble Bed Correlations

This section discusses heat transfer coefficient correlations available for modeling beds of spherical pebbles. The techniques to measure the heat transfer coefficient in pebble beds include:

1. Heat transfer from an electrically-heated sphere in an unheated packing; if mixing effects and conduction between spheres are small, this can yield accurate measurements of the convection coefficient. The Nusselt number may be over-predicted by an order of magnitude at low Reynolds number if the spheres contacting the single heat sphere are not of low thermal conductivity [67].
2. Mass transfer tests; analogies between heat and mass transfer allow experiments at extremes in dimensionless numbers that would be difficult to obtain using heat transfer. Mass transfer tests typically use spheres coated in naphthalene, which undergoes sublimation in air. This eliminates most heat transfer modes due to a negligible temperature difference between the solid and the fluid. However, the object's temperature must still be known accurately since it has a strong impact on the vapor pressure of naphthalene.
3. Regenerative heating (unsteady heating)

In the limit of $Re \rightarrow 0$ for a single sphere surrounded by fluid, it can be shown that $Nu = 2$. Many of the correlations shown in this section include this limiting behavior. However, some authors argue that using a limiting Nu only applies for a single sphere, and not for *beds* of spheres [19].

In a spherical coordinate system, conduction in a constant thermal conductivity fluid surrounding a sphere is dictated by:

$$\frac{k}{r^2} \frac{\partial}{\partial r} \left(r^2 \frac{\partial T}{\partial r} \right) = 0 \quad (10.1)$$

Solving this equation with the BCs $T(R) = T_o$ and $T(r \rightarrow \infty) = T_\infty$ gives:

$$T(r) = \frac{R(T_o - T_\infty)}{r} + T_\infty \quad (10.2)$$

Matching the heat flux at R with the convection heat flux gives:

$$k \frac{R(T_o - T_\infty)}{R^2} = h(T_o - T_\infty) \quad (10.3)$$

Because $D = 2R$, solving the above for hD/k gives $Nu = 2$ for a sphere in stagnant fluid.

Heat transfer coefficient correlations for packed beds either average or explicitly account for the dependence on porosity. α decreases approximately linearly with porosity, though with a weaker dependence on porosity than the friction coefficients discussed in Section 9. A 1% change in the infinite medium porosity gives about 3% change in the fluid-pebble heat transfer coefficient. In the center of the bed, correlations that do not account for porosity variation could be used with relatively minor error. However, towards the edges of the bed where porosity is very high, there are two competing effects:

1. A less tortuous fluid path due to the higher porosity reduces α .
2. The higher-velocity wall bypass flow increases α .

Whether α is overall higher or lower at the edges of the bed depends on how ϵ and V change relative to one another.

10.1.1 Correlations Independent of Porosity Variation

This section provides several heat transfer coefficient correlations that do not directly account for the bed porosity. Fig. 13 shows a comparison of several of the most common of these heat transfer coefficients.

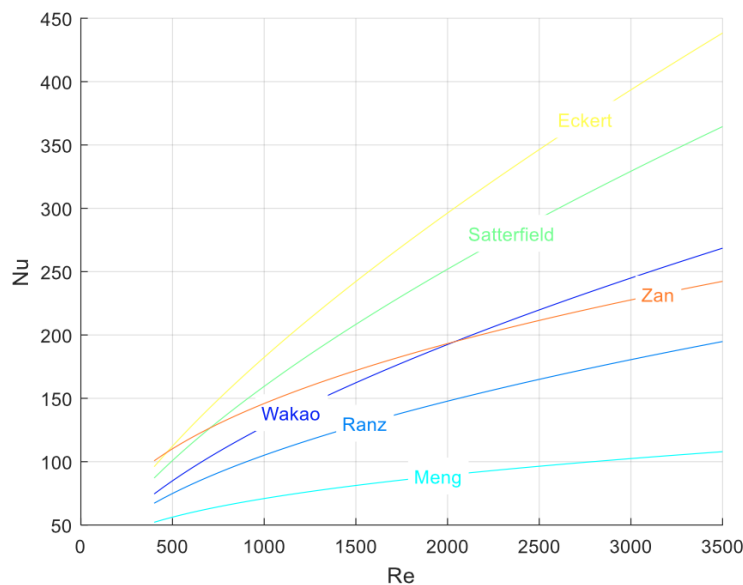


Figure 13: A comparison of the Nusselt number computed using a variety of common porosity-independent heat transfer coefficients [95].

10.1.1.1 WakaoPebbleBedHTC

The Wakao correlation can be obtained by mass-heat analogy [98]:

$$Nu = 2 + 1.1Pr^{1/3}Re^{0.6} \quad (10.4)$$

This correlation is valid for $15 \leq Re \leq 8500$ and $\epsilon = 0.4$. At lower Re , the correlation slightly under predicts experimental data.

10.1.2 Correlations Dependent on Porosity Variation

This section provides several heat transfer coefficient correlations that explicitly depend on porosity, and hence are capable of modeling wall effects provided using a globally-determined correlation for local effects is valid. Researchers have assumed validity for friction coefficient correlations generated on a global basis - the same validity is assumed here for heat transfer coefficients. Fig. 14 shows a comparison of several of the most common of these heat transfer coefficient correlations.

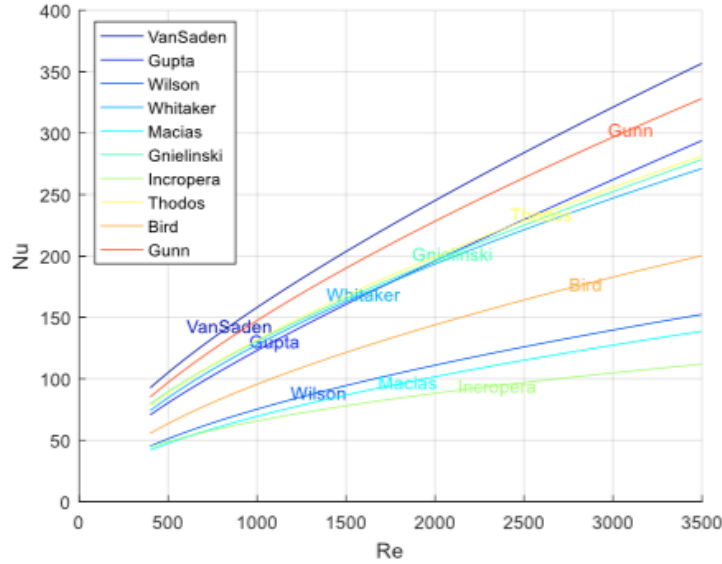


Figure 14: A comparison of the Nusselt number computed using a variety of common porosity-dependent heat transfer coefficients [95]. “VanSaden” corresponds to the KTA correlation.

10.1.2.1 GnielinskiPebbleBedHTC

Gnielinski developed a semi-empirical correlation by introducing the appropriate length (d_p) and velocity scales (\vec{V}) to transform the heat transfer from a flat plate to flow around spherical particles [67]:

$$Nu = [1 + 1.5(1 - \epsilon)] \left(2 + \sqrt{Nu_{lam}^2 + Nu_{turb}^2} \right) \quad (10.5)$$

$$Nu_{lam} = 0.664Re_i^{0.5}Pr^{1/3} \quad (10.6)$$

$$Nu_{\text{turb}} = \frac{0.037Re_i^{0.8}Pr}{1 + 2.443Re_i^{-0.1}(Pr^{2/3} - 1)} \quad (10.7)$$

This correlation is valid for $Re_i \leq 7.7 \times 10^5$, $0.7 \leq Pr \leq 10^4$, and $0.26 \leq \varepsilon \leq 0.935$. The Gnielinski correlation matches experimental data fairly well at high Re , but may over predict at low Re . This correlation was experimentally verified by Achenbach using a single heated sphere in an unheated packing [67].

10.1.2.2 KTAPebbleBedHTC

KTA proposed the following correlation for pebble bed reactors [99].

$$Nu = 1.27 \frac{Pr^{1/3}Re^{0.36}}{\varepsilon^{1.18}} + 0.033 \frac{Pr^{0.5}Re^{0.86}}{\varepsilon^{1.07}} \quad (10.8)$$

This correlation is used in TRACE and PEBBED [95]. This correlation is valid for $100 \leq Re \leq 10^5$, $0.36 < \varepsilon < 0.42$, and a bed height greater than four times the pebble diameter. If plane-averaged values of the porosity are used, then the bed diameter must be 20 times greater than the pebble diameter. Because it is assumed that this correlation uses local values, this restriction does not apply. The material properties of the gas should be evaluated at the mean value of the pebble surface temperature and the gas temperature. For the first layer of pebbles, Eq. (10.8) should be halved to account for poorer heat transfer due to entrance effects.

10.2 Wall-to-Fluid Correlations

This section presents correlations for α_w , which captures heat transfer between the bed and a solid wall. This heat transfer mode is represented by the green lines in Fig. 16. This heat transfer occurs through the thermal boundary layer, which is generally much smaller than the pebble diameter. For turbulent flows, most heat is transferred by the fluid to the wall, rather than by the solid to the wall, since the solid thermal conductivity was found to not have a significant impact on the wall heat transfer coefficient (provided the system is isothermal) [100]. For this reason, convection heat transfer could be approximated as only occurring between the bed fluid and the containing wall.

The thermal boundary layer's impact on heat transfer to the wall is most important for high Prandtl number fluids, since these fluids have relatively small thermal boundary layers that are nearly fully-contained within the momentum boundary layer [37]. For these cases, using only bulk correlations for the heat transfer coefficient will give very inaccurate results.

The heat flux from the wall to the pebbles is not smoothly-varying, as it is a strong function of the pebble-scale flow behavior. Fig. 15 shows the (a) velocity vectors, (b) conceptual diagram of flow paths, and (c) heat flux from a wall to a pebble bed [5]. Nijemeisland and Dixon found that the heat flux was highest at the pebble-wall contact areas, and lowest at the vortices that form on the back sides of pebbles and in regions where flow paths join.

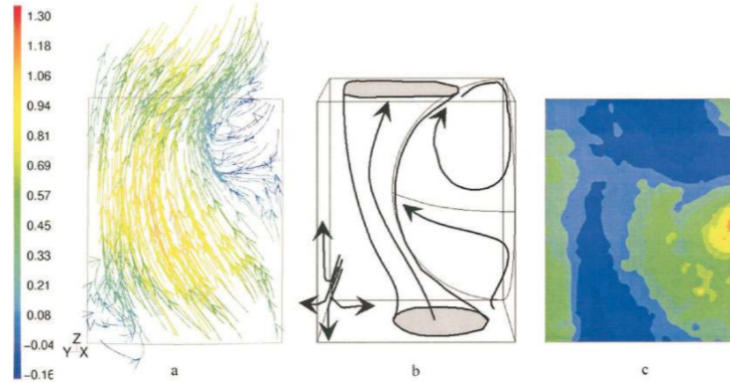


Figure 15: A unit cell for comparing (a) velocity vectors, (b) conceptual flow field diagram, and (c) heat flux from a cylindrical wall to a pebble bed [5].

10.2.1 AchenbachPebbleBedWallHTC

Using the mass-heat analogy with naphthalene sublimation experiments [67]:

$$Nu = \left(1 - \frac{d_p}{d_{bed}}\right) Re^{0.61} Pr^{1/3} \quad (10.9)$$

This correlation is valid for $50 < Re < 2 \times 10^4$. This correlation cannot be extended to lower Re because at that point diffusion becomes substantially more important than convection, causing the thermal boundary layer thickness to be of the order of the pebble diameter.

10.2.2 WakaoPebbleBedWallHTC

Using heat and mass transfer experiments, Yagi and Wakao developed a correlation for bed-to-wall heat transfer based on Reynolds number, but due to an insufficient range in Prandtl numbers, a typical heat transfer correlation in terms of both Reynolds and Prandtl numbers could not be obtained. By comparing results with the heat transfer from a flat plate recommended by Colburn, good agreement was reached with their correlation by replacing the distance along the plate x by the pebble diameter [100]:

$$Nu_{wall} = 0.036 Pr^{1/3} Re^{0.8} \quad (10.10)$$

The pebbles essentially act to break up an otherwise continuous wall boundary layer, and hence the boundary layer likely never becomes fully-developed at the wall. By using a shortened characteristic length (the pebble diameter), this break-up effect is approximately captured.

11 Effective Solid Thermal Conductivity κ_s

The effective solid thermal conductivity κ_s is used in lieu of k_s in the solid heat diffusion kernel because conduction in a pebble bed is impacted by the presence of the two mixed phases. Conduction occurs both within a single pebble, and *between* pebbles at contact points and across solid voids (fluid regions) by radiation and fluid conduction. These additional heat transfer mechanisms are not present in a filled solid ($\epsilon = 0$) because regions of the solid cannot “see” each other across fluid regions and heat is not restricted to flow between solid regions at solid contact zones. Fig. 16 depicts the various heat transfer mechanisms that are represented by κ_s , in addition to several other heat transfer processes that are discussed in other sections of this manual.

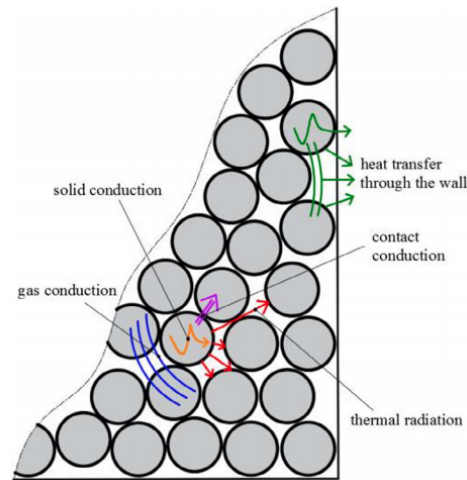


Figure 16: Various heat transfer processes in a pebble bed [92].

κ_s consists of three components -

1. Conduction in a pebble and radiation between pebbles across a transparent fluid. This is represented by the orange and red lines in Fig. 16, and is denoted as $\kappa_{\text{radiation}}$.
2. Conduction in a pebble and conduction in the fluid between pebbles. This is represented by the orange and blue lines in Fig. 16, and is denoted as $\kappa_{\text{fluid conduction}}$.
3. Conduction in a pebble and conduction between pebbles at contact areas. This is represented by the orange and pink lines in Fig. 16, and is denoted as $\kappa_{\text{solid conduction}}$.

All three of these processes occur in “stagnant” beds, where the fluid is stationary. For this reason, κ_s is often referred to as the “stagnant” effective thermal conductivity. The green lines in Fig. 16 represent heat transfer between the packed bed and the wall, and is discussed in Section 10.2. Not shown in Fig. 16 is the heat transfer path described by conduction within a pebble and convection in the fluid. This heat transfer path can be neglected at all values of Reynolds number [101], though some authors suggest that this assumption is not valid for pore spaces on the order of several centimeters, which is generally the pore size for nuclear reactor applications [90].

κ_s is the primary constitutive relationship that captures heat transfer mechanisms in loss of coolant accidents when convective cooling becomes negligible. Accurate correlations are essential to the prediction of decay heat removal in such accidents. Using slightly different correlations for κ_s shows temperature differences on the order of 75°C for some of the SANA benchmark cases [55] and 25°C for a gas-cooled reactor system [81].

The correlations discussed in the next sections are often provided in terms of the solid-to-fluid conductivity ratio, defined here for convenience:

$$\lambda = \frac{k_s}{k_f} \quad (11.1)$$

Representative thermal conductivities for several common reactor materials are given in Table 16. k_s decreases with temperature for nuclear-grade graphite [102]. Because the thermal conductivity of gases has a very small pressure dependence, the Thorium High Temperature Reactor (THTR) results also apply for the High Temperature Reactor Power Module (HTR-PM) reactor, though the HTR-PM operators at 7 MPa [21].

Table 16: Representative k_s for common reactor materials at operating conditions. The solid material is assumed to be 100 °C higher than the fluid [2]. The graphite k is averaged over several different types of nuclear graphite [102].

Reactor	Solid	Fluid	P (MPa)	T_f (C)	k_s (W/m·K)	k_f (W/m·K)	λ
PBMR [103]	graphite	helium	8.4	500/900	100/70	0.31/0.41	323/171
PB-FHR [3]	graphite	flibe	0.1	600/700	90/80	1.07/1.12	84/71
THTR [75]	graphite	helium	3.9	250/750	115/75	0.23/0.37	500/203

Because different heat transfer modes in beds can be isolated from one another, most literature provides correlations for only one component of κ_s at a time. In the Pronghorn input file, the user selects which correlation to use for each component of κ_s separately. In addition, a correction treatment is frequently applied in the vicinity of walls, where a different correlation is used [36].

The combination of BreitbachBarthels, ZBS, and ChanTien correlations for the radiation, fluid conduction, and solid conduction components, respectively, matches the model used in THERMIX [104]. There are several sources that provide semi-empirical correlations for κ_s in entirety; these are the focus of the next section.

11.1 Models for κ_s

This section presents models for all three combined heat transfer paths that comprise κ_s . These combined models are separated into distinct components that are then discussed in Sections 11.2, 11.3, and 11.4.

A good model for κ_s should obey certain logical limits in porosity, k_s , and k_f . For example, as porosity goes to zero or unity, κ_s should tend towards k_s and k_f , respectively. Many correlations for κ_s developed do not meet all of these criteria - only the Zehner and Bauer correlation discussed in Section 11.1.2 meets these criteria, and as such this model has been recommended for use [90]. However, in order to provide some intuition on how κ_s might vary with other system parameters that may not be obvious from a complicated correlation, several rudimentary models are first discussed in Section 11.1.1.

11.1.1 Parallel and Series Heat Transfer

The most rudimentary formulation would simply be a volume average of the fluid and solid thermal conductivities:

$$\kappa_s = \epsilon k_f + (1 - \epsilon)k_s \quad (11.2)$$

Eq. (11.2) is equivalent to assuming heat transfer occurs in parallel between the two phases. Alternatively, series

heat transfer could also be assumed:

$$\frac{1}{\kappa_s} = \frac{\varepsilon}{k_f} + \frac{1-\varepsilon}{k_s} \quad (11.3)$$

Eqs. (11.2) and (11.3) provides bounds on the actual κ_s of the medium, with series heat transfer representing the minimum (all heat must eventually pass through the lower-conducting phase) and parallel heat transfer the maximum (the low-conducting phase can be bypassed). Because no parameters related to radiation heat transfer or contact conduction area appear, Eq. (11.2) and Eq. (11.3) can be interpreted as a very rudimentary models for $\kappa_{\text{fluid conduction}}$. Eq. (11.2) and (11.3) would also in principle be used to calculate κ_f .

Some authors simply use linear combinations of Eqs. (11.2) and (11.3), with a recommended value of 20% of the heat occurring in series [90]. Many early researchers, such as Maxwell and Lord Rayleigh, provide analytical correlations, but these are rather limited in applicability and often did not consider the radiation or contact area conduction components of κ_s [90, 105]. Hence, none of these simpler models will be described further here.

11.1.2 Zehner, Bauer, and Schlunder

The Zehner, Bauer, and Schlunder correlation gives κ_s as [90, 92]:

$$\kappa_s = \varepsilon k_f (1 - \sqrt{1 - \varepsilon}) \left([\varepsilon - 1 + 1/\mathcal{K}_D]^{-1} + \mathcal{K}_R \right) + k_f \sqrt{1 - \varepsilon} (\varphi \lambda + (1 - \varphi) \mathcal{K}_{SF}) \quad (11.4)$$

where φ is the contact area fraction, also known as the deformation ratio. \mathcal{K}_D represents a modified gas thermal conductivity that accounts for Knudsen effects when the mean free path of the fluid is on the order of the pebble diameter:

$$\frac{1}{\mathcal{K}_D} = 1 + \frac{\tilde{\lambda}_{mfp}}{d_p} \quad (11.5)$$

where $\tilde{\lambda}_{mfp}$ is a modified mean free path, which can be calculated according to [90]. The mean free path is much smaller than d_p for Pronghorn's application space, so to a good approximation, $\mathcal{K}_D = 1$. This approximation is performed for Eqs. (11.14) and (11.22). \mathcal{K}_{SF} represents the complicated conduction-radiation and conduction-conduction processes that occur between the solid and fluid phases:

$$\mathcal{K}_{SF} = \frac{2}{a} \left[\frac{B(\lambda + \mathcal{K}_R - 1)}{a^2 \lambda \mathcal{K}_D} \ln \frac{\lambda + \mathcal{K}_R}{B(\mathcal{K}_D + (1 - \mathcal{K}_D)(\lambda + \mathcal{K}_R))} \right] + \frac{2}{a} \left[-\frac{B-1}{a \mathcal{K}_D} + \frac{B+1}{2B} \left(\frac{\mathcal{K}_R}{\mathcal{K}_D} - B \left\{ 1 + \frac{1 - \mathcal{K}_D}{\mathcal{K}_D} \mathcal{K}_R \right\} \right) \right] \quad (11.6)$$

where B is given by

$$B = C \left(\frac{1 - \varepsilon}{\varepsilon} \right)^m \quad (11.7)$$

For the case where Eq. (11.4) is simplified to represent only the fluid conduction component (by setting $\mathcal{K}_R = 0$ and $\varphi = 0$), Zehner and Schlunder recommend $C = 1.25$ and $m = 10/9$ to exactly fit the geometrical constraint on the shape factor B , but Hsu by a least squares procedure determined $C = 1.364$ and $m = 1.055$ better match the geometrical

constraint. However, when all three components are considered, Hsu argues that the values for C and m in Eq. (11.7) should be modified [106]. Hsu provides graphical data for computing C and m as a function of the deformation ratio, but because the deformation does not change appreciably for pebble bed designs of practical interest, the constant values of $C = 1.25$ and $m = 10/9$ are used [92, 106].

a is defined as:

$$a = \left[1 + \frac{\mathcal{K}_R - B\mathcal{K}_D}{\lambda} \right] \frac{1}{\mathcal{K}_D} - B \left(\frac{1}{\mathcal{K}_D} - 1 \right) \left(1 + \frac{\mathcal{K}_R}{\lambda} \right) \quad (11.8)$$

The contact area fraction ϕ has commonly been specified in the literature in terms of empirical values or graphical data that do not correlate well with the wide variety of porosities encountered [92, 106]. ϕ is on the order of 0.01-0.001 for most systems of practical interest [90]. $d_c/d_p \approx 0.002$ is a good constant approximation [92]. You et. al. provide equations for ϕ using elastic deformation theory, though ϕ can only be approximated, since it is affected by the packing structure and surface roughness [92]. You et. al estimate ϕ as:

$$\phi = \frac{N_c}{4} \left(\frac{d_c}{d_p} \right)^2 \quad (11.9)$$

where N_c is the coordination number discussed in Section 8.2. Eq. (8.6) is used here to calculate N_c . Then, the same Hertz deformation theory as used in the Chan and Tien correlation discussed in Section 11.4.1 is used to calculate d_c/d_p as in Eq. (11.16) and the force F as in Eq. (11.20). \mathcal{K}_R is defined as [90]:

$$\mathcal{K}_R = 4\sigma \frac{1}{2/\epsilon_{r,s} - 1} T^3 \frac{d_p}{k_f} \quad (11.10)$$

where σ is the Stefan-Boltzmann constant and $\epsilon_{r,s}$ is the emissivity of the pebbles. A variety of other models have also been proposed for calculating \mathcal{K}_R [92]. In the present work, any of these other models can be used by simply setting $\mathcal{K}_R = 0$ in Eq. (11.4) and adding the radiative component separately.

Most experimental data points lie within $\pm 30\%$ of Eq. (11.4). These data points include solid-fluid suspensions and liquid-liquid emulsions, and hence the correlations is expected to be valid for transparent liquid-saturated beds, though original development focused on gas-saturated beds [90]. Eq. (11.4) is valid for essentially all values of porosity and $1 < \lambda < 2000$. However, Eq. (11.4) has critics, primarily related to the author's neglect to consider radiation heat transfer between distant parts of the bed. At the very high temperatures in HTGRs, this underpredicts κ_s , and many authors switch to different correlations above $\approx 1600^\circ\text{C}$ [107].

11.2 Models for $\kappa_{\text{radiation}}$

In Loss of Coolant Accident (LOCA) conditions, the radiation component is most significant due to the lack of fluid conduction and high temperatures ($\approx 2000\text{-}3000^\circ\text{C}$ in a fluid-stagnant HTR) [108]. In gas reactors, the radiation component tends to be the most significant even in normal operating conditions, at least until temperatures drop below about $300\text{-}400^\circ\text{C}$ [92, 104], though some have concluded otherwise, and neglected the radiation component [58]. Many of the correlations developed scale as $4\sigma T_s^3 d_p$, which demonstrates the increasing importance as temperature increases. In all of the correlations described in this section, it is assumed that the fluid is transparent to radiation; this is a good approximation for helium, but should always be investigated before application of these correlations to other fluids [14].

11.2.1 ZBS

Zehner and Schleunder developed an analytical expression based on a unit cell consisting of two half-spheres in contact (with conduction between the spheres) with simultaneous radiation exchange [108]. It was assumed that this unit cell is closed to radiation heat transfer from neighboring unit cells. All gas boundaries are assumed to be specular reflecting surfaces. The solid spheres were assumed to be opaque and have grey surfaces.

$$\kappa_{\text{radiation}} = \left[\frac{(1 - \sqrt{1 - \varepsilon})\varepsilon}{2/\varepsilon_{r,s} - 1} + \frac{\sqrt{1 - \varepsilon}}{2/\varepsilon_{r,s} - 1} \frac{B + 1}{B} \frac{1}{1 + \frac{1}{(2/\varepsilon_{r,s} - 1)\Lambda}} \right] 4\sigma T_s^3 d_p \quad (11.11)$$

$$\Lambda = \frac{k_s}{4\sigma T_s^3 d_p} \quad (11.12)$$

where B is given in Eq. (11.7). The first term represents direct radiation exchange (and can be obtained retaining the term with \mathcal{K}_R in Eq. (11.4) with Eq. (11.10) used for \mathcal{K}_R), while the second represents the combined radiation-conduction heat transfer. This correlation, applied to temperatures above its applicability range, under-predicts κ_s at high temperatures, which is expected based on the assumptions made that no radiation heat transfer occurs between other unit cells [108]. This model also does not function well with low solid emittance, since the assumption of the pebble interior having the same emissivity of the pebble surface is less accurate.

Vortmeyer followed a similar approach as Zehner and Schleunder, except that the geometry under consideration consisted of layers of unit cells. Using 1-D heat conduction solutions, where the layers of unit cells can communicate with each other, a more accurate correlation was obtained. This correlation, however, requires obtaining values for B from plots, and is hence more difficult to implement numerically [108].

11.2.2 BreitbachBarthels

Experiments performed with graphite pebble beds (high emittance) and ZrO_2 (low emittance) at temperatures up to 1000-1500 °C were used to experimentally validate corrections made to the Zehner and Schluender correlation given in Eq. (11.11) such that it can be applicable at high temperatures. For this improved derivation, the interior pebble surfaces are treated as black surfaces, instead of having the same emittance as the pebble surfaces:

$$\kappa_{\text{radiation}} = \left[(1 - \sqrt{1 - \varepsilon})\varepsilon + \frac{\sqrt{1 - \varepsilon}}{2/\varepsilon_{r,s} - 1} \frac{B + 1}{B} \frac{1}{1 + \frac{1}{(2/\varepsilon_{r,s} - 1)\Lambda}} \right] 4\sigma T_s^3 d_p \quad (11.13)$$

where Λ is given in Eq. (11.12).

11.3 Models for $\kappa_{\text{fluid conduction}}$

This section presents correlations used for $\kappa_{\text{fluid conduction}}$. Because the thermal conductivity of the solid phase is usually greater than that of the fluid phase for graphite-fueled systems, if Eq. (11.2) is used to provide a very rough estimate of $\kappa_{\text{conduction}}$, then $\kappa_{\text{conduction}}$ decreases with porosity, and will therefore be lowest near the walls of the bed.

11.3.1 ZBS

For a bed of spherical particles, the Zehner, Bauer, and Schlunder correlation discussed in Section 11.1.2 can be simplified to only consider the fluid conduction component by setting $\mathcal{K}_R = 0$ and $\varphi = 0$ in Eq. (11.4) [92, 105,

106, 109]. This correlation was experimentally validated by Prasad et. al using several combinations for fluids and beads [109]. This correlation predicts values close to the minimum predicted by series heat transfer in Eq. (11.3).

$$\kappa_{\text{fluid conduction}} = k_f \left\{ 1 - \sqrt{1 - \varepsilon} + \sqrt{1 - \varepsilon} \mathcal{K}_{SF} \right\} \quad (11.14)$$

$$\mathcal{K}_{SF} = \frac{2}{1 - B/\lambda} \left[\frac{B(1 - 1/\lambda)}{(1 - B/\lambda)^2} \ln \frac{\lambda}{B} - \frac{B - 1}{1 - B/\lambda} - \frac{B + 1}{2} \right] \quad (11.15)$$

11.4 Models for $\kappa_{\text{solid conduction}}$

In pebble-to-pebble contact, the contact area, contact roughness, and surface film contamination (especially if the surface is heavily oxidized) all have an impact on the conduction heat transfer. These three resistances to heat transfer occur in series. The correlations discussed in this section only address the contact area factor, which for spherical particles also tends to be the most important [110].

11.4.1 ChanTien

Chan and Tien developed a correlation for pebble-to-pebble heat conduction for hollow, solid, and solid-coated spheres in between two infinite plane surfaces at different temperatures. The diameter of the contact area between the spheres, d_c is given by the Hertz relation for elastic contact of two smooth, linearly elastic, solid spheres of radius d_p under collinear force F :

$$d_c = 2 \left(\frac{3}{4} \frac{1 - \nu^2}{E} F \frac{d_p}{2} \right)^{1/3} \quad (11.16a)$$

$$\frac{d_c}{d_p} = \left(\frac{3}{4} \frac{1 - \nu^2}{E} \frac{4F}{d_p^2} \right)^{1/3} \quad (11.16b)$$

where ν is the Poisson ratio of the solid and E the Young's modulus. This relationship is accurate provided $d_c \ll d_p$. It is assumed that the contact surface has a uniform heat flux and the remainder of the surface is insulated such that heat transfer only occurs through the contact area. The resistance to contact heat transfer is related to the resistance r_{th} within a single sphere with one contact point:

$$r_{th} = \frac{4\Delta T}{q_0 \pi d_c^2} \quad (11.17)$$

where q_0 is the constant heat flux through the contact area and ΔT is the temperature drop over the contact area. For other packing patterns where the sphere has more than two 180-degree-separated contact points, a modified thermal resistance can be defined by multiplying r_{th} by a geometrical factor. For the regular lattice structures considered, each sphere has the same contact pattern with its neighbors, so the resistance to conduction contact heat transfer for each should be the same. Hence, the effective thermal conductivity of the entire bed is given by:

$$\kappa_{\text{solid conduction}} = \frac{N_A}{N_L} \frac{1}{r_{th}} \quad (11.18)$$

where N_A and N_L are the number of spheres per unit area and length in the unit cell, respectively. It is assumed that each unit cell layer is isothermal such that contact points only touching *other* layers contribute to the heat transfer. By

assuming that the solution for a solid sphere is the same as that for a hollow sphere in the limit of the wall thickness going to the sphere radius:

$$\begin{aligned} \kappa_{\text{solid conduction}} &= \frac{k_s d_c}{2 \cdot 0.53} \frac{N_A}{N_L} \\ &= \frac{k_s}{0.53} \frac{N_A}{N_L} \left(\frac{3}{4} \frac{1 - \nu^2}{E} F \frac{d_p}{2} \right)^{1/3} \end{aligned} \quad (11.19)$$

where Eq. (11.18) was used to express the modified resistance to the resistance of a simple cubic arrangement and Eq. (11.16) is used to expand d_c . The force is given in terms of the pressure P exerted by the pebble weight:

$$F = S_F \frac{P}{N_A} \quad (11.20)$$

where S_F is a factor that relates the total force to the vertical component (the only component in which gravity is applied), since pebbles do not only contact each other along the vertical axis. The pressure is approximated as:

$$P(z) \approx (1 - \epsilon_\infty) \rho_s \mathcal{V}(z) |g_z| \quad (11.21)$$

where $\mathcal{V}(z)$ is the total volume above the z -plane on which the sphere lies (because *all* particles above a sphere exert a contact force on it), the factor $1 - \epsilon_\infty$ approximates the fraction of this volume that is solid, and $|g|$ is the magnitude of the gravitational acceleration in the direction of the force. Table 17 provides values of the coefficients appearing in the above correlations for the various packings investigated. Interpolation is performed between these values given the infinite medium porosity.

Table 17: Values appearing in the Chan and Tien correlation for various packing arrangements.

	Simple cubic	Body-centered cubic	Face-centered cubic
N_A	$\frac{1}{4R_p^2}$	$\frac{1}{2\sqrt{3}R_p^2}$	$\frac{3}{16R_p^2}$
N_L	$\frac{1}{2R_p}$	$\frac{\sqrt{3}}{2\sqrt{2}R_p}$	$\frac{\sqrt{3}}{2R_p}$
S_F	1	$\frac{1}{\sqrt{6}}$	$\frac{\sqrt{3}}{4}$
ϵ	0.48	0.32	0.26

11.4.2 ZBS

The Zehner, Bauer, and Schlunder correlation in Eq. (11.4) can be simplified to neglect the radiation component by setting $\mathcal{K}_R = 0$. Then, subtracting the fluid conduction component in Eq. (11.14) such that the correlation only provides the solid conduction component, the solid conduction component can be extracted [92, 106]:

$$\kappa_{\text{solid conduction}} = k_f \sqrt{1 - \epsilon} (\phi \lambda - \phi \mathcal{K}_{SF}) \quad (11.22)$$

where \mathcal{K}_{SF} is given by Eq. (11.15), B is given by Eq. (11.7), and ϕ is given by Eq. (11.9).

11.5 Variation of κ_s with System Parameters

This section provides a brief description of how κ_s varies with system parameters in order to aid the understanding of the correlations used and their expected impact on simulation results. In addition to a dependence on temperature, pressure, and λ , κ_s also depends on the pebble diameter and the dose. The larger the pebble diameter, the larger the radiation component, as more pebbles can “see” each other; this effect can be quite significant [92]. The higher the dose, the lower the solid thermal conductivity, which can reduce κ_s by about 20% at high temperatures [96].

Temperature

The three components of κ_s are individually plotted as a function of solid temperature in Fig. 17. κ_s increases exponentially with temperature. The radiation component is most significant at high temperatures because that component scales as T^3 . The contact component decreases with temperature because solid thermal conductivities generally decrease with temperature. Lastly, the fluid conduction component increases with temperature because fluid thermal conductivities generally increase with temperature. However, the variation of these two components with temperature is much smaller than the radiation component variation.

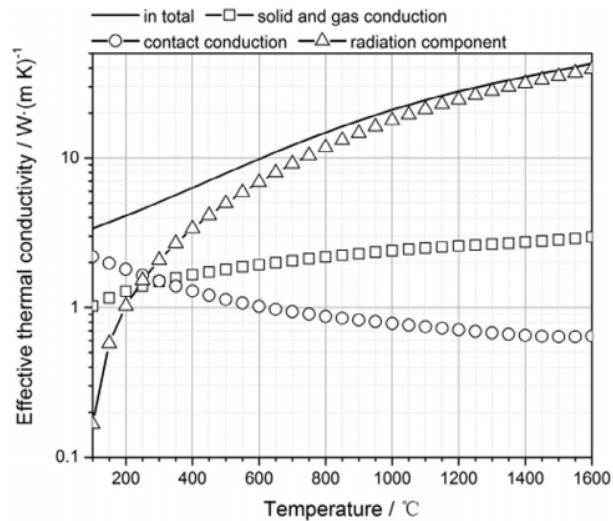


Figure 17: κ_s components as a function of temperature for the SANA experiments [92].

Pressure

Thermal conductivities of gases are independent of pressure. At atmospheric pressure and above, the mean free path of the fluid is much smaller than the characteristic dimension of a pebble bed, so the majority of the path lengths are computed according to collisions with other fluid molecules. When the path length of the fluid is very large, however, the path lengths are often lower in a porous media than in a fluid-only medium because fluid-solid collisions cause the path lengths to be reduced. At low pressures, on the order of 1000 Pa, the pressure dependence of κ_s begins to become evident. κ_s decreases with pressure reductions beginning around 1000 Pa. Because these pressures are much lower than those expected in reactor analysis, even under accident conditions, the pressure dependence of κ_s can be effectively neglected.

Solid to Fluid Thermal Conductivity Ratio λ

Using Eq. (11.2) as an approximate model for κ_s , holding k_f constant but varying k_s shows that as λ decreases, κ_s decreases. While λ increases, κ_s also increases. At the extremes of very small and very large λ , plateaus are reached in κ_s , with about an order of magnitude difference in the asymptotic values.

12 Effective Fluid Thermal Conductivity κ_f

The effective fluid thermal conductivity κ_f introduced in Eqs. (2.208) and (2.209) is used in lieu of the material property thermal conductivity of the fluid in the diffusive kernel because conduction within the bed is amplified by thermal dispersion (convection). The majority of porous media codes appear to neglect thermal dispersion, and simply approximate the decrease in conduction by the decrease in flow area:

$$\kappa_f = \epsilon k_f \quad (12.1)$$

Pronghorn currently also makes this assumption, though future work will involve the implementation of the thermal dispersion models discussed in this section. Because thermal dispersion acts to increase the diffusive effects, neglecting thermal dispersion is conservative in the sense that peak temperatures are often higher [81]. If only a single energy equation is used, a volume-average of k_s and k_f would be sufficient to a first-order approximation:

$$\kappa_f = \epsilon k_f + (1 - \epsilon)k_s \quad (12.2)$$

The emphasis in this section is on beds of spherical particles, and none of the correlations discussed in this section should be used for plate or prismatic solid geometries.

Thermal dispersion arises due to the secondary flow effects of mixing and recirculation of local fluid flows [54]. κ_f generally increases with Reynolds and Prandtl numbers. Many researchers have proposed correlations dependent on these two dimensionless numbers. Because the experimental focus has generally cylindrical coordinate systems, thermal dispersion correlations in the literature are usually only available for radial and axial flow directions - azimuthal dispersion coefficients are rarely measured. For an r - z coordinate system, κ_f is:

$$\kappa_f \equiv \begin{bmatrix} \kappa_{f,R} & 0 \\ 0 & \kappa_{f,A} \end{bmatrix} \quad (12.3)$$

where $\kappa_{f,R}$ represents the radial thermal dispersion and $\kappa_{f,A}$ the axial thermal dispersion. The thermal dispersion varies considerably between the axial and radial directions in a cylindrical packed bed. The dispersion thermal conductivity is usually about five times larger in the axial direction than in the radial direction (except for $Re < 10$, where convective effects are nearly negligible), so use of different correlations for each direction are important [111]. Correlations for κ_f are often quoted in terms of diffusivities. For the fluid energy equation, the diffusivity (which is in general a tensor) in scalar form is:

$$\mathbb{D} \equiv \frac{k}{\rho_f C_{pf}} \quad (12.4)$$

The literature often presents correlations for κ_f in terms of two different diffusivities. When the material property thermal conductivity, or k_f is used for k in Eq. (12.4), \mathbb{D} is referred to as the “molecular” diffusivity. Alternatively, when κ_f is used for k in Eq. (12.4), \mathbb{D} is referred to as the “axial” or “radial” diffusivity based on the component of κ_f used. This section will present correlations for the axial, \mathbb{D}_A , and radial, \mathbb{D}_R , diffusivities, which are defined in a manner similar to the axial and radial components of κ_f provided the diffusivity is assumed to not be a scalar:

$$\mathbb{D} \equiv \begin{bmatrix} \mathbb{D}_R & 0 \\ 0 & \mathbb{D}_A \end{bmatrix} \quad (12.5)$$

Experiments have shown that \mathbb{D}_A and \mathbb{D}_R are functions of Re and Pr independently, though most often data is simply plotted as a function of Pe [111]. This is also done in part because the majority of thermal dispersion experiments

have only been performed using air or water, for which an appreciable range in Pr could not be obtained.

Plotting \mathbb{D}_A/\mathbb{D} and \mathbb{D}_R/\mathbb{D} as a function of Peclet number shows a nearly linear increase with Pe , which is intuitive based on high Reynolds number flows improving dispersion mixing. Like the diffusivity, the Peclet number can be based on either k_f or κ_f , and the same notation used for differentiating between diffusion coefficients is used for Peclet numbers in this section. Pe_A and Pe_R are Peclet numbers based on either the axial or radial components of κ_f , respectively.

The greatest variation in experimental data is evident when Pe_A and Pe_R are plotted as a function of Pe . Rather than showing a monotonic increase, a plateau is reached for $Pe > 10^4$ [111]. At low Pe , Pe_A and Pe_R usually monotonically increase. In the low and high Pe range, the axial and radial Peclet numbers are typically characterized by [85, 111]:

$$\frac{1}{Pe_A} = \frac{1}{\mathcal{T}} \frac{1}{Pe} + \frac{1}{Pe_{A,\infty} f} \quad (12.6a)$$

$$Pe_A = \frac{2\mathcal{T}Pe}{2 + \mathcal{T}Pe} \quad (12.6b)$$

$$\frac{1}{Pe_R} = \frac{1}{\mathcal{T}} \frac{1}{Pe} + \frac{1}{Pe_{R,\infty} f} \quad (12.7a)$$

$$Pe_R = \frac{12\mathcal{T}Pe}{12 + \mathcal{T}Pe} \quad (12.7b)$$

where \mathcal{T} is the tortuosity, described in Section 8.3. $Pe_{A,\infty}$ and $Pe_{R,\infty}$ are the asymptotic values of the effective Peclet numbers in an unconfined bed, i.e. as the bed to particle diameter ratio tends to infinity. This limiting value has been obtained analytically to be about 8 [85]. f is a correction factor that accounts for the presence of the wall on the bed that accounts for two separate factors:

- Flow maldistribution increases as the wall is radially approached due to the no-slip condition. The effective radial diffusivity near the wall is roughly half that in an unconfined bed.
- Flow channeling occurs at the wall.

Tsotsas et. al show that f can be interpreted as the ratio of the bed-averaged superficial velocity to the center-averaged superficial velocity [85]. The extent to which this ratio is greater than one indicates the extent to which the wall effect characterizes the entire flow.

Deviations from Eqs. (12.6) and (12.7) occur in the intermediate Peclet number range. This deviation is primarily caused by the wall-channeling effect and the magnitude of the Prandtl number. Generally, the deviation is largest for small bed to particle diameter ratios and large Prandtl numbers [85]. For very small beds, the wall channeling effect is more significant, and the radial diffusion coefficient will be smaller due to impedance by the wall. Because gases generally have smaller Prandtl numbers than liquids, the simple additive models in Eqs. (12.6) and (12.7) are appropriate for gases, but may not be for liquids.

Axial and radial diffusivities are often provided in terms of five thermal dispersion regimes, given here in terms of approximate bounding Pe :

1. *Molecular diffusion regime* - $Pe < 0.3$; diffusion-dominated. In this range, dispersion is solely determined by molecular diffusion, and:

$$\mathbb{D}_A = \frac{\mathbb{D}}{\mathcal{T}} \quad (12.8)$$

$$\mathbb{D}_R = \frac{\mathbb{D}}{\mathcal{J}} \quad (12.9)$$

2. *Diffusion and convection regime* - $0.3 < Pe < 5$; diffusion and dispersion are of the same magnitude
3. *Mechanical dispersion regime* - $5 < Pe < 300$; dispersion begins to dominate
4. *Pure mechanical dispersion regime* - $300 < Pe < 10^5$; full dispersion domination
5. - $Pe > 10^5$; at very high fluid velocities, the limiting values for Pe_A and Pe_R suggested from Eqs. (12.6) and (12.7) can be used to show that the axial and radial diffusivities should increase linearly with velocity:

$$\mathbb{D}_A \approx \frac{vd_p}{2} \quad (12.10)$$

$$\mathbb{D}_R \approx \frac{vd_p}{12} \quad (12.11)$$

A common approximation is that the diffusive and convective limits are additive, such as suggested by the $k_f + k_{dis}$ in Eq. (2.210). This superposition is valid especially for the radial direction because there is no sustained radial flow [94]. However, simply adding Eqs. (12.8) and (12.10) will not correctly predict behavior at intermediate Pe , though correct asymptotic behavior is shown for low and high Pe . A summation-type correlation is sufficient for gases, but not for liquids [111].

A complication associated with most of the correlations shown in the next sections are that they were constructed using bed-averaged dimensionless numbers, which in principle would then only give constant values for the axial and radial components of κ_f . Schertz et. al show that, for correlations of the form developed by Yagi and Kunii, that when using Re_i in place of Re , local values for the effective thermal conductivities can be obtained using the correlations originally developed for bed-average representations [65]. All of the correlations discussed in the following sections were developed for beds of particles on the order of 1 mm diameter, though pebble fuel in HTGR designs is on the order of several cm in diameter. Larger pebble diameters equates to larger pore diameters, which increases the potential for flow recirculation. Abdulmohsin conducted experiments with large pebbles, and found that the correlations developed for mm-size particles are suitable for nuclear reactor analysis [19].

Gunn states that dispersion coefficients are independent of bed to particle diameter ratios given their derivation of the dispersion coefficients for a two-region bed consisting of an inner and outer region characterized by two different porosities; the porosity change for their example exactly cancelled the velocity change, so the difference in the interstitial velocity between the two bed regions is negligible [112].

12.1 Axial Effective Thermal Conductivity

Amiri expresses the axial component as [54]:

$$\kappa_{f,A} = \frac{k_f}{\mathcal{J}} + 0.5RePrk_f \quad (12.12)$$

which is roughly five times larger than the radial component given in Eq. (12.14) with $C_0 = 1/8$.

12.2 Radial Effective Thermal Conductivity

Most researchers correlate \mathbb{D}_R simple as a superposition of the diffusion and convection limits as:

$$\mathbb{D}_R = \frac{\mathbb{D}}{\mathcal{J}} + C_0 v d_p \quad (12.13)$$

which can also be written as follows using Eq. (12.4):

$$\kappa_{f,R} = \frac{k_f}{\mathcal{J}} + C_0 Re Pr k_f \quad (12.14)$$

where C_0 captures mixing effects due to particle shape and packing [65, 85, 100, 101]. Yagi et. al provides a table showing the value of C_0 obtained by various researchers - values are all of the same order of magnitude [101]. Most of the values presented by researchers do not consider the dependence of C_0 on position or d_{bed}/d_p . A singular value proposed by Yagi and Wakao of $C_0 = 0.11$, valid for $20 < Re < 800$ and for $0.021 < d_p/d_{\text{bed}} < 0.072$, fits well with other values obtained in the literature [100] and has been used for reactor analysis [36]. By varying C_0 by a factor of four, only minor changes are obtained in the bulk bed temperatures, where lower C_0 results in slightly higher bed temperatures since heat is removed less effectively near walls [36].

Tsotsas et. al show that C_0 depends on the bed to particle diameter ratio, and that C_0 can be approximated as:

$$C_0 = \frac{1}{Pe_\infty f} \quad (12.15)$$

where $Pe_\infty \approx 8$ is the limiting value of the effective Peclet number as the molecular Peclet number tends to infinity [85], and f is a correction factor given by:

$$f = \begin{cases} 2 - \left(1 - 2 \frac{d_p}{d_{\text{bed}}}\right)^2 & |r - R_{\text{bed}}/2| < d_p \\ 1 & |r - R_{\text{bed}}| > d_p \end{cases} \quad (12.16)$$

This formulation for f is based on the assumption that within one pebble diameter of the wall, \mathbb{D}_R decreases by a factor of two. Smirnov et. al extended this formulation for non-spherical particles, and found remarkably good agreement [113]. Finally, most researchers have fitted Eq. (12.14) only using bed-averaged values, but accurate point-wise values can be obtained by simply replacing Re by Re_i [65].

13 Fluid Properties

In addition to the EOS available in the fluid properties MOOSE module and RELAP-7, which are discussed in Section 7, Pronghorn permits custom fluid property definitions. This section discusses those custom fluid properties currently available in Pronghorn. Future extensions are planned. Table 18 shows the units assumed in the thermophysical correlations for both fluid and solid properties. For consistency, therefore, these must be the same set of units used by the modeler for other parameters such as Initial Condition (IC)s and BCs.

Table 18: Set of units assumed in Pronghorn for the fluid and solid properties.

Quantity	Unit
pressure	Pa
temperature	K
weight	kg
distance	m
time	s

13.1 Gases

This section presents the fluid properties for gases available in Pronghorn. It should be noted that liquid and solid properties for these gases are not implemented. If temperatures and pressures reach the point where condensation or sublimation occur, then the results predicted using the vapor properties will be inaccurate. However, reaching melting or sublimation points for Pronghorn's application space is highly unlikely.

13.1.1 Helium

Petersen provides correlations for helium that are valid in the range $1 \leq P \leq 100$ bar and $273 \leq T_f \leq 1800$ K [114] that have been used by KTA in their pebble bed HTGR analyses [115]. Standard deviations for these thermophysical properties can be found in [114]. Constant specific heats of $C_p = 5195$ J/kg·K and $C_v = 3117$ J/kg·K are used. In SI units, with pressure P in Pa and temperature T_f in K,

$$\rho_f \text{ (kg/m}^3\text{)} = 48.14 \frac{10^{-5}P}{T_f} \left(1 + 0.4446 \frac{10^{-5}P}{T_f^{1.2}} \right)^{-1} \quad (13.1)$$

$$\mu \text{ (Pa}\cdot\text{s)} = (3.674 \times 10^{-7}) T_f^{0.7} \quad (13.2)$$

$$k_f \text{ (W/m}\cdot\text{K)} = 2.682 \times 10^{-3} \left(1 + 1.123 \times 10^{-8}P \right) T_f^{0.71(1-2 \times 10^{-9}P)} \quad (13.3)$$

and other thermodynamic quantities, such as specific internal energy and specific enthalpy can be calculated as

$$e = C_v T_f \quad (13.4)$$

$$h = C_p T_f \quad (13.5)$$

Because helium is a noble gas, there is little deviation in the density correlation from the ideal gas EOS, though deviations are larger at higher pressures and lower temperatures. At the pressure of 60 bar and 550 K typical of HTGR

operating conditions, the difference in ρ_f from that predicted by the ideal gas EOS is less than 1.5%, so an appropriate approximation here would be the use of the ideal gas properties.

In some cases, it is also desirable to express helium's properties as functions of specific volume ($v \equiv 1/\rho_f$) and specific internal energy (e). For example, pressure can be obtained as an function of (v, e) as

$$P = \frac{10^5 T_f}{48.14v - \frac{0.4446}{T_f^{0.2}}} \quad (13.6)$$

with $T_f = e/C_v$.

13.2 Liquid Salts

This section presents the fluid properties for liquid salts available in Pronghorn. Vapor properties are not implemented for these salts because it is highly unlikely, even in accident scenarios, to experience boiling of the coolant, because melting points of these salts are on the order of 1400°C. Solid properties of these salts are also not implemented, though there is less margin to salt freezing than salt boiling in typical reactor designs. The user should be aware that entry into the liquid or vapor regimes for these salts will result in inaccurate results when using the liquid properties discussed in this section. Melting and boiling points for the salts in this section are shown in Table 19 to provide approximate bounds on correlation applicability.

Table 19: Melting and boiling points for the liquid salts discussed in this section [62]. Boiling points are approximate.

Salt	Melting Point (°C)	Boiling Point (°C)
LiF-BeF ₂ (flibe)	458	1400
NaF-ZrF ₄ (nafzirf)	500	1350
LiF-NaF-KF (flinak)	454	1570
KF-ZrF ₄	390	1450

The pressure dependence of all properties is neglected for the liquid salts, since there is little variation with pressure. For example, TRACE approximates the pressure dependence on density by including an additional $1.7324 \times 10^{-7}P$ term, where P is in Pa [62]. At typical reactor conditions, densities are on the order of 1000 kg/m³, where this additional term is on the order of 0.1-0.01 kg/m³, and hence is negligible.

Specific heats show very little variation with temperature, and hence constant values for all salts are assumed using experimental or analytical evaluations at 700°C. The thermal conductivity also varies only slightly with temperature. All salts show a linear variation of density and an exponential variation of viscosity with temperature.

13.2.1 LiF-BeF₂

The thermophysical property data here assumes the 67% LiF and 33% BeF₂ eutectic composition, with 99.995% enrichment in Li-7 [62]. A constant specific heat of $C_p = 2416$ J/kg·K is used, with an uncertainty of 2%. The uncertainty on the density is very low, only 0.05%. The uncertainties on the viscosity and thermal conductivity are 20% and 15%, respectively.

$$\rho_f \text{ (kg/m}^3\text{)} = -0.4884T_f + 2413 \quad (13.7)$$

$$\mu \text{ (Pa}\cdot\text{s)} = (1.16E - 4)e^{3755/T_f} \quad (13.8)$$

$$k_f \text{ (W/m}\cdot\text{K)} = (5E - 4)T_f + 0.63 \quad (13.9)$$

13.2.2 NaF-ZrF

The thermophysical property data here assumes the 59.5% NaF and 40.5% ZrF mixture [62]. A constant isobaric specific heat of $C_p = 1172 \text{ J/kg}\cdot\text{K}$ is assumed, with uncertainty of 10%. The uncertainty on the density is very low, only 2%. The uncertainties on the viscosity and thermal conductivity are 20% and 15%, respectively.

$$\rho_f \text{ (kg/m}^3\text{)} = -0.889T_f + 3827 \quad (13.10)$$

$$\mu \text{ (Pa}\cdot\text{s)} = (7.67E - 5)e^{3977/T_f} \quad (13.11)$$

$$k_f \text{ (W/m}\cdot\text{K)} = (5E - 4)T_f + 0.0052 \quad (13.12)$$

13.2.3 LiF-NaF-KF

The thermophysical property data here assumes the 46.5% LiF, 11.5% NaF, and 42% KF eutectic mixture [62]. A constant specific heat of $C_p = 2010 \text{ J/kg}\cdot\text{K}$ is assumed, with uncertainty of 20%. The uncertainty on the density is very low, only 2%. The uncertainties on the viscosity and thermal conductivity are 20% and 15%, respectively.

$$\rho_f \text{ (kg/m}^3\text{)} = -0.73T_f + 2729 \quad (13.13)$$

$$\mu \text{ (Pa}\cdot\text{s)} = (4.0E - 5)e^{4170/T_f} \quad (13.14)$$

$$k_f \text{ (W/m}\cdot\text{K)} = (5E - 4)T_f + 0.43 \quad (13.15)$$

13.2.4 KF-ZrF₄

The thermophysical property data here assumes the 58% KF and 42% ZrF₄ mixture [62].

$$\rho_f \text{ (kg/m}^3\text{)} = -0.887T_f + 3658 \quad (13.16)$$

$$\mu \text{ (Pa}\cdot\text{s)} = (1.59E - 4)e^{3179/T_f} \quad (13.17)$$

$$k_f \text{ (W/m}\cdot\text{K)} = (5E - 4)T_f - 0.032 \quad (13.18)$$

The density of KF-ZrF₄ has not been measured experimentally, but has been estimated using well-known density correlations of its KF and ZrF₄ constituents [62]. Because this salt has not been measured experimentally, it has the highest uncertainty of the salts (5%) available in Pronghorn. The uncertainties on the viscosity and thermal conductivity are 20% and 15%, respectively. An analytical method is used to predict a constant value of $C_p = 1051 \text{ J/kg}\cdot\text{K}$, with uncertainty of 20%.

14 Solid Properties

Custom solid properties are required to provide the specific heat, thermal conductivity, and density for the solid material. In addition, depending on the models used for κ , the emissivity, Poisson ratio, and Young's modulus are also required. This section discusses the models available in Pronghorn for common solid materials. It is a common approximation that solid properties are relatively independent of pressure, so none of the correlations discussed in this section are functions of pressure. Table 18 shows the units assumed in the correlations in this section.

14.1 ElectricGraphite

In support of the SANA benchmark, density and thermal conductivity measurements performed for the Sigris Al 2-500 electric graphite pebbles are available in [18]. Two repeated measurements were performed, and the "Measurement 3" is arbitrarily selected here to provide the constant density of $\rho_s = 1673 \text{ kg/m}^3$ and tabular thermal conductivity. This tabular data is fitted as:

$$k_s \text{ (W/m}\cdot\text{K)} = (2.5738 \times 10^4) T_s^{-0.86367} \quad (14.1)$$

Butland collected isobaric specific heat data from a variety of sources for many types of graphite, none actually including nuclear graphite, and then attempted to aggregate the data sets that best represent nuclear graphite into a single correlation [116]. Because nuclear graphite is well graphitized and very pure, the measurements of poorly graphitized materials were rejected from the data set. No experimental errors are provided for the data used in the polynomial fit, but it is expected that the experimental data agrees within their mean probably error.

$$C_{p,s} \text{ (J/kg}\cdot\text{K)} = 4184 \left(0.54212 - (2.42667 \times 10^{-6}) T_s - \frac{90.2725}{T_s} \right) + 4184 \left(-\frac{43449.3}{T_s^2} + \frac{1.59309 \times 10^7}{T_s^3} - \frac{1.43688 \times 10^9}{T_s^4} \right) \quad (14.2)$$

14.2 StainlessSteel

Stainless steel thermal conductivity is given as [117]:

$$k_s \text{ (W/m}\cdot\text{K)} = 15.17 + 13.3 \frac{T_s - 273}{1000} \quad (14.3)$$

which is valid for $173\text{K} < T < 1023\text{K}$. Using a constant density of $\rho_s = 7863 \text{ kg/m}^3$, the specific heat is given as [117]:

$$C_{p,s} \text{ (J/kg}\cdot\text{K)} = \frac{7.8 \times 10^6}{\rho_s} \left(0.4533 + 0.382 \frac{T_s - 273}{1000} \right) \quad (14.4)$$

which is valid for $T < 1473\text{K}$.

15 Stabilization Methods

This section introduces the need for stabilization methods for convection-diffusion equations through simple examples. This is followed by a discussion of general, higher-dimensional stabilizations. After providing examples and motivation for stabilization via the 1-D convection-diffusion equation, extension of stabilization schemes to the general compressible Navier-Stokes equations, and finally to the Pronghorn conservative and primitive equation sets, are given.

15.1 An Example: The 1-D Convection-Diffusion Equation

Consider the 1-D convection-diffusion equation:

$$-k \frac{d^2 \phi}{dx^2} + V \frac{d\phi}{dx} = 0 \quad (15.1)$$

where V is the velocity and k the diffusivity. For simplicity, throughout this discussion it is assumed that the flow is incompressible such that $\nabla \cdot \vec{V} = 0$, giving the simplified form above. This is purely for pedagogic reasons, and the conclusions that are reached extend to compressible flow. The convection-diffusion equation is conditionally stable when using the standard Bubnov-Galerkin method. For an interior node with index n , the nodal equation is:

$$(-Pe_{el} - 1)\phi_{n-1} + 2\phi_n + (Pe_{el} - 1)\phi_{n+1} = 0 \quad (15.2)$$

where Pe_{el} is the element Peclet number:

$$Pe_{el} = \frac{Pe}{2} \quad (15.3)$$

This is identical to the nodal equations that are obtained when using the central difference method to approximate the first and second derivatives, and hence the Galerkin method for 1-D linear elements (of constant size, velocity, and diffusivity, and no terms besides advection and diffusion) is equivalent to a central difference method.

Consider a 1-D linear finite element, with end nodes x_n and x_{n+1} and shape functions ψ corresponding to those nodes as:

$$\psi_n = \frac{x_{n+1} - x}{h_e} \quad (15.4a)$$

$$\psi_{n+1} = \frac{x - x_n}{h_e} \quad (15.4b)$$

where h_e is the element size. The Bubnov-Galerkin weak form of Eq. (15.1) is obtained by multiplying by the weight function ψ and integrating by parts to give a nonlinear system $K_{ij}\phi_j = f_i$, where

$$K_{ij} = \int_0^L \left(\psi_i V \frac{d\psi_j}{dx} + \frac{d\psi_i}{dx} k \frac{d\psi_j}{dx} \right) dx \quad (15.5a)$$

$$f_i = -\bar{q}\psi_i \Big|_0^L \quad (15.5b)$$

$$(15.5c)$$

and ϕ_j is the vector of expansion coefficients to be solved for. An equation for a typical node x_a that is not subject to any BCs (so that $f_i = 0$ and complications associated with Dirichlet conditions can be neglected) can be determined in terms of the solutions at x_{n-1} and x_{n+1} by solving for K_{ij} and f_i given the shape functions in Eq. (15.4). Performing the integrations gives the system:

$$\left(\frac{V}{2} \begin{bmatrix} -1 & 1 \\ -1 & 1 \end{bmatrix} + \frac{k}{h_e} \begin{bmatrix} +1 & -1 \\ -1 & +1 \end{bmatrix} \right) \begin{bmatrix} \phi_n \\ \phi_{n+1} \end{bmatrix} = \begin{bmatrix} 0 \\ 0 \end{bmatrix} \quad (15.6)$$

In 1-D, the global stiffness matrix is assembled by “tessellating” the local stiffness matrices along the diagonal such that inter-element continuity is guaranteed.

$$\begin{bmatrix} a & b & 0 & 0 & 0 & 0 \\ c & d+a & b & 0 & 0 & 0 \\ 0 & c & d+a & b & 0 & 0 \\ 0 & 0 & c & d+a & b & 0 \\ & & & & \dots & \dots \end{bmatrix} \begin{bmatrix} \dots \\ \phi_{n-1} \\ \phi_n \\ \phi_{n+1} \\ \dots \end{bmatrix} = \begin{bmatrix} 0 \\ 0 \\ 0 \\ 0 \\ 0 \end{bmatrix} \quad (15.7)$$

where $a = -Pe_{el} + 1, b = Pe_{el} - 1, c = -Pe_{el} - 1, d = Pe_{el} + 1$. Selecting an arbitrary interior node such as ϕ_n , Eq. (15.2) is obtained.

Eq. (15.2) gives purely oscillatory (nonphysical) results as $Pe_{el} \rightarrow \infty$. The stability of the above equation can be assessed in terms of recursion relations. Assuming the solution for $\phi_j = m^j$, where m is a constant, the above equation gives two possible values for m , and hence two possible solutions for ϕ_j :

$$\phi_j = 1^j \quad (15.8a)$$

$$\phi_j = \left(-\frac{Pe_{el} + 1}{Pe_{el} - 1} \right)^j \quad (15.8b)$$

If $Pe_{el} > 1$, the solution will oscillate due to the alternating powers of j . These results may appear to be tied to the rather specific 1-D convection diffusion equation selected, but the instability is actually related to the non-self adjointness of convection operators. To see why the 1-D convection-diffusion equation is non-self adjoint, begin with the weak form of Eq. (15.1):

$$\int_0^L \frac{d\Psi}{dx} k \frac{d\phi}{dx} dx + k \frac{d\phi}{dx} \Psi \cdot \vec{n} \Big|_0^L - \int_0^L V \phi \frac{d\Psi}{dx} + V \Psi \phi \cdot \vec{n} \Big|_0^L = 0 \quad (15.9)$$

Now, reverse-integrate the first term by parts by recognizing that:

$$\int_0^L \frac{d}{dx} \left(k \frac{d\Psi}{dx} \right) \phi dx = - \int_0^L \frac{d\Psi}{dx} k \frac{d\phi}{dx} dx + k \frac{d\Psi}{dx} \phi \cdot \vec{n} \Big|_0^L \quad (15.10)$$

Eq. (15.9) can then equivalently be expressed as:

$$\underbrace{\int_0^L \left(-\frac{d}{dx} \left(k \frac{d\Psi}{dx} \right) - V \frac{d\Psi}{dx} \right) \phi dx}_{\text{adjoint of original problem}} + k \frac{d\Psi}{dx} \phi \cdot \vec{n} \Big|_0^L - k \frac{d\phi}{dx} \Psi \cdot \vec{n} \Big|_0^L + V \Psi \phi \cdot \vec{n} \Big|_0^L = 0 \quad (15.11)$$

The adjoint of the original problem that appears in the weak form above has the opposite sign on the convective term, and hence convection produces non-self-adjoint equations. Fig. 18 shows the FE and exact solutions to Eq. (15.1) obtained with Pronghorn. For $Pe_{el} > 1$, the solution is oscillatory, with the oscillation magnitude increasing with Pe_{el} . The oscillatory behavior in the vicinity of the downstream boundary is partly caused by the selection of the BCs, since steep gradients are restricted to narrower and narrower regions as $Pe_{el} \rightarrow \infty$. However, the numerical algorithm should still give stable and accurate results because as long as *some* diffusion is present, it is valid to specify BCs on all boundaries.

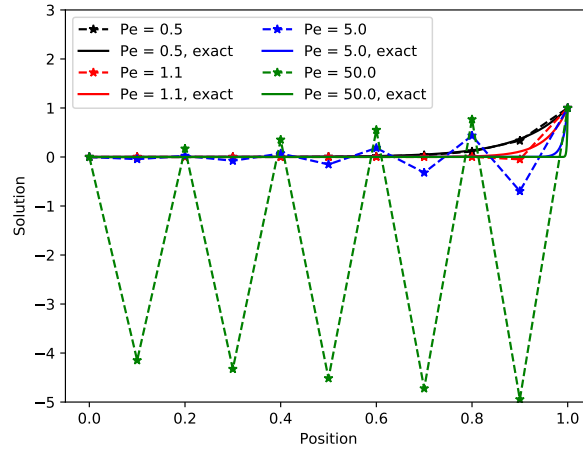


Figure 18: Solution to the the 1-D convection-diffusion problem in Eq. (15.1) with $h_e = 0.1$ for various Pe_{el} with BCs of $\phi(0) = 0, \phi(1) = 1$. The exact solution for these BCs is $\phi(x) = (1 - \exp(Pe_{el}x/L))/(1 - \exp(Pe_{el}))$.

In higher dimensions, solving Eq. (15.1) without the diffusive term (amplifying the instability) with Pronghorn gives the results shown in Fig. 19. Convection-dominated instabilities generally manifest themselves as nodal oscillations.

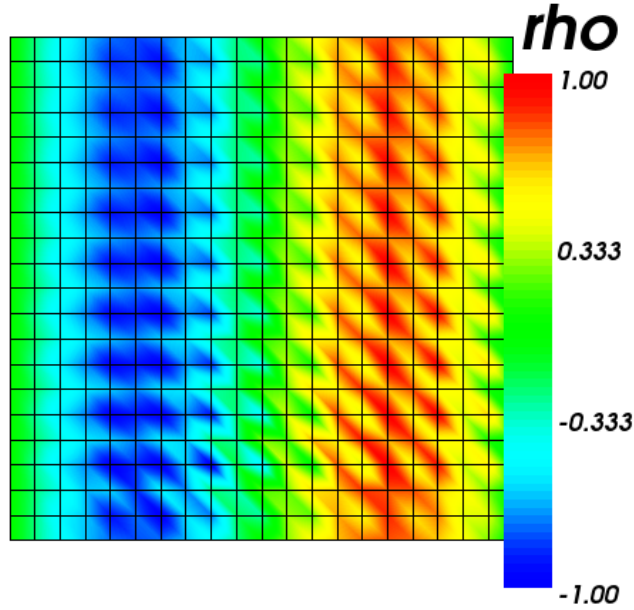


Figure 19: Solution to Eq. (15.1) with zero diffusive term and a source term $2\pi \cos(2\pi x)$. The solution should be $\rho = \sin(2\pi x) \sin(2\pi t)$. Results are shown on $0 \leq x \leq 1$ at $t = 1.15s$.

For convection-dominated problems, Pe_{el} can be very large. But as long as some diffusion is present, in theory the mesh can be refined until $Pe_{el} < 1$, since the element size h_e appears in the definition of Pe_{el} . The level of mesh refinement becomes increasingly demanding for convection-dominated problems, and many methods have been developed to circumvent the Pe_{el} stability criteria such that stability is independent of Pe_{el} , allowing engineering-scale meshes when only engineering-scale results are desired. Reactor applications will be convection-dominated, which necessitates the inclusion of stabilization schemes in Pronghorn. Not only do stabilization methods improve stability, but they in general can also enhance convergence rates during the iterative solution of the linear system [118]. Several stabilization methods are discussed next.

15.2 Upwinding

One of the first attempts to circumvent the Pe_{el} stability criterion was the use of upwind finite differencing within the Finite Difference (FD) community. Because information propagates in the direction of velocity when diffusive effects are small, it is somewhat unnatural to use a symmetric FD to approximate the convective term. Instead, upwinding uses one-sided finite differences are used to approximate the convective derivative term, such that instead of the central difference approximation:

$$\frac{d\phi}{dx} \approx \frac{\phi_{n+1} - \phi_{n-1}}{h_e} \quad (15.12)$$

a one-sided approximation is used:

$$\frac{d\phi}{dx} \approx \frac{\phi_n - \phi_{n-1}}{h_e} \quad (15.13)$$

where a positive velocity has been assumed. The upwinding approximation is only used for the convective derivative, while the central difference approximation is retained for the diffusive term. To illustrate how such a choice eliminates the Pe_{el} stability criterion discussed in Section 15.1, repeat the derivation of the equation governing a representative non-boundary node using upwind differencing of the first derivative and central differencing of the second derivative to give:

$$(-2Pe_{el} - 1)\phi_{n-1} + (2Pe_{el} + 2)\phi_n + (-1)\phi_{n+1} = 0 \quad (15.14)$$

Performing the same recursion analysis as in Section 15.1, the following two solutions are obtained:

$$\phi_j = 1^j \quad (15.15a)$$

$$\phi_j = (2Pe_{el} + 1)^j \quad (15.15b)$$

Neither of these solutions give oscillatory results because the arguments are always positive. Hence, upwinding fully eliminates all oscillatory behavior. But, upwinding does not necessarily give the *correct* solution. The full upwinding shown here only gives nodally exact values for either $Pe_{el} = 0$ (purely diffusive) or $Pe_{el} = \infty$ (purely convective). In addition to the difficulty of determining the appropriate amount of upwinding when both convective and diffusive forces are present, it is not immediately clear how to extend the upwinding FD method to a FE weak form. There are many ways in which investigators have extended upwinding to the FE framework such that the FD equivalent in Eq. (15.14) is obtained when looking at a non-boundary node. The remaining methods discussed in this section can give nodally exact results in 1-D, but fail when extended in an ad hoc manner to higher dimensions.

15.2.1 Petrov-Galerkin Stabilization

Petrov-Galerkin methods, as opposed to Bubnov-Galerkin methods, select the shape function and the weight function from different spaces of functions. The weight function is modified to be the sum of the original, element-continuous weight functions ψ , and a discontinuous portion ψ^* :

$$\tilde{\psi} = \psi + \alpha_{pg}\psi^* \quad (15.16)$$

where α_{pg} is a scaling parameter. Using a consistent Petrov-Galerkin scheme, using Eq. (15.16) as the shape function in Eq. (15.14) gives the following weak form:

$$K_{ij} = \int_0^L \left(\psi_i V \frac{d\psi_j}{dx} + \frac{d\psi_i}{dx} k \frac{d\psi_j}{dx} \right) dx + \sum_{nel} \left[\int_0^L \left(\alpha_{pg} \psi_i^* V \frac{d\psi_j}{dx} + \frac{d(\alpha_{pg} \psi_i^*)}{dx} k \frac{d\psi_j}{dx} \right) dx \right] \quad (15.17a)$$

$$f_i = -\tilde{q}\psi_i \Big|_0^L \quad (15.17b)$$

where instead of a continuous integral over the entire domain, the term containing the inter-element discontinuous shape functions ψ^* is restricted to the element interiors. This summation simply indicates that integration by parts is not performed on the second integral in Eq. (15.17a), which eliminates complications with having to modify BCs or losing inter-element continuity. There are many possible choices for ψ^* , but one choice that is often selected in 1-D is:

$$\psi_i^* = \frac{h_e \vec{V}}{2|\vec{V}|} \frac{d\psi_i}{dx} \quad (15.18)$$

Performing the same analysis of a typical non-boundary node using Eq. (15.18) in Eq. (15.16) gives the same nodal equation in Eq. (15.14) as long as α_{pg} is selected as 1 (full upwinding). For the convection-diffusion equation under consideration, it can be shown that nodally-exact values for constant-size linear Lagrange elements can be obtained if α_{pg} is given by:

$$\alpha_{pg} = \frac{h_e}{2\|\vec{V}\|} \left(\coth |Pe_{el}| - \frac{1}{|Pe_{el}|} \right) \quad (15.19)$$

Fig. 20 shows the nodally-exact results obtained for the same problem shown in Fig. 18 with optimal upwinding given by Eq. (15.19). Even if no oscillations are observed in Fig. 18, such as is the case for $Pe_{el} = 1.1$, upwinding still improves the solution accuracy in Fig. 20.

Eq. (15.19) can be derived by asserting that the non-self-adjoint convection-diffusion equation, when fully-expanded, be self-adjoint. This is accomplished by multiplying the operator by a function p , and then determining the form of p that makes the equation self-adjoint. For instance, the weak form of the 1-D convection-diffusion equation, multiplied by p is:

$$\int_0^L p\Psi \left(-\frac{d}{dx} \left(k \frac{d\phi}{dx} \right) + V \frac{d\phi}{dx} \right) dx = 0 \quad (15.20)$$

Integrating by parts (and applying the chain rule to the derivative of $p\Psi$):

$$\int_0^L \left(\Psi \frac{d\phi}{dx} \underbrace{\left(pV + k \frac{dp}{dx} \right)}_{\text{non-self-adjoint}} + p \frac{d\Psi}{dx} k \frac{d\phi}{dx} \right) dx - p\Psi k \frac{d\phi}{dx} \cdot \vec{n} \Big|_0^L = 0 \quad (15.21)$$

The optimal stabilization will be such that the equation is self-adjoint. This leads to an ODE for p :

$$pV + k \frac{dp}{dx} = 0 \quad (15.22)$$

Solving this equation gives the functional form for p . Plugging this form into the equation (multiplying it through the original equation) and then applying all the algebra to obtain the typical nodal equation gives Eq. (15.19). If p is defined as continuous across the elements, however, the system is not well-conditioned. Restricting p to element-wise constant definitions solves this issue, but introduces asymmetries into the stiffness matrix. This method of determining an appropriate function such that the equation is forced to be self-adjoint, is the most general way to derive optimal upwinding terms.

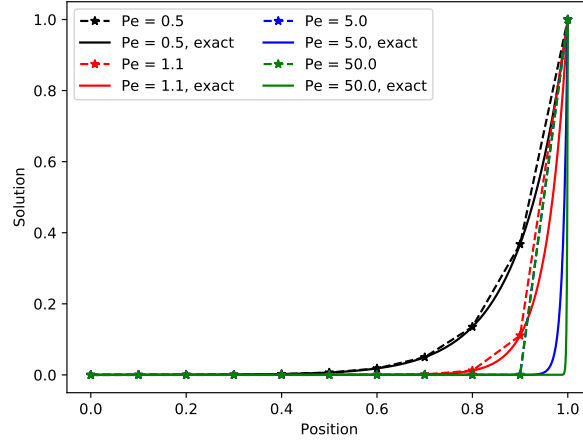


Figure 20: Solution to the 1-D convection-diffusion problem in Eq. (15.1) with α_{pg} given by Eq. (15.19) and $h_e = 0.1$ for various Pe_{el} with BCs of $\phi(0) = 0, \phi(1) = 1$. The exact solution for these BCs is $\phi(x) = (1 - \exp(Pe_{el}x/L))/(1 - \exp(Pe_{el}))$.

The Petrov-Galerkin method is the most correct way of translating upwinding to a weak formulation, since from Eq. (15.16), the method is consistent. That is, if the perturbation $\alpha_{pg}\Psi^*$ is added to each term in the weak form, then the true solution is also a solution to the stabilized equation because the true solution has a zero residual. All of the remaining methods discussed in this section are *inconsistent*, producing incorrect results usually characterized by excessive crosswind diffusion. However, understanding these other methods is important for appreciating Petrov-Galerkin stabilizations.

15.2.2 Isotropic Diffusion Stabilization

If central differencing is performed for the diffusive term, there are no terms present besides the convective and diffusive terms (such as source terms), and linear Lagrange elements are used, then upwinding can be interpreted as “adding diffusion” to the equation. Within these two limitations, upwinding is equivalent to amplifying the diffusivity by an amount \tilde{k} . But, inappropriately increasing the diffusivity outside the realm of validity leads to an inconsistent method. Applying upwinding to the convective term and central differencing to the diffusive term, Eq. (15.14) is obtained if:

$$\tilde{k} = \frac{Vh\alpha_{pg}}{2} \quad (15.23)$$

Instead of consistently applying the Petrov-Galerkin scheme, early investigators simply added \tilde{k} to the diffusivity and then used a standard Bubnov-Galerkin discretization. This method is referred to as the “isotropic diffusion stabilization” method. This approach only gives correct results if only terms convective and diffusive terms are present and linear Lagrange elements are used. In simulations with source terms, significant crosswind diffusion is observed.

15.2.3 Modified Quadrature Rules and Weight Functions

Still within a Bubnov-Galerkin framework, some researchers have modified the quadrature rule on the convective term so that a single quadrature point is placed upstream of the node, with coordinates dictated by Pe_{el} . Quadrature Upwinding (QU), like the isotropic diffusion method, is inconsistent, and produces excessive crosswind diffusion. Others have modified the weight functions for the convective term so that they are weighted more heavily upwind of a node. For 1-D flow towards the right, Fig. 21 shows several perturbed weight functions relative to a linear Lagrange

shape function. The Petrov-Galerkin method described by Eq. (15.16) also use weight functions weighted more heavily upwind, but they are weighted based on the velocity, and are weighted within *every* term so that the method is consistent.

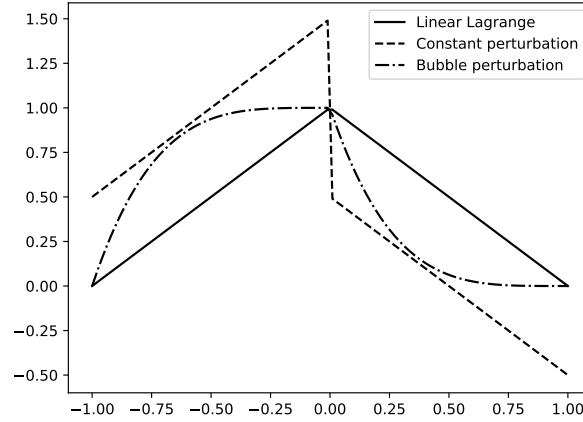


Figure 21: Example perturbed upwinding weight functions for a 1-D element, with a standard Lagrange function for comparison [119].

15.3 Streamline-Upwind Petrov-Galerkin Stabilization

The first attempts to extend the optimal 1-D upwinding to higher dimensions involved ad-hoc extensions of the inconsistent methods discussed in Section 15.2. The results were so poor that often the standard Bubnov-Galerkin method gave superior results. In 1982, Brooks became the first to use a consistent Petrov-Galerkin formulation to extend upwinding to higher dimensions for the incompressible Navier-Stokes equations [119]. The SUPG method is now one of the most commonly-used schemes for stabilizing convection-diffusion equations. A very detailed description of the method can be found in [120]. Because convection is only active in the direction of flow, the SUPG method only applies upwinding in directions parallel to the velocity. Eliminating upwinding perpendicular to the flow direction is also desirable from the viewpoint of reducing crosswind diffusion. The SUPG method is therefore an anisotropic artificial diffusion method. To derive the SUPG method for both higher spatial dimensions and systems of equations, consider an arbitrary convective equation such as that given by Eq. (2.223), written in quasi-linear form as in Eq. (2.225). With this linearization, the SUPG method leads to the following weak form that applies to the entire system of equations:

$$\int_{\Omega} \vec{R}(\vec{U}) \cdot \vec{W} d\Omega + \sum_{n_{el}} \int_{\Omega_e} \mathbf{A}_i \frac{\partial \vec{W}}{\partial x_i} \cdot \tau_{SUPG} \vec{R}(\vec{U}) d\Omega = 0 \quad (15.24a)$$

$$\int_{\Omega} R_j \phi d\Omega + \sum_{n_{el}} \int_{\Omega_e} A_i(j,k) \frac{\partial \phi}{\partial x_i} \tau_{SUPG_{kl}} R_l d\Omega = 0 \quad (15.24b)$$

For a 5-equation system in 3 spatial dimensions, $j, k, l = 1, 2, 3, 4, 5$ and $i = 1, 2, 3$. Eq. (15.24b) shows the weak form for equation j in suffix notation. $A_i(j, k)$ represents the j, k entry of matrix A_i . \vec{W} is the vector of weight functions, ϕ is the weight function for equation j , and τ_{SUPG} is a matrix representing the diagonal and cross-term stabilization parameters (more complicated versions of the α_{pg} parameter from the 1-D examples).

The first term in Eq. (15.24) is the non-stabilized weak form, except that integration by parts is not shown. The second term in Eq. (15.24) is the discontinuous stabilization term; the discontinuous aspect allows inter-element continuity to be maintained and eliminates the need to add additional boundary terms. Eq. (15.24) stabilizes each

equation considering all of the other equations in the nonlinear system. That is, each equation may be stabilized by its own residual, and possibly the residuals of the other coupled equations.

The remainder of this section derives each of the terms in Eq. (15.24) using the conservative equations solved in Pronghorn. Occasionally, simplifications such as the non-porous Euler equations are used to discuss characteristics of the method, but this will be noted when appropriate. Because a stationary solid is assumed in Pronghorn, the coupling between the fluid and solid phases occurs only through the convective heat transfer term (i.e. the solid energy equation is purely diffusive because there is no advective coupling to the fluid velocity). Therefore, no stabilization of the solid energy equation is required, so the SUPG scheme only needs to stabilize the coupled fluid equations. Section 19.1 provides specific values for \mathbf{A}_i and \mathbf{K}_{ij} .

Section 15.4 discusses modifications made to the SUPG scheme shown in this section for use with Pronghorn's primitive equation set.

15.3.1 Solution, Inviscid Flux, Diffusive Flux, and Source Vectors

All of the equations and vectors must be cast in terms of the five conserved variables $U_0, U_1, U_2, U_3,$ and U_4 defined as the entries of \vec{U} in Eq. (2.224):

$$\vec{U} = [U_0 \quad U_1 \quad U_2 \quad U_3 \quad U_4]^T \quad (15.25)$$

One inviscid flux vector exists for each spatial dimension $i \leq 3$:

$$\vec{F}_i = \begin{bmatrix} U_i \\ \frac{U_1 U_i}{U_0} + \delta_{1i} P \\ \frac{U_2 U_i}{U_0} + \delta_{2i} P \\ \frac{U_3 U_i}{U_0} + \delta_{3i} P \\ U_i H \end{bmatrix} \quad (15.26)$$

In order to pull out a factor of porosity from \vec{G}_i , and keep accounting easier, we assume Eq. (12.1):

$$\vec{G}_i = \varepsilon \left[0 \quad 0 \quad 0 \quad 0 \quad k_f \frac{\partial T_f}{\partial x_i} \right]^T \quad (15.27)$$

The source vector is:

$$\vec{S} = \begin{bmatrix} 0 \\ -\varepsilon U_0 g_1 + W U_1 - P \frac{\partial \varepsilon}{\partial x_1} \\ -\varepsilon U_0 g_2 + W U_2 - P \frac{\partial \varepsilon}{\partial x_2} \\ -\varepsilon U_0 g_3 + W U_3 - P \frac{\partial \varepsilon}{\partial x_3} \\ -\varepsilon (g_1 U_1 + g_2 U_2 + g_3 U_3) + \alpha (T_f - T_s) - \dot{q}_f \end{bmatrix} \quad (15.28)$$

15.3.2 Variable Derivatives

Derivatives of the conserved variables, as well as pressure, enthalpy, and temperature (if including the thermal diffusion term) with respect to one another are required in Eq. (15.24). Total enthalpy, defined in Eq. (2.160), can be expressed

as:

$$H = \frac{U_4 + P}{U_0} \quad (15.29)$$

The derivatives of total enthalpy with respect to the conserved variables are:

$$\frac{\partial H}{\partial U_0} = \frac{1}{U_0} \left(\frac{\partial P}{\partial U_0} - H \right) \quad (15.30a)$$

$$\frac{\partial H}{\partial U_i} = \frac{1}{U_0} \frac{\partial P}{\partial U_i} \quad (15.30b)$$

$$\frac{\partial H}{\partial U_4} = \frac{1}{U_0} \left(1 + \frac{\partial P}{\partial U_4} \right) \quad (15.30c)$$

For the conservative variable formulation, both pressure and temperature are given by EOSs, so the SUPG stabilization is implicitly dependent on the EOS selected. The ideal gas EOS gives pressure as Eq. (7.10)b, which gives the following derivatives with respect to the conserved variables:

$$P = (\gamma - 1) \left(U_4 - \frac{U_1^2 + U_2^2 + U_3^2}{2U_0} \right) \quad (15.31)$$

$$\frac{\partial P}{\partial U_0} = \frac{(\gamma - 1)(U_1^2 + U_2^2 + U_3^2)}{2U_0^2} = \frac{1}{2}(\gamma - 1) \|\vec{V}\|_2^2 \quad (15.32a)$$

$$\frac{\partial P}{\partial U_i} = \frac{(1 - \gamma)U_i}{U_0} = (1 - \gamma)V_i \quad (15.32b)$$

$$\frac{\partial P}{\partial U_4} = \gamma - 1 \quad (15.32c)$$

The ideal gas EOS gives temperature as Eq. (7.14), which gives the following derivatives with respect to conserved variables:

$$T_f = \frac{1}{C_v} \left(\frac{U_4}{U_0} - \frac{U_1^2 + U_2^2 + U_3^2}{2U_0^2} \right) \quad (15.33)$$

$$\frac{\partial T_f}{\partial U_0} = \frac{1}{C_v} \left(-\frac{U_4}{U_0} + \frac{U_1^2 + U_2^2 + U_3^2}{U_0^2} \right) = \frac{1}{\rho C_v} \left(\|\vec{V}\|_2^2 - \frac{\rho E}{\rho} \right) \quad (15.34a)$$

$$\frac{\partial T_f}{\partial U_i} = -\frac{U_i}{C_v U_0} = -\frac{V_i}{\rho C_v} \quad (15.34b)$$

$$\frac{\partial T_f}{\partial U_4} = \frac{1}{\rho C_v} \quad (15.34c)$$

where $i = 1, 2, 3$ in Eqs. (15.30)b, (15.32)b, and (15.34)b.

15.3.3 Inviscid Flux Jacobian Matrices

The inviscid flux Jacobian matrices defined in Eq. (2.226) are given as follows by canceling derivative terms that are zero and Kronecker deltas of the form δ_{4i} (since $i \leq 3$ depending on the spatial dimension):

$$\mathbf{A}_i = \begin{bmatrix} 0 & \delta_{1i} & \delta_{2i} & \delta_{3i} & 0 \\ \frac{-U_1 U_i}{U_0^2} + \delta_{1i} \frac{\partial P}{\partial U_0} & \delta_{1i} \left[\frac{2U_1}{U_0} + \frac{\partial P}{\partial U_1} \right] + \tilde{\delta}_{1i} \frac{U_i}{U_0} & \delta_{i2} \frac{U_1}{U_0} + \delta_{1i} \frac{\partial P}{\partial U_2} & \delta_{i3} \frac{U_1}{U_0} + \delta_{1i} \frac{\partial P}{\partial U_3} & \delta_{1i} \frac{\partial P}{\partial U_4} \\ \frac{-U_2 U_i}{U_0^2} + \delta_{2i} \frac{\partial P}{\partial U_0} & \delta_{1i} \frac{U_2}{U_0} + \delta_{2i} \frac{\partial P}{\partial U_1} & \delta_{2i} \left[\frac{2U_2}{U_0} + \frac{\partial P}{\partial U_2} \right] + \tilde{\delta}_{2i} \frac{U_i}{U_0} & \delta_{i3} \frac{U_2}{U_0} + \delta_{2i} \frac{\partial P}{\partial U_3} & \delta_{2i} \frac{\partial P}{\partial U_4} \\ \frac{-U_3 U_i}{U_0^2} + \delta_{3i} \frac{\partial P}{\partial U_0} & \delta_{1i} \frac{U_3}{U_0} + \delta_{3i} \frac{\partial P}{\partial U_1} & \delta_{2i} \frac{U_3}{U_0} + \delta_{3i} \frac{\partial P}{\partial U_2} & \delta_{3i} \left[\frac{2U_3}{U_0} + \frac{\partial P}{\partial U_3} \right] + \tilde{\delta}_{3i} \frac{U_i}{U_0} & \delta_{3i} \frac{\partial P}{\partial U_4} \\ U_i \frac{\partial H}{\partial U_0} & U_i \frac{\partial H}{\partial U_1} + \delta_{1i} H & U_i \frac{\partial H}{\partial U_2} + \delta_{2i} H & U_i \frac{\partial H}{\partial U_3} + \delta_{3i} H & U_i \frac{\partial H}{\partial U_4} \end{bmatrix} \quad (15.35)$$

where $\tilde{\delta}_{ij} \equiv (1 - \delta_{ij})$ is defined for conciseness.

15.3.4 Diffusive Flux Jacobian Matrices

The diffusive flux Jacobian matrices defined in Eq. (2.227) are zero if $i \neq j$, and because only the last entry of \vec{G}_i is nonzero, only the last row in \mathbf{K}_{ii} is nonzero:

$$\mathbf{K}_{ii} = k_f \begin{bmatrix} 0 & 0 & 0 & 0 & 0 \\ 0 & 0 & 0 & 0 & 0 \\ 0 & 0 & 0 & 0 & 0 \\ 0 & 0 & 0 & 0 & 0 \\ \frac{\partial T_f}{\partial U_0} & \frac{\partial T_f}{\partial U_1} & \frac{\partial T_f}{\partial U_2} & \frac{\partial T_f}{\partial U_3} & \frac{\partial T_f}{\partial U_4} \end{bmatrix} \quad (15.36)$$

15.3.5 The Stabilizing Effect

The stabilizing effect is obtained via the second term in Eq. (15.24). The form of this equation will be different for each of the mass, momentum, and energy equations, and will contain a mix of strong residuals from each equation. For simplicity, assume that τ_{SUPG} is a diagonal matrix with components defined in Eq. (15.50), where for simplicity it is in this section assumed that $\tau_{u1} = \tau_{u2} = \tau_{u3} \equiv \tau_u$. In the continuity equation, the following term is added to the weak form:

$$\sum_{n_{el}} \int_{\Omega_e} \tau_u \nabla \phi_i \cdot \vec{R}_u d\Omega \quad (15.37)$$

where \vec{R}_u is the vector of momentum equation residuals. The continuity equation is therefore stabilized by a term proportional to the momentum equation strong residuals. In the j th momentum equation, the following term is added to the weak form:

$$\sum_{n_{el}} \int_{\Omega_e} \left[\tau_u \left((1 - \gamma) \vec{V} \cdot \vec{R}_u \frac{\partial \phi_i}{\partial x_j} + \vec{V} \cdot \nabla \phi_i R_{uj} + V_j \nabla \phi_i \cdot \vec{R}_u \right) + \tau_e R_e (\gamma - 1) \frac{\partial \phi_i}{\partial x} \right] d\Omega + \sum_{n_{el}} \int_{\Omega_e} \left[\tau_c R_c \left(-V_j \vec{V} \cdot \nabla \phi_i + \frac{1}{2} (\gamma - 1) \|\vec{V}\|_2^2 \frac{\partial \phi_i}{\partial x_j} \right) \right] d\Omega \quad (15.38)$$

where R_c is the continuity equation strong residual and R_e is the energy equation strong residual. The momentum equations are therefore stabilized by terms proportional to the continuity, momentum, and energy equation residuals. In the fluid energy equation, the following term is added to the weak form:

$$\sum_{n_{el}} \int_{\Omega_e} \left[\frac{1}{2} \tau_u \left(h \nabla \psi_i \cdot \vec{R}_u + (1 - \gamma) (\vec{V} \cdot \vec{R}_u) (\vec{V} \cdot \nabla \psi_i) \right) + \tau_e R_e \gamma \vec{V} \cdot \nabla \psi_i \right] d\Omega + \sum_{n_{el}} \int_{\Omega_e} \left[\tau_c R_c \left(\frac{1}{2} (\gamma - 1) \|\vec{V}\|_2^2 - h \right) \vec{V} \cdot \nabla \psi_i \right] d\Omega \quad (15.39)$$

The energy equation is therefore stabilized by a term proportional to the continuity, momentum, and energy equation residuals. The stabilizing effect of the above terms is not immediately apparent. The stabilizing effect is apparent for the simple 1-D convection diffusion equation in Eq. (15.1), extended to higher dimensions and time dependence:

$$\frac{\partial \phi}{\partial t} + \nabla \cdot (\phi \vec{V}) - \nabla \cdot (k \nabla \phi) = 0 \quad (15.40)$$

The solution, inviscid flux, and diffusive vectors are:

$$\vec{U} = [\phi], \quad \vec{F}_i = [\phi V_i], \quad \vec{G}_i = \left[-k \frac{\partial \phi}{\partial x_i} \right] \quad (15.41)$$

The inviscid flux Jacobian is:

$$\mathbf{A}_i = \left[\frac{\partial(\phi V_i)}{\partial \phi} \right] = [V_i] \quad (15.42)$$

Then, the stabilizing term added to the equation becomes:

$$\sum_{n_{el}} \int_{\Omega_e} d\Omega \tau_{cd} \vec{V} \cdot \nabla \psi_i \underbrace{\left(\frac{\partial \phi}{\partial t} + \nabla \cdot (\phi \vec{V}) - \nabla \cdot (k \nabla \phi) \right)}_{\vec{R}(\vec{U})} \quad (15.43)$$

where τ_{cd} is the stabilization parameter for this convection-diffusion equation. The overall weak form, with both the SUPG and original terms, becomes:

$$\underbrace{\left(\frac{\partial \phi}{\partial t}, \psi \right) + (k \nabla \phi, \nabla \psi) + (-\phi \vec{V}, \nabla \psi) + (-k \nabla \phi + \phi \vec{V}, \psi)}_{\text{original weak form}} + \underbrace{\left(\frac{\partial \phi}{\partial t}, \tau_{cd} \vec{V} \cdot \nabla \psi \right) + (\nabla \cdot (\phi \vec{V}), \tau_{cd} \vec{V} \cdot \nabla \psi) + (-\nabla \cdot (k \nabla \phi), \tau_{cd} \vec{V} \cdot \nabla \psi)}_{\text{SUPG term}} = 0 \quad (15.44)$$

The weak form of the diffusion kernel is $(k \nabla \phi, \nabla \psi)$. The presence of two gradients, $\nabla \phi$ and $\nabla \psi$, gives the diffusion term nice numerical properties. For this system of equations consisting of one equation, the SUPG method is analogous to adding a perturbation term to the weight function ψ such that $\psi \rightarrow \psi + \tau_{cd} \vec{V} \cdot \nabla \psi$. With this extra component, the weak form for the advective term becomes $(\tau_{cd} \nabla \cdot (\phi \vec{V}) - \phi, \vec{V} \cdot \nabla \psi)$. The SUPG method adds a derivative of the nonlinear variable ϕ to the advective kernel to mimics the two derivatives seen in the diffusive term. It is this similarity to solving a diffusion kernel, when actually solving a convection kernel, that gives the SUPG method its stabilizing effect. Not all terms added to the original weak forms have stabilizing effects, but overall, the SUPG method stabilizes

convection-diffusion equations well. The diffusive portion of the SUPG term, $(-\nabla \cdot (k\nabla\phi), \tau_{cd}\vec{V} \cdot \nabla\psi)$, will disappear if the shape function order used to approximate ϕ is first order or lower. Under these conditions, the SUPG method is no longer conservative. However, this lack of consistency is rarely a practical concern, because the diffusive term becomes negligible as the Reynolds number increases.

Equivalently, the stabilizing effects of the SUPG method arise because the method increases the symmetry of the system. The one-equation SUPG method is equivalent to a linear combination of the standard Galerkin FEM and the Galerkin Least Squares (GLS) method. The GLS method requires the square of the residual to be zero, and hence produces symmetric stiffness matrices. So, the SUPG method can be interpreted as increasing the symmetry of the stiffness matrix.

For the 1-D convection-diffusion equation given in Eq. (15.1), the Galerkin FEM gives the following weighted residual form, with BCs omitted for simplicity:

$$\int_{\Omega} \psi \left(-k \frac{d^2\phi}{dx^2} + v \frac{d\phi}{dx} \right) d\Omega = 0 \quad (15.45)$$

The GLS weighted residual form is, also with BCs omitted:

$$\int_{\Omega} \left(-k \frac{d^2\psi}{dx^2} + v \frac{d\psi}{dx} \right) \left(-k \frac{d^2\phi}{dx^2} + v \frac{d\phi}{dx} \right) d\Omega \quad (15.46)$$

Writing a new weighted residual statement as a linear combination of Eqs. (15.45) and (15.46) scaled by a parameter ζ :

$$\int_{\Omega} \left[\psi + \zeta \left(-k \frac{d^2\psi}{dx^2} + v \frac{d\psi}{dx} \right) \right] \left[-k \frac{d^2\phi}{dx^2} + v \frac{d\phi}{dx} \right] d\Omega = 0 \quad (15.47)$$

If the second derivative term $d^2\psi/dx^2$ is neglected (possible when using linear Lagrange shape functions), then if ζ is chosen to equal $\alpha_{pg}h/2|\vec{V}|$, this linear combination is equal to the one-equation SUPG method.

15.3.6 Shock-Capturing

The SUPG method does not preserve monotonicity. In the vicinity of shocks or very sharp gradients in the solution, Gibbs phenomena, or the over/undershoots that results from approximating an infinite-term series with a finite number of terms, results in nonphysical numerical oscillations. Because the governing equations are nonlinear, these oscillations can rapidly pollute the entire solution. In the vicinity of shocks, there are several additional numerical tweaks that can be applied to recover the shock-like behavior of the true solution. These treatments will be added as needed.

15.3.7 Calculation of the Stabilization Parameter τ_{SUPG}

The stabilization parameter τ_{SUPG} is an $N \times N$ matrix of intrinsic time scales associated with the N -equation nonlinear system. The accuracy of the SUPG method is dependent on a good choice for this matrix that balances accuracy and stability. Optimal values for τ_{SUPG} are only available for the most simple of equations, such as the 1-D constant-coefficient advection-diffusion equation. For multidimensional problems, τ_{SUPG} involves the solution of an eigenvalue problem at each quadrature point. τ_{SUPG} is a combination of the waves generated by each eigenvalue: $\|\vec{V}\|$, $\|\vec{V}\| + c$, and $\|\vec{V}\| - c$, where c is the sound speed. These waves travel along the streamwise direction.

For the 1-D equivalent of Eq. (15.35), the inviscid flux Jacobian matrix becomes:

$$\mathbf{A}_1 = \begin{bmatrix} 0 & 1 & 0 \\ -V^2 + \frac{\partial P}{\partial U_0} & 2V + \frac{\partial P}{\partial U_1} & \frac{\partial P}{\partial U_4} \\ V \left(\frac{\partial P}{\partial U_0} - h \right) & V \frac{\partial P}{\partial U_1} + h & V \left(1 + \frac{\partial P}{\partial U_4} \right) \end{bmatrix} \quad (15.48)$$

Without the presence of additional inhomogeneous terms, the governing equations represent the time-dependent Euler equations, which have the following eigenvalues:

$$\lambda_1 = V \quad (15.49a)$$

$$\lambda_{2,3} = V + \frac{1}{2} \left(\frac{\partial P}{\partial U_1} + V \frac{\partial P}{\partial U_4} \right) \pm \frac{1}{2} \sqrt{4 \left(\frac{\partial P}{\partial U_0} + V \frac{\partial P}{\partial U_1} + h \frac{\partial P}{\partial U_4} \right) + \left(\frac{\partial P}{\partial U_1} + V \frac{\partial P}{\partial U_4} \right)^2} \quad (15.49b)$$

For a given EOS, the partial derivatives of pressure with respect to the nonlinear variables can be determined. It can be shown that the above eventually simplifies to $\lambda_{2,3} = V \pm c$ for the ideal gas EOS.

Because solving an eigenvalue problem at each quadrature point is CPU-intensive, many authors have instead relied on ad hoc extensions of the optimal 1-D expressions to higher-dimensions. It is common to only use a diagonal τ_{SUPG} :

$$\tau_{SUPG} \equiv \begin{bmatrix} \tau_c & 0 & 0 & 0 & 0 \\ 0 & \tau_{u1} & 0 & 0 & 0 \\ 0 & 0 & \tau_{u2} & 0 & 0 \\ 0 & 0 & 0 & \tau_{u3} & 0 \\ 0 & 0 & 0 & 0 & \tau_e \end{bmatrix} \quad (15.50)$$

where subscript c represents the continuity equation, u_i the i -th momentum equation, and e the energy equation. Only diagonal τ_{SUPG} are considered in Pronghorn. When a diagonal matrix is chosen as an approximation to the full matrix, strong discontinuity capturing operators must be used for compensation.

A summary of the values of diagonal τ_{SUPG} entries used in the literature is shown below, with reference to the equation set solved, either Compressible Navier-Stokes (CNS) or Compressible Euler (CE).

Table 20: Summary of the values used for τ_c found in the literature.

Source	Equation Set	τ_c
MOOSE Navier Stokes	CNS	$\left[\left(\frac{\ V\ }{h_e} \right)^2 + \left(\frac{2}{\Delta t} \right)^2 \right]^{-1/2}$
BIGHORN	CE	$\left[\left(\frac{\ V\ }{h_e} \right)^2 + \left(\frac{\ V\ +c}{h_e} \right)^2 \right]^{-1/2}$
Kirk, [121]	CNS	$\left[\left(\frac{2(\ V\ +c)}{h_e} \right)^2 + \left(\frac{2}{\Delta t} \right)^2 \right]^{-1/2}$

Table 21: Summary of the values used for τ_{u_i} found in the literature.

Source	Equations	τ_u
MOOSE Navier Stokes	CNS	$\left[\left(\frac{\ V\ }{h_e} \right)^2 + \left(\frac{2}{\Delta t} \right)^2 + \left(\frac{\mu}{\rho h_e^2} \right)^2 \right]^{-1/2}$
BIGHORN	CE	$\left[\left(\frac{\ V\ }{h_e} \right)^2 + \left(\frac{\ V\ +c}{h_e} \right)^2 + \left(\frac{\mu}{\rho h_e^2} \right)^2 \right]^{-1/2}$
Kirk, [121]	CNS	$\left[\left(\frac{2(\ V\ +c)}{h_e} \right)^2 + \left(\frac{2}{\Delta t} \right)^2 + \left(\frac{4\mu}{\rho h_e^2} \right)^2 \right]^{-1/2}$

Table 22: Summary of the values used for τ_e found in the literature.

Source	Equations	τ_e
MOOSE Navier Stokes	CNS	$\left[\left(\frac{\ V\ }{h_e} \right)^2 + \left(\frac{2}{\Delta t} \right)^2 + \left(\frac{k}{\rho C_p h_e^2} \right)^2 \right]^{-1/2}$
BIGHORN	CE	$\left[\left(\frac{\ V\ }{h_e} \right)^2 + \left(\frac{\ V\ +c}{h_e} \right)^2 + \left(\frac{k}{\rho C_p h_e^2} \right)^2 \right]^{-1/2}$
Kirk, [121]	CNS	$\left[\left(\frac{2(\ V\ +c)}{h_e} \right)^2 + \left(\frac{2}{\Delta t} \right)^2 + \left(\frac{4k}{\rho C_p h_e^2} \right)^2 \right]^{-1/2}$

The remainder of this section discusses several methods by which the τ_{SUPG} entries have been calculated. Simpler methods have been used that typically only consider spatial (maximize spatial accurate) or temporal (maximize phase accuracy) criteria. These methods do not lead naturally to the forms shown in the tables above, and are not discussed here. The τ_{SUPG} entries are generally unique for each element because they contain the element size h_e as a parameter.

The clearest way to derive the τ_{SUPG} components in Tables 20-22 is by nondimensionalizing the element matrices and vectors that arise directly from the FEM discretization. If the terms in the integrals are assumed 1-D and constant over each element, then a simple form amenable for implementation in Pronghorn is obtained. The advantages of this approach are that the local element length scales, velocities, and temporal scales are automatically taken into account, and the procedure for computing τ_{SUPG} is independent of the element order. By dividing integrals by the advective term, the τ_{SUPG} components represent advection-dominated, transient-dominated, and diffusion-dominated physics. The scalar value τ_j ($j = c, u_1, u_2, u_3$, or e) used to stabilize each equation is defined to be the sum of the advective, transient, and diffusive limits for that equation [118]:

$$\tau_j = \left[\frac{1}{(\tau_{adv})^\chi} + \frac{1}{(\tau_{temporal})^\chi} + \frac{1}{(\tau_{diff})^\chi} \right]^{-1/\chi} \quad (15.51)$$

where τ_{adv} , $\tau_{temporal}$, and τ_{diff} are the advection-, temporal-, and diffusion-dominated nondimensional terms to be derived below. This method of summing the various physics-limited τ_j 's is known as the "switching method" because the magnitude of χ indicates how quickly you switch between these different limits. All solution variables in this section are assumed to be in a linear Lagrange basis such that integral evaluation in 1-D is easy. The weak form of the continuity equation is:

$$\underbrace{\int_{\Omega} \frac{\partial \rho}{\partial t} \psi d\Omega - \int_{\Omega} \rho \vec{V} \cdot \nabla \psi d\Omega + \int_{\partial\Omega} \rho \vec{V} \cdot \vec{n} \psi d\Gamma}_{\text{non-stabilized term}} + \underbrace{\sum_{nel} \int_{\Omega_e} \tau_c \vec{V} \cdot \nabla \psi \left[\frac{\partial \rho}{\partial t} + \nabla \cdot (\rho \vec{V}) \right]}_{\text{stabilized term}} d\Omega = 0 \quad (15.52)$$

An incompressible advective limit $\tau_{adv,inc}$ can be defined as the ratio of the magnitudes of the advective term in the stabilized term to the advective term in the non-stabilized term [118]:

$$\begin{aligned}\tau_{adv,inc} &\equiv \left(\frac{\| \int_{\Omega_e} (\vec{V} \cdot \nabla \psi) \nabla \cdot (\rho \vec{V}) d\Omega \|}{\| \int_{\Omega_e} \rho \vec{V} \cdot \nabla \psi d\Omega \|} \right)^{-1} \\ &= \left(\frac{2\|V\|}{h_e} \right)^{-1}\end{aligned}\quad (15.53)$$

This advective term applies for incompressible flow, since ρ was assumed constant so that it could be moved outside the integration to cancel in the numerator and denominator. A compressible version of Eq. (15.53) is formed in an ad hoc manner by simply replacing $\|\vec{V}\|$ by $\|\vec{V}\| + c$, the largest eigenvalue:

$$\tau_{adv,com} \equiv \left(\frac{2(\|\vec{V}\| + c)}{h_e} \right)^{-1} \quad (15.54)$$

Authors disagree on how to assemble τ_{adv} given the incompressible and compressible limits in Eqs. (15.53) and (15.54). Because the compressible limit does not provide a well-behaved incompressible limit, some authors define τ_{adv} as the sum of the incompressible and compressible limits, which also gives increased robustness near stagnation points [122].

The temporal limit can be defined as the ratio of the magnitudes of the time term in the stabilized term to the advective term in the non-stabilized term [118]. A factor of $\Delta t/2$ is used to both obtain the correct units and obtain a Lax-Wendroff method [123].

$$\begin{aligned}\tau_{temporal} &\equiv \left(\frac{2}{\Delta t} \frac{\| \int_{\Omega_e} \rho \vec{V} \cdot \nabla \psi d\Omega \|}{\| \int_{\Omega_e} \rho \vec{V} \cdot \nabla \psi d\Omega \|} \right)^{-1} \\ &= \left(\frac{2}{\Delta t} \right)^{-1}\end{aligned}\quad (15.55)$$

There are no diffusive terms in the continuity equation, so no diffusion-limited components are defined. The time and advective terms in the momentum equation give the same weak form shown in Eq. (15.52) except with ρ is replaced by $\rho_f V_i$ for $i = 1, 2, 3$. So, the momentum equation has the same advection- and transient-limited τ_{ui} components. A diffusive limit for the i -th momentum equation can be derived by neglecting the pressure and gravitational forces, giving the following weak form:

$$\begin{aligned}\underbrace{\int_{\Omega} \frac{\partial(\rho_f V_i)}{\partial t} \psi d\Omega - \int_{\Omega} \rho_f V_i \vec{V} \cdot \nabla \psi d\Omega + \int_{\partial\Omega} \rho_f V_i \vec{V} \cdot \vec{n} \psi d\Gamma + \int_{\Omega} \tau : \nabla \psi d\Omega - \int_{\partial\Omega} \tau : \vec{n} \psi d\Gamma}_{\text{non-stabilized term}} \\ + \underbrace{\sum_{n_{el}} \int_{\Omega_e} \tau_{ui} \vec{V} \cdot \nabla \psi \left(\frac{\partial(\rho_f V_i)}{\partial t} + \nabla \cdot (\rho_f V_i \vec{V}) - \nabla \cdot \tau \right) d\Omega}_{\text{stabilized term}} = 0\end{aligned}\quad (15.56)$$

A diffusive limit for the momentum equation can be defined as the ratio of the magnitudes of the diffusive term in

the stabilized term to the advective term in the non-stabilized term:

$$\begin{aligned}\tau_{diff} &\equiv \left(\frac{\| \int_{\Omega_e} \vec{V} \cdot \nabla \psi \nabla \cdot \tau d\Omega \|}{\| \int_{\Omega_e} \rho_f V_i \vec{V} \cdot \nabla \psi d\Omega \|} \right)^{-1} \\ &= \left(\frac{4\mu}{\rho h_e^2} \right)^{-1}\end{aligned}\quad (15.57)$$

where the final form has assumed incompressibility in order to simplify the evaluation of the tensor gradient. Using the form of the energy equation given in Eq. (2.185) with the compression work, viscous heating, and volumetric viscous heating effects neglected, the weak form is:

$$\begin{aligned}\underbrace{\int_{\Omega} \rho C_p \frac{\partial T}{\partial t} \psi d\Omega + \int_{\Omega} \rho C_p \vec{V} \cdot \nabla T \psi d\Omega - \int_{\Omega} k \nabla T \cdot \nabla \psi d\Omega + \int_{\partial\Omega} k \nabla T \cdot \vec{n} \psi d\Gamma}_{\text{non-stabilized term}} + \\ \underbrace{\sum_{n_{el}} \int_{\Omega_e} \tau_e \vec{V} \cdot \nabla \psi \left[\rho C_p \frac{\partial T}{\partial t} + \rho C_p \vec{V} \cdot \nabla T + \nabla \cdot (k \nabla T) \right] d\Omega}_{\text{stabilized term}} = 0\end{aligned}\quad (15.58)$$

A diffusive limit for the energy equation can be defined as the ratio of the magnitudes of the diffusive term in the stabilized term to the advective term in the non-stabilized term:

$$\begin{aligned}\tau_{diff} &\equiv \left(\frac{\| \int_{\Omega_e} \vec{V} \cdot \nabla \psi \nabla \cdot (k \nabla T) d\Omega \|}{\| \int_{\Omega_e} \rho C_p \vec{V} \cdot \nabla T \psi d\Omega \|} \right)^{-1} \\ &= \left(\frac{4k}{\rho C_p h_e^2} \right)^{-1}\end{aligned}\quad (15.59)$$

In conclusion, using the approach of stabilizing each equation independently in order to solve for the physics-limited τ_j 's, then using these τ_j 's as the diagonal entries of τ_{SUPG} for the matrix-stabilized approach shown in Eq. (15.24), τ_c , τ_m , and τ_e from Eq. (15.50) are defined as follows for the incompressible Navier-Stokes equations with $\chi = 2$:

$$\tau_c = \left[\left(\frac{2\|V\|}{h_e} \right)^2 + \left(\frac{2}{\Delta t} \right)^2 \right]^{-1/2} \quad (15.60a)$$

$$\tau_m = \left[\left(\frac{2\|V\|}{h_e} \right)^2 + \left(\frac{2}{\Delta t} \right)^2 + \left(\frac{4\mu}{\rho h_e^2} \right)^2 \right]^{-1/2} \quad (15.60b)$$

$$\tau_e = \left[\left(\frac{2\|V\|}{h_e} \right)^2 + \left(\frac{2}{\Delta t} \right)^2 + \left(\frac{4k}{\rho C_p h_e^2} \right)^2 \right]^{-1/2} \quad (15.60c)$$

Note that the forms in Eq. (15.60) do not exactly match those shown in Tables 20-22. but all terms are roughly the same. Instead of taking the sum of the various components, some authors take the minimum of each of the limits [63, 122]. The element lengths do not necessarily need to be the same in the advective and diffusive terms, and some authors select different length scales for each component of τ and for each limiting physics [63]. It is sensible that the advective element length be a flow-aligned length scale, but this need not be the case for the diffusive term,

since there is both streamwise and crosswind diffusion. However, in unidirectional flow, the streamwise advection balances the streamwise diffusion, while any crosswind diffusion is to be minimized. For this reason, the diffusive length is often taken equal to the same length scale that is used in the advective limit [122]. Alternatively, the diffusive length can be computed as an average of the representative element lengths.

Methods to compute stabilization parameters unique to each node have also been developed; a comparison amongst the τ computed via Eq. (15.51), via matrix methods, and via vector methods gave almost exactly the same results, so for simplicity these matrix and vector methods are not pursued in Pronghorn [118].

15.4 SUPG Stabilization with the Primitive Equation Set

Work is currently ongoing to include SUPG stabilization for the primitive equation set in Pronghorn.

15.5 SUPG Stabilization with a Single Equation

The previous sections describe the correct system-based way to use SUPG stabilization in Pronghorn, a single-equation stabilization form also exists. For a single equation, such as a problem that only solves the momentum equation given some assumed pressure and density field, Eq. (15.44) shows that SUPG stabilization of that equation requires simply adding a term:

$$\left(S, \tau_j \vec{V} \cdot \nabla \psi \right) \tag{15.61}$$

to each kernel, where S is the strong form of that kernel and τ_j is some scalar stabilization parameter. Because there is only one equation, cross-equation stabilization terms do not exist. For almost every kernel in Pronghorn, a one-equation SUPG kernel exists that provides the residual above. The naming convention is to append SUPG to the name of the kernel to which the SUPG stabilization applies. Note that the single-equation stabilization is *only* correct if the system being solved consists of a single equation.

16 The Finite Element Method

This section discusses the spatial discretization used for the governing equations described in Section 2. The temporal discretization is discussed in Section 17. MOOSE is a FE-based framework. A comprehensive description of the FEM is beyond the scope of this manual, but a brief discussion is given here to introduce the more important terminology and concepts associated with weighted residual methods, of which the FEM is a subset. Then, the most important features of the FEM are described. Finally, a brief discussion on the choice of element size with regards to the porous media method is given.

16.1 Weighted Residual Methods and the Galerkin Method

The FEM is an element-wise application of a weighted residual method that provides specific means for selecting the interpolation functions and BCs that are not specified for a generic weighted residual method. A weighted residual method seeks a solution to a differential equation by assuming the solution u can be expressed as a summation of coefficients C and shape functions ϕ to give an approximate solution u_N .

$$u \approx u_N = \sum_{j=1}^N C_j \phi_j \quad (16.1)$$

where N is the number of shape functions chosen to express the solution. Any differential equation can in general be expressed as $A(u) = f$, where A is an operator that acts on the true solution u , and f is a function that does not contain u . For example, for the continuity equation, this operator is:

$$A() = \left(\frac{\partial()}{\partial t} + \vec{V} \cdot \nabla() + () \cdot \nabla \vec{V} \right) \quad (16.2)$$

and because there are no sources of mass, $f = 0$. To keep the discussion of the numerical method general, all equations will simply be discussed in the form $A(u) = f$. The approximation in Eq. (16.1) in most cases (unless we were extremely lucky in guessing the form of the solution to within a number of multiplicative constants) will not be the true solution, and hence if u_N is substituted back into the governing equation, the equation will not be strictly satisfied. Rather,

$$R = A(u_N) - f \quad (16.3)$$

where R is the residual. The objective is to minimize the residual with respect to a particular norm. The choice of norm about which to minimize is not a trivial manner, and the choice of the norm determines the flavor of the weighted residual approach. A weighted residual method is, in general, a requirement that the integral of the residual over the phase space, multiplied by some weighting function ψ , be zero:

$$\int_{\Omega} R \psi d\Omega = 0 \quad (16.4)$$

Suppose the norm about which to minimize the residual is selected to be the L^2 norm, defined as:

$$\|T\|_2^2 \equiv \int_{\Omega} R^* R d\Omega \quad (16.5)$$

Minimizing the residual with respect to this norm then requires that the residual is minimized with respect to

each coefficient C_j that appears in Eq. (16.1):

$$\frac{\partial}{\partial C_j} \left(\int_{\Omega} R^* R d\Omega \right) = \int_{\Omega} 2R \frac{\partial R}{\partial C_j} d\Omega = 0 \quad (16.6)$$

where differentiation was brought inside the integral because the bounds of the domain are assumed fixed and the residual is assumed real. Eq. (16.6) defines N equations that can be solved to determine the C_j for $j = 1, 2, \dots, N$. This method is called the “Method of Least Squares,” for obvious reasons. A different approach forces the residual to be zero at a discrete number of locations Ω_i such that $R(\Omega_i) = 0$. This can also be written in integral form using delta functions as:

$$\int_{\Omega} R \delta(\Omega - \Omega_i) d\Omega = 0 \quad (16.7)$$

Eq. (16.7) is a collocation method, a term that is generally used for situations where the solution is forced to be exact at discrete locations in the phase space. Both the collocation method and the method of least squares are weighted residual methods, and differ in their selection of ψ in Eq. (16.4), but the methods are not as widely used as the FEM due to the higher computational cost required to obtain the same level of accuracy.

A common choice for ψ is given by the Galerkin method. The Galerkin method chooses optimal weight functions in order to most closely minimize the error:

$$e \equiv u - u_N \quad (16.8)$$

The functions used to construct u_N in Eq. (16.1) “live” in a particular function space, and the true solution may or may not exist within that space. However, for the error to be minimized, e should be orthogonal to u_N , since that will minimize the “distance” between u_N and the true solution. This requires:

$$u_N \cdot e = 0 \quad (16.9)$$

However, the error is not known unless the analytical solution is known, so the above requirement does not provide a useful condition. The best approximation to the error can be given by the residual R . Hence, Galerkin’s method seeks to minimize the residual by requiring that it be orthogonal to the approximate solution u_N :

$$u_N \cdot R = 0 \quad (16.10)$$

While only in special cases are the error and residual the same, Galerkin’s method effectively obtains an approximate solution. Galerkin’s method technically only supplies one equation, while there are N unknowns. However, an even stricter requirement is that the above be true for every C_j in the expansion for u_N provides the needed N equations for N unknowns:

$$\int_{\Omega} C_j \phi_j (A(C_j \phi_j) - f) d\Omega = 0 \quad \text{for } j = 1, 2, \dots, N \quad (16.11)$$

The FEM is most commonly implemented as a Galerkin weighted residual method. The additional stipulations required by the FEM over the Galerkin method discussed here are given in Section 16.2.

16.2 The Finite Element Method

What further differentiates the FEM from the generic Galerkin method is the 1) formulation of the weak form of the differential equation to reduce differentiability requirements, 2) the systematic selection of shape functions that lead

to an element-wise application of the Galerkin method, and 3) the BCs required of the shape functions.

16.2.1 The Weak Form

Many solutions to physical problems are not continuously differentiable. When the higher-order derivatives in the operator A are integrated, infinite or singular values may result, which would make application of the Galerkin method impossible unless higher-order shape functions were used. However, by constructing a weak form, the differentiability requirements on the solution are lowered (a significant cost savings) by transferring some of the differentiation to the weight function. The weak form is constructed by integrating terms by parts when possible, resulting in lower-order terms plus boundary terms. This also provides a very natural way to impose certain BCs. These weak forms have been given for the Pronghorn equations in Eq. (2.301). The weak form is actually more accurate than the strong form because it doesn't assume anything about differentiability of material properties or the solution (more than what is found in the weak form itself). The weak form is identical to the strong form provided the true solution is sufficiently smooth to satisfy the strong form, so the weak form is still an exact representation of the governing physics.

16.2.2 Shape Functions

In addition to solving the weak form of Eq. (16.4), the FEM prescribes specific shape functions. These shape functions are selected such that the domain can be divided into a number of finite elements, where each element has n_{en} element nodes. The solution over the entire domain is then divided into the solution over each of these elements. The solution over a single element, u_h , is the summation of the expansion coefficients in that element, multiplied by the shape functions over that element. One unknown is present for each node in a FE.

$$u_h = \sum_{j=1}^{n_{en}} C_j \phi_j \quad (16.12)$$

The shape functions are defined such that ϕ_j is unity at node j and zero at all other nodes. This results in localized shape functions and a sparse matrix system because distant shape functions do not overlap in space. This also allows the FEM to be applied element-wise.

By requiring the shape functions to be zero on all nodes but one, continuity is enforced along elements edges, since the solution along a boundary between two or more elements is defined only by the nodes that lie along that boundary (and the local-to-global mapping discussed in the next section ensures continuity at nodes).

A 2-D four-node element can, in principle, be either a rectangle or some other 2-D shape - consider a triangle with a centrally-positioned node, for example. The solution at any point in this triangle is given by:

$$u(\xi_1, \xi_2) = C_1 + C_2 \xi_1 + C_3 \xi_2 + C_4 \xi_1 \xi_2 \quad (16.13)$$

Along edges of the rectangle, $\xi_1 = \pm 1$ or $\xi_2 = \pm 1$. Inserting, for instance, $\xi_1 = 1$ into the above equation gives $u = (C_1 + C_2) + (C_3 + C_4)\xi_2$ - a solution that is linear along the edge. Because two nodes exist on that edge, a linear function can be exactly described, and the solution between two rectangular elements will be continuous at all points along the shared boundary. On the other hand, consider a four-node triangle with one edge described by $\xi_1 = \xi_2$. Along this edge, the solution is $u = C_1 + (C_2 + C_3)\xi_2 + C_4 \xi_2^2$. This quadratic cannot be exactly described using only the two nodes that exist on the triangle edge, and hence the solution will only be continuous at shared nodes.

In principle, any set of functions can be used as the shape functions provided that the integrals in the weak form remain finite. One way to ensure that the integrals remain finite is to require the shape functions to "live" within a particular function space. The Hilbert Sobolev space is defined as $H^l(\Omega)$, where l refers to the highest finite derivative

of the function. For instance, a square wave lives in $H^0(\Omega)$, since its first derivative is infinite at locations where the wave height changes. A piecewise function lives in $H^1(\Omega)$, since first derivatives are everywhere defined, but jumps in the second derivatives lead to infinite integrals when measured in the H^2 norm. The Hilbert-space norm is defined in 1-D for a vector u consisting of I entries as:

$$\|u\|_{H^l(\Omega)} \equiv \left[\sum_{j=0}^l \int_{\Omega} \frac{d^j u}{dx^j} \frac{d^j u}{dx^j} d\Omega \right]^{1/l} \quad (16.14)$$

A function is in $H^l(\Omega)$ if $\|u\|_{H^l(\Omega)} < \infty$. The weight functions in the Bubnov-Galerkin method are equivalent to the shape functions, so both must be at least the minimum Hilbert space required from the weak form. These preliminaries would also apply to a generic weighted residual method, and it is really that the shape functions are nodal, i.e. unity at a single node and zero elsewhere, that is a defining characteristic of the FEM. In addition, the shape functions should be complete (contain all lower orders) and linearly independent.

When a kernel is integrated by parts, a new volume integral and a boundary integral result. In this boundary integral, it is convenient to require the shape functions to go to zero at Dirichlet nodes, since this then eliminates one of the BCs from the solve (though its information must be removed from the solve to avoid singularities, as discussed near Eq. (16.22)). Shape functions that are zero at boundaries are not required to satisfy Neumann BCs, however, so Neumann conditions are only weakly imposed.

The most common shape functions used in the FEM are the Lagrange, Hermite, and Spline shape functions, with linear Lagrange shape functions used by default in MOOSE. Lagrange shape functions are simply polynomials that interpolate between nodes. The order of Lagrange shape functions refers to the order of the polynomial over each element. The Lagrange shape functions are a nodal basis, and satisfy:

$$\sum_{j=1}^{n_{en}} \phi_j(\Omega_j) = 1 \quad (16.15a)$$

$$\sum_{j=1}^{n_{en}} \frac{\partial \phi_j}{\partial \Omega} = 0 \quad (16.15b)$$

Lagrange shape functions have discontinuous derivatives at element boundaries, but if continuity is desired, then Hermite shape functions can be used.

16.2.3 Implementation Considerations

The shape functions discussed in Section 16.2.2 would be very tedious to compute for each element, since each element is positioned in a different location in space with different coordinates that must be interpolated by a polynomial. So, all shape functions are defined over a “master” element, and all calculations are performed in this master domain. The master domain can be mapped back to the physical domain, giving the desired numerical solution. This master domain, for a general 3-D domain, is defined for $-1 \leq \xi_1 \leq 1, -1 \leq \xi_2 \leq 1, -1 \leq \xi_3 \leq 1$. To solve on the master domain, all integrals must be transformed to the master domain. The transformation between physical and master domains is given by:

$$d\vec{x} = \mathcal{J} d\vec{\xi} \quad (16.16)$$

where the Jacobian matrix of the transformation has entries given by:

$$dx_i = \frac{\partial x_i}{\partial \xi_j} d\xi_j \quad (16.17)$$

Then, an integral in higher dimensions is transformed as:

$$\int_a^b \int_c^d \int_e^f f(x_1, x_2, x_3) dx_1 dx_2 dx_3 \rightarrow \int_{-1}^1 \int_{-1}^1 \int_{-1}^1 f(x_1(\xi_1, \xi_2, \xi_3), x_2(\xi_1, \xi_2, \xi_3), x_3(\xi_1, \xi_2, \xi_3)) |J| d\xi_1 d\xi_2 d\xi_3 \quad (16.18)$$

In 1-D, the Jacobian simplifies to $J = dx/d\xi$, which for constant-size elements gives $J = h_e/2$. In 1-D, the Jacobian can be interpreted as the ratio of element length in the physical domain to that in the master domain. While volume integrals transform according to Eq. (16.18), boundary integrals do not. Boundary integrals transform according to Nanson's rule, since the boundary does not necessarily transform in a manner proportional to how the volume transforms. To transform a boundary integral, denoted here as a 2-D integration:

$$dx_1 dx_2 = \left(|J| J^{-T} \cdot \vec{n}_x \right) \cdot \vec{n}_\xi d\xi_1 d\xi_2 \quad (16.19)$$

where \vec{n}_x and \vec{n}_ξ are unit vectors to the surfaces in the physical and master domains, respectively. The mapping $x_i(\xi_1, \xi_2, \xi_3)$ can take a variety of forms, but is generally categorized into three main types:

1. Subparametric - the mapping is of lower order than the shape functions. This mapping is used when the physical data is of lower-order than the desired solution order.
2. Isoparametric - the mapping is of the same order as the shape functions. This mapping, which tends to be the most common, is usually performed using the shape functions of the numerical solution:

$$x_i(\xi_1, \xi_2, \xi_3) = \sum_{i=1}^{n_{en}} X_i \phi_i(\xi_1, \xi_2, \xi_3) \quad (16.20)$$

where X_i is the physical node coordinate.

3. Superparametric - the mapping is of higher order than the shape functions. This type of mapping is used to capture physically-curved geometries without needing to use high-order shape functions. In other words, linear elements can be used to obtain the solution in curved domains, where the *domain* is approximated using higher-order mappings.

Quadrature rules are used for approximating the integrals that appear in the residual statements because analytical integration is generally not possible. An integral is approximated by sampling the integrand at n_{qp} quadrature points, multiplying each evaluation by a weight w , and then summing over all quadrature points:

$$\int_a^b f(x) dx \approx \sum_{i=1}^{n_{qp}} w_i f(x_i) \quad (16.21)$$

Quadrature rules can often be interpreted as interpolating the integrand into a polynomial, and then integrating that polynomial exactly. The error in the quadrature rule can then be related to the error in interpolating the integrand into a polynomial of a certain order. Because all integrals occur over $-1 \leq \xi_i \leq 1$, quadrature rules defined over this range can readily be used. The quadrature rule is selected in LibMesh. Extra computational effort expended in obtaining higher accuracy numerical integration is better spent refining the mesh than using a higher-order quadrature rule. The

error is lowest at the quadrature points, and hence some finite element codes use the values at the quadrature points for the purposes of post-processing.

Two of the most common quadrature sets are the Newton-Cotes and Gaussian quadrature sets. Newton-Cotes quadrature rules are derived by expanding the integrand in Lagrange polynomials using equally-space quadrature points, and then analytically performing the integration to determine the weights. All Newton-Cotes quadrature rules of order \mathcal{N} will exactly integrate polynomials of order $\mathcal{N} - 1$. But, odd- \mathcal{N} rules gain an extra degree of integration, due to higher-order derivatives dropping from Taylor series expansions, so an odd- \mathcal{N} order quadrature rule will exactly integrate a polynomial of order \mathcal{N} .

Gaussian quadrature rules use unevenly-spaced nodes with locations optimized to maximize the polynomial degree that can be exactly integrated. The nodes are generally located closer to the domain boundaries, but do not include the boundaries themselves. Gaussian quadrature is generally preferred to Newton-Cotes quadrature for several reasons:

1. For higher-order polynomials, evenly-spaced node placement causes some weights to be negative, leading to unpredictable behavior and catastrophic cancellation. For fluids applications, having more quadrature points closer to the edges of an element is also advantageous from a boundary layer perspective.
2. Closed Newton-Cotes rules, which place some nodes on the boundaries of the domain, incur difficulties when there are inherent discontinuities at those boundaries. While the solution is continuous at element boundaries when using continuous FEM, its gradient may not be, which would complicate integration.
3. Gaussian quadrature rules can exactly integrate polynomials of higher degree with less quadrature points. An \mathcal{N} -point Gaussian quadrature rule can integrate exactly a polynomial of degree $2\mathcal{N} - 1$.

While the error associated with a Newton-Cotes quadrature rule can easily and cost-effectively be estimated by application of two different Newton-Cotes quadrature rules (since nodes are usually repeated in quadrature rules of varying order), because Gaussian quadrature does not lead to large numbers of shared nodes between different \mathcal{N} -point rules, Gaussian-Kronrod quadrature rules are developed in pairs such that the nodes for the $2\mathcal{N} + 1$ point Kronrod rule re-use all nodes of the corresponding pair \mathcal{N} -point Gaussian rule. Gauss-Kronrod rules provide high accuracy and a reliable error estimate, and hence form the basis of many quadrature rule packages.

Before solving a matrix system $\mathbf{A}\vec{x} = \vec{b}$, Dirichlet coefficients must be removed from the problem, or else the system is singular and unsolvable. The matrix system can be written as:

$$\begin{bmatrix} A_{uu} & A_{uk} \\ A_{ku} & A_{kk} \end{bmatrix} \begin{bmatrix} u_u \\ u_k \end{bmatrix} = \begin{bmatrix} b_u \\ b_k \end{bmatrix} \quad (16.22)$$

where u refers to unknown values (non-Dirichlet nodes) and k refers to known values (Dirichlet nodes). Hence the actual equation that is solved is $A_{uu}x_u = b_u - A_{uk}x_k$. The known Dirichlet information is subtracted from the RHS vector. Section 17 discusses the methods used to solve the discretized matrix system and how the solve is marched forward in time.

An alternative to removing the Dirichlet nodes from the solve is to use the “penalty” method. This method essentially applies another force to the weak form that simulates a spring force with a very high spring constant that acts to “pull” the solution to the Dirichlet value on a boundary. A penalty term is added to the stiffness matrix:

$$\text{penalty term} = P^* \int_{\partial\Omega} \psi(d - u)d\Gamma \quad (16.23)$$

where P^* is a large positive constant number, and d is the value on the Dirichlet boundary. The penalty method is associated with several important problems, however. Because P^* must be very large to get accurate enforcement of Dirichlet conditions, the stiffness matrix will contain terms that are very large relative to other

terms at locations corresponding to boundary nodes, and this may produce an ill-conditioned system. However, if weak enforcement of Dirichlet conditions is acceptable, the penalty method may be useful.

16.3 The Accuracy of the Finite Element Method

This section address the accuracy of the FEM using functional notation. A generic bilinear functional B is an operation that returns a scalar from an input of two variables and is linear with respect to those two variables. A generic linear functional L is similar to a bilinear functional, except that it depends on only one variable. This section assumes that the shape and weight functions exist in the same functional space, i.e. a Bubnov-Galerkin discretization. For a symmetric stiffness matrix, the weak form can be stated in terms of functionals as:

$$B(u_N, \Psi) = L(\Psi) \quad (16.24)$$

A norm useful for evaluating the accuracy of the FEM is the energy norm, defined as:

$$\|u\|_{E(\Omega)}^2 \equiv B(u, u) \quad (16.25)$$

The error, when measured in the energy norm, satisfies the following convergence property:

$$\|u - u_h\|_{E(\Omega)} \leq C(u, \mathcal{N}) h_e^{\min(r-1, \mathcal{N})} \quad (16.26)$$

where \mathcal{N} is the order of the shape functions, r is the regularity of the exact solution, and C is an unknown constant that depends on the polynomial order and the exact solution. For C^∞ smooth functions, the regularity is infinite. For rough solutions, the lowest theoretical value of r is $3/2$. When measured in the Hilbert norm for $r \geq s$:

$$\|u - u_h\|_{H^s(\Omega)} \leq C(u, \mathcal{N}) h_e^{\min(r-s, \mathcal{N}+1-s)} \quad (16.27)$$

Both Eq. (16.26) and (16.27) are global norms, where h_e should be taken to be the largest element in the mesh. Based on Eq. (16.27), to reduce the error it is almost always preferable to increase polynomial order than to refine the mesh.

For symmetric B , the finite element method satisfies the “best approximation property.” Eq. (16.24) can be written for both the true and numerical solutions:

$$B(u, \Psi) = L(\Psi) \quad (16.28a)$$

$$B(u_h, \Psi) = L(\Psi) \quad (16.28b)$$

Subtracting the two equations from each other gives:

$$B(e_h, \Psi) = 0 \quad (16.29)$$

where e_h is the error on a single element:

$$e_h \equiv u - u_h \quad (16.30)$$

e_h, u_h , and ψ all lie in the same space, so subtracting off a function ψ from e_h produces another function z_h in the same space. Hence, $e_h - \psi \equiv u - u_h - \psi = u - z_h$ is true for any function z_h that also satisfies the Dirichlet BCs. Using this, the following can be defined, where the critical assumption of the best approximation property is that B is linear such that $B(e_h, \psi) = B(\psi, e_h)$.

$$B(e_h - \psi, e_h - \psi) = B(e_h, e_h) - \cancel{2B(e_h, \psi)} + B(\psi, \psi) \quad (16.31)$$

where Eq. (16.29) has been used. Because $B(\psi, \psi)$ is always positive:

$$B(u - z_h, u - z_h) \geq B(u - u_h, u - u_h) \quad (16.32)$$

This is the best approximation property of the FEM. Any function z_h that also satisfies the Dirichlet BCs will have a higher error when measured in the energy norm than the FE solution. Hence, when measured in the energy norm, the FE solution is the closest possible solution to the true solution. This best approximation property only applies for linear B , however, and does not hold for the nonlinear system of equations in Pronghorn.

For symmetric systems, the weak form can also be cast in terms of a minimization principle. This is equivalent to viewing a differential equation as a minimization of total energy, as opposed to the more traditional means of viewing an equation stating conservation of energy. The weight function is a virtual change, or a variation, of the primary variable. A potential \mathcal{Y} can be defined by manipulation of the definition of the energy norm in Eq. (16.25):

$$\begin{aligned} \|u - \psi\|_{E(\Omega)}^2 &\equiv B(u - \psi, u - \psi) \equiv B(u, u) - 2B(u, \psi) + B(\psi, \psi) \\ &= 2B(u, u) - B(u, u) - 2B(u, \psi) + B(\psi, \psi) \\ &= -B(u, u) + B(\psi, \psi) - 2B(u, \psi - u) \\ &= -B(u, u) + B(\psi, \psi) - 2L(\psi) + 2L(u) \\ &= 2\mathcal{Y}(\psi) - 2\mathcal{Y}(u) \end{aligned} \quad (16.33)$$

which leads naturally to the definition of the potential as:

$$\mathcal{Y}(\psi) = \frac{1}{2}B(\psi, \psi) - L(\psi) \quad (16.34)$$

Because the energy norm is always positive, $\mathcal{Y}(\psi) \geq \mathcal{Y}(u)$. In other words, if u represents the true solution and ψ the FE solution, the FE solution always has higher potential energy than the true solution. In addition, the true solution has the *minimum* potential energy. This is often referred to as the “principal of minimum potential energy,” which can be shown by applying a small perturbation λv to $\mathcal{Y}(u)$ and then taking the partial derivative of \mathcal{Y} with respect to λ for $\lambda = 0$. The perturbation is set to zero at the minimum because a zero perturbation corresponds to the exact solution. For instance, for 1-D heat conduction, this minimization process is:

$$\begin{aligned} \left. \frac{\partial \mathcal{Y}(u + \lambda v)}{\partial \lambda} \right|_{\lambda=0} &= \left. \frac{\partial}{\partial \lambda} \left[\frac{1}{2} \int_{\Omega} k \left(\frac{d(u + \lambda v)}{dx} \right)^2 dx - \int_{\Omega} f(u + \lambda v) dx \right] \right|_{\lambda=0} \\ &= \left. \frac{1}{2} \int_{\Omega} 2k \frac{d(u + \lambda v)}{dx} \frac{dv}{dx} dx \right|_{\lambda=0} - \left. \int_{\Omega} f(v) dx \right|_{\lambda=0} \\ &= \int_{\Omega} \frac{du}{dx} k \frac{dv}{dx} dx - \int_{\Omega} f(v) dx \end{aligned} \quad (16.35)$$

This minimization process simply returns the weak form. By setting the above equal to zero, we require that the potential be at a minimum at the true solution. By taking the second derivative of \mathcal{Y} with respect to λ , it

can be shown that \mathcal{Y} represents a minimum (as opposed to a maximum).

$$\frac{\partial^2 \mathcal{Y}(u + \lambda v)}{\partial \lambda^2} = \int_{\Omega} \frac{dv}{dx} k \frac{dv}{dx} \equiv \|v\|_{E(\Omega)}^2 \geq 0 \quad (16.36)$$

Only symmetric systems can be written as a minimization problem, however, so the discussion here, like the “best approximation property,” does not apply to Pronghorn.

16.4 The Choice of Mesh Size

The porous media equations are derived by averaging the local conservation equations over a representative volume of fluid and solid with dimensions larger than the pore scale, but smaller than the characteristic scale of the system. This feature of the method should *not* impact mesh refinement size. The mesh used for the FE discretization should be made as fine as desired to achieve a given *numerical* error, with the recognition that a small numerical error does not necessarily translate to a small error in representing a complicated fluid-solid mixture. The mesh size should be selected based on the desired numerical accuracy in solving the governing porous media equations.

Several researchers have coupled DEM codes with porous media CFD codes, where the coupling primarily occurs through the calculation of porosity and specific surface areas for use in the porous media code [56,87]. The commonly-used approach for computing porosity from a bed of spheres for use in a porous media code is to compute the ratio of fluid to solid volume in each CFD cell. This approach has two major limitations:

1. If the CFD mesh elements are too small, then the statistical noise in computing porosity is very high, and the porosity will vary substantially from element to element. In small core regions such as defueling chutes where small elements are needed for the CFD solution, special treatments for computing porosity such as averaging over multiple elements, has to be performed [56]. A minimum element size to avoid high statistical noise also limits the possibility of mesh refinement studies.
2. Computing porosity (and other quantities such as pebble power [56]) by averaging over the element restricts the representation in the CFD code to elementwise constant values. For Finite Volume (FV) porous media codes that restrict the solution space to elementwise constant values, this may not be a concern. But for FE and spectral CFD codes, this loss of information may degrade accuracy, especially when the elements cannot be made smaller due to the previous issue.

From the theoretical discussion surrounding the choice of averaging volume size in Section 2.2, one solution to this problem is to compute porosity not on a one-to-one mapping of DEM volume to CFD cell, but by averaging porosity over a larger space in the DEM solution, and applying the averaged value to the cell at the centroid of that space in the CFD mesh [76]. For example, the porosity for a CFD cell could be computed by averaging the porosity of that cell, and all of its neighbors, in the DEM space. The average in neighboring CFD cells would not be completely linearly independent, but the variation from cell to cell would be smoother than that shown in [56]. For mesh refinement studies, the number of neighboring cells to average over could be made proportional to the inverse of the element size to retain approximate equivalence in porosity and other constitutive terms across mesh sizes.

17 Solution of Nonlinear Equations

Systems of linear equations will always have zero, one, or infinitely many (eigenvalue problem) solutions. Nonlinear systems, however, can have any number of solutions, and will not necessarily have a solution for every choice of BCs. There are many examples of the Navier-Stokes equations yielding non-unique solutions and bifurcations from one flow state to another from the same BCs and ICs [22] (chapter 2). Several of these non-unique solutions are predicted from theory, so experimental observations cannot simply be attributed to a lack of precision. Non-unique solutions tend to exist once a representative dimensionless number reaches a threshold value; for linear systems, a steady-state solution may not exist, but existence is not determined by a dimensionless number threshold. Upon reaching this threshold, the system state will transition between the possible states stationary and non-stationary solutions; if no stationary solutions exist, a steady-state solution cannot be obtained, even if the BCs and all source terms are constant. Very accurate discretizations and solution schemes are required to resolve multiple solutions and bifurcations.

The most well-known example of the non-uniqueness of the Navier-Stokes equations is flow past a circular cylinder. For this system, the vorticity generated in the boundary layers diffuses into the flow and causes two symmetrical vortices to develop on the back side of the cylinder. The strength of these vortices increases with Reynolds number. Beyond a critical Reynolds number, the slightest instability causes one of these vortices to increase in strength above the other, drawing the other vortex into it and breaking symmetry. This stronger vortex is convected away from the cylinder, allowing the smaller vortex to increase and continue the same growth and consumption/destruction process, known as vortex shedding, in a periodic fashion. Provided the Reynolds number is above the critical threshold, this system never reaches steady state despite steady BCs [22] (chapter 2). Accounting for the finite length of the cylinder and compressibility still show non-unique solutions and bifurcations between multiple steady solutions and multiple non-steady solutions, where the Mach number also dictates the presence of multiple solutions.

This section discusses the method for solving the nonlinear system of equations in Pronghorn. Section 16 discussed the spatial discretization of the governing equations using the FEM into a form:

$$\vec{R}(u) = 0 \quad (17.1)$$

where \vec{R} represents a vector of discretized equations (the residual vector) and u the numerical solution vector. For simplicity, the remainder of this section departs from the convention in the rest of this manual of indicating vectors with an arrow. This section discusses the solution to this nonlinear, discretized equation. The nonlinear methods discussed in this section are all forms of fixed point iteration, where the solution is successively improved by iteration. Eq. (17.1) cannot be solved directly using *linear* algebra methods because it is not of the form of a *linear* problem such as:

$$\mathbf{A}x = b \quad (17.2)$$

where \mathbf{A} is a matrix, x is the solution vector, and b is the RHS vector. The first step of solving nonlinear equations is to linearize the equation into the form in Eq. (17.2). Once in a linear form, one of the linear solution methods discussed in Section 17.2 is used to solve for the next iterate. So, the numerical method in MOOSE consists of (at least) two iteration loops -

1. An outer loop over *nonlinear* iterations that compute better and better guesses to u in Eq. (17.1), and
2. an inner loop over *linear* iterations that compute better and better guesses to x in Eq. (17.2).

Once the linear solution method has computed x that sufficiently solves Eq. (17.2), that x is used in a simple update formula to compute the updated u . In the remainder of this section, i is used for the outer loop iteration index and k

for the inner loop index. MOOSE solves nonlinear equations using the Jacobian-Free Newton Krylov (JFNK) method, which is a combination of a Newton method for the outer iterations and a Generalized Minimum Residual Method (GMRES) Krylov subspace method for the inner iterations. After discussing Newton methods in Section 17.1 and Krylov methods in Section 17.2, Section 17.3 combines the two pieces together.

17.1 Newton's Method

Newton's method forms a linear approximation (about the current iterate u_i) to the root-finding problem in Eq. (17.1) by forming the Taylor series expansion for the next solution iterate:

$$\vec{R}(u_{i+1}) = \vec{R}(u_i) + \frac{\partial \vec{R}(u_i)}{\partial u} (u_{i+1} - u_i) + \mathcal{O}((u_{i+1} - u_i)^2) = 0 \quad (17.3)$$

By neglecting quadratic and higher-order terms, an iterative update formula results:

$$\frac{\partial \vec{R}(u_i)}{\partial u} (u_{i+1} - u_i) = -\vec{R}(u_i) \quad (17.4a)$$

$$\mathbf{J}(u_i) \delta_i = -\vec{R}(u_i) \quad (17.4b)$$

where \mathbf{J} is the Jacobian of the Newton solve:

$$\mathbf{J}(u_i) \equiv \frac{\partial \vec{R}(u_i)}{\partial u} \quad (17.5a)$$

$$J_{lm}(u_i) \equiv \frac{\partial R_l(u_i)}{\partial u_m} \quad (17.5b)$$

Eq. (17.4) is of the form $\mathbf{A}x = b$ and is solved for:

$$\delta_i \equiv u_{i+1} - u_i \quad (17.6)$$

using one of the linear solution methods discussed in Section 17.2.

For the conservative equation set in Pronghorn, \vec{R} is:

$$\vec{R} = [\vec{R}_c \quad \vec{R}_u \quad \vec{R}_f \quad \vec{R}_s]^T \quad (17.7)$$

where \vec{R}_i represents a discretized residual vector:

$$\begin{aligned}
R_c(\rho_f) &= \left(\varepsilon \frac{\partial \rho_f}{\partial t}, \Psi \right) + \left(-\varepsilon \rho_f \vec{V}, \nabla \Psi \right) + \left\langle \varepsilon \rho_f \vec{V}, \Psi \right\rangle \\
\vec{R}_u(\rho_f \vec{V}) &= \left(\varepsilon \frac{\partial \rho_f V_i}{\partial t} - \varepsilon \rho_f g_i + W \rho_f V_i - P \nabla \varepsilon, \Psi \right) + \left(-\varepsilon \rho_f V_i \vec{V} - \varepsilon P, \nabla \Psi \right) + \left\langle \varepsilon \rho_f V_i \vec{V} + \varepsilon P, \Psi \right\rangle \\
R_f(\rho_f E) &= \left(\varepsilon \frac{\partial (\rho_f E)}{\partial t} - \varepsilon \vec{g} \cdot \rho_f \vec{V} + \alpha (T_f - T_s) - q_f, \Psi \right) + \left(-\varepsilon H_f \rho_f \vec{V} + \kappa_f \nabla T_f, \nabla \Psi \right) + \left\langle \varepsilon H_f \rho_f \vec{V} - \kappa_f \nabla T_f, \Psi \right\rangle \\
R_s(T_s) &= \left((1 - \varepsilon) \rho_s C_{p,s} \frac{\partial T_s}{\partial t} + \alpha (T_s - T_f) - q_s, \Psi \right) + \left(\kappa_s \nabla T_s, \nabla \Psi \right) - \left\langle \kappa_s \nabla T_s, \Psi \right\rangle
\end{aligned} \tag{17.8}$$

where the subscripts c , m , s , and f refer to the continuity, momentum, fluid energy, and solid energy equations, respectively. The solution vector u is a single vector containing all problem unknowns. For example, the solution vector is of the form:

$$u = \left[\rho_{f,1} \quad (\rho_f V)_{x,1} \quad (\rho_f V)_{y,1} \quad (\rho_f V)_{z,1} \quad (\rho_f E)_1 \quad T_{s,1} \quad \cdots \quad \rho_{f,n} \quad \rho_f V_{x,n} \quad \rho_f V_{y,n} \quad \rho_f V_{z,n} \quad (\rho_f E)_n \quad T_{s,n} \right]^T \tag{17.9}$$

where the numbered subscripts denote node numbers, n is the total number of nodes, and the entries of u are the expansion coefficients C_j from Eq. (16.12). The Jacobian is a matrix, where each row corresponds to a particular governing equation, and each column to a particular solution variable. For the conservative equation set in Pronghorn, the nonlinear variables are ρ , $\rho_f \vec{V}$, $\rho_f E$, and T_s . The Jacobian is then:

$$\mathbf{J} = \begin{bmatrix} \frac{\partial R_c}{\partial \rho_f} & \frac{\partial R_c}{\partial (\rho_f \vec{V})} & \frac{\partial R_c}{\partial (\rho_f E)} & \frac{\partial R_c}{\partial T_s} \\ \frac{\partial R_m}{\partial \rho_f} & \frac{\partial R_m}{\partial (\rho_f \vec{V})} & \frac{\partial R_m}{\partial (\rho_f E)} & \frac{\partial R_m}{\partial T_s} \\ \frac{\partial R_f}{\partial \rho_f} & \frac{\partial R_f}{\partial (\rho_f \vec{V})} & \frac{\partial R_f}{\partial (\rho_f E)} & \frac{\partial R_f}{\partial T_s} \\ \frac{\partial R_s}{\partial \rho_f} & \frac{\partial R_s}{\partial (\rho_f \vec{V})} & \frac{\partial R_s}{\partial (\rho_f E)} & \frac{\partial R_s}{\partial T_s} \end{bmatrix} \tag{17.10}$$

Note that the Jacobian is not a 4×4 matrix - it is a 4×4 *blocked* matrix, where each block is $n \times n$.

For simple roots (roots that do not also coincide with the root of a derivative of \vec{R}), Newton's method converges quadratically. However, for multiple roots, Newton's method only converges linearly. These linear and quadratic convergence rates are only valid for starting points sufficiently close to the true solution, and if the solve begins too far away from the solution, Newton's method may not converge. Damped Newton methods, available in MOOSE, improve the likelihood of convergence when using a Newton method by restricting the step size taken in each iteration so that overshoot past small features of \vec{R} is reduced. The convergence of Newton's method is greatly aided when all of the entries of the Jacobian are known. In general this is not analytically possible, and writing derivatives may be error-prone. So, while most of the classes in Pronghorn provide on-diagonal and off-diagonal Jacobian entries, some are only approximated.

17.2 Solution of Linear Equations

After linearization of the nonlinear problem, any number of linear solution methods can be applied to solve the resulting system of equations. The true solution to Eq. (17.2) is denoted as x_* . The residual R is defined in Eq. (16.3), with $u_N \leftarrow x$. The error e is defined in Eq. (16.8), with $u_N \leftarrow x$. The error usually cannot be known, since this implies

knowledge of the true solution, so the residual is often used as an indication of the accuracy of the numerical solution. However, if a large change in the numerical solution leads to a correspondingly small change in the residual, then the residual will not be a good indication of convergence. An equivalent form of Eq. (17.2) is:

$$\mathbf{A}e = -R \quad (17.11)$$

Eq. (17.2) can be solved with either direct or iterative methods, which are discussed in Sections 17.2.1 and 17.2.2, respectively.

17.2.1 Direct Methods

Direct methods solve the linear system by factoring \mathbf{A} and performing forward and/or backward substitution. Direct methods are most commonly applied to dense \mathbf{A} because the cost of the repeated matrix-vector products required of the iterative methods discussed in Section 17.2.2 is often of the same order as the factorization. In addition, iterative methods are not always guaranteed to converge. And, although not applicable for the systems of equations in Pronghorn, if \mathbf{A} is a constant matrix, then direct methods permit a single factorization to be used repeatedly to solve for x for any number of vectors b . Direct methods are typically not useful for sparse \mathbf{A} because factorization can result in substantial fill-in such that the factorized \mathbf{A} can be significantly denser than the original matrix. Because the default time discretization method is implicit, the governing equations are nonlinear, and direct methods do not perform well for the sparse matrices that results from the FEM, direct methods are not used in MOOSE and are not discussed further in this manual.

17.2.2 Iterative Methods

Iterative methods are well-suited for sparse \mathbf{A} because the cost of a sparse matrix-vector product is low enough that multiple iterations are still less expensive than direct methods. The FEM produces sparse systems, so iterative methods are a natural choice in MOOSE. The remainder of this section presents a detailed description of some of the most common iterative methods to provide the necessary concepts to understand the GMRES algorithm that is used in MOOSE. All iterative methods begin from some initial guess x_0 and successively update this initial guess at each iteration:

$$\begin{aligned} x_{k+1} &= x_k + \alpha_k p_k \\ &= x_0 + \sum_{i=0}^k \alpha_i p_i \end{aligned} \quad (17.12)$$

where α_k is a step length and p_k the update vector. By recursion, this update is equivalent to adding k update vectors to the initial guess x_0 . By definition of the error in Eq. (16.8), subtracting x_* from both sides of Eq. (17.12) gives an equivalent form:

$$\begin{aligned} e_{k+1} &= e_k + \alpha_k p_k \\ &= e_0 + \sum_{i=0}^k \alpha_i p_i \end{aligned} \quad (17.13)$$

By the definition of the residual in Eq. (16.3), multiplying Eq. (17.12) by $-\mathbf{A}$ and adding b to both sides produces

a third equivalent form, which by recursion can also be written as successive subtractions from an initial residual.

$$\begin{aligned} R_{k+1} &= R_k - \alpha_k \mathbf{A} p_k \\ &= R_0 - \sum_{i=0}^k \alpha_i \mathbf{A} p_i \end{aligned} \quad (17.14)$$

When iterative methods are given good beginning guesses, they can converge very rapidly. For transient simulations, the starting vector is often selected as the solution from the most recently computed time step, which generally improves convergence properties with every time step (provided the time steps are not extremely large). The differences in the iterative methods discussed in this section reduce to differences in the selection of the α_k and p_k . A useful construct in the development of iterative methods for Symmetric Positive Definite (SPD) systems discussed in Sections 17.2.2.2-17.2.2.4 is the “quadratic form” $\mathcal{Y}(x)$:

$$\mathcal{Y}(x) \equiv \frac{1}{2} x^T \mathbf{A} x - b^T x \quad (17.15)$$

By comparing Eq. (17.15) to Eq. (16.34), the quadratic form is the same as the potential \mathcal{Y} introduced earlier, but written in vector notation. The gradient of the quadratic form with respect to x is:

$$\begin{aligned} \frac{\partial \mathcal{Y}(x)}{\partial x} &= \frac{1}{2} (x^T \mathbf{A} + \mathbf{A} x) - b \\ &= \frac{1}{2} (\mathbf{A}^T x + \mathbf{A} x) - b \\ &= \mathbf{A} x - b \end{aligned} \quad (17.16) \quad (\text{if } \mathbf{A} \text{ is symmetric})$$

Hence, if \mathbf{A} is symmetric, the solution to the linear equation occurs where the gradient of $\mathcal{Y}(x) = 0$. In other words, for symmetric \mathbf{A} , the solution to the equation can be equivalently found by setting $\mathcal{Y}'(x) = 0$. The location(s) at which $\mathcal{Y}'(x) = 0$ depends on the properties of \mathbf{A} , which determine the shape of $\mathcal{Y}(x)$. A matrix can be either definite or indefinite, as defined in Section 18.5. If \mathbf{A} is symmetric and definite, then the location at which $\mathcal{Y}'(x) = 0$ either corresponds to minimization of $\mathcal{Y}(x)$ (SPD \mathbf{A}) or maximization of $\mathcal{Y}(x)$ (Symmetric Negative Definite (SND) \mathbf{A}). If \mathbf{A} is indefinite, the solution is a saddle point, and $\mathcal{Y}'(x) = 0$ does not correspond to a minimum or a maximum. If \mathbf{A} is not symmetric, then iterative methods that seek to minimize $\mathcal{Y}(x)$ actually find a solution to the system $(\mathbf{A}^T x + \mathbf{A} x)/2 - b = 0$, which is symmetric.

In order to determine why a definite matrix corresponds to minimization or maximization of $\mathcal{Y}(x)$, evaluate Eq. (17.15) at a point slightly perturbed by an error e from the true solution:

$$\begin{aligned} \mathcal{Y}(x_* + e) &= \frac{1}{2} (x_* + e)^T \mathbf{A} (x_* + e) - b^T (x_* + e) \\ &= \frac{1}{2} (x_*^T \mathbf{A} x_* + e^T \mathbf{A} e + x_*^T \mathbf{A} e + e^T \mathbf{A} x_*) - b^T x_* - b^T e \\ &= \mathcal{Y}(x_*) + \frac{1}{2} (x_*^T \mathbf{A} e + e^T \mathbf{A} x_*) + \frac{1}{2} e^T \mathbf{A} e - b^T e \end{aligned} \quad (17.17)$$

If \mathbf{A} is symmetric:

$$\begin{aligned} \mathcal{Y}(x_* + e) &= \mathcal{Y}(x_*) + e^T \mathbf{A} x_* + \frac{1}{2} e^T \mathbf{A} e - b^T e \\ &= \mathcal{Y}(x_*) + \frac{1}{2} e^T \mathbf{A} e \end{aligned} \quad (17.18)$$

If \mathbf{A} is SPD, the second term in Eq. (17.18) is always positive, so the true solution occurs at the minimum of $\mathcal{Y}(x)$. If \mathbf{A} is SND, the second term is always negative, and the true solution occurs at the maximum of $\mathcal{Y}(x)$.

A SND matrix can always be transformed to a SPD matrix by negating it, so the remainder of this section will refer to the true solution as the *minimum* of $\mathcal{Y}(x)$, with the understanding that the nomenclature applies for both SPD and SND matrices. From Eq. (17.18), minimizing the energy norm of the error is equivalent to minimizing \mathcal{Y} .

For symmetric \mathbf{A} , the contour lines of \mathcal{Y} are n -dimensional ellipsoids. The Steepest Descent (SD) and Conjugate Gradient (CG) methods discussed in Sections 17.2.2.2 and 17.2.2.4 are methods that utilize information regarding the contours of \mathcal{Y} to iterate an initial guess to a point near where $\mathcal{Y}'(x) = 0$. Other, simpler iterative methods do not utilize information regarding contour lines of \mathcal{Y} . Rather, these matrix splitting algorithms, discussed in Section 17.2.2.1, convert the system in Eq. (17.2) to a split fixed-point form.

17.2.2.1 Matrix Splitting Methods

The Jacobi, Gauss-Seidel, and Successive Over-Relaxation (SOR) methods are classical iterative methods that are based on splitting \mathbf{A} into multiple matrices, at least one of which is easy to invert. \mathbf{A} is split into diagonal, lower triangular, and upper triangular matrices:

$$\mathbf{A} = \mathbf{D} + \mathbf{L} + \mathbf{U} \quad (17.19)$$

The simplest example of a matrix splitting method is the Jacobi method. The Jacobi method only uses previously-known values to update diagonal entries, so the problem becomes:

$$\mathbf{D}x_{k+1} = -(\mathbf{L} + \mathbf{U})x_k + b \quad (17.20a)$$

$$x_{k+1} = \mathbf{B}x_k + z \quad (17.20b)$$

where \mathbf{B} is given by:

$$\mathbf{B} \equiv \mathbf{D}^{-1}(\mathbf{L} + \mathbf{U}) \quad (17.21)$$

This method is an iterative method - the solution is obtained by repeatedly applying \mathbf{B} to an initial guess. Consider the generic update in Eq. (17.20)b. Express the previous iterate x_k as the true solution plus some error:

$$x_{k+1} = \mathbf{B}(x_* + e_k) + z \quad (17.22a)$$

$$e_{k+1} = \mathbf{B}e_k \quad (17.22b)$$

Provided the spectral radius of \mathbf{B} is less than unity, each iteration reduces the eigenvector components of the error. Hence, matrix-splitting methods are referred to as “smoother” methods, since with every iteration all eigenvector error components are decreased. The large-eigenvalue components will be the slowest to converge. However, because the matrix \mathbf{B} has different properties than \mathbf{A} , Jacobi is not guaranteed to converge for every \mathbf{A} , or even for every positive-definite \mathbf{A} .

17.2.2.2 The Steepest Descent Method

The SD method updates each iterative guess x_k by searching along the direction of SD of $\mathcal{Y}(x_k)$ and selecting the next guess x_{k+1} to lie somewhere along this SD direction [124]. By definition, the gradient corresponds to the direction

of steepest *increase* of $\mathcal{Y}(x)$. So, the SD direction is simply the negative of the gradient given in Eq. (17.16). By the definition of the residual in Eq. (16.3),

$$-\frac{\partial \mathcal{Y}(x)}{\partial x} = R \quad (17.23)$$

The SD method selects $p_k = R_k$. The step size along this direction is selected such that $\mathcal{Y}'(x_{k+1}) = 0$ along the line p_k (x_{k+1} provides the minimum of $\mathcal{Y}(x_{k+1})$ along the search direction). This gives:

$$\begin{aligned} \frac{\partial \mathcal{Y}(x_{k+1})}{\partial \alpha} &= \frac{\partial}{\partial \alpha} \left[\frac{1}{2} (x_k + \alpha_k p_k)^T \mathbf{A} (x_k + \alpha_k p_k) - b_k^T (x_k + \alpha_k p_k) \right] \\ &= \frac{\partial}{\partial \alpha} \left[\frac{1}{2} x_k^T \mathbf{A} x_k + \alpha_k p_k^T \mathbf{A} x_k + \frac{\alpha_k^2}{2} p_k^T \mathbf{A} p_k - b_k^T (x_k + \alpha_k p_k) \right] \quad (\text{symmetric } \mathbf{A}) \\ &= p_k^T \mathbf{A} x_k + \alpha_k p_k^T \mathbf{A} p_k - b_k^T p_k \end{aligned} \quad (17.24)$$

Setting the above equal to zero in order to find the minimum gives:

$$\alpha_k = \frac{p_k^T R_k}{p_k^T \mathbf{A} p_k} \quad (17.25)$$

The directional derivative in Eq. (17.24) can also be written in compact, chain-rule form to provide an important interpretation of this choice of α_k :

$$\begin{aligned} \frac{\partial \mathcal{Y}(x_{k+1})}{\partial \alpha} &= \frac{\partial \mathcal{Y}(x_{k+1})}{\partial x_{k+1}} \frac{\partial x_{k+1}}{\partial \alpha} \\ &= -R_{k+1}^T p_k \\ &= (\mathbf{A} e_{k+1})^T p_k \\ &= e_{k+1}^T \mathbf{A} p_k \quad (\text{symmetric } \mathbf{A}) \end{aligned} \quad (17.26)$$

where the update in Eq. (17.12) has been used to compute $\partial x_{k+1} / \partial \alpha$ and the last form uses Eq. (17.11). So with this choice of α , the residual at the next iterate is orthogonal to the previous search direction, which can equivalently be interpreted as the next iterate's error being A-orthogonal to the previous search direction. The SD method requires that the error at the next iterate by A-orthogonal to the previous search direction. The fact that the updated residual and previous search direction are orthogonal makes sense when considering the minimization process performed in Eq. (17.24) - the minimum of $\mathcal{Y}(x)$ will occur at a location tangent to a contour line of \mathcal{Y} , and the gradient is always orthogonal to the contour lines of a field. For the SD method, where the search direction is taken equal to the residual, this means that the next search direction is orthogonal to the previous search direction (likewise, the next residual is orthogonal to the previous residual).

The SD method has two important downsides - \mathbf{A} has to be SPD and the convergence rate of the method is relatively poor. For a SPD matrix where the condition number is given by Eq. (18.22), the convergence rate is given as:

$$\begin{aligned} \|e_{k+1}\|_A^2 &\leq \left(\frac{\kappa - 1}{\kappa + 1} \right) \|e_k\|_A^2 \\ &\leq \left(\frac{\kappa - 1}{\kappa + 1} \right)^{k+1} \|e_0\|_A^2 \end{aligned} \quad (17.27)$$

Consider an SPD \mathbf{A} such that \mathbf{A} has n linearly independent eigenvectors. The error can be expressed as a linear combination of orthonormalized (such that $v_i^T v_j = \delta_{ij}$) eigenvectors:

$$e_k = \sum_{j=1}^n \xi_j v_j \quad (17.28)$$

where ξ_j is the coefficient for each term in the summation. From Eq. (17.13) with α_k from Eq. (17.25) and $p_k \equiv R_k$:

$$\begin{aligned} e_{k+1} &= e_k + \alpha_k p_k \\ &= e_k + \frac{R_k^T R_k}{R_k^T \mathbf{A} R_k} R_k \\ &= e_k + \frac{\sum_{j=1}^n \lambda_j^2 \xi_j^2}{\sum_{j=1}^n \lambda_j^3 \xi_j^2} R_k \end{aligned} \quad (17.29)$$

If the initial error has only one eigenvector component, only one iteration is required to reach the exact solution, since the eigenvectors align with the axes of the ellipsoid and the search direction passes through the exact solution. Alternatively, if all the eigenvalues are equal, then from Eq. (17.11), $R_k = -\lambda e_k$, convergence is also obtained in exactly one iteration, since the contour lines are circular, and any starting point has a residual that points directly to the center. For either of these simple cases, choosing $\alpha_k = \lambda^{-1}$ gives convergence in one iteration. Because there will most often be multiple eigenvector components, the fraction in Eq. (17.29) can be interpreted as a weighted value of $1/\lambda$, where the weights ξ_j^2 emphasize that the largest terms are decreased with highest priority. In any iteration, not all eigenvector error components are guaranteed to decrease (as they are with matrix-splitting methods), so the SD and CG method discussed in Section 17.2.2.4 are known as “rougher methods.”

Recall from Eq. (17.18) that minimization of the energy norm of the error is equivalent to minimization of \mathcal{U} . By Eq. (17.13) and with $p_k \equiv R_k$ and α_k from Eq. (17.25):

$$\begin{aligned} \|e_{k+1}\|_A^2 &= (e_k + \alpha_k R_k)^T \mathbf{A} (e_k + \alpha_k R_k) \\ &= e_k^T \mathbf{A} e_k + 2\alpha_k R_k^T \mathbf{A} e_k + \alpha_k^2 R_k^T \mathbf{A} R_k \quad (\text{symmetric } \mathbf{A}) \\ &= \|e_k\|_A^2 \left[1 - \frac{(R_k^T R_k)^2}{(R_k^T \mathbf{A} R_k)(e_k^T \mathbf{A} e_k)} \right] \\ &= \|e_k\|_A^2 \left[1 - \frac{\left(\sum_{j=1}^n \xi_j^2 \lambda_j^2 \right)^2}{\sum_{j=1}^n \xi_j^2 \lambda_j^3 \sum_{j=1}^n \xi_j^2 \lambda_j} \right] \end{aligned} \quad (17.30)$$

For \mathbb{R}^2 , the above becomes:

$$\|e_{k+1}\|_A^2 = \|e_k\|_A^2 \left[1 - \frac{(\xi_1^2 \lambda_1^2 + \xi_2^2 \lambda_2^2)^2}{(\xi_1^2 \lambda_1^3 + \xi_2^2 \lambda_2^3)(\xi_1^2 \lambda_1 + \xi_2^2 \lambda_2)} \right] \quad (17.31)$$

For a normal matrix, the condition number is given by Eq. (18.22). The slope of e_k relative to the coordinate system defined by the eigenvectors is $\mu \equiv \xi_2/\xi_1$. In terms of these definitions, the above becomes:

$$\|e_{k+1}\|_A^2 = \|e_k\|_A^2 \left[1 - \frac{(\kappa^2 + \mu^2)^2}{(\kappa + \mu^2)(\kappa^3 + \mu^2)} \right] \quad (17.32)$$

If the initial error is an eigenvector (slope is zero or infinite), or if the condition number is unity (contour lines are circular), then the method converges in one iteration. The worst convergence is obtained for large condition numbers and poor starting guesses, though the condition number is the more indicative of the two.

Large condition numbers lead to very skinny ellipsoids, resulting in many back-and-forth iterations that do not move very quickly to the solution. The worst-case convergence can be bounded by taking the partial derivative of the parenthesis term above with respect to κ to find that the worst convergence is obtained for $\mu^2 = \kappa^2$. Substituting this into the above gives the convergence rate given in Eq. (17.27).

17.2.2.3 The Conjugate Directions Method

A major drawback of the SD method is obvious from Eq. (17.26) - because each search direction is only orthogonal to the *previous* direction, the same directions are searched over and over again without expanding the space of the search with each iteration. The Conjugate Directions (CD) method is based on the idea that convergence could be obtained in n iterations, where each iteration exactly zeros one component of the error [124]. This requirement is read as:

$$e_{k+1}^T p_k = 0 \quad (17.33a)$$

$$(e_k + \alpha_k p_k)^T p_k = 0 \quad (17.33b)$$

where Eq. (17.13) is used to rewrite e_{k+1} . Solving for α_k gives:

$$\alpha_k = -\frac{e_k^T p_k}{p_k^T p_k} \quad (17.34)$$

However, this would require that e_k be known at every iteration, which is not possible. Instead, the method of CD requires that e_{k+1} be A-conjugate to p_k , the same requirement (and resulting formula for α_k in Eq. (17.25)) as the SD method shown in Eq. (17.26). While simply choosing $p_k = R_k$ will not necessarily lead to convergence in n iterations, selecting A-conjugacy of the search directions will lead to exact convergence in n iterations. So for the CD method, select:

$$p_i^T \mathbf{A} p_j = 0, \quad i \neq j \quad (17.35)$$

To show that Eq. (17.35) leads to exact convergence in n iterations, because mutually A-orthogonal vectors are linearly independent, the initial error can be expressed as a linear combination of search directions with (positive) coefficients ξ_j :

$$e_0 = \sum_{j=0}^{n-1} \xi_j p_j \quad (17.36)$$

where indexing begins at zero such that the indexing is consistent with the zero-indexing in Eq. (17.13). Then, by A-conjugacy of the search directions, premultiplying both sides above by $p_k^T \mathbf{A}$ picks out a single term from the summation in Eq. (17.36):

$$p_k^T \mathbf{A} e_0 = \xi_k p_k^T \mathbf{A} p_k \quad (17.37)$$

Solving for δ_k and using Eq. (17.13) (for e_k instead of e_{k+1} as written) to rewrite e_0 gives:

$$\begin{aligned}
\xi_k &= \frac{p_k^T \mathbf{A} e_0}{p_k^T \mathbf{A} p_k} \\
&= \frac{p_k^T \mathbf{A} \left(e_0 + \sum_{i=0}^{k-1} \alpha_i p_i \right)}{p_k^T \mathbf{A} p_k} \quad (\text{A-conjugate } p_k) \\
&= \frac{p_k^T \mathbf{A} e_k}{p_k^T \mathbf{A} p_k} \\
&= -\alpha_k
\end{aligned} \tag{17.38}$$

Hence, the step length α_k is identical to the length of the error's p_k component - because this term is successively subtracted from the error, the CD method is exact in n iterations. Eq. (17.13) becomes:

$$\begin{aligned}
e_{k+1} &= e_0 + \sum_{i=0}^k \alpha_i p_i \\
&= \sum_{j=0}^{n-1} \xi_j p_j - \sum_{i=0}^k \xi_i p_i \\
&= \sum_{j=k+1}^{n-1} \xi_j p_j
\end{aligned} \tag{17.39}$$

So, if $k = n$, the CD method has converged to the exact solution. A conjugate Gram-Schmidt process is used to generate the set of A-orthogonal search directions. Starting from a set of n linearly independent (i.e. orthogonal) vectors u_i , subtract from each of these vectors the components that are not A-orthogonal:

$$p_i = u_i - \sum_{j=0}^{i-1} \beta_{ij} p_j \tag{17.40}$$

The choice for β_{ij} can be determined by multiplying both sides above by $p_i^T \mathbf{A}$ and taking advantage of A-conjugacy of the search directions. The CG method aims to provide a better set of orthogonal vectors such that better convergence is obtained. From Eq. (17.13) and by A-conjugacy of the search directions giving the result in Eq. (17.38), with each iteration, the error is minimized in the space $e_0 + \mathcal{K}_k$, where \mathcal{K}_k is the subspace span of the search directions:

$$\mathcal{K}_k \equiv \text{span}\{p_0, p_1, \dots, p_k\} \tag{17.41}$$

such that $e_{k+1} \in e_0 + \mathcal{K}_k$. Because the error is a vector, "minimization" actually refers to minimization in the energy norm. To show this, express the energy norm in terms of linear combinations of the search directions, where e_{k+1} is given by Eq. (17.39) and A-conjugacy of the search directions is used:

$$\begin{aligned}
\|e_{k+1}\|_A &= \sum_{i=k+1}^{n-1} \sum_{j=k+1}^{n-1} \xi_i \xi_j p_i^T \mathbf{A} p_j \\
&= \sum_{i=k+1}^{n-1} \xi_i^2 p_i^T \mathbf{A} p_i
\end{aligned} \tag{17.42}$$

Each term in this summation represents a search direction that has not yet been traversed. Any other vector will have at least one of these additional terms present because this vector would be linearly independent from e_{k+1} , and

hence e_{k+1} must have the minimum energy norm in the space $e_0 + \mathcal{K}_k$. Minimization of \mathcal{Y} along the search direction in a single step is shown by Eq. (17.26). At further iterations, \mathcal{Y} is not only minimized over the single step search direction, but over the entire space $x_0 + \mathcal{K}_k$! This was not the case with the SD method, which only minimizes along a single line. Because the search directions are mutually A-orthogonal, in a circular contour space, they are orthogonal, and hence when allowed to search on the hyperplane $x_0 + \mathcal{K}_k$, \mathcal{Y} is minimized on the plane.

At each step, the hyperplane $x_0 + \mathcal{K}_k$ is tangent to the ellipsoid on which x_{k+1} lies based on the choice of α_k in Eq. (17.25). Because the residual by definition is orthogonal to the ellipsoidal contour lines, $R_{k+1} \perp \mathcal{K}_k$. From Eq. (17.41), each new search direction is mutually A-orthogonal to all previous search directions, so R_{k+1} is orthogonal to *all* previous search directions. From Eq. (17.11), e_{k+1} is A-orthogonal to all previous search directions. It can also be shown that if R_{k+1} is orthogonal to the vectors spanning \mathcal{K}_k , that R_{k+1} is orthogonal to all of the previous vectors used to form the initial set of linearly independent vectors u_i that were conjugated to form \mathcal{K}_k .

17.2.2.4 The Conjugate Gradient Method

The CG method is simply the CD method, with u_i taken to be R_i such that the search directions are determined by conjugation of the residuals [124]. R_{k+1} is orthogonal to \mathcal{K}_k , so the residual is guaranteed to provide new, linearly independent search direction for the next iteration. Because the search directions are built by conjugation of the residuals, the space defined in Eq. (17.41) can be expanded to include Eq. (17.43)b, c, and d:

$$\mathcal{K}_k \equiv \text{span}\{p_0, p_1, \dots, p_k\} \quad (17.43a)$$

$$= \text{span}\{R_0, R_1, \dots, R_k\} \quad (17.43b)$$

$$= \text{span}\{p_0, \mathbf{A}p_0, \dots, \mathbf{A}^{k-1}p_0\} \quad (17.43c)$$

$$= \text{span}\{R_0, \mathbf{A}R_0, \dots, \mathbf{A}^{k-1}R_0\} \quad (17.43d)$$

From Eq. (17.14), each residual is a linear combination of the previous residual and $\mathbf{A}p_k$. So, because $p_k \in \mathcal{K}_k$, each successive subspace is formed as the union of the previous subspace and $\mathbf{A}\mathcal{K}_k$, giving Eqs. (17.43)c and (17.43)d. A Krylov subspace is a subspace created by repeatedly applying a matrix to a vector. \mathcal{K}_k is therefore a Krylov space. Because $R_{k+1} \perp \mathcal{K}_k$, and because $\mathcal{K}_{k+1} \perp \mathcal{K}_k$, $R_{k+1} \perp \mathcal{K}_{k+1}$. Hence, because \mathcal{K}_{k+1} is A-orthogonal to \mathcal{K}_k , R_{k+1} is A-orthogonal to \mathcal{K}_k . So, the Gram-Schmidt conjugation process becomes substantially easier, since R_{k+1} only needs to be A-conjugated with \mathcal{K}_k , since the residual is already A-conjugate to all of the previous search directions except p_k .

17.2.2.5 The Arnoldi Process and the GMRES Algorithm

The GMRES algorithm is one of the most widely used iterative algorithms that alleviates the SPD requirement of the SD and CG methods. The GMRES algorithm solves a least-squares problem in every iteration to find the best solution in the space $x_0 + \mathcal{K}_k$. To solve this least-squares problem, we require an orthonormal basis for \mathcal{K}_k , which is denoted as:

$$\mathbf{Q}_k = \begin{bmatrix} q_1 & q_2 & \dots & q_k \end{bmatrix}^T \quad (17.44)$$

where each column of \mathbf{Q}_k represents an orthonormal vector of length n , and n of these vectors are required to span \mathcal{K}_k . The vectors in \mathbf{Q}_k can be determined in an iterative procedure via the Arnoldi process. Similar to the process of determining the next search direction for the CG method (which we simply took to be the residual), each iteration of the Arnoldi process requires starting from some new linearly independent vector u and orthonormalizing it to \mathcal{K}_k using a Gram-Schmidt procedure. A natural choice would be simply to compute the next vector in the Krylov space,

$\mathbf{A}^k R_0$. However, as k becomes large, the vectors in \mathcal{K}_k become increasingly linearly dependent because formation of the Krylov subspace in this manner is equivalent to power iteration. So, the vectors in the Krylov space are not used directly.

The starting vector u_{k+1} for computing q_{k+1} is selected as $u_{k+1} = \mathbf{A}q_k$. Because q_k is orthonormalized against all previous basis vectors in \mathbf{Q}_k , this new direction does not tend to be aligned with an eigenvector. In addition, with this choice, the Arnoldi process can be interpreted as building up a factorization of \mathbf{A} (which is needed to solve the least-squares problem). For each iteration, u_{k+1} is orthogonalized via a Gram-Schmidt procedure against all previous vectors in \mathbf{Q}_k ; after orthogonalization, u_{k+1} is normalized to a unit vector. For each iteration, the Arnoldi process adds one vector, q_{k+1} to \mathbf{Q}_k by the following procedure:

$$\begin{aligned} u_{k+1} &= \mathbf{A}q_k \\ u_{k+1} &= u_{k+1} - \underbrace{q_i^T u_{k+1}}_{h_{ik}} q_i, \quad \text{for } i < k+1 \quad (\text{orthogonalization}) \end{aligned} \quad (17.45)$$

$$q_{k+1} = u_{k+1} / \underbrace{\|u_{k+1}\|}_{h_{k+1,k}} \quad (\text{normalization}) \quad (17.46)$$

From the definitions of h_{ik} and $h_{k+1,k}$ in the algorithm above, we can define a matrix of these values of size $k+1 \times k$:

$$\tilde{\mathbf{H}}_k = \begin{bmatrix} h_{11} & h_{12} & h_{13} & \cdots & h_{1k} \\ \|u_2\| & h_{22} & h_{23} & \cdots & h_{2k} \\ 0 & \|u_3\| & h_{33} & \cdots & h_{3k} \\ 0 & 0 & \|u_4\| & \ddots & h_{4k} \\ 0 & 0 & 0 & \cdots & \|u_{k+1}\| \end{bmatrix} \quad (17.47)$$

Truncating this matrix to size $k \times k$ by eliminating the last row defines the upper Hessenberg matrix \mathbf{H}_k . In iteration k , the newly-computed, orthonormalized vector is:

$$u_{k+1} = \mathbf{A}q_k - h_{1k}q_1 - h_{2k}q_2 - \cdots - h_{kk}q_k \quad (17.48)$$

Repeating this pattern for u_i , $i < k+1$ shows that:

$$\begin{aligned} \mathbf{A}\mathbf{Q}_k &= \mathbf{Q}_k \mathbf{H}_k + u_{k+1} e_k^T \\ &= \mathbf{Q}_{k+1} \tilde{\mathbf{H}}_k \end{aligned} \quad (17.49)$$

where $e_k = [0 \ 0 \ \cdots \ 1]^T$. If the Arnoldi process is performed for $k = n$ iterations, then in the n -th iteration, we will find that $\mathbf{A}q_n$ lies in \mathcal{K}_n because the basis \mathbf{Q}_n is already all of \mathbb{R}^n . So, subtracting out all components that are \mathbf{A} -orthogonal results in $q_{n+1} = 0$, so there is no $h_{n+1,n} \equiv \|u_{n+1}\|$ or q_{n+1} values. So, after performing n iterations in the Arnoldi process, Eq. (17.49) becomes:

$$\mathbf{A}\mathbf{Q} = \mathbf{Q}\mathbf{H} \quad (17.50a)$$

$$\mathbf{A} = \mathbf{Q}\mathbf{H}\mathbf{Q}^T \quad (17.50b)$$

Eq. (17.50) shows that complete application (n iterations) of the Arnoldi process reduces \mathbf{A} to upper-Hessenberg form by a similarity transformation. The objective of the Arnoldi process, however, is *not* to perform n iterations.

Instead, after some smaller number of iterations, we want to compute the next iterate x_{k+1} from the space $x_0 + \mathcal{K}_k$ by minimizing the L^2 norm of the residual over $x_0 + \mathcal{K}_k$. Because the vectors in \mathbf{Q}_k form a basis for \mathcal{K}_k , we can instead specify that x_{k+1} be in:

$$x_{k+1} = x_0 + \mathbf{Q}_k y_k \quad (17.51)$$

for some vector $y_k \in \mathbb{R}^k$. The residual is:

$$\begin{aligned} R_{k+1} &= b - \mathbf{A}(x_0 + \mathbf{Q}_k y_k) \\ &= R_0 - \mathbf{A} \mathbf{Q}_k y_k \\ &= R_0 - \mathbf{Q}_{k+1} \tilde{\mathbf{H}}_k y_k \end{aligned} \quad (17.52)$$

where Eq. (17.49) is used. Because the first column in \mathbf{Q}_{k+1} is simply the starting point of the Arnoldi process, $R_0 / \|R_0\|$, the residual can be expressed as:

$$R_0 = \mathbf{Q}_{k+1} \eta \quad (17.53)$$

where $\eta = \left[\|R_0\|_2 \quad 0 \quad \cdots \quad 0 \right]^T$. So, R_{k+1} becomes:

$$R_{k+1} = \mathbf{Q}_{k+1} (\eta - \tilde{\mathbf{H}}_k y_k) \quad (17.54a)$$

$$\|R_{k+1}\|_2 = \|\eta - \tilde{\mathbf{H}}_k y_k\|_2 \quad (17.54b)$$

where the norm of both sides is taken, using $\mathbf{Q}_{k+1}^T \mathbf{Q}_{k+1} = \mathbf{I}$. So, in each iteration of GMRES, the next iterate solution is obtained by minimization of the L^2 norm of the residual by solving a least squares problem for y_k , and then using Eq. (17.51) to solve for the next iterate x_{k+1} :

$$\min_{y_k \in \mathbb{R}^k} \|\eta - \tilde{\mathbf{H}}_k y_k\| \quad (17.55)$$

Note that the GMRES algorithm does not perform a least squares minimization over the entire space \mathcal{K}_k , but over the smaller space built up by the Arnoldi process of solving a least squares problem over k basis vectors for \mathcal{K}_k .

17.3 The Jacobian-Free Newton-Krylov Method

MOOSE combines an outer Newton iteration to solve for the solution u with an inner Krylov subspace method to solve for the linear approximation x . This combination is referred to as a ‘‘Newton-Krylov’’ method, though this name is often used in the literature to imply one extra caveat - that the Jacobian is never explicitly formed. $\mathbf{J}(u_i) \delta_i$ in Eq. (17.4) simply represents the directional derivative of $\vec{R}(u_i)$ in the direction of the vector δ_i . While the Jacobian holds directional derivative information for all directions, the goal of iterative methods is to perform searches in a small number of directions such that the directional derivative information is only needed for a few of these directions such that formation of the Jacobian is not needed. ‘‘Newton-Krylov’’ methods, or JFNK methods, approximate the action of the Jacobian on the vector δ_i using a first-order accurate FD derivative:

$$\mathbf{J}(u_i) \approx \frac{\vec{R}(u_i + \epsilon \delta_i) - \vec{R}(u_i)}{\epsilon} \quad (17.56)$$

where ϵ is a small number, typically chosen as $\epsilon = \sqrt{\epsilon_{mach}}$, where ϵ_{mach} is the machine precision, to balance accuracy of the FD approximation with potential overflow from division by a small number. Eq. (17.56) means that the user never needs to supply a Jacobian for the kernels in MOOSE - the Jacobians are provided solely for preconditioning purposes. Due to the importance of preconditioning, however, Jacobians should always be provided when possible.

17.4 Time Stepping

The MOOSE framework, like virtually all FE codes, uses separable space-time shape functions. Space-time elements, where $\psi = \psi(\vec{r}, t)$, are typically reserved for research codes and are an uncommon approach to transient finite element analysis because time steps in the future can impact time steps in the past (which has no physical basis), there is a big increase in the number of unknowns, and the majority of codes use the Method of Lines (MOL) time discretization, which would be difficult to adapt. With separable space-time shape functions, the shape functions are only functions of space, while the expansion coefficients are time-dependent. At discrete points in time, the nonlinear system of equations is solved, and the solution is then advanced in time using a time integration method.

MOOSE uses the MOL time discretization method, where the solution is marched forward in time with any of a wide variety of Ordinary Differential Equation (ODE) solvers. To illustrate the MOL method, consider the use of the Backward Euler (BE) method, the default time discretization method in MOOSE, for a time-dependent diffusion equation:

$$\frac{du}{dt} - k \frac{d^2u}{dx^2} = 0 \quad (17.57)$$

The weak form is derived by multiplying through by a weight function and integrating the diffusive term by parts giving a matrix system $M_{ij}\dot{C}_j + K_{ij}C_j = 0$, where:

$$M_{ij} = \int_{\Omega} \phi_i \phi_j dx \quad (17.58a)$$

$$K_{ij} = \int_{\Omega} \frac{d\phi_i}{dx} k \frac{d\phi_j}{dx} dx \quad (17.58b)$$

and C_j are the expansion coefficients of the solution and Neumann BCs have been assumed for simplicity. In matrix form, the discrete equation is:

$$\mathbf{M}\dot{\mathbf{a}} + \mathbf{K}\mathbf{a} = 0 \quad (17.59)$$

For the BE time discretization method, the MOL becomes:

$$M_{ij} \frac{C_{j,n+1} - C_{j,n}}{\Delta t} + K_{ij} C_{j,n+1} = 0 \quad (17.60)$$

The solution at each successive time step is obtained by solving for $C_{j,n+1}$ in terms of $C_{j,n}$. For implicit methods such as the BE method, an iterative method such as a Newton method is required to solve at each time step.

Time stepping to reach a steady-state solution is often performed due to the enhanced stability of the transient equation. Generally, time-independent fluid equations have different mathematical character (hyperbolic, parabolic, elliptic) depending on the Mach number [22] (chapter 3). However, the same equations, in transient form, have the same mathematical character regardless of dimensionless numbers, which permits better selection of a numerical method to solve for all flow regimes. If difficulty related to stability of steady-state problems is encountered, try time

stepping to the steady-state solution. For these cases, it is preferable to only approximately solve the system at each time step because time accuracy is not required - a similar idea is used in coupled Monte Carlo-CFD simulations [63, 125].

18 Mathematical Definitions and Concepts

This section discusses some mathematical definitions and concepts that appear throughout this manual.

18.1 The Material Derivative

A material derivative represents a total derivative of a quantity from the Eulerian perspective, and hence accounts for both local changes ($\partial(\cdot)/\partial t$) and changes that occur as the fluid particle moves about ($\vec{V} \cdot \nabla(\cdot)$). The material derivative is defined as:

$$\frac{d(\cdot)}{dt} \equiv \underbrace{\frac{\partial(\cdot)}{\partial t}}_{\text{local derivative}} + \underbrace{\vec{V} \cdot \nabla(\cdot)}_{\text{convective derivative}} \quad (18.1)$$

The convective derivative portion is equivalent to the component of the gradient of (\cdot) along the streamline (parallel to \vec{V}).

18.2 Norms

A vector norm is a measure of the “size” of a vector. The p -norm, also known as L^p norm, of a vector \vec{x} of n entries is defined as:

$$\|\vec{x}\|_p \equiv \left(\sum_{i=1}^n |x_i|^p \right)^{1/p} \quad (18.2)$$

Other norms are used throughout this manual, and are introduced where appropriate.

18.3 Suffix Notation

Suffix notation, sometimes referred to as “Einsteinien” notation, is commonly used in mechanics fields to shorten summation notation. Suffix notation obeys the following rules:

1. A single appearance of a suffix in a term does not get summed.
2. Two appearances of a suffix in a term indicates summation (usually up to 3, the typical number of spatial dimensions used).
3. No more than two appearances of the same suffix can appear in a single term.

For example, a dot product between a vector \vec{a} and \vec{b} is represented in suffix notation as:

$$\begin{aligned} \vec{a} \cdot \vec{b} &\equiv \sum_{i=1}^3 a_i b_i \\ &= a_i b_i \end{aligned} \quad (18.3)$$

A cross product can be represented in suffix notation as:

$$(\vec{a} \times \vec{b})_i = \epsilon_{ijk} a_j b_k \quad (18.4)$$

where ϵ_{ijk} is the permutation, defined as:

$$\epsilon_{ijk} = \begin{cases} +1 & \text{cyclic permutation of 1, 2, 3} \\ -1 & \text{anti-cyclic permutation of 1, 2, 3} \\ 0 & \text{otherwise} \end{cases} \quad (18.5)$$

Another useful term that appears when using suffix notation is the Kronecker delta, defined as:

$$\delta_{ij} = \begin{cases} +1 & i = j \\ 0 & i \neq j \end{cases} \quad (18.6)$$

18.4 Vectors and Tensors

A vector is an ordered triplet (for 3-D) of numbers, together with a rule defining how the vector transforms under a change of coordinate axes. This rule can be easily obtained by considering two different sets of axes, each composed of three mutually orthogonal axes. Denoting one of these axes with primes and the other without, a vector can be expressed equivalently in either frame:

$$\vec{r} = x_k \vec{e}_k = x_{k'} \vec{e}_{k'} \quad (18.7)$$

Dotting this expression with either $\vec{e}_{i'}$ or \vec{e}_i :

$$x_{i'} = \vec{e}_k \cdot \vec{e}_{i'} x_k = a_{ik} x_k \quad (18.8a)$$

$$x_i = \vec{e}_{k'} \cdot \vec{e}_i x_{k'} = a_{ki} x_{k'} \quad (18.8b)$$

where a_{ik} is the transformation rule. As long as a matrix satisfies the transformation rule in Eq. (18.8), the matrix is a vector. Because the transformation matrices are independent of time, they can be differentiated with respect to time (or multiplied by constants) to show that physical quantities such as velocities and forces are also vectors, so long as position is a vector.

Tensors t are defined in a similar manner. A tensor is essentially a matrix that transforms one vector to another vector with the following transformation rule, where a is defined as in Eq. (18.8). Tensors therefore transform vectors into new vector spaces.

$$t_{ik'} = a_{ij} a_{kl} t_{jl} \quad (18.9)$$

A symmetric tensor S_{ij} satisfies the relation $S_{ij} = S_{ji}$, while an antisymmetric tensor A_{ij} satisfies the relation $A_{ij} = -A_{ji}$. The product of a symmetric tensor with an asymmetric tensor must equal zero:

$$S_{ij} A_{ij} \rightarrow S_{ji} A_{ij} \rightarrow -S_{ji} A_{ji} \rightarrow -S_{ij} A_{ij} \quad (18.10)$$

where the dummy indices were swapped on the last term.

18.5 Essential Linear Algebra

A matrix is indefinite if:

$$\vec{x}^T \mathbf{A} \vec{x} = 0 \quad (18.11)$$

for some nonzero vector \vec{x} . Contrarily, a matrix is definite if:

$$\vec{x}^T \mathbf{A} \vec{x} \neq 0 \quad (18.12)$$

A definite matrix can be either positive or negative. A matrix is positive-definite if:

$$\vec{x}^T \mathbf{A} \vec{x} > 0 \quad (18.13)$$

Similarly, a matrix is negative-definite if:

$$\vec{x}^T \mathbf{A} \vec{x} < 0 \quad (18.14)$$

A singular matrix does not have a unique solution, and the set of solutions is a line or hyperplane, rather than a point in \mathbb{R}^n . A singular matrix has a zero determinant.

The eigenvectors of \mathbf{A} are nonzero vectors \vec{v} that do not rotate (but may change magnitude) when \mathbf{A} is applied to them. This definition is represented in equation form as:

$$\mathbf{A} \vec{v} = \lambda \vec{v} \quad (18.15)$$

where λ is the eigenvalue corresponding to the eigenvector \vec{v} . The eigenvalue represents the scaling of \vec{v} when \mathbf{A} is applied to it. The eigenvalues do not need to be unique. Each eigenvector can be scaled by an arbitrary constant β , and still have the same eigenvalue:

$$\mathbf{A}(\beta \vec{v}) = \beta \mathbf{A} \vec{v} = \beta \lambda \vec{v} \quad (18.16)$$

Repeated application of \mathbf{A} to an eigenvector will cause the resultant vector either to grow to infinity or diminish to zero depending on the magnitude of the eigenvalue:

$$\mathbf{A}^i \vec{v} = \lambda^i \vec{v} \quad (18.17)$$

If \mathbf{A} is symmetric, then there exist n linearly independent eigenvectors. A set of n linearly independent vectors defines a basis in \mathbb{R}^n , so any vector in \mathbb{R}^n can therefore be written as a linear combination of the eigenvectors. So, applying \mathbf{A} to an arbitrary vector \vec{f} is equivalent to applying \mathbf{A} to a linear combination of eigenvectors:

$$\mathbf{A}^i \vec{f} = \sum_{j=1}^n C_j \lambda_j^i \vec{v}_j \quad (18.18)$$

where C_j are the coefficients in the linear sum defining \vec{f} . Repeated application of \mathbf{A} will stretch \vec{f} in the direction of the eigenvector with the largest eigenvalue. If all of the eigenvalues of \mathbf{A} have magnitude less than unity, then the

above result diminishes to zero as $i \rightarrow \infty$. Otherwise, the components with $|\lambda_j| > 1$ will diverge. The spectral radius $\rho(\mathbf{A})$ is a useful measure of the eigenvalues:

$$\rho(\mathbf{A}) \equiv \max_j |\lambda_j| \quad (18.19)$$

The eigenvalues of a positive definite matrix are all positive, while the eigenvalues of a negative definite matrix are all negative:

$$\begin{aligned} \mathbf{A} \vec{v} &= \lambda \vec{v} \\ \vec{v}^T \mathbf{A} \vec{v} &= \lambda \vec{v}^T \vec{v} \end{aligned} \quad (18.20)$$

Because eigenvectors are non-zero vectors, $\lambda \mathbf{I} - \mathbf{A}$ must be singular:

$$\begin{aligned} \mathbf{A} \vec{v} &= \lambda \mathbf{I} \vec{v} \\ (\mathbf{A} - \lambda \mathbf{I}) \vec{v} &= 0 \end{aligned} \quad (18.21)$$

The condition number κ of a matrix is a measure of how sensitive the output of the matrix is to a perturbation in its input. For SPD matrices, the condition number is related to the ratio between the maximum and minimum eigenvalues:

$$\kappa \equiv \frac{\lambda_{max}}{\lambda_{min}} \quad (18.22)$$

19 Appendix

19.1 Ideal Gas SUPG

This section presents the matrices involved in the SUPG stabilization when the ideal gas law is used to close the system.

19.1.1 1-D

$$\mathbf{A}_1 = \begin{bmatrix} 0 & 1 & 0 \\ \frac{\gamma-1}{2} \|\vec{V}\|_2^2 - V_1^2 & (3-\gamma)V_1 & \gamma-1 \\ V_1 \left(\frac{\gamma-1}{2} \|\vec{V}\|_2^2 - H \right) & (1-\gamma)V_1^2 + H & V_1\gamma \end{bmatrix} \quad (19.1)$$

$$\mathbf{K}_{11} = \frac{k_f}{\rho C_v} \begin{bmatrix} 0 & 0 & 0 \\ 0 & 0 & 0 \\ \|\vec{V}\|_2^2 - E & -V_1 & 1 \end{bmatrix} \quad (19.2)$$

19.1.2 2-D

$$\mathbf{A}_1 = \begin{bmatrix} 0 & 1 & 0 & 0 \\ \frac{\gamma-1}{2} \|\vec{V}\|_2^2 - V_1^2 & (3-\gamma)V_1 & (1-\gamma)V_2 & \gamma-1 \\ -V_2V_1 & V_2 & V_1 & 0 \\ V_1 \left(\frac{\gamma-1}{2} \|\vec{V}\|_2^2 - H \right) & (1-\gamma)V_1^2 + H & (1-\gamma)V_1V_2 & V_1\gamma \end{bmatrix} \quad (19.3a)$$

$$\mathbf{A}_2 = \begin{bmatrix} 0 & 0 & 1 & 0 \\ -V_1V_2 & V_2 & V_1 & 0 \\ \frac{\gamma-1}{2} \|\vec{V}\|_2^2 - V_2^2 & (1-\gamma)V_1 & (3-\gamma)V_2 & \gamma-1 \\ V_2 \left(\frac{\gamma-1}{2} \|\vec{V}\|_2^2 - H \right) & (1-\gamma)V_1V_2 & (1-\gamma)V_2^2 + H & V_2\gamma \end{bmatrix} \quad (19.3b)$$

$$\mathbf{K}_{11} = \mathbf{K}_{22} = \frac{k_f}{\rho C_v} \begin{bmatrix} 0 & 0 & 0 & 0 \\ 0 & 0 & 0 & 0 \\ 0 & 0 & 0 & 0 \\ \|\vec{V}\|_2^2 - E & -V_1 & -V_2 & 1 \end{bmatrix} \quad (19.4)$$

19.1.3 3-D

$$\mathbf{A}_1 = \begin{bmatrix} 0 & 1 & 0 & 0 & 0 \\ \frac{\gamma-1}{2}\|\vec{V}\|_2^2 - V_1^2 & (3-\gamma)V_1 & (1-\gamma)V_2 & (1-\gamma)V_3 & \gamma-1 \\ -V_2V_1 & V_2 & V_1 & 0 & 0 \\ -V_3V_1 & V_3 & 0 & V_1 & 0 \\ V_1\left(\frac{\gamma-1}{2}\|\vec{V}\|_2^2 - H\right) & (1-\gamma)V_1^2 + H & (1-\gamma)V_1V_2 & (1-\gamma)V_1V_3 & V_1\gamma \end{bmatrix} \quad (19.5a)$$

$$\mathbf{A}_2 = \begin{bmatrix} 0 & 0 & 1 & 0 & 0 \\ -V_1V_2 & V_2 & V_1 & 0 & 0 \\ \frac{\gamma-1}{2}\|\vec{V}\|_2^2 - V_2^2 & (1-\gamma)V_1 & (3-\gamma)V_2 & (1-\gamma)V_3 & \gamma-1 \\ -V_3V_2 & 0 & V_3 & V_2 & 0 \\ V_2\left(\frac{\gamma-1}{2}\|\vec{V}\|_2^2 - H\right) & (1-\gamma)V_1V_2 & (1-\gamma)V_2^2 + H & (1-\gamma)V_2V_3 & V_2\gamma \end{bmatrix} \quad (19.5b)$$

$$\mathbf{A}_3 = \begin{bmatrix} 0 & 0 & 0 & 1 & 0 \\ -V_1V_3 & V_3 & 0 & V_1 & 0 \\ -V_2V_3 & 0 & V_3 & V_2 & 0 \\ \frac{\gamma-1}{2}\|\vec{V}\|_2^2 - V_3^2 & (1-\gamma)V_1 & (1-\gamma)V_2 & (3-\gamma)V_3 & \gamma-1 \\ V_3\left(\frac{\gamma-1}{2}\|\vec{V}\|_2^2 - H\right) & (1-\gamma)V_1V_3 & (1-\gamma)V_2V_3 & (1-\gamma)V_3^2 + H & V_3\gamma \end{bmatrix} \quad (19.5c)$$

$$\mathbf{K}_{11} = \mathbf{K}_{22} = \mathbf{K}_{33} = \frac{k_f}{\rho C_v} \begin{bmatrix} 0 & 0 & 0 & 0 & 0 \\ 0 & 0 & 0 & 0 & 0 \\ 0 & 0 & 0 & 0 & 0 \\ 0 & 0 & 0 & 0 & 0 \\ \|\vec{V}\|_2^2 - E & -V_1 & -V_2 & -V_3 & 1 \end{bmatrix} \quad (19.6)$$

20 Notation

All notation used in this manual is defined in this section, along with the equation numbers in which the symbol is defined. No equations are listed for symbols that do not have a mathematical definition. As with any large document, full consistency between notation in different sections cannot always be obtained, so contextual clues should be used to differentiate between identical symbols with different interpretations. When a notation choice can be limited to a certain section of the manual, this is indicated.

Units are provided for all quantities. Units of “1” signifies a dimensionless quantity, while \boxtimes indicates that the quantity may have many different units (such as a solution vector). Vector units are indicated with an overarrow, while matrix or tensor units are indicated by square brackets. Consistent notation for vectors and matrices is not always used - the symbol in the units column shows the underlying dimensionality of the quantity.

20.1 Greek Symbols

α	Fluid-to-solid within-bed convective coefficient, <i>or</i> Linear update step size (Section 17 only)	W/m 1	Eq. (2.203) —
α_{pg}	Petrov-Galerkin scaling parameter	1	—
α_T	Compressibility	Pa	Eq. (2.238)
α_w	Within-bed fluid-to-wall convective coefficient	W/m	—
β	Expansivity	1/K	Eq. (2.183)
χ	Switching method parameter	1	—
δ	Diffusivity, <i>or</i> A differential change independent of end states	m^2/s 1	— —
δ_i	Newton update for iteration i	\boxtimes	Eq. (17.6)
δ_{ij}	Kronecker delta	1	Eq. (18.6)
$\tilde{\delta}_{ij}$	$1 - \delta_{ij}$	1	—
$\vec{\delta r}$	Incremental distance vector	\vec{m}	—
ε	Fluid porosity	1	Eq. (2.15)
ε_{pipe}	Pipe roughness	m	—
$\varepsilon_{r,s}$	Phase s emissivity	1	—
ε_∞	Porosity infinitely far from a bounding wall	1	—
ε_{ijk}	Permutation	1	Eq. (18.5)
ε_{mach}	Machine precision	1	—
γ	Specific heat ratio	1	Eq. (7.11)
Γ	Boundary	\boxtimes	—
κ	Effective thermal conductivity	W/m-K	—
κ	Condition number	1	—
$\kappa_{f,A}$	Axial component of κ_f tensor	W/m-K	Eq. (12.3)
$\kappa_{f,R}$	Radial component of κ_f tensor	W/m-K	Eq. (12.3)
$\kappa_{\text{fluid conduction}}$	Solid-to-fluid-to-solid conduction component of κ_s	W/m-K	—
$\kappa_{\text{radiation}}$	Solid-to-solid radiation component of κ_s	W/m-K	—
$\kappa_{\text{solid conduction}}$	Solid-to-solid contact conduction component of κ_s	W/m-K	—
λ	Solid-to-fluid thermal conductivity ratio, <i>or</i> Newtonian fluid constitutive term, <i>or</i> Eigenvalue	1 $Pa \cdot s$ \boxtimes	Eq. (11.1) Eq. (2.85) —
λ_{mfp}	Momentum exchange mean free path	m	—
$\tilde{\lambda}_{mfp}$	Modified mean free path	m	—
Λ	Normalized radiation thermal conductivity	1	Eq. (11.12)

μ	Dynamic viscosity	Pa·s	—
$\tilde{\mu}$	Effective porous media viscosity	Pa·s	—
η	Fuel-to-graphite-matrix heat transfer coefficient	W/m ² K	—
ν	Specific volume, <i>or</i> Poisson ratio	m ³ /kg 1	—
ω	Vorticity	$\frac{1}{s}$	Eq. (2.73)
Ω	Domain	\boxtimes	—
ρ	Density	kg/m ³	—
ρ_f	Intrinsic fluid density	kg/m ³	—
$\overline{\omega}$	Fluid constant in stiffened gas EOS	1	—
ϕ	Shape function	1	—
$\phi_{g,f}$	Gravitational potential	1/s ²	Eq. (2.115)
Φ	Generic field, <i>or</i>	\boxtimes	—
φ	Contact area fraction, deformation ratio	1	—
ψ	Weight function	1	—
ψ^*	Element-discontinuous weight function	1	—
$\tilde{\psi}$	Petrov-Galerkin shape function	1	Eq. (15.16)
Ψ	KTA correlation parameter	1	Eq. (9.5)
σ	Stefann-Boltzmann constant	W/m ⁴ ·K	—
σ_{ij}	Stress tensor	$[N/m^2]$	Eq. (2.52)
ζ	GLS linear combination parameter	1	—
τ	Deviatoric stress tensor	$[N/m^2]$	Eq. (2.92)
τ_{adv}	Advection-dominated component of τ_{SUPG}	s	—
$\tau_{adv,com}$	Advection-dominated compressible component of τ_{SUPG}	s	—
$\tau_{adv,inc}$	Advection-dominated incompressible component of τ_{SUPG}	s	—
τ_c	Continuity equation τ_{SUPG} component	s	Eq. (15.50)
τ_{cd}	Convection-diffusion stabilization parameter	s	—
τ_{diff}	Diffusion-dominated component of τ_{SUPG}	s	—
τ_e	Energy equation τ_{SUPG} component	s	Eq. (15.50)
τ_{SUPG}	SUPG stabilization parameter matrix	$[s]$	—
$\tau_{SUPG,comp}$	τ_{SUPG} for compressible flows	$[s]$	—
$\tau_{SUPG,inc}$	τ_{SUPG} for incompressible flows	$[s]$	—
$\tau_{temporal}$	Transient-dominated component of τ_{SUPG}	s	—
τ_{u_i}	<i>i</i> -th momentum equation τ_{SUPG} component	s	Eq. (15.50)
θ	angle	1	—
ξ_{ij}	Antisymmetric stress tensor	$[N/m^2]$	Eq. (2.68)
$\vec{\xi}$	Position vector in master finite element	\vec{m}	—
ζ	Bulk viscosity	Pa·s	Eq. (2.93)

20.2 English Symbols

a	κ_s correlation parameter	1	Eq. (11.8)
a_{ij}	Tensor transformation matrix	[1]	Eq. (18.8)
a_w	Wetted convective heat transfer length	m	Eq. (2.204)
A	Generic operator	\boxtimes	—
A_c	Churchill correlation parameter	1	Eq. (9.11)
A_w	Eisfeld correlation parameter	1	Eq. (9.8)
\mathbf{A}	Generic matrix	\boxtimes	—
\mathbf{A}_i	i -th inviscid flux Jacobian matrix	\boxtimes	Eq. (2.226)
$\tilde{\mathbf{A}}_i$	i -th chain rule inviscid flux Jacobian matrix	\boxtimes	Eq. (2.236)
\mathcal{A}	Second-order viscous stress approximation tensor	$\left[1/m^2\right]$	Eq. (2.120)
b	Linear RHS vector	\boxrightarrow	—
\vec{b}	Body force vector, i.e. \vec{g} if only gravitational	m/s^2	—
B	Geometric shape factor, <i>or</i> Bilinear functional (Section 16 only)	1 \boxtimes	Eq. (11.7) —
\vec{B}	Boundary flux vector	\boxrightarrow	—
\mathbf{B}	Jacobi application matrix	\boxtimes	Eq. (17.21)
B_c	Churchill correlation parameter	1	Eq. (9.12)
B_w	Eisfeld correlation parameter	1	Eq. (9.9)
\mathcal{B}	Third-order viscous stress approximation tensor	$\left[s/m^3\right]$	Eq. (2.120)
Br	Brinkman number	1	Eq. (2.298)
c	Speed of sound	m/s	Eq. (2.269)
c_{ijkl}	Newtonian fluid proportionality tensor	$[Pa \cdot s]$	Eq. (2.85)
C	Vector of numerical solution expansion coefficients	\boxtimes	Eq. (16.1)
C_p	Isobaric specific heat	J/kg	Eq. (2.176)
C_v	Isochoric specific heat	J/kg	Eq. (2.177)
\mathcal{C}	Third-order fluctuating velocity approximation tensor	m/s	Eq. (2.121)
d_{bed}	Cylindrical bed diameter	m	—
d_c	Radius of pebble-pebble contact area	m	—
d_p	Pebble diameter	m	—
D	Hydraulic diameter	m	Eq. (2.288)
\mathbf{D}	Generic diagonal matrix	\boxtimes	—
\mathcal{D}	Darcy prefactor tensor	$\left[s/m^2\right]$	Eq. (2.146)
\mathbb{D}	Fluid energy equation diffusivity	m^2/s	Eq. (12.4)
\mathbb{D}_A	Axial fluid energy equation diffusivity	m^2/s	Eq. (12.5)
\mathbb{D}_R	Radial fluid energy equation diffusivity	m^2/s	Eq. (12.5)
e	Internal energy per unit mass, <i>or</i> Error (Sections 16 and 17 only)	J/kg \boxtimes	— Eq. (16.8)
e_{ij}	Symmetric stress tensor	N/m^2	Eq. (2.67)
\vec{e}_i	Mutually orthogonal basis vectors, $i = 1, 2, 3$	$\vec{1}$	—
E	Total energy per unit mass, <i>or</i> Young's modulus	J/kg Pa	Eq. (2.154) —
\mathcal{E}	Second-order pressure approximation tensor	[1]	Eq. (2.122)
Ec	Eckert number	1	Eq. (2.297)
f	Phase function, <i>or</i> Thermal dispersion correction factor, <i>or</i> Force vector	1 1 \boxrightarrow	Eq. (2.10) — —
\vec{f}	Stress vector	N/m^2	Eq. (2.52)
f_s	Surface tension force	N	—
F	Collinear force	N	—
\vec{F}	Inviscid flux vector	\boxrightarrow	Eq. (2.224)
\mathcal{F}	Forchheimer prefactor tensor	[1]	Eq. (2.148)

\vec{g}	Gravitational acceleration vector	m/s^2	—
G	Gibbs function	J/kg	Eq. (2.179)
\vec{G}	Diffusive flux vector	\boxtimes	Eq. (2.224)
h	Enthalpy per unit mass	J/kg	Eq. (2.159)
h_c	Convective heat transfer coefficient	W/m^2	—
h_e	Finite element size	m	—
h_{ij}	Arnoldi process matrix	\boxtimes	Eqs. (17.45) and (17.46)
H	Total enthalpy per unit mass	J/kg	Eq. (2.160)
$H(\Omega)$	Hilbert-Sobolev space	$\{1\}$	—
\mathbf{H}	Upper Hessenberg matrix of h_{ij} entries	\boxtimes	—
$\tilde{\mathbf{H}}$	Matrix of h_{ij} entries	\boxtimes	Eq. (17.47)
i	Nonlinear loop iteration index	1	—
\mathbf{I}	identity matrix	$[1]$	—
\mathbf{J}	Jacobian matrix of the Newton solve	\boxtimes	Eq. (17.5)
\mathcal{J}	Jacobian matrix of physical-to-master transformation	$[1]$	Eq. (16.17)
k	Thermal conductivity, <i>or</i> Linear loop iteration index (Section 17 only)	$W/m \cdot K$ 1	—
\tilde{k}	Isotropic diffusion stabilization thermal conductivity	$W/m \cdot K$	—
k_d	Thermal dispersion thermal conductivity	$W/m \cdot K$	—
K_{ij}	Stiffness matrix	\boxtimes	Eq. (17.58)b
\mathbf{K}_{ij}	Diffusive flux Jacobian matrix	\boxtimes	Eq. (2.227)
$\tilde{\mathbf{K}}_{ij}$	Diffusive flux chain rule Jacobian matrix	\boxtimes	Eq. (2.234)
K_T	Isothermal bulk modulus	Pa	Eq. (2.188)
\mathcal{K}	Permeability tensor	$[1/m^2]$	Eq. (2.129)
\mathcal{K}_D	Normalized gas diffusion thermal conductivity	1	Eq. (11.5)
\mathcal{K}_k	Krylov space of dimension k (Section 17 only)	$\{\boxtimes\}$	Eq. (17.41)
\mathcal{K}_{SF}	Normalized radiation-conduction thermal conductivity	1	Eq. (11.6)
\mathcal{K}_R	Normalized radiation thermal conductivity	1	—
Kn	Knudsen number	1	Eq. (2.1)
l	Pore flow length scale	m	—
L	Engineering flow length scale, <i>or</i> Linear functional (Section 16 only)	m \boxtimes	—
\mathbf{L}	Generic lower triangular matrix	\boxtimes	—
\mathcal{L}	Fourth-order fluctuating velocity approximation tensor	$[1]$	Eq. (2.121)
\mathbf{M}	Chain rule differentiation matrix	\boxtimes	Eq. (2.233)
M_{ij}	Mass matrix	\boxtimes	Eq. (17.58)a
\mathcal{M}	Third-order pressure approximation tensor	$[m/Pa]$	Eq. (2.122)
Ma	Mach number	1	Eq. (2.296)
n_{el}	Number of elements	1	—
n_{en}	Number of nodes per element	1	—
n_s	Number of spatial dimensions	1	—
n_{qp}	Number of quadrature points	1	—
N	Number of shape functions per numerical variable	1	—
N_c	Coordination number	1	—
N_A	Number of spheres per unit area	$1/m^2$	Table 17
N_L	Number of spheres per unit length	$1/m$	Table 17
\mathcal{N}	Polynomial order	1	—
Nu	Nusselt number	1	Eq. (2.290)a
Nu_h	Nusselt number	1	Eq. (2.290)b
Nu_{lam}	Gnielinski correlation parameter	1	Eq. (10.6)
Nu_{turb}	Gnielinski correlation parameter	1	Eq. (10.7)
\vec{n}	Unit outward normal vector	\vec{m}	—
\mathcal{O}	Of order	1	—

p	Linear update vector	$\vec{\boxtimes}$	—
P	Thermodynamic pressure	Pa	—
P'	Reduced pressure	Pa	Eq. (2.102)
P_d	Hydrodynamic pressure	Pa	Eq. (2.192)
P_∞	Fluid constant in stiffened gas EOS	Pa	—
\mathcal{P}	Generic normal tensor	$[\boxtimes]$	—
Pe	Peclet number	1	Eq. (2.295)
Pe_{el}	Element Peclet number	1	Eq. (15.3)
Pe_A	Peclet number based on axial component of κ_f	1	—
$Pe_{A,\infty}$	Pe_A in an unconfined bed	1	—
Pe_R	Peclet number based on radial component of κ_f	1	—
$Pe_{R,\infty}$	Pe_R in an unconfined bed	1	—
Pr	Prandtl number	1	Eq. (2.294)
q	Volumetric heat source	W/m^3	—
\vec{q}	Heat flux vector, <i>or</i> Columns of \mathbf{Q} (Section 17 only)	W/m^2 $\vec{\boxtimes}$	— Eq. (17.44)
\bar{q}	Known heat flux	W/m^2	—
q_B	Binding energy of fluid in stiffened gas EOS	J/kg	—
\mathbf{Q}_k	Orthonormal basis for \mathcal{K}_k	$[\boxtimes]$	Eq. (17.44)
r	Radial coordinate	m	—
r_{th}	Thermal resistance	K/W	—
R	Universal gas constant, <i>or</i> Scalar residual	J/kg·K \boxtimes	Eq. (7.10) Eq. (16.3)
R_{bed}	Bed diameter	m	—
R_p	Pebble diameter	m	—
\vec{R}	Strong residual vector	$\vec{\boxtimes}$	Eq. (2.225)
\vec{R}_u	Vector of momentum equation strong residuals	$kg/m^2 \cdot s^2$	—
\mathbb{R}^n	Space of real numbers of dimension n	1	—
Re	Reynolds number	1	Eq. (2.287)a
Re_b	Reynolds number	1	Eq. (2.287)d
Re_h	Reynolds number	1	Eq. (2.287)b
Re_i	Reynolds number	1	Eq. (2.287)c
Re_k	Reynolds number	1	Eq. (2.287)e
s	Arc length, <i>or</i> Entropy	m J/K	— —
S	Surface	m^2	—
\vec{S}	Source term vector	$\vec{\boxtimes}$	Eq. (2.224)
S_e	Non-interface portion of a surface	m^2	—
S_i	Phase-interface portion of a surface	m^2	—
S_F	Component of collinear force that is aligned with gravity	1	Table 17
S_R	Geometrical factor in Chan and Tien correlation	1	—
t	Time	s	—
t_{ij}	Generic tensor	$[\boxtimes]$	Eq. (18.9)
Δt	Time step size	s	—
T	Temperature	K	—
u	True solution, <i>or</i> Numerical solution (Section 17 only)	\boxtimes $\vec{\boxtimes}$	— —
u_N	Numerical solution over the entire domain	$\vec{\boxtimes}$	Eq. (16.1)
\vec{U}	Vector of conserved quantities	$\vec{\boxtimes}$	Eq. (2.224)
\mathbf{U}	An upper triangular matrix	$[\boxtimes]$	—
V	Volume	m^3	—
\vec{v}	Extrinsic, superficial, or Darcy velocity, <i>or</i> Eigenvector	m/s $\vec{\boxtimes}$	— Eq. (18.15)
\vec{V}	Intrinsic phase velocity	m/s	—

\vec{V}'	Relative velocity of fluid with respect to interface	$\frac{m}{s}$	Eq. (2.248)
\mathcal{V}	Velocity of material interface	$\frac{m}{s}$	Eq. (2.251)
w	Quadrature weight	1	—
\vec{w}	Velocity of the phase interface	m/s	—
W	Porous media friction coefficient	1/s	Eq. (2.152)
\vec{W}	Vector of weight functions	$\vec{1}$	—
x	Linear solution vector	\boxtimes	—
\vec{x}	Position vector	\vec{m}	—
x_*	True linear solution vector	\boxtimes	—
X	Physical coordinate	m	—
\mathcal{Y}	Finite element potential function	\boxtimes	Eq. (16.34), Eq. (17.15)
z	Height	m	—
\mathcal{Z}	Nondimensional distance	1	Eq. (8.2)

20.3 Math Symbols

Some of the math symbols are described using dummy variables x and y for clarity.

dx/dt	Material derivative of x	Eq. (18.1)
\otimes	Outer product	—
$\partial x/\partial y$	Partial derivative of x with respect to y	—
$Tr(x)$	Trace of x	—
\parallel	Parallel to	—
\diamond	Placeholder variable	—
$\langle x \rangle$	Spatial average of x	—
$\langle x_k \rangle$	Spatial phase (extrinsic) average of x	Eq. (2.11)
$\langle x_k \rangle^k$	Spatial phase (intrinsic) average of x	Eq. (2.12)
(x, Ψ)	Volume inner product	Eq. (2.300)a
$\langle x, \Psi \rangle$	Boundary inner product	Eq. (2.300)b
$\ x\ _i$	L^i norm of x	Eq. (18.2)
$\ x\ _{E(\Omega)}$	Energy norm of x	Eq. (16.25)
$\ x\ _{H^1(\Omega)}$	Hilbert-space norm of x	Eq. (16.14)
$ x $	Absolute value of x (if x is a scalar), <i>or</i> Determinant of x (if x is a matrix)	—

20.4 Subscripts

e	Pertaining to a finite element
f	Fluid
h	Pertaining to a finite element (of size h_e)
k	Generic phase k
max	Maximum
min	Minimum
o	Reference value
p	Pebble
s	Solid
$stag$	Stagnation value
x, y, z	x, y, z components of Cartesian space
0	An initial value

20.5 Superscripts and Overbars

Some of the overbars are described using a dummy variable x for clarity.

\bar{x}	Area average of x
\hat{x}	Spatial fluctuating component of x
+	nondimensional quantity
*	Hermitian complex conjugate
T	transpose

References

- [1] S. Morris. ME160: Advanced Fluid Mechanics. Technical report, University of California-Berkeley, 2016.
- [2] C.Y. Wu, Y.M. Ferng, C.C. Chieng, and C.C. Liu. Investigating the Advantages and Disadvantages of Realistic Approach and Porous Approach for Closely Packed Pebbles in CFD Simulation. *Nuclear Engineering and Design*, 240:1151–1159, 2010.
- [3] C. Andreades, A. Cisneros, J. Choi, A. Chong, M. Fratoni, S. Hong, L. Huddar, K. Huff, D. Krumwiede, M. Laufer, M. Munk, R. Scarlat, N. Zweibaum, E. Greenspan, and P. Peterson. Technical Description of the "Mark 1" Pebble-Bed Fluoride-Salt-Cooled High-Temperature Reactor (PB-FHR) Power Plant. Technical Report UCBTH-14-002, University of California, Berkeley, 2014.
- [4] E. Zarifi, G. Jahanfarnia, and F. Veysi. Thermal-Hydraulic Modeling of Nanofluids as the Coolant in VVER-1000 Reactor Core by the Porous Media Approach. *Annals of Nuclear Energy*, 51:203–212, 2013.
- [5] M. Nijemeisland and A.G. Dixon. CFD Study of Fluid Flow and Wall Heat Transfer in a Fixed Bed of Spheres. *American Institute of Chemical Engineers Journal*, 50, 2004.
- [6] Y. Bai, N. Gui, X. Yang, J. Tu, and S. Jiang. Computational Fluid Dynamics Investigation of Thermal-Hydraulic Characteristics in a Simplified Pebbled Bed Modular Reactor Core Using Different Arrangements of Fuel Elements. *Journal of Computational Multiphase Flows*, 0:1–9, 2017.
- [7] J. Ge, C. Wang, Y. Xiao, W. Tian, S. Qiu, G. Su, D. Zhang, and Y. Wu. Thermal-Hydraulic Analysis of a Fluoride-Salt-Cooled Pebble-Bed Reactor with CFD Methodology. *Progress in Nuclear Energy*, 91:83–96, 2016.
- [8] J. Lee, S. Yoon, G. Park, and W. Jee. Turbulence-Induced Heat Transfer in PBMR Core Using LES and RANS. *Nuclear Science and Technology*, 44:985–996, 2007.
- [9] H. Li, S. Qiu, Y. Zhang, G. Su, and W. Tian. Thermal Hydraulic Investigations with Different Fuel Diameters of Pebble Bed Water Cooled Reactor in CFD Simulation. *Annals of Nuclear Energy*, 42:135–147, 2012.
- [10] S. Song, X. Cai, Y. Liu, Q. Wei, and W. Guo. Pore Scale Thermal Hydraulics Investigations of Molten Salt Cooled Pebble Bed High Temperature Reactor with BCC and FCC Configurations. *Science and Technology of Nuclear Installations*, 2014, 2014. <http://dx.doi.org/10.1155/2014/589895>.
- [11] R.O. Scarlat. *Design of Complex Systems to Achieve Passive Safety: Natural Circulation Cooling of Liquid Salt Pebble Bed Reactors: Chapter 2*. PhD thesis, University of California, Berkeley, 2012.
- [12] J. Lee and S. Lee. Flow Visualization in the Scaled Up Pebble Bed of High Temperature Gas-Cooled Reactor Using Particle Image Velocimetry Method. *Journal of Engineering for Gas Turbines and Power*, 131, 2009.
- [13] Y. Hassan and E. Dominguez-Ontiveros. Flow Visualization in a Pebble Bed Reactor Experiment Using PIV and Refractive Index Matching Techniques. *Nuclear Engineering and Design*, 238:3080–3085, 2008.
- [14] Y. Ferng and K. Lin. Investigating Effects of BCC and FCC Arrangements on Flow and Heat Transfer Characteristics in Pebbles Through CFD Methodology. *Nuclear Engineering and Design*, 258:66–75, 2013.
- [15] M. Aufiero and M. Fratoni. Development of Multiphysics Tools for Fluoride-Cooled High-Temperature Reactors. In *Proceedings of PHYSOR*, 2016.
- [16] V. Rintala, H. Suikkanen, J. Leppanen, and R. Kyrki-Rajamaki. Modeling of Realistic Pebble Bed Reactor Geometries Using the Serpent Monte Carlo Code. *Annals of Nuclear Energy*, 77:223–230, 2015.
- [17] S. Zhang, X. Zhao, and Z. Yang. Flow Simulations in a Pebble Bed Reactor by a Combined DEM-CFD Approach. *Nuclear Science and Engineering*, 189:135–151, 2018.
- [18] B. Stocker and H. Nieben. Data Sets of the SANA Experiment 1994–1996. Technical report, Forschungszentrum Julich, 1996.

- [19] R. Abdulmohsin. *Gas Dynamics and Heat Transfer in a Packed Pebble-Bed Reactor for the 4th Generation Nuclear Energy*. PhD thesis, Missouri University of Science and Technology, 2013.
- [20] M. Elmo and O. Cioni. Low Mach Number Model for Compressible Flows and Application to HTR. *Nuclear Engineering and Design*, 222:117–124, 2003.
- [21] Z. Zhang, Y. Dong, F. Li, Z. Zhang, H. Wang, X. Huang, H. Li, B. Liu, X. Wu, H. Wang, X. Diao, H. Zhang, and J. Wang. The Shandong Shidao Bay 200 MWe High-Temperature Gas-Cooled Reactor Pebble-Bed Module (HTR-PM) Demonstration Power Plant: An Engineering and Technological Innovation. *Engineering*, 2:112–118, 2016.
- [22] C. Hirsch. *Numerical Computation of Internal and External Flows*. 2007.
- [23] W. Gray and K. O'Neill. On the General Equations for Flow in Porous Media and Their Reduction to Darcy's Law. *Water Resources Research*, 12:148–154, 1976.
- [24] M. Kaviany. *Principles of Heat Transfer in Porous Media, Chapter 2*. Springer-Verlag, 1991.
- [25] W. H. Gray. A derivation of the equations for multi-phase transport. *Chemical Engineering Science*, 30(2):229–233, February 1975. [https://doi.org/10.1016/0009-2509\(75\)80010-8](https://doi.org/10.1016/0009-2509(75)80010-8).
- [26] H. Oehme and J. Schoning. Design, Features, and Engineering Status of the THTR 300 MWe Prototype Power Station. Technical Report 2/113.
- [27] G.K. Batchelor. *An Introduction to Fluid Dynamics*. Cambridge University Press, 2000.
- [28] I. Kececiloglu and Y. Jiang. Flow Through Porous Media of Packed Spheres Saturated With Water. *Transactions of the ASME*, 116:164–170, 1994.
- [29] I.F. Macdonald, M.S. El-Sayed, K. Mow, and F.A.L. Dullien. Flow Through Porous Media - the Ergun Equation Revisited. *Ind. Eng. Chem. Fundam.*, 18:199–207, 1979.
- [30] S. Ergun. Fluid Flow Through Packed Columns. *Chem. Eng. Prog.*, 48, 1952.
- [31] B. Eisfeld and K. Schnitzlein. The Influence of Confining Walls on the Pressure Drop in Packed Beds. *Chemical Engineering Science*, 56:4321–4329, 2001.
- [32] D.A. Nield and A. Bejan. *Convection in Porous Media*. Springer, 2013.
- [33] R.D. Barree and M.W. Conway. Beyond Beta Factors: A Complete Model for Darcy, Forchheimer, and Trans-Forchheimer Flow in Porous Media. *Society of Petroleum Engineers*, pages 1–8, 2004.
- [34] X. Wang, F. Thauvin, and K.K. Mohanty. Non-Darcy Flow Through Anisotropic Porous Media. *Chemical Engineering Science*, 54:1859–1869, 1998.
- [35] M. Giese, K. Rottschäfer, and D. Vortmeyer. Measured and Modeled Superficial Flow Profiles in Packed Beds with Liquid Flow. *American Institute of Chemical Engineers Journal*, 44:484–490, 1998.
- [36] G.J. Auwerda, Y. Zheng, D. Lathouwers, and J.L. Kloosterman. Effect of Non-Uniform Porosity Distribution on Thermal Hydraulics in a Pebble Bed Reactor. In *Proceedings of NURETH-14*, 2011.
- [37] K. Vafai and C.L. Tien. Boundary and Inertia Effects on Flow and Heat Transfer in Porous Media. *International Journal of Heat and Mass Transfer*, 37:195–203, 1980.
- [38] D. Vortmeyer and J. Schuster. Evaluation of Steady Flow Profiles in Rectangular and Circular Packed Beds By a Variational Method. *Chemical Engineering Science*, 38:1691–1699, 1983.
- [39] H. Huang and J. Ayoub. Applicability of the Forchheimer Equation for Non-Darcy Flow in Porous Media. *Society of Petroleum Engineers*, pages 1–14, 2006.

- [40] R.M.Fand, B.Y.K. Kim, A.C.C. Lam, and R.T. Phan. Resistance to the Flow of Fluids Through Simple and Complex Porous Media Whose Matrices are Composed of Randomly Packed Spheres. *Transactions of the ASME*, 109:268–273, 1987.
- [41] R.D. Barree and M.W. Conway. Reply to Discussion of "Beyond Beta Factors: A Complete Model for Darcy, Forchheimer, and Trans-Forchheimer Flow in Porous Media". *Society of Petroleum Engineers*, pages 73–74, 2005.
- [42] KTA. Reactor Core Design of High-Temperature Gas-Cooled Reactors Part 3: Loss of Pressure through Friction in Pebble Bed Cores. Technical Report KTA 3102.3, Nuclear Safety Standards Commission, 1981.
- [43] D.A. Nield. Resolution of a Paradox Involving Viscous Dissipation and Nonlinear Drag in a Porous Medium. *Transport in Porous Media*, 41:349–357, 2000.
- [44] J.L. Lage, B.V. Antohe, and D.A. Nield. Two Types of Nonlinear Pressure-Drop Versus Flow-Rate Relation Observed for Saturated Porous Media. *Transactions of the ASME*, pages 700–706, 1997.
- [45] D. van Batenburg and D. Milton-Taylor. Discussion of SPE 89325, "Beyond Beta Factors: A Complete Model for Darcy, Forchheimer, and Trans-Forchheimer Flow in Porous Media". *Journal of Petroleum Technology*, pages 72–73, 2005.
- [46] J.H. Yang and S.L. Lee. Effect of Anisotropy on Transport Phenomena in Anisotropic Porous Media. *International Journal of Heat and Mass Transfer*, 42:2673–2681, 1999.
- [47] S.L. Lee and J.H. Yang. Modeling of Darcy-Forchheimer Drag for Fluid Flow Across a Bank of Circular Cylinders. *International Journal of Heat and Mass Transfer*, 40:3149–3155, 1997.
- [48] A.F. Pilehvar, M. Aghaie, M.H. Esteki, A. Zolfaghari, A. Minuchehr, A. Daryabak, and A. Safavi. Evaluation of Compressible Flow in Spherical Fueled Reactors Using the Porous Media Model. *Annals of Nuclear Energy*, 57:185–194, 2013.
- [49] Y. Li and W. Ji. Thermal Analysis of Pebble-Bed Reactors Based on a Tightly Coupled Mechanical-Thermal Model. In *Proceedings of NURETH*, 2016.
- [50] C.G. du Toit, P.G. Rousseau, G.P. Greyvenstein, and W.A. Landman. A Systems CFD Model of a Packed Bed High Temperature Gas-Cooled Nuclear Reactor. *International Journal of Thermal Sciences*, 45:70–85, 2006.
- [51] T.J.R. Hughes, L.P. Franca, and M. Mallet. A New Finite Element Formulation for Computational Fluid Dynamics: I. Symmetric Forms of the Compressible Euler and Navier-Stokes Equations and the Second Law of Thermodynamics. *Computer Methods in Applied Mechanics and Engineering*, 54:223–234, 1986.
- [52] C. Li and R. Glowinski. Modeling and Numerical Simulation of Low-Mach-Number Compressible Flows. *International Journal for Numerical Methods in Fluids*, 23:77–103, 1996.
- [53] A. Nakayama, F. Kuwahara, and Y. Kodama. An Equation for Thermal Dispersion Flux Transport and its Mathematical Modelling for Heat and Fluid Flow in a Porous Medium. *Journal of Fluid Mechanics*, 5:81–96, 2006.
- [54] A. Amiri and K. Vafai. Analysis of Dispersion Effects and Non-Thermal Equilibrium, Non-Darcian, Variable Porosity Incompressible Flow Through Porous Media. *International Journal of Heat and Mass Transfer*, 37:939–954, 1994.
- [55] L. Zou, A.J. Novak, R.C. Martineau, and H.D. Gougar. Validation of Pronghorn with the SANA Experiments, INL/EXT-17-44085. Technical report, Idaho National Laboratory, 2017.
- [56] H. Suikkanen, V. Rintala, and R. Kyrki-Rajamaki. Development of a Coupled Multi-Physics Code System for Pebble Bed Reactor Core Modeling. In *Proceedings of the HTR 2014*, 2014.
- [57] N.Z. Cho, H. Yu, and J.W. Kim. Two-Temperature Homogenized Model for Steady-State and Transient Thermal Analyses of a Pebble with Distributed Fuel Particles. *Annals of Nuclear Energy*, 36:448–457, 2009.

- [58] V. Sobes, B. Forget, and A. Kadak. Individual Pebble Temperature Peaking Factor Due to Local Pebble Rearrangement in a Pebble Bed Reactor Core. *Nuclear Engineering and Design*, 241:124–133, 2011.
- [59] J. Shentu, S. Yun, and N.Z. Cho. A Monte Carlo Method for Solving Heat Conduction Problems with Complicated Geometry. *Nuclear Engineering and Technology*, 39:207–214, 2007.
- [60] J.D. Hales, R.L. Williamson, S.R. Novascone, D.M. Perez, B.W. Spencer, and G. Pastore. Multidimensional Multiphysics Simulation of TRISO Particle Fuel. *Journal of Nuclear Materials*, 443:531–543, 2013.
- [61] H. Park, D.A. Knoll, D.R. Gaston, and R.C. Martineau. Tightly Coupled Multiphysics Simulations for Pebble Bed Reactors. In *International Conference on Mathematics, Computational Methods & Reactor Physics*, May 2009.
- [62] J. Richard, D. Wang, G. Yoder, J. Carbajo, D. Williams, B. Forget, and C. Forsberg. Implementation of Liquid Salt Working Fluids Into TRACE. In *Proceedings of ICAPP 2014*, 2014.
- [63] G. Hauke and T.J.R. Hughes. A Comparative Study of Different Sets of Variables for Solving Compressible and Incompressible Flows. *Computational Methods in Applied Mechanical Engineering*, 153:1–44, 1998.
- [64] G. Hauke and T.J.R. Hughes. A Unified Approach to Compressible and Incompressible Flows. *Computational Methods in Applied Mechanical Engineering*, 113:389–395, 1994.
- [65] W. Schertz and K. Bischoff. Thermal and Material Transport in Nonisothermal Packed Beds. *American Institute of Chemical Engineers Journal*, 15:597–604, 1969.
- [66] H. Fenech. *Heat Transfer and Fluid Flow in Nuclear Systems*. Pergamon Press, New York, 1981.
- [67] E. Achenbach. Heat and Flow Characteristics of Packed Beds. *Experimental Thermal and Fluid Sciences*, 10:17–27, 1995.
- [68] M.M. Wakil. *Nuclear Heat Transport*. American Nuclear Society, 1978.
- [69] A. Glaser and M.V. Ramana. Weapon-Grade Plutonium Production Potential in the Indian Prototype Fast Breeder Reactor. Technical report, Princeton University, 2007.
- [70] D.G. Roychowdhury et. al. Thermal Hydraulic Design of PFBR Core. Technical report, Indira Ghandi Centre for Atomic Research.
- [71] R. Baumer, I. Kalinowski, E. Rohler, J. Schoning, and W. Wachholz. Construction and Operating Experience with the 300-MW THTR Nuclear Power Plant. *Nuclear Engineering and Design*, 121:155–166, 1990.
- [72] B. Sutharshan, M. Mutyala, R.P. Vijuk, and A. Mishra. The AP1000 Reactor: Passive Safety and Modular Design. *Energy Procedia*, 7:293–302, 2011.
- [73] Westinghouse. AP1000 Design Control Document. Technical report.
- [74] R. A. Berry, J. W. Peterson, H. Zhang, R. C. Martineau, H. Zhao, L. Zou, and D. Andrš. RELAP-7 Theory Manual. Technical Report INL/EXT-14-31366, Idaho National Laboratory, February 2014. <http://tinyurl.com/ojygjzw>.
- [75] K. Hofmann and W. Trapp. THTR 300 MWe Prototype Reactor - Safety Assessment. Technical Report 16.07.2001, RWTUV Anlagentechnik GmbH.
- [76] C.H. Rycroft, G.S. Grest, J.W. Landry, and M.Z. Bazant. Analysis of Granular Flow in a Pebble-Bed Nuclear Reactor. *Physical Review*, 74, 2006.
- [77] C.G. du Toit. Radial Variation in Porosity in Annular Packed Beds. *Nuclear Engineering and Design*, 238:3073–3079, 2008.
- [78] G.J. Auwerda, J.Kloosterman, D.Lathouwers, and T. Van Der Hagen. Macroscopic and Microscopic Packing Properties of Experimental and Computational Pebble Beds. *Nuclear Technology*, 183:272–286, 2013.

- [79] A. Klerk. Voidage Variation in Packed Beds at Small Column to Particle Diameter Ratio. *American Institute of Chemical Engineers*, 49:2022–2029, 2003.
- [80] G. Peter. Numerical Simulation of Accident Scenario in HTGR (Pebble Bed Reactor) Using COMSOL Code. In *Proceedings of ICONE*, 2013.
- [81] S. Becker and E. Laurien. Three-Dimensional Numerical Simulation of Flow and Heat Transport in High-Temperature Nuclear Reactors. In *High Performance Computing in Science and Engineering*, 2002.
- [82] G. Zhao, P. Ye, and T. Obala. Variant Porosity Pebble Bed Reactor Core Thermal Hydraulic Simulation. In *Proceedings of ICONE*, May 2010.
- [83] Z. Gao and L. Shi. Thermal Hydraulic Calculation of the HTR-10 for the Initial and Equilibrium Core. *Nuclear Engineering and Design*, 218:51–64, 2002.
- [84] B. Boer, J.L. Kloosterman, D. Lathouwers, T.H.J.J. van der Hagen, and H. van Dam. Optimization of a Radially Cooled Pebble Bed Reactor. *Nuclear Engineering and Design*, 240:2384–2391, 2010.
- [85] E. Tsotsas and E. Schlünder. Some Remarks on Channeling and on Radial Dispersion in Packed Beds. *Chemical Engineering Science*, 43:1200–1203, 1988.
- [86] Y. Li and W. Ji. Effects of Fluid-Pebble Interactions on Mechanics in Large-Scale Pebble-Bed Reactor Cores. *International Journal of Multiphase Flow*, 73:118–129, 2015.
- [87] R. Mardus-Hall, M. Ho, G. Yeoh, and V. Timchenko. Coupled CFD-DEM Analysis of Molten Salt-Cooled Pebble-Bed Reactor Experiment. In *Transactions of the American Nuclear Society*, 2017.
- [88] G.J. Auwerda, J.L. Kloosterman, D. Lathouwers, and T.H.J.J. van der Hagen. Effects of Random Pebble Distribution on the Multiplication Factor in HTR Pebble Bed Reactors. *Annals of Nuclear Energy*, 37:1056–1066, 2010.
- [89] W.K. Terry, A.M. Ougouag, F. Rahnema, and M.S. McKinley. Effects of Spatial Variations in Packing Fraction of Reactor Physics Parameters in Pebble-Bed Reactors. In *Nuclear Mathematical and Computational Sciences: A Century in Review, A Century Anew*, 2003.
- [90] E. Tsotsas and H. Martin. Thermal Conductivity of Packed Beds: A Review. *Chemical Engineering Processes*, 22:19–37, 1987.
- [91] F.J. Keil. *Modeling of Process Intensification*. Wiley-VCH, 2007.
- [92] E. You, X. Sun, F. Chen, L. Shi, and Z. Zhang. An Improved Prediction Model for the Effective Thermal Conductivity of Compact Pebble Bed Reactors. *Nuclear Engineering and Design*, 323:95–102, 2017.
- [93] B. Boudreau. The Diffusive Tortuosity of Fine-Grained Unlithified Sediments. *Geochimica et Cosmochimica Acta*, 60:3139–3142, 1996.
- [94] D. Gunn. Axial and Radial Dispersion in Fixed Beds. *Chemical Engineering Science*, 42:363–373, 1987.
- [95] P. Avigni. TRACE Loop Modeling of the Liquid Salt Test Loop. Technical report, Oak Ridge National Laboratory, 2016.
- [96] V. Seker and T. Downar. Multiphysics Methods Development for High Temperature Gas Cooled Reactor Analysis. In *PROCEEDINGS in the International Conference on Emerging Nuclear Energy Systems*, 2007.
- [97] S.W. Churchill. Friction-Factor Equation Spans All Fluid-Flow Regimes. *Chemical Engineering*, 84:91–92, 1977.
- [98] N. Wakao, S. Kaguei, and T. Funazkri. Effect of Fluid Dispersion Coefficients on Particle-to-Fluid Heat Transfer Coefficients in Packed Beds: Correlation of Nusselt Number. *Chemical Engineering Science*, 34:325–336, 1979.

- [99] KTA. Reactor Core Design of High-Temperature Gas-Cooled Reactors Part 3: Heat Transfer in Spherical Fuel Elements. Technical Report KTA 3102.2, Nuclear Safety Standards Commission, 1983.
- [100] S. Yagi and N. Wakao. Heat and Mass Transfer from Wall to Fluid in Packed Beds. *American Institute of Chemical Engineers Journal*, 5:79–85, 1959.
- [101] S. Yagi and D. Kunii. Studies on Effective Thermal Conductivities in Packed Beds. *American Institute of Chemical Engineers Journal*, 3:373–381, 1957.
- [102] T.L. Albers, L. Batty, and D.M. Kaschak. High-Temperature Properties of Nuclear Graphite. In *Proceedings of the 4th International Topical Meeting on High Temperature Reactor Technology*, 2008.
- [103] S. Ball. Sensitivity Studies of Modular High-Temperature Gas-Cooled Reactor (MHTGR) Postulated Accidents. In *2nd International Topical Meeting on HTR Technology*, 2004.
- [104] IAEA. Heat Transport and Afterheat Removal for Gas Cooled Reactors Under Accident Conditions. Technical Report IAEA-TECDOC-1163, IAEA, 2000.
- [105] M. Kandula. On the Effective Thermal Conductivity of Porous Packed Beds with Uniform Spherical Particles. *Journal of Porous Media*, 14(10):919–926, 2011.
- [106] C. T. Hsu, P. Cheng, and K. W. Wong. Modified Zehner-Schlunder Models for Stagnant Thermal Conductivity of Porous Media. *International Journal of Heat and Mass Transfer*, 37:2751–2759, 1994.
- [107] A. Nouri-Borujerdi and S.I.T. Ghomsheh. An Improved Porous Media Approach to Thermal-Hydraulic Analysis of High-Temperature Gas-Cooled Reactors. *Annals of Nuclear Energy*, 76:485–492, 2015.
- [108] G. Breitbach and H. Barthels. Radiant Heat Transfer in the HTR Core After Failure of the Afterheat Removal Systems. *Transactions of the American Nuclear Society*, 31:421–422, 1979.
- [109] V. Prasad, N. Kladas, A. Bandyopadhyaya, and Q. Tian. Evaluation of Correlations for Stagnant Thermal Conductivity of Liquid-Saturated Porous Beds of Spheres. *International Journal of Heat and Mass Transfer*, 32(9):1783–1796, 1989.
- [110] C. K. Chan and C. L. Tien. Conductance of Packed Spheres in Vacuum. *Transactions of the ASME*, pages 302–308, 1973.
- [111] J. Delgado. Longitudinal and Transverse Dispersion in Porous Media. *Chemical Engineering Research and Design*, 85:1245–1252, 2007.
- [112] H. Tavassoli, E.A.J.F. Peters, and J.A.M. Kuipers. Direct Numerical Simulation of Fluid-Particle Heat Transfer in Dense Arrays of Non-Spherical Particles. In *The 14th International Conference on Fluidization From Fundamentals to Products*, 2013.
- [113] E. Smirnov, V. Kuzmin, and I. Zolotarskii. Radial Thermal Conductivity in Cylindrical Beds Packed by Shaped Particles. *Chemical Engineering Research and Design*, 82:293–296, 2004.
- [114] H. Petersen. The Properties of Helium: Density, Specific Heats, Viscosity, and Thermal Conductivity at Pressures from 1 to 100 bar and from Room Temperature to about 1800 K. Technical report, Danish Atomic Energy Commission, 1970.
- [115] KTA. Reactor Core Design of High-Temperature Gas-Cooled Reactors Part 1: Calculation of the Material Properties of Helium. Technical Report KTA 3102.1, Nuclear Safety Standards Commission, 1978.
- [116] A. T. D. Butland and R. J. Maddison. The Specific Heat of Graphite: An Evaluation of Measurements. *Journal of Nuclear Materials*, 49:45–56, 1973.
- [117] H. Gerwin, W. Scherer, A. Lauer, and G. Strydom. TINTE - A Two-Dimensional Code for Reactor Dynamics. Technical Report JUL-4294, Institute for Energy Research.

- [118] T.E. Tezduyar and Y. Osawa. Finite Element Stabilization Parameters Computed from Element Matrices and Vectors. *Computer Methods in Applied Mechanics and Engineering*, 190:411–430, 2000.
- [119] A.N. Brooks. *A Petrov-Galerkin Finite Element Formulation for Convection Dominated Flows*. PhD thesis, California Institute of Technology, 1981.
- [120] J.W. Peterson. Notes on Compressible Navier Stokes. Technical report, Idaho National Laboratory, 2015.
- [121] B.S. Kirk. *Adaptive Finite Element Simulation of Flow and Transport Applications on Parallel Computers*. PhD thesis, ASE-EM dept., The University of Texas at Austin, May 2007. <http://tinyurl.com/j7erk2u>.
- [122] G. Hauke. Simple Stabilizing Matrices for the Computation of Compressible Flows in Primitive Variables. *Computational Methods of Applied Mechanical Engineering*, 190:6881–6893, 2001.
- [123] T.E. Tezduyar and T.J.R. Hughes. Finite Element Formulations for Convection Dominated Flows with Particular Emphasis on the Compressible Euler Equations. *21st Aerospace Sciences Meeting*, 1983.
- [124] J. Shewchuk. An Introduction to the Conjugate Gradient Method Without the Agonizing Pain. Technical Report 1.25, Carnegie Mellon University, 1994.
- [125] D.F. Gill, D.P. Griesheimer, and D.L. Aumiller. Numerical Methods in Coupled Monte Carlo and Thermal-Hydraulic Calculations. *Nuclear Science and Engineering*, 185:194–205, 2017.

